

SYNTHESIS, CHARACTERIZATION, AND KINETICS
OF
MIXED COPPER-ALUMINUM AND IRON-ALUMINUM OXIDES
FOR
HIGH-TEMPERATURE
DESULFURIZATION

Thesis by
Valerie Patrick

In Partial Fulfillment of the Requirements
for the Degree of
Doctor of Philosophy

California Institute of Technology
Pasadena, California
1989

(Submitted October 27, 1988)

© 1989

Valerie Patrick

All Rights Reserved

The days go by. And then, if it is a lucky day, and a lucky laboratory, somebody makes a mistake...

The misreading is not the important error; it opens the way. The next step is the crucial one. If the investigator can bring himself to say, "But even so, look at that!" then the new finding, whatever it is, is ready for snatching. What is needed, for progress to be made, is the move based on the error.

Lewis Thomas, *The Medusa and the Snail*

Bodily exercise, when compulsory, does no harm to the body; but knowledge which is acquired under compulsion obtains no hold on the mind.

Plato, *Phaedo*

Reading is to the mind what exercise is to the body.

Sir Richard Steele, *Tatler*

ACKNOWLEDGEMENTS

I wish to thank my thesis advisor, Dr. G.R. Gavalas, for his patience and attention regarding my professional growth. This project grabbed hold of me from his first mention of it, and has been exciting and challenging ever since. Moreover, his enthusiasm and endless flow of ideas and suggestions have doubled the fun, and have helped me to maintain a high level of motivation. He has faithfully supplied input of just the right kind, at just the right time, while allowing me the freedom to pursue my research interests, and my approaches to research.

Special thanks go to certain individuals from JPL whose efforts have helped me with many aspects of this project. Lynn Lowry answered my numerous questions regarding the interpretation of x-ray data, and provided piles and piles of x-ray powder patterns. Miretta Flytzani-Stephanopoulos (now at M.I.T.) generously supplied Cu-Al-O pellets and information on the modification of a Dupont TGA to accommodate corrosive gases. Pramod Sharma was another source of answers throughout my graduate career, especially pertaining to the citrate process. Finally, Mark Anderson performed diffuse reflectance spectroscopic analysis on some Cu-Al-O samples.

A few of my peers have had a significant impact on this project. Not only is John Brewer a fine chemist in his own right, but he is genuinely interested in solving the research problems encountered by others. Johnny-my-baby greatly influenced the course of this work by saying three words: atomic absorption spectroscopy. I hope to escape CalTech before Kathy Kaneshige catches up with me to do push-ups. On the other hand, I thoroughly enjoyed the hours spent

with Kathy, obtaining Raman spectra. Fellow group members, Sergio Edelstein, Scott Northrop, and Suk Woo Nam were always willing to discuss research and to supply hands-on help in the laboratory. Not only is the technical help provided by these individuals appreciated, but in addition, they have all been good friends.

I graciously acknowledge financial support from General Electric, the Department of Energy, and the Chemical Engineering Department at CalTech.

Among my most enjoyed labors as a graduate student were the many hours spent shooting, developing, and mounting scanning electron micrographs in the company of Pat and Jean. Pat and Jean combined patience, good conversation, and expertise to create an atmosphere that I could not stay away from for longer than a few weeks at a time.

I have come to appreciate the importance of a life balanced between work and play, thanks to the example set by the many friends I have made during my stay at CalTech. Frank, Eric, and Matt deserve special recognition for throwing me in their pool, and for all their parties—I can not wait until Halloween, guys. Blowing off steam with my fellow fatburners, Tammy and Marsha, was great fun and kept me hanging in there during my last toughest weeks as a graduate student. Enthusiastic aerobic participants at N&A Plus, Brignoles, and CalTech have been very important to my mental and physical well-being. Kathy Mannix-Klauschie, aerobics coordinator at the Pasadena N&A Plus, has been a special confidant. August 19th and April 13th are never going to be the same without Anne McQueen around. Anne has tremendous potential and has been a paradigm of self-assertiveness that I have always admired. Being one of the guys with Scott, Opie, and John has certainly had its special moments—I really appreciate how terrific these guys have been to me, especially considering that they were the ones who had to live with Grumpy. In addition, I love the

“Peace, Love, & Rock ‘n Roll” tape given to me by the Ope-man.

My most memorable adventures outside of school have been as “bearfeed” in the company of Mike Kosinski, Roger Hart, and Todd Przybycien, when I participated in such activities as cross-country skiing, snow-shoeing, dodging lightning, downhill skiing, hiking by moonlight, escaping the whiteout, portaging, climbing Half Dome, riding the rapids, bushwacking, experiencing the altitude of Mounta Whitney, slipping up and slipping down San Gorgonio, and capsizing. It is great to have “officemates” that I get along with so well—usually.

I am very lucky to have a stable source of love and support from a very special family. Thank you Mom, Dad, Mike, Doug, Jim, and Lisa for shaping me into the person I am, and for all your love.

Words do not do justice in describing what Todd’s caring and understanding have meant to me. He has been my chauffeur, my best friend, my colleague, my consultant, my favorite biking enthusiast, my not-so-favorite cook, my unsurpassed manamanator, and my ultimate escape from the trials and tribulations that go along with being a graduate student. Todd’s extraordinary skill as a writer, a precision experimentalist, and a creative builder of experimental systems has been a continued inspiration for me to work hard. This thesis, which has dominated my life for four years, would not mean the same to me without Todd.

ABSTRACT

Hot-gas desulfurization is an important step for optimizing the process economics of new schemes for power generation from coal. Mixed oxides such as $\text{CuO} \cdot \text{Al}_2\text{O}_3$ and $\text{Fe}_2\text{O}_3 \cdot \text{Al}_2\text{O}_3$ are attractive as high-temperature, regenerable, desulfurization sorbents because they exhibit higher performance than CuO and Fe_2O_3 .

Mixed copper-aluminum and iron-aluminum oxides were prepared in porous form by the citrate process under various calcination conditions for subsequent reduction and sulfidation studies. The oxide samples were characterized by several techniques to determine chemical structure and texture. For the mixed copper-aluminum oxides, atomic absorption spectroscopy (AAS) provided the fractions of copper, soluble and insoluble, in hot nitric acid which closely corresponded to CuO and CuAl_2O_4 , respectively; x-ray diffraction (XRD) provided complementary information about the content of the pure and compound oxides; and a combination of x-ray line broadening, scanning electron microscopy (SEM), and transmission electron microscopy (TEM) provided an estimate of the size of crystallites or phase domains. For the mixed iron-aluminum oxides, XRD identified crystalline phases, SEM revealed the changing surface texture with iron composition, and BET surface area measurements indicated the content of free alumina.

Temperature-programmed reduction (TPR) of mixed oxides was more complex than TPR of the pure, reducible oxides. The compound oxide, CuAl_2O_4 , and part of CuO closely associated with Al_2O_3 were reduced much more slowly than bulk CuO . Similarly, the compound oxide, FeAl_2O_4 , a solid solution between Fe_3O_4 and FeAl_2O_4 , and Fe_3O_4 in close association with alumina were

reduced much more slowly than bulk Fe_3O_4 . While oxides of +1 oxidation state, Cu_2O and CuAlO_2 , were identified as reduction intermediates for TPR of CuAl_2O_4 , no oxides of +1 oxidation state were identified for reduction of iron-aluminum oxides.

Mixed copper-aluminum oxides were studied more extensively than mixed iron-aluminum oxides. The interaction between CuO and Al_2O_3 seen in TPR studies was further examined by XRD, diffuse reflectance spectroscopy, and laser Raman spectroscopy. Pronounced sintering of CuAl_2O_4 was observed to commence at temperatures in excess of 700°C , and the dispersion of copper on reduction of CuAl_2O_4 was poorer than that obtained by reduction of mixed oxide, CuO and Al_2O_3 .

In studies using a thermogravimetric analyzer, sulfidation of reduced sorbents produced high-temperature digenite ($\text{Cu}_{9+x}\text{S}_5$) in the case of copper-aluminum samples, and high-temperature pyrrhotite (Fe_{1-x}S) in the case of iron-aluminum samples as the major crystalline products. Both CuAl_2O_4 and FeAl_2O_4 were found to be resistant to sulfidation as compared to the pure oxides, CuO and Fe_2O_3 , and to mixed oxides, $\text{CuO-Al}_2\text{O}_3$ and $\text{Fe}_2\text{O}_3\text{-Al}_2\text{O}_3$. Formation of copper sulfate during air regeneration of sulfided Cu-Al-O samples was increased in the presence of free alumina.

TABLE OF CONTENTS

<i>Acknowledgements</i>	iv
Abstract	vii
<i>List of Tables</i>	xiii
<i>List of Figures</i>	xvi
CHAPTER I Introduction	1
1.1 Overview of Coal Technology	2
1.2 Coal Structure and Cleaning	4
1.3 Clean Coal Technologies	7
1.4 Motivation and Objectives	14
<i>References</i>	17
CHAPTER II Preparation and Preliminary Characterization of Cu-Al-O Sorbents	25
2.1 Background	26
2.2 Experimental Techniques	30
<i>2.2.1 Preparation</i>	30
<i>2.2.2 Wet Chemical Analysis</i>	30
<i>2.2.3 X-Ray Diffraction</i>	31
2.3 High-Temperature Calcination	32
<i>2.3.1 General Trends</i>	32
<i>2.3.2 Activation Energy</i>	33
2.4 Low-Temperature Calcination	34
<i>References</i>	37
CHAPTER III Characterization of Cu-Al-O Sorbents	50

3.1 Background	51
3.2 Experimental Techniques	57
3.2.1 Preparation	57
3.2.2 Temperature-Programmed Reduction	57
3.2.3 X-Ray Diffraction	57
3.2.4 Electron Microscopy	58
3.2.5 Laser Raman Spectroscopy	58
3.2.6 Diffuse Reflectance Spectroscopy	59
3.3 Chemical Properties According to TPR	60
3.3.1 General Trends	60
3.3.2 Effect of Sintering	61
3.3.3 Effect of Copper Aluminate	62
3.3.4 Effect of Alumina	63
3.3.5 Mechanism of Sorbent Reduction	65
3.4 Physical Characterization	68
3.5 Spectroscopic Studies	72
3.5.1 Raman Spectroscopy	72
3.5.2 Diffuse Reflectance Spectroscopy	75
References	78
 CHAPTER IV Reduction and Oxidation Studies of Copper and	
Mixed Copper-Aluminum Oxides	108
4.1 Background	109
4.2 Reduction of Porous CuO	111
4.2.1 Temperature-Programmed Studies	112
4.2.2 Isothermal Studies	114
4.3 Reduction of Cu-Al-O Materials by TPR	120

4.4 REDOX of Cu-Al-O Materials	123
<i>References</i>	129
CHAPTER V Reduction, Sulfidation, and Regeneration of	
Cu-Al-O Powders and Pellets	146
5.1 Background	147
5.2 Experimental Techniques	148
5.2.1 <i>Sorbent Preparation</i>	148
5.2.2 <i>X-Ray Diffraction</i>	149
5.2.3 <i>Scanning Electron Microscopy</i>	149
5.2.4 <i>Thermogravimetric Analysis</i>	150
5.3 Sorbent Characterization	151
5.4 Isothermal TGA Experiments	152
5.4.1 <i>Reduction and Sulfidation Experiments</i>	152
5.4.2 <i>Regeneration Experiments</i>	154
5.4.3 <i>Sulfur Chemisorption on Alumina</i>	156
5.5 TGA Experiments in the Absence of Sulfur Deposition	157
5.5.1 <i>Reduction and Sulfidation Experiments</i>	157
5.5.2 <i>Regeneration Experiments</i>	161
5.5.3 <i>Reduction and Sulfidation of Cu-Al-O Pellets</i>	162
5.5.4 <i>Simultaneous Reduction-Sulfidation</i>	164
<i>References</i>	167
CHAPTER VI Reduction and Sulfidation of Mixed Iron-	
Aluminum Oxidic Powders	192
6.1 Background	193
6.2 Experimental Techniques	194
6.2.1 <i>Sorbent Preparation</i>	194

6.2.2 X-Ray Diffraction	195
6.2.3 Scanning Electron Microscopy	196
6.2.4 Thermogravimetric Analysis	196
6.3 Sorbent Characterization	197
6.3.1 Mechanism of Sorbent Reduction	197
6.3.2 Effect of Different Fe:Al Ratios	201
6.4 Sorbent Reduction and Sulfidation	206
6.4.1 Simultaneous Reduction-Sulfidation	206
6.4.2 Consecutive Reduction-Sulfidation	207
References	213
CHAPTER VII Conclusions and Recommendations	236
7.1 Conclusions	237
7.2 Recommendations for Future Work	242
References	246

LIST OF TABLES

Table 1.1: Common organic sulfur functionalities found in coals.....	20
Table 1.2: Common minerals found in coals	21
Table 1.3: Systems studied for high-temperature desulfurization of coal-derived synthesis gas	22
Table 2.1: Techniques for low-temperature synthesis of mixed metal oxides.....	42
Table 2.2: Stoichiometric samples (1:2 molar ratio of Cu:Al) pre- pared by the citrate process	43
Table 2.3: Effect of sample size on CuAl_2O_4 yield	44
Table 2.4: Yield of CuAl_2O_4 for partitioned versus unpartitioned precursors.....	44
Table 3.1: Stoichiometric samples (1:2 molar ratio of Cu:Al) pre- pared by the citrate process for TPR studies	82
Table 3.2: Nonstoichiometric Cu-Al-O samples prepared by the citrate process	82

Table 3.3: Gibbs free energies of formation for various Cu-, Al-, and Cu-Al-containing species	83
Table 3.4: CuO and CuAl ₂ O ₄ crystallite sizes in fresh Cu-Al-O samples	83
Table 3.5: CuAl ₂ O ₄ crystallite size estimated before and after hot nitric-acid extraction	84
Table 4.1: T _{max} measured for the reduction of CuO by the method of TPR	131
Table 4.2: Activation energies measured for the reduction of CuO	131
Table 4.3: T _{max} for CuO and CuAl ₂ O ₄ peaks in Figure 4.7	132
Table 4.4: Experimental parameters for Figures 4.9 and 4.10	132
Table 4.5: Conditions of TPR and TPO for the XRD patterns of Figure 4.11	133
Table 4.6: Conditions of isothermal REDOX for the XRD pat- terns of Figure 4.12	133
Table 5.1: Fresh Cu-Al-O sorbents used for sulfidation-regenera- tion studies	170

Table 5.2: Maximum rates of reduction and sulfidation accompany- ing Figures 5.21 and 5.22.....	170
Table 6.1: Chemical and physical properties of fresh Fe-Al-O samples.....	216
Table 6.2: Kinetic data for the reduction of Fe-Al-O samples obtained from Figures 6.5 and 6.7	217
Table 6.3: Sulfidation equilibrium constants and equilibrium outlet H ₂ S concentrations for iron oxide	218
Table 6.4: Estimated conversions of Fe-Al-O samples to pyrrhotite, following consecutive reduction-sulfidation at 600°C	219

LIST OF FIGURES

Figure 1.1: A Texaco-based IGCC plant with low-temperature gas cleanup	23
Figure 1.2: A proposed IGCC plant with high-temperature gas cleanup	24
Figure 2.1: XRD patterns of fresh Cu-Al-O samples calcined at different temperatures	45
Figure 2.2: Effect of evaporation conditions on the yield of CuAl_2O_4	46
Figure 2.3: The Carter equation applied to fresh Cu-Al-O materials	47
Figure 2.4: XRD patterns of Cu-Al-O materials subjected to various calcination conditions	48
Figure 2.5: XRD patterns of CuO prepared by calcination for 4 hours at different temperatures	49
Figure 3.1: Schematic of the thermogravimetric system used for TPR experiments	85
Figure 3.2: Normalized weight-loss curves for TPR of CuO and Cu-Al-O samples	86

Figure 3.3: Enlargement of the initial reduction periods for 4 of the 7 curves depicted in Figure 3.2	87
Figure 3.4: Normalized weight-loss curves for repeated isother- mal REDOX of 11-1-CA3 (right) and 72-1-CA (left)	88
Figure 3.5: Normalized weight-loss curves for TPR of Cu-Al-O samples prepared with a molar ratio Cu:Al ₂ of 3:2	89
Figure 3.6: Normalized weight-loss curves for TPR of Cu-Al-O samples prepared with a molar ratio Cu:Al ₂ of 2:1	90
Figure 3.7: Normalized weight-loss curves for TPR of CuO (11-1-CA3, a), CuAl ₂ O ₄ (92-1-CA, c), and samples prepared with a molar ratio Cu:Al ₂ < 1 (b,d)	91
Figure 3.8: Normalized weight-loss curves for TPR of CuO (11-1-CA3, a), and Cu-Al-O samples calcined at 350°C (c) and 400°C (b)	92
Figure 3.9: XRD patterns of partially reduced 92-1-CA after quench- ing separate TPR experiments as indicated	93
Figure 3.10: XRD patterns of partially reduced 56-1-CA after quench- ing separate TPR experiments as indicated	94

Figure 3.11: XRD patterns of partially reduced 72-1-CA after quench- ing separate TPR experiments as indicated	95
Figure 3.12: Maximum intensity CuO peaks in XRD patterns of 72-1-CA reduced for short times by TPR	96
Figure 3.13: Scanning electron micrographs (markers are $1\mu\text{m}$) of fresh versus reduced 92-1-CA	97
Figure 3.14: Scanning electron micrographs (markers are $1\mu\text{m}$) of fresh versus reduced 11-1-CA3 (a and b) and 72-1-CA (c and d)	98
Figure 3.15: Scanning electron micrographs (markers are $1\mu\text{m}$) of fresh Cu-Al-O samples: 72-1-CA (a, 5 mol% CuAl_2O_4), 59-1-CA (b, 10 mol% CuAl_2O_4), 56-1-CA (c, 48 mol% CuAl_2O_4), and 19-1-CA (d, 80 mol% CuAl_2O_4)	99
Figure 3.16: Schematic of the diffraction pattern observed for a sample of 92-1-CA by TEM (Figure 3.17) with indexing accord- ing to a $\langle 111 \rangle$ zone axis for an fcc array	100
Figure 3.17: TEM bright-field image and corresponding dark-field image for the indicated diffraction spot for a a sample of 92-1-CA	101

Figure 3.18: Enlargement of a portion of the bright-field and corresponding dark-field images in Figure 3.17 (see arrow)	102
Figure 3.19: TEM bright-field image and corresponding dark-field image in poor focus showing an isolated CuAl_2O_4 crystallite	103
Figure 3.20: CuO and CuAl_2O_4 crystallite sizes in fresh Cu-Al-O samples as a function of calcination temperature (Table 3.3)	104
Figure 3.21: Scanning electron micrographs (markers are $1\mu\text{m}$) of fresh versus extracted Cu-Al-O samples: 15-1-CA (a and b), and 59-1-CA (c and d)	105
Figure 3.22: Laser Raman spectra of ultrapure CuO and two fresh Cu-Al-O samples	106
Figure 3.23: Diffuse reflectance spectra of sample 92-1-CA (a), CuAl_2O_4 reported in [3] (b), octahedrally coordinated Cu^{+2} reported in [3] (c), 10 wt% CuO on Al_2O_3 reported in [8] (d), sample 72-1-CA (e), sample 13-1-CA7 (f), ultrapure CuO (g), and Al_2O_3 (h)	107
Figure 4.1: XRD patterns of partially reduced 11-1-CA3 (pure CuO) after quenching separate TPR experiments as indicated	134

Figure 4.2: Reaction rate versus temperature for different TPR runs of CuO, sample 11-1-CA3	135
Figure 4.3: Reaction rate as a function of conversion for the isothermal reduction of CuO, sample 11-1-CA3.....	136
Figure 4.4: Roginskii-Shul'ts plots for the isothermal reduction of CuO, sample 11-1-CA3, at 400°C.....	137
Figure 4.5: An example of some Prout-Tompkins plots for the isothermal reduction of CuO, sample 11-1-CA3.....	138
Figure 4.6: H ₂ partial pressure dependence of the apparent reaction rate constant (left), and temperature dependence of the true reaction rate constant (right) for the reduction of CuO, sample 11-1-CA3	139
Figure 4.7: Reaction rate versus temperature for six Cu-Al-O samples (left) and CuO (right) prepared by the citrate process	140
Figure 4.8: Values of T _{max} estimated from Figure 4.8 for CuO and CuAl ₂ O ₄ as a function of concentration (left) and calcination temperature (right).....	141

Figure 4.9: Normalized weight-loss curves for isothermal REDOX of CuAl ₂ O ₄ (sample 92-1-CA) at 463°C (a), 506°C (b), 636°C (c), and 774°C (d).....	142
Figure 4.10: XRD patterns accompanying Figure 4.9 (left) com- pared to those of fresh Cu-Al-O samples (right) pre- pared by calcination at different temperatures	143
Figure 4.11: XRD patterns for 56-1-CA (left), 15-1-CA (middle), and 92-1-CA (right) oxidized by TPO following TPR	144
Figure 4.12: XRD patterns for 72-1-CA (left) and 33-1-CA6 (right) following isothermal REDOX at 600°C (a), 700°C (b), and 800°C (c).....	145
Figure 5.1: Schematic of the thermogravimetric system used for exper- iments requiring the use of corrosive gases, or of mixtures containing more than one reactive component, or both.....	171
Figure 5.2: XRD patterns of samples 11-1-CA3 (a), 33-1-CA6 (b), and 72-1-CA (c)	172
Figure 5.3: Scanning electron micrographs (markers are 1μm) of fresh Cu-Al oxides prepared by the citrate process.....	173

Figure 5.4: Normalized weight-loss curves for TPR of 11-1-CA3 (a), 72-1-CA (b), and 33-1-CA6 (c) using a heating rate of 1.7°C/min from 233°C to 912°C.....	174
Figure 5.5: Normalized weight-loss curves for reduction, sulfida- tion, and air regeneration, in series, of sample 72-1-CA at 600°C (a), 700°C (b), 800°C (c), and 900°C (d).....	175
Figure 5.6: Scanning electron micrographs of sample 72-1-CA (markers are 1μm) in a fresh state (a), after reduction at 700°C (b), and after step-wise reduction-sulfidation at 700°C in a platinum pan (c), and in a quartz pan (d)	176
Figure 5.7: Normalized weight-loss curves for reduction followed by sulfidation of pure Al ₂ O ₃ contained in a platinum pan at different temperatures.....	177
Figure 5.8: Normalized weight-loss curves for reduction, sulfidation, and regeneration, in series, of different samples at 700°C contained in a platinum (P) and a quartz (Q) pan	178
Figure 5.9: Normalized weight-loss curves for reduction, sulfidation, and regeneration, in series, of different samples at 800°C contained in a platinum (P) and a quartz (Q) pan	179

Figure 5.10: XRD patterns of samples 11-1-CA3 (a), 33-1-CA6 (b), and 72-1-CA (c) cooled following sulfidation at 700°C (left) and 800°C (right)	180
Figure 5.11: Scanning electron micrographs of sample 33-1-CA6 (markers are 1μm) in a fresh state (a), after reduction at 700°C (b), and after step-wise reduction-sulfidation at 700°C in a platinum pan (c), and in a quartz pan (d)	181
Figure 5.12: Scanning electron micrographs of sample 11-1-CA3 (markers are 10μm) in a fresh state (a), and after step-wise reduction-sulfidation at 700°C (b), and of a pellet (markers are 1μm) reduced (c), and reduced, then sulfided at 700°C (d)	182
Figure 5.13: Maximum rate of sulfidation as a function of the extent of reduction at 400°C for sample 72-1-CA	183
Figure 5.14: Scanning electron micrographs of a pellet (markers are 10μm) reduced at 700°C (a), and reduced, then sulfided at 700°C (b) with enlargements (markers are 1μm) of the bottom center (c) and upper right (d) of micrograph b	184
Figure 5.15: Normalized weight-loss curves for consecutive reduction-sulfidation-regeneration of Cu-Al-O pellets at 700°C (left) and 725°C (right)	185

Figure 5.16: Plots of reaction rate, $\frac{d\alpha}{dt}$, versus time, t, obtained by transformation of the data contained in Figure 5.15	186
Figure 5.17: Normalized weight-loss curves for the isothermal reaction of sample 11-1-CA3 with a mixture of 13% H ₂ , 4% H ₂ S, and balance N ₂ (- - -), and step-wise reduction-sulfidation (—) of sample 11-1-CA3, both followed by regeneration in air	187
Figure 5.18: Normalized weight-loss curves for the isothermal reaction of sample 72-1-CA with a mixture of 13% H ₂ , 4% H ₂ S, and balance N ₂ (- - -), and step-wise reduction-sulfidation (—) of sample 72-1-CA, both followed by regeneration in air	188
Figure 5.19: Normalized weight-loss curves for the isothermal reaction of sample 33-1-CA6 with a mixture of 13% H ₂ , 4% H ₂ S, and balance N ₂ (- - -), and step-wise reduction-sulfidation (—) of sample 33-1-CA6, both followed by regeneration in air	189
Figure 5.20: Rate of reduction (first peak) and rate of sulfidation (second peak) versus time for samples 72-1-CA (left), 33-1-CA6 (middle), and 11-1-CA3 (right) at 700°C	190
Figure 5.21: Rate of reduction (first peak) and rate of sulfidation (second peak) versus time for samples 72-1-CA (left), 33-1-CA6 (middle), and 11-1-CA3 (right) at 800°C	191

Figure 6.1: XRD patterns of fresh F650 (a) and FA650 (b), and corresponding normalized weight-loss profiles for TPR using a heating rate of $1.7^{\circ}\text{C}/\text{min}$ from 233°C to 912°C	220
Figure 6.2: XRD patterns of partially reduced F650 after quenching during the TPR experiment as indicated (the single peak for Fe is observed only in the bottom pattern)	221
Figure 6.3: XRD patterns of partially reduced FA650 after quenching during the TPR experiment as indicated.....	222
Figure 6.4: Reaction rate versus time for TPR of F650 (- - -) and FA650 (—).....	223
Figure 6.5: Normalized weight-loss profiles for TPR of Fe-Al-O samples calcined at 600°C (- - -), 700°C (—), and 800°C (— -).....	224
Figure 6.6: Scanning electron micrographs (markers are $1\mu\text{m}$) of fresh samples comparing F650 to Fe-Al-O materials calcined at 600°C with different Fe:Al ratios.....	225
Figure 6.7: Reaction rate versus time for TPR of Fe-Al-O samples calcined at 600°C (- - -), 700°C (—), and 800°C (— -).....	226

Figure 6.8: Normalized weight-loss curves for the reaction of FA650 (—) and F650 (- - -) at 700°C with a mixture containing 13% H ₂ , 4% H ₂ S, and balance N ₂ followed by regeneration in air	227
Figure 6.9: Normalized weight-loss curves for reduction followed by sulfidation at 600°C of 2FA600 (—), 2FA700 (- - -), and 2FA800 (— -)	228
Figure 6.10: Sulfur uptake versus extent of reduction for different Fe-Al-O samples	229
Figure 6.11: The XRD pattern of F2A600 sulfided at 600°C	230
Figure 6.12: Normalized weight-loss curves for reduction followed by sulfidation at 600°C of 2FA600 (a), F650 (b), FA600 (c), and F2A600 (d)	231
Figure 6.13: Scanning electron micrographs (markers are 1μm) of Fe-Al-O samples reduced at 600°C for ~ 15 minutes	232
Figure 6.14: Scanning electron micrographs (markers are 1μm) of Fe-Al-O samples sulfided at 600°C for ~ 35 minutes	233

Figure 6.15: Scanning electron micrographs of F2A600 (markers are $1\mu\text{m}$)	
in a fresh state (a), after reduction at 600°C (b), and after	
step-wise reduction-sulfidation at 600°C (c), with an	
enlargement of micrograph c (d)	234

Figure 6.16: Scanning electron micrographs of 2FA600 (markers are $1\mu\text{m}$)	
in a fresh state (a), after reduction at 600°C (b), and after	
step-wise reduction-sulfidation at 600°C (c)	235

CHAPTER I

Introduction

1.1 Overview of Coal Technology

Coal emerged as a primary energy source with the industrial revolution in the 1760's and became a secondary energy source with the rapid growth of crude oil and natural gas production in the 1950's. Although coal can not compete with crude oil and natural gas in terms of the cost and economic impact involved in the production of synthetic fuels, coal is competitive with crude oil for generation of electricity. Coal will remain an indispensable source of energy because while world supplies of petroleum oil are diminishing, coal reserves are abundant. Thus, improvement and advancement of current coal technology must continue.

There are four major markets for coal consumption: house and commercial use (*e.g.*, briquettes), industry (*e.g.*, coke ovens), transportation, and electricity [1,2]. In 1950, when coal still accounted for approximately 60% of world energy production, primary coal consumption was by coke manufacture in industry. Coal markets have shifted significantly since 1950 in response to oil and natural gas markets. By 1970, coal was used primarily by electricity-generation utilities (~57%), and secondarily by industry (~40%). In North America alone, 81% of the coal produced in 1978 was used for the production of electricity.

Production of electricity from coal began in the 19th century: fuel gas, produced by gasifiers for illumination, was used in Europe and the United States for small-scale electricity generation [3]. Early in the 20th century, however, coal-fired central stations were invented for large-scale production of electricity. With this invention, the use of coal-derived fuel gas for power generation was discontinued. In 1903, a modified steam turbine, originally developed as a propulsion system for marine applications, was recognized as having potential

for electricity generation. Soon after this recognition, central-station, pulverized coal plants became the dominant technology for generating electric power. Improvements in thermal efficiency grew steadily until 1960, when a plateau in efficiency gain was attained. A modern, pulverized coal steam plant converts approximately one-third of the thermal energy in coal to electric power.

Currently, plants providing coal-derived electricity are operating at maximum efficiency, but are plagued by environmental regulations on atmospheric pollutants and solid waste disposal. For example, in existing pulverized coal-combustion processes, SO_2 , NO_x , and particulates are produced during combustion, and large quantities of waste sludge are produced during SO_2 removal in wet scrubbers. New controls on emission of SO_2 , NO_x , and particulates, and on storage of waste sludge [4] mean added cost for improvement. This cost, unfortunately, can not be offset by efficiency gain. Thus, parallel to improving existing pulverized coal technology, electric utilities are investigating new, cleaner, alternative technologies. In particular, there are three major projects under current development aimed at simultaneously maintaining coal as a source of low-cost electricity, and combatting the environmental problems associated with its usage. These projects are improvement of the existing pulverized coal-combustion process, expansion of fluidized bed combustion (FBC), and integration of a coal gasifier with an advanced, high-efficiency, power-generation system such as combined-cycle power generation or molten carbonate fuel cell [5]. Each of these projects is associated with a coal conversion process that requires sulfur removal at a specific stage: during coal conversion for FBC, and after coal conversion for coal gasification, or pulverized coal combustion.

1.2 Coal Structure and Cleaning

Coal consists of three major components, which in order of increasing concentration are moisture, mineral matter, and organic matter. Coal is a valuable substance because its richest component, organic matter, can be converted into energy. The amount and distribution of mineral matter in the coal, however, dictates economic and technical limitations to energy-conversion processes. For example, mineral matter content affects the ash-fusion temperature and slag viscosity of the coal. If ash slagging occurs during coal combustion or coal gasification, then the overall operation and heat-transfer efficiency of the system can be affected. Furthermore, sulfur incorporated in mineral matter and both sulfur and nitrogen incorporated in the organic matrix of coal are major sources of atmospheric pollutants during coal combustion and coal gasification. In the oxidizing environment produced during coal combustion, nitrogen forms toxic oxides (NO_x), while sulfur forms SO_2 . In the reducing environment prevailing during coal gasification, nitrogen forms ammonia (NH_3) and sulfur forms H_2S . Sulfur dioxide emissions lead to acid rain, the formation and transport of sulfuric acid [65], and both hydrogen sulfide and NO_x are highly toxic. The challenge of new coal technologies is to accommodate the wide range of economic and technical limitations resulting from the complex nature of coal.

Coal is a heterogeneous material formed by the processes of peatification and coalification. During peatification, bacteria decompose less resistant plant material into various gases, while more resistant plant tissues, lignin and cellulose, survive and concentrate into a peat deposit [7]. Peat so derived accumulates in swamps where it incorporates into sedimentary strata and transforms into coal by slow physical and chemical changes known collectively as coalification. The

metamorphosis of peat into coal is a geological process that occurs over a time frame of approximately 200 million years. There are as many varieties of coals as there are source materials, depositional conditions, temperature-pressure histories, and degrees of coalification.

Coals are classified by two independent categories, type or rank. Coal type refers to the relative proportions of macerals and minerals present. Macerals, the primary species in coal, are organic substances of three major classes: vitrinite, liptinite, and inertite. Minerals are inorganic constituents arising from a variety of sources and emplaced in coal throughout its formation. Coal rank refers to the degree of coalification. Ranks in order of increasing extent of metamorphosis include lignites, sub-bituminous coals, bituminous coals, and anthracites. Coals of different ranks vary in appearance and composition because of the changes accompanying coalification: decreases in moisture content, oxygen content, volatile matter, and aromaticity, and increases in carbon content and density [8]. Liptinites, in general, are hydrogen-rich and thus can be converted to gaseous fuel more readily than vitrinites and inertites. However, vitrinites comprise greater than 80% of the maceral composition of a coal and thus determine coal convertability.

The chemical structure of the organic coal matrix is not certain. There is evidence, however, that the organic matter is a cross-linked structure of high molecular weight consisting of mainly carbon, hydrogen, oxygen, nitrogen, and sulfur [9]. There has been extensive research on the chemical structure and reactivity of the organic sulfur compounds in coal [10-13]. Organic sulfur is sulfur chemically bound to the hydrocarbon structure of coal. Since it is difficult to isolate organic sulfur compounds without altering the organic substituents, organic sulfur is identified by the functional group in which it appears. The

types of organic sulfur compounds that have been isolated (Table 1.1) are categorized as thiophenes, sulfides, or thiols. The relative stability of these sulfur compounds to thermal decomposition and hydrogenation (to H_2S) is in order of increasing stability: aliphatic thiols, aliphatic sulfides, cyclic sulfides, aryl thiols, aryl sulfides and thiophenes. Unfortunately, most of coal's organic sulfur is in the form of the most chemically inert structures, thiophenes and aryl sulfides. For example, the organic sulfur content of bituminous coal is approximately 50% thiophenic sulfur, 30% aryl sulfide, and 20% aliphatic sulfide. Chemical [5,14-16] and biological [17-19] techniques for removal of organic sulfur from coal prior to coal conversion are in early stages of development. Removals of 20 to 50% of the organic sulfur have been reported by implementation of biological techniques; however, there is no information about the effect of this removal on the energy content of the coal. Potential drawbacks to chemical and biological desulfurization are incomplete desulfurization requiring additional treatment, and degradation of the energy value of the coal.

The total sulfur content of coal varies from 0.2 to 10 weight % but is 1 to 4 weight % for the majority of coals [10]. The ratio of inorganic to organic sulfur is between 4:1 and 1:3 but is most often close to 2:1. Inorganic sulfur is in the form of disulfides, sulfides, and sulfates. These species represent a small fraction of the major minerals that comprise the mineral matter of coal. Common coal minerals are ordered approximately from most abundant to least abundant, according to classification in Table 1.2 [7]. Mineral matter composition is unique to every coal as a result of several mechanisms for incorporation of minerals throughout coalification.

Mineral matter or ash leads to problems during coal conversion because at high temperatures it is thermally altered, partially volatilized and melted. The

ash component of coal is largely reduced by physical and biological cleaning techniques implemented prior to coal conversion. Traditional physical processes involve crushing the coal to liberate some of the inherent mineral matter from the organic coal matrix, followed by a separation based solely on differences in particle densities. This separation effectively removes most of the adventitious mineral matter, ash present as discrete particles, and a portion of the inherent mineral matter, ash finely distributed within particles, but is not selective to pyritic sulfur. A new physical process under development involves the addition of bacteria to a broth containing finely ground coal. The bacteria change the surface properties of pyrite particles, causing them to settle more readily. While cleaning techniques effectively remove a large portion of adventitious mineral matter, a fraction of sulfur-containing inherent mineral matter and all organic sulfur are inaccessible to these techniques.

1.3 Clean Coal Technologies

The new chemical and physical cleaning methods under development are one step towards the improvement of existing pulverized coal combustion facilities [5,20]. Sulfur that can not be removed by coal cleaning will form SO_2 during combustion. The SO_2 is currently removed from the flue gas by wet scrubbing, which requires large volumes of water to create an alkaline slurry for reaction with the SO_2 . Since disposal of the scrubber sludge is becoming severely constrained, methods to convert the sludge to commercial products are being considered. In addition, two new dry scrubbing approaches are under development. One approach is spray drying, which involves a slurry of calcium hydroxide that dries as it reacts with SO_2 in the exhaust stream. The second

approach is injection of dry calcium-based sorbents either directly into the flame region or into the pipeline located downstream in the convective heat transfer region. In this configuration, the sorbent combines with SO_2 as it is generated, forming a solid waste.

Since combustion involves a rapid oxidation of coal, NO_x formation from the organic nitrogen in coal is also a concern. Modification of the combustion process is being investigated to reduce NO_x emissions. Specific alternatives being studied, for example, are mixing the fuel and air more gradually, and staging the combustion. A technology under development is selective catalytic reduction, which involves mixing the flue gas with ammonia in the presence of a catalyst to convert NO_x into N_2 and water. Unfortunately, investment into reducing SO_2 and NO_x emissions can not be offset by improvements in thermal efficiency.

FBC is a new technology developed within the last two decades that has the advantages of fuel flexibility and retention of pollutants in the furnace [5]. Coal and limestone are fluidized by air jets in a furnace so that as coal combustion proceeds, the limestone particles react with SO_2 and are removed as dry-waste product. An FBC unit can remove up to 95% of coal sulfur. NO_x emissions are below EPA standards because of the low temperature (800 to 900 °C) of the combustion process. However, regulations regarding solid waste disposal are a potential economic disadvantage to this technology.

Coal gasification involves two processes: high-temperature chemical conversion of carbon and hydrogen in coal to dominantly CO and H_2 , and partial combustion of coal to generate thermal energy in excess of that required by the chemical conversion processes [21]. The types of gasification systems available are fixed bed, fluidized bed and entrained bed. Depending on the coal com-

position, reactant gas mixture, operating conditions, and gasifier configuration, a wide range of product gas compositions are possible. Product gases can be classified by calorific value or acid gas content [22]. Calorific value is the energy content of the gas-per-unit volume and is the major factor in determining the cost of transmitting the gas for consumption. Acid gas content is the amount of CO₂ and H₂S in the product gas. Key gasification reactions for the carbon present in coal are the water-gas reaction with inlet steam:



and the partial-combustion reaction with inlet oxygen:



The following reactions may also occur:



known as the shift and methanation reactions, respectively [23]. An oxygen-deficient, gaseous feed containing mainly steam results in an overall reducing environment in the gasifier so that sulfur in the coal is released as primarily H₂S while nitrogen in the coal is released as N₂ and ammonia. Traces of other compounds such as COS and hydrogen cyanide are also formed. All the above reactions are exothermic with the exception of the water-gas reaction. Thus, the partial combustion of coal supplies most of the thermal energy needed for the production of fuel components, H₂ and CO.

The H₂S level that can be tolerated in the coal-derived gas depends on the type of power-generation facility the fuel gas is being supplied to. Two

high-efficiency, power-generation technologies under current development are combined-cycle power production and molten carbonate fuel cell.

Power production by combined-cycle technology is at a more advanced stage of development than power production by molten carbonate fuel cell . Moreover, the H_2S level of the fuel gas need meet only environmental regulations, a level of below approximately 100 ppm. Combined cycle refers to the use of gas turbine and steam cycle in series resulting in a higher efficiency than can be realized by steam turbines alone as are currently used in pulverized fuel power stations [22]. In the gas turbine, hot combustion gases from the coal gasifier are expanded to drive the compressor and generate power. Exhaust gases from the gas turbine are used to generate further power in a conventional steam cycle. It is important for the coal-derived gas entering the gas turbine to be at a high temperature because the higher the inlet temperature, the more work that can be extracted during its expansion. Maximizing the efficiency of the gas turbine in this way also improves the efficiency of the ensuing steam turbine which is limited by the temperature at which the heat can be recovered.

The fuel gas must have an H_2S level of less than 1 ppm for use in a molten carbonate fuel cell because of the problem of poisoning by sulfur compounds. The advantage of a fuel cell over gas and steam turbines is the absence of the Carnot-cycle, efficiency limitation [22]. Chemical energy is converted directly to electricity in a fuel cell, whereas heat energy is converted to mechanical power in a turbine. A molten carbonate fuel cell consists of nickel-based electrodes separated by an alumina matrix impregnated with a mixture of alkaline carbonates. The cell consumes both H_2 and CO and operates in a temperature range of 600 to $700^{\circ}C$ and a pressure range of 3 to 10 bars.

Commercially available processes for clean-up of H_2S are low-temperature

techniques operating at near-ambient temperatures. For example, there are a number of commercial processes based on reversible physical absorption of H_2S or CO_2 or both in a solvent. The recovered H_2S can then be converted to elemental sulfur either by the Claus process or by liquid-phase oxidation. In the Claus process, H_2S is partially burned in a furnace to produce elemental sulfur and SO_2 . Subsequently, the SO_2 and remaining H_2S are reacted at 200°C over an alumina catalyst to complete the conversion to elemental sulfur [22]. In liquid-phase oxidation, first the H_2S -rich gas stream is washed with an aqueous solution containing a proprietary mixture of inorganic salts, and, second, the salts are regenerated by oxidation with air to recover elemental sulfur. During washing, the solution absorbs the H_2S , while the salts selectively oxidize the H_2S to elemental sulfur.

Figure 1.1 illustrates the general configuration for an integrated, gasification combined-cycle (IGCC) power plant that uses commercially available low-temperature gas cleanup. Gas cleanup consists of particulate removal by water scrubbing and, subsequently, desulfurization by the Selexol process, a reversible physical absorption of H_2S in a dimethyl ether of polyethylene glycol [22]. Since the Selexol process operates at near ambient temperature, the hot fuel gas exiting the gasifier at $\sim 2400^\circ\text{F}$ must be cooled in two stages to near ambient temperature; then the clean fuel gas must be reheated to at least $\sim 600^\circ\text{F}$ for use in the gas turbine [24,25]. Extensive economic evaluation of this plant known as the oxygen-based Texaco IGCC plant reveals that the capital for construction would be approximately equivalent to that required for a coal-fired steam plant equipped with adequate environmental control, and that electricity production would be cost-competitive with that produced by a conventional, coal-fired steam plant. The substitution of high-temperature gas cleanup for low-

temperature gas cleanup would further increase the economic margin between IGCC and coal-fired steam plants, because high-temperature gas cleanup has the potential to reduce sulfur removal costs and to eliminate gas cooling and reheating equipment. The basic building blocks for an IGCC plant equipped with hot-gas cleanup technology are shown in Figure 1.2.

One high-temperature desulfurization approach is the addition of dolomitic sorbent to a fluidized bed gasifier for *in situ* removal of sulfur. This approach can remove over 90% of coal sulfur, which meets the current environmental regulation of ≤ 100 parts per million (ppm) H_2S in the fuel gas. An alternative high-temperature desulfurization approach is the selective reaction of H_2S in the coal-derived gas with a sorbent. This approach has the potential to reduce the H_2S concentration of a coal-derived gas below 1 ppm. Furthermore, the sorbent is chosen to be regenerable with the potential for elemental sulfur recovery. A regenerable sorbent is preferred over the nonregenerable dolomitic sorbent, because solid waste production is dramatically reduced. In addition, desulfurization using a sorbent is applicable to all three of the available gasifiers while *in situ* sulfur removal is limited to one type of gasifier. Process flexibility is an essential ingredient to accommodate the complexity of the raw material, coal. Also, while *in situ* desulfurization produces a suitable purity for application in a combined-cycle, gas-turbine, power plant, it can not meet the 1 ppm sulfur level required by a molten carbonate fuel cell.

As of 1978, the feasibility of using a number of different metal oxides as high-temperature H_2S sorbents had been extensively studied. The sorbents tested for this application included oxides of iron, zinc, calcium, magnesium, manganese, copper, nickel, cobalt, lead, tin, bismuth, cadmium, niobium, tantalum, molybdenum, tungsten, chromium, sodium, and vanadium. Among these,

oxides of iron, zinc, calcium, and copper were reported as the most promising, high-temperature H_2S sorbents [26,27]. Each of these oxides exhibited distinct advantages and disadvantages when exposed to simulated, hot coal-gas containing H_2O , H_2 , CO , CO_2 , H_2S , and N_2 . For example, while iron oxide exhibited the most rapid sulfidation kinetics, it did not possess the most favorable thermodynamic efficiency, defined such that a high efficiency is equivalent to a low-equilibrium level of H_2S above the sorbent. Calcium oxide, on the other hand, possessing a higher thermodynamic efficiency than iron oxide, exhibited kinetic limitations because of the accumulation of a sulfide diffusion barrier, and the deposition of carbon. Zinc oxide, similarly, possessing a higher thermodynamic efficiency than either calcium oxide or iron oxide, exhibited slower kinetics than either calcium oxide or iron oxide. Furthermore, zinc oxide at temperatures near or in excess of 650°C slowly reduced to volatile elemental sulfur. Copper oxide, possessing the highest thermodynamic efficiency, was reported to be present as metallic copper in the coal-gas atmosphere, leading to a lower thermodynamic efficiency than is theoretically possible for copper preserved in the form of cupric or cuprous oxide. Iron oxide suffered from a similar limitation, being present as magnetite rather than hematite in the coal-gas atmosphere, which possesses the lower thermodynamic efficiency. It was concluded [26], however, that the best strategy for high-temperature H_2S removal was sorption of H_2S by iron oxide or copper oxide, followed by regeneration of the sulfided sorbent in air. The SO_2 produced during regeneration would then be captured by calcium, or converted to elemental sulfur by reduction over carbon.

Liquid-phase sorbents have been considered for high-temperature desulfurization in addition to solid-phase metal oxides. Liquid-phase sorbents include molten metals and molten salts. For example, molten potassium carbonate is

reported to possess a higher thermodynamic efficiency than iron oxide at temperatures above 760°C.

A summary from contract and patent literature up to 1980 of the major liquid-phase and solid-phase sorbents under investigation for use in a high-temperature desulfurization process is reproduced in Table 1.3 [28]. Solid-phase sorbents include dolomite calcined under various conditions, supported metal oxides, supported metals, supported mixed metals, and unsupported metal oxides. Liquid-phase sorbents include molten metals and molten salts.

1.4 Motivation and Objectives

In the last decade, the Department of Energy, the electric utility industry, and various industrial and academic research organizations have considered performance of mixed metal oxides in different configurations for removal of H_2S at high temperatures from simulated and actual coal-derived gases. Key to these performance evaluations has been the type of metal oxide system used. For example, single metal oxides, supported metal oxides, and mixed metal oxides have been considered for application to high-temperature desulfurization. The mixed metal oxides have been prepared by a variety of techniques, including solid-state reaction, coprecipitation, and complexation.

One study [29] pioneered the citrate process, a complexation technique, to synthesize regenerable, high-temperature, desulfurization sorbents. The sorbents, binary and ternary metal oxides, exhibited unexpectedly high performance in desulfurization tests. For example, copper oxide has been one sorbent considered for desulfurization [26-30], but its sulfidation equilibrium constant was not high enough to provide adequate H_2S removal. When prepared in asso-

ciation with aluminum oxide by the citrate process, however, copper oxide had much better H_2S removal [27]. Similarly, for iron oxide prepared in association with aluminum oxide, observed sulfidation equilibrium was higher than that for pure iron oxide (Chapter VI).

The purpose of this work was to examine the nature of the interaction between copper oxide and aluminum oxide in binary oxides of copper and aluminum prepared by the citrate process. Therefore, this study involved preparation of the mixed copper-aluminum oxides, examination of the effect of preparation variables on the properties of the resulting binary oxides, and development of extensive physical and chemical characterization techniques for the binary oxides. This information was needed for a subsequent investigation of the physical and chemical transformations accompanying the sulfidation and regeneration of these materials. In addition, some of the same techniques were extended to a brief study of binary iron-aluminum oxides.

In the next chapter, details of the citrate complexation method for synthesis of binary copper-aluminum oxides are discussed. In particular, wet chemical analysis and x-ray diffraction are used to characterize the products as a function of preparation conditions. In Chapter III, techniques commonly used for characterization of impregnated catalysts have revealed information regarding the shape, size, and boundaries of phases in bulk, mixed, copper-aluminum oxides. These techniques include temperature-programmed reduction (TPR), scanning electron microscopy (SEM), transmission electron microscopy (TEM), Raman spectroscopy, and diffuse reflectance spectroscopy. The contents of Chapters II and III, with the exception of Section 3.5, have been accepted for publication (to *J. Amer. Cer. Soc.*). Chapter IV presents supplemental reduction and oxidation experiments not included in Chapter III, and additional interpretation

of TPR data presented in Chapter III. In addition, Chapter IV includes a kinetic study of the reduction of copper oxide at high temperature, based on data obtained by isothermal gravimetry. Chapter V presents the mechanism and relative reaction rates accompanying reduction, sulfidation, and regeneration of Cu-Al-O materials prepared by the citrate process. Techniques such as XRD, SEM, and thermogravimetric analysis are used to obtain this information. The bulk of the material contained in Chapter V, with the exception of Sections 5.3.3 and 5.3.4, has been combined with information obtained from independent microreactor experiments, and accepted for publication (to *Ind. Engrng. Chem. Res.*). Chapter VI is a brief look at the characterization, reduction, and sulfidation of Fe-Al-O materials prepared by the citrate process, using some of the same techniques mentioned above in connection with the Cu-Al-O system. The content of Chapter VI is currently under preparation for submission to a journal. Finally, Chapter VII summarizes the major conclusions of this project with recommendations for future work in this area.

REFERENCES

1. Merrick, D., *Coal Combustion and Conversion Technology* (Macmillan Publishers Ltd.: London, 1984), p.1-23,101-163.
2. Hottel, H.C. and Howard, J.B., *New Energy Technology—Some Facts and Assessments* (The MIT Press: Cambridge, Massachusetts, 1971), p.3-11.
3. Alpert, S.B. and Gluckman, M.J., "Coal Gasification Systems for Power Generation," *Ann. Rev. Energy*, **11**, 315, 1986.
4. Yeager, K.E., "Coal Clean-up Technology," *Ann. Rev. Energy*, **5**, 357, 1980.
5. Shepard, M., "Coal Technologies for A New Age," *EPRI Journal*, **7**(11), 4, 1988.
6. Gould, R.R., "Energy and Acid Rain," *Ann. Rev. Energy*, **9**, 529, 1984.
7. Renton, J.J., "Mineral Matter in Coal" in *Coal Structure* ed. by R.A. Meyers (Academic Press: New York, 1982), p.283.
8. Neavel, R.C., "Coal Structure and Coal Science: Overview and Recommendations" in *Coal Structure* ed. by M.L. Gorbaty (American Chemical Society: Washington, D.C., 1981), p.1.
9. Green, T., Kovac, J., Brenner, D. and Larsen, J.W., "The Macromolecular Structure of Coals" in *Coal Structure* ed. by R.A. Meyers (Academic Press: New York, 1982), p.199.
10. Attar, A. and Corcoran, W.H., "Sulfur Compounds in Coal," *Ind. Eng. Chem. Prod. Res. Dev.*, **16**(2), 168, 1977.
11. Attar, A., "Sulfur Removal in Coal Pyrolysis and Hydrogenation," *Chem. Eng. Prog., Tech. Manual*, "Coal Processing Technology," **4**, 26, 1978.
12. Attar, A., "Chemistry, Thermodynamics and Kinetics of Reactions of Sul-

- phur in Coal-Gas Reactions: A Review," *Fuel*, **57**, 201, 1978.
13. Attar, A. and Dupuis, F., "Data on the Distribution of Organic Sulfur Functional Groups in Coals" in *Coal Structure* ed. by M.L. Gorbaty (American Chemical Society: Washington, D.C., 1981), p.239.
 14. Kalena, W.S., *Ph.D. Thesis*, California Institute of Technology, 1984.
 15. Kralik, J.G., *Ph.D. Thesis*, California Institute of Technology, 1982.
 16. Vasilakos, N.P., *Ph.D. Thesis*, California Institute of Technology, 1980.
 17. Olson, G.J. and Brinckman, F.E., "Bioprocessing of Coal," *Fuel*, **65**, 1638, 1986.
 18. Chandra, D., Roy, P., Mishra, A.K., Chakrabarti, J.N. and Sengupta, B., "Microbial Removal of Organic Sulphur from Coal," *Fuel*, **58**, 549, 1979.
 19. Gökçay, C.F. and Yurteri, R.N., "Microbial Desulfurization of Lignites by a Thermophilic Bacterium," *Fuel*, **62**, 1223, 1983.
 20. Whitaker, R., "Developing the Next Generation of Sulfur Controls," *EPRI Journal*, **12**(6), 23, 1987.
 21. Marqueen, T.J., Carbone, D.J. and Ligammari, J., "Coal Gasification Combined Cycle Systems-Technical Horizons," *Proc. Am. Pow. Conf.*, **48**, 235, 1986.
 22. Merrick, D., *Coal Combustion and Conversion Technology* (Macmillan Publishers Ltd.: London, 1984), p.101.
 23. Clark, E.J., "Major Technical Issues Facing Low and Medium Btu Gasification" in *Coal Conversion Technology* ed. by A.H. Pelofsky (American Chemical Society: Washington, D.C., 1979), p.183.
 24. Gluckman, M.J. and Louks, B.M., "Second Generation Gasification Combined-Cycle Power Plants for U.S. Utilities-Detailed Performance and Cost Estimates," *Appl. Energy*, **11**, 85, 1982.

25. Howard-Smith, I. and Werner, G.J., *Coal Conversion Technology* (Millmeran Coal Pty. Ltd.: New Jersey, 1976).
26. MERC Hot Gas Cleanup Task Force, "Chemistry of Hot Gas Cleanup in Coal Gasification and Combustion," Final Report (MERC/SP 78/2, February, 1978).
27. Westmoreland, P.R. and Harrison, D.P., "Evaluation of Candidate Solids for High-Temperature Desulfurization of Low-BTU Gases," *Environ. Sci. Technol.*, **10**(7), 659, 1976.
28. Giner, Inc., "Studies Involving High Temperature Desulfurization/Regeneration Reactions of Metal Oxides for the Fuel Cell Program," Final Report, Argonne National Laboratory, 12, 1981.
29. Flytzani-Stephanopoulos, M., Tamhankar, S.S., Gavalas, G.R., Bagajewicz, M.J. and Sharma, P.K., "High-Temperature Regenerative Removal of H₂S by Porous Mixed Oxide Sorbents," *Prepr. Pap. Am. Chem. Soc. Div. Fuel Chem.*, **30**(4), 16, 1985.
30. Westmoreland, P.R., Gibson, J.B. and Harrison, D.P., "Comparative Kinetics of High-Temperature Reaction Between H₂S and Selected Metal Oxides," *Environ. Sci. Technol.*, **11**(5), 488, 1977.

Table 1.1 : Common organic sulfur functionalities found in coals.

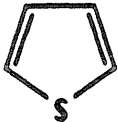
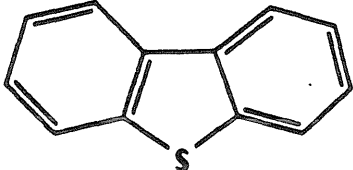
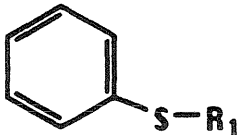
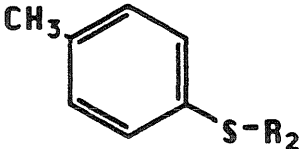
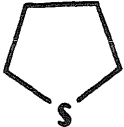
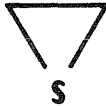
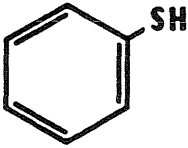
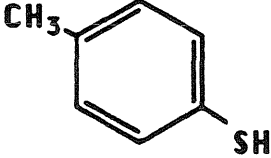
<u>Classification</u>	<u>Examples</u>
Thiophenes	  <p>etc.</p>
Aryl Sulfides	  <p>etc.</p>
Cyclic Sulfides	  <p>etc.</p>
Aliphatic Sulfides	R_1-S-R_2
Aryl Thiols	  <p>etc.</p>
Aliphatic Thiols	R_1-SH

Table 1.2: Common minerals^a found in coals.

Quantity	Classification		Name	Formula
Major	Silicates	Clay Minerals	Kaolinite	$\text{Al}_2\text{Si}_2\text{O}_5(\text{OH})_4$
			Illite	^b
			Mixed Layer	^c
			Chlorite	$(\text{MgFeAl})_6(\text{SiAl})_4\text{O}_{10}(\text{OH})_8$
			Quartz	Quartz
Minor	Silicates	Carbonates	Quartz	SiO_2
			Calcite	CaCO_3
			Siderite	FeCO_3
			Dolomite	$\text{Ca,Mg}(\text{CO}_3)_2$
			Ankerite	$\text{Ca}(\text{FeMg})\text{CO}_3$
		Disulfides	Pyrite	FeS_2 (cubic)
			Marcasite	FeS_2 (orthorhombic)
		Sulfates	Bassanite	$\text{CaSO}_4 \cdot \frac{1}{2}\text{H}_2\text{O}$
			Anhydrite	CaSO_4
			Szmolnokite	$\text{FeSO}_4 \cdot \text{H}_2\text{O}$
			Coquimbite	$\text{Fe}_2(\text{SO}_4)_3 \cdot 9\text{H}_2\text{O}$
			Jarosite	$\text{KFe}_3(\text{SO}_4)_2(\text{OH})_6$
			Gypsum	$\text{CaSO}_4 \cdot 2\text{H}_2\text{O}$
		Feldspars	Plagioclase	$(\text{NaCa})\text{Al}(\text{AlSi})\text{Si}_2\text{O}_8$
			Orthoclase	KAlSi_3O_8
		Sulfides	Sphalerite	ZnS
			Galena	PbS
			Pyrrhotite	FeS

^a Slightly modified version of a table from [19].

^b Illite has a composition similar to muscovite $[\text{KAl}_2(\text{Si}_3\text{Al})\text{O}_{10}(\text{OH})_2]$ except for less K^+ and more SiO_2 and H_2O .

^c Mixed layer clays are usually randomly interstratified mixtures of illite lattices with montmorillonitic lattices, chlorite lattices, or both.

Table 1.3: Systems studied for high-temperature desulfurization of a coal-derived synthesis gas.^a

Process	Agent	T _{Des} (°C) ^b	H ₂ S(ppm) ^c	Regeneration	Disadvantages
Dolomite					
• Calcined dolomite	CaO-MgO	870-930	600	600-650°C in CO ₂ /steam	Rapid coking, sorbent degradation, corrosion.
• Conoco half-calcined dolomite	CaCO ₃ -MgO	900	200-300	700°C in CO ₂ /steam	Sulfidation kinetics inferior to FeO _x , poor regenerability.
• Westinghouse dolomite	CaCO ₃ -MgO	815-925	< 600	800°C in air	Creates excessive non-regenerated ash (CaSO ₄ /MgO).
• U.S. Steel dolomite	CaO-MgO	1000	< 65	proprietary, produces H ₂ S	Produces hydrated unregenerated dolomitic ash.
Molten Metals/Salts					
• Battelle molten salt molten salt	Li,Na,K,Ca carbonate	850-1000	< 40	complex aqueous carbonation with H ₂ S to Claus	Complex regeneration, salt carryover, and corrosion.
• IGT Meissner	Pb	330-1200	?	> 330°C, electrolysis	Corrosion, Pb volatilization.
Metal/Metal Oxides					
• Appleby Frodingham	Iron oxide granules	355-420	150	600-800°C in air	Sorbent attrition and pipe corrosion.
• METC	Iron oxide silica	400-750	200-800	950°C in air/steam	High effluent S, sorbents tend to degrade.
• Catalysts and Chemicals	ZnO	150-650	?	Not evaluated	Not effective above 650°C.
• IFP ZnO	supported ZnO	400-600	10	600-900°C in air	Information unavailable.
• METC Zinc ferrite-ZnO	Zn ferrite-ZnO binder carrier	400-650	10	to 650°C in air/steam	Requires good T _{reg} control, sorbent life undetermined.
• Exxon	La ₂ O ₃ – Al ₂ O ₃	150-930	?	150-930°C in air/steam	Proprietary.
• Foster-Wheeler	Ni support	540-790	?	540-790°C in air	Not published.
• Johns Hopkins	Cu/Cr/V	350-820	?	Air	Failure to sustain sulfur removal capacity.
• Atlantic Refining	Cu/Pb/Zn alumino-silicate	90-540	?	370-540°C in air/steam	Low removal efficiency.
• Kennecott	Cu/CuO/Cu(OH) ₂	480-500	?	820°C in air	Difficult regeneration.
• Esso	Cu/SiO ₂	300-980	?	400-740°C solid-state reaction with Cu ₂ O	Temperature control requires circulation.

^a Slightly modified version of a table from [27].

^b Temperature of desulfurization.

^c Outlet concentration of H₂S in parts per million, ppm.

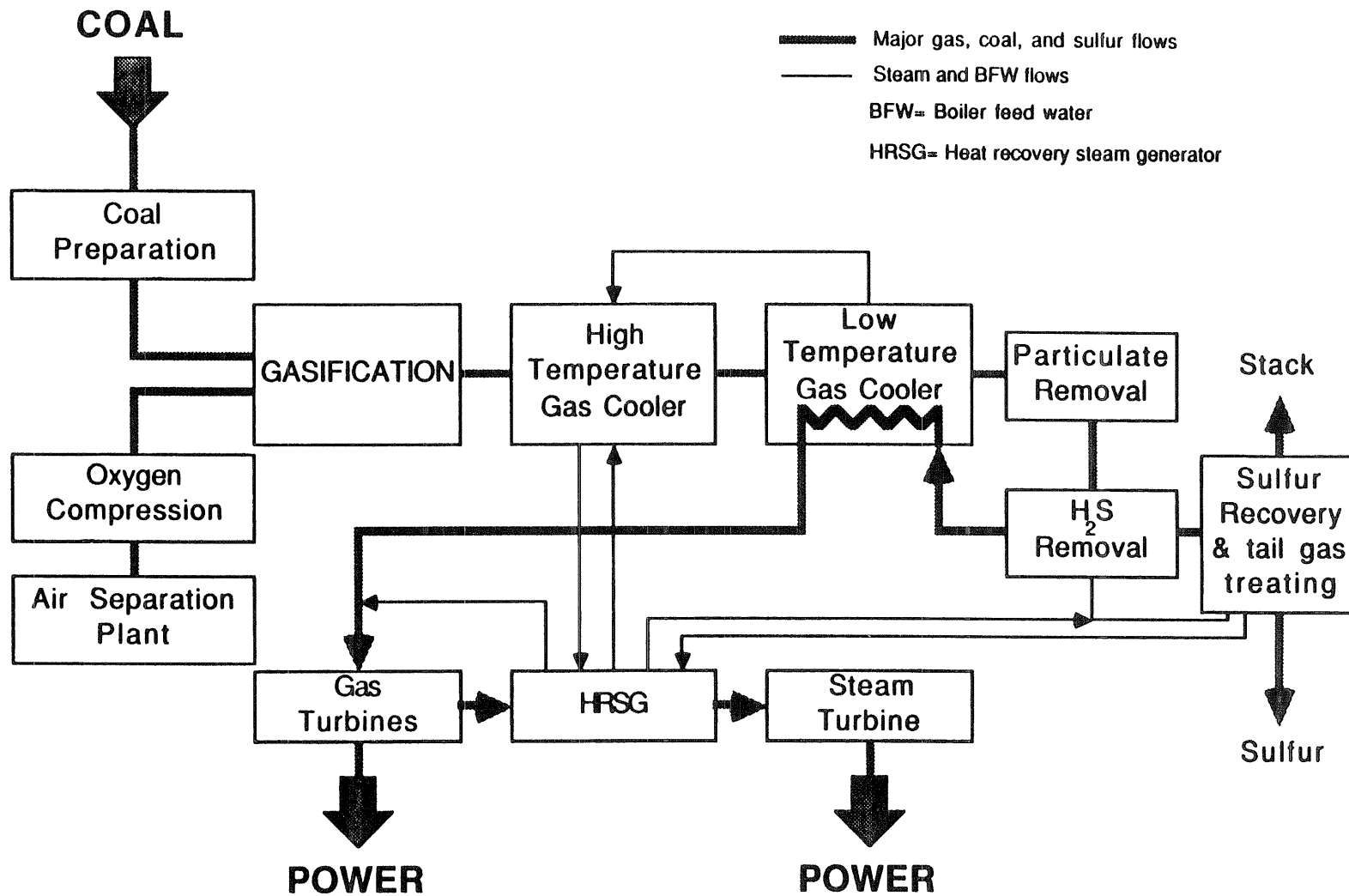


Figure 1.1.: A Texaco-based IGCC plant with low-temperature gas clean-up [23].

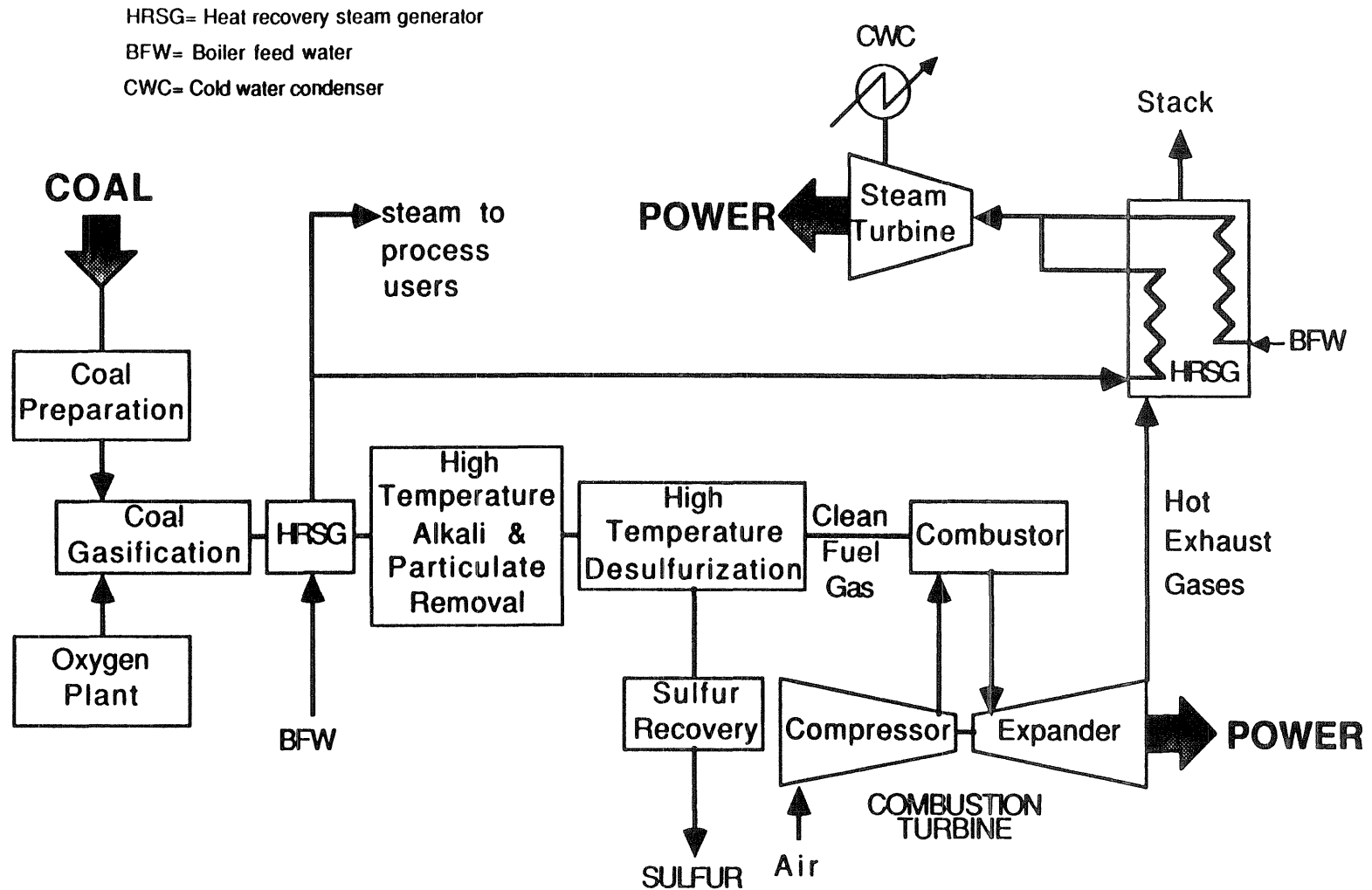


Figure 1.2.: A proposed IGCC plant with high-temperature gas clean-up [20].

CHAPTER II

*Preparation and Preliminary
Characterization
of
Cu-Al-O Sorbents*

2.1 Background

Mixed metal oxides are complex and versatile materials that have attracted considerable attention because of their refractory, electronic, magnetic, and optical properties. In addition, mixed metal oxides have been found to exhibit extraordinary behavior as catalysts and sorbents. The latter application includes the removal of hydrogen sulfide from coal-derived gas at high temperatures in connection with power generation by molten carbonate fuel cells or combined-cycle, power plants [1]. These are promising technologies under current development (Chapter I). The application to catalysis has led to extensive characterization studies of mixed-metal oxides (Chapter III), which have provided fundamental information for selecting sorbents.

Over the past decade, numerous studies addressing the use of transition metal oxides for high-temperature hydrogen sulfide removal were reported [2-6]. Copper oxide is one of the sorbents considered, but its sulfidation equilibrium constant is not high enough to provide adequate H_2S removal. Work in our laboratory [7] has shown, however, that when prepared in association with aluminum oxide, copper oxide has much better sulfidation equilibrium and results in much better H_2S removal than the pure oxide. The chemical basis for this difference is roughly as follows: When pure copper oxide is contacted with a fuel gas, it is quickly reduced to metallic copper, which controls the equilibrium of the subsequent sulfidation reaction. In association with alumina, copper oxide is reduced more slowly to the metal, and reaction with hydrogen sulfide involves the +1 or +2 copper ions that have higher sulfidation equilibrium constants. The purpose of the work presented in this chapter was to examine the nature of the association between copper oxide and aluminum oxide as a function of

preparation conditions.

The chemical and physical structure of mixed copper-aluminum oxides are determined by the steps comprising the synthesis. Traditionally, mixed-metal oxides were prepared by the ceramic method [8,9], high-temperature reaction of oxides, carbonates, nitrates, or other compounds of the component metals with frequent grinding and firing for extended periods. Oxides derived by the ceramic method exhibited low surface area and high crystallinity as a result of the extended exposure to high temperature during synthesis. Furthermore, because of large diffusion paths on the order of $\sim 100\,000\text{ \AA}$ between reactants, the final material possessed poor compositional homogeneity. New methods based on coprecipitated materials [10], metal-organic precursors [11-13], and solid-solution precursors [14-18] involve smaller reactant-diffusion paths than those inherent in the ceramic method: 500 \AA in coprecipitated reactants and 10 \AA in precursor compounds. In comparison to the ceramic method, while reactant-diffusion paths in coprecipitated materials are still too large to obtain monophasic products, reactant temperatures are lower, allowing synthesis of larger surface-area products. The small reactant diffusion distances afforded by precursor compounds ensure monophasic products as long as the homogeneous distribution of component metals established in the precursor is not disrupted during the course of subsequent treatment for product formation.

Synthesis of metal oxides by decomposition of metal-organic or solid-solution precursors has many advantages over the ceramic method and coprecipitation, including shorter reaction times, lower reaction temperatures, more precise product stoichiometry, better product homogeneity, and more favorable conditions for the formation of new metastable phases. New metastable phases that can not be isolated by the ceramic method are new materials with unique prop-

erties, and are important to isolate for determining the mechanisms of solid-state reactions. In addition, the use of lower preparation temperatures has an effect on product morphology, the size, form, and elementary grain texture of the particles. By controlling heat treatment during and after synthesis, it is conceivable to be able to tailor product morphology to specific needs. A major disadvantage of precursor techniques, however, is that simple decomposition in air of the precursor often leads to demixing and a subsequent polyphasic product. This necessitates a careful choice of gas composition and temperature schedule in order to produce a monophasic system. One problem encountered as a result was traces of carbon impurities in phases obtained in reducing environments. The only difference between solid solution and metal-organic precursor routes to the synthesis of metal oxides is that solid solution precursors have no limitations on product stoichiometry.

Techniques to synthesize metal oxides are sometimes categorized by the mechanism of oxide formation involved rather than by the method of combining the constituent oxides. For example, topotactic reactions proceed such that the product can be derived from the reactant, a solid solution precursor or metal oxide, by a series of crystallographic operations (*e.g.*, removal of a fraction of atoms from a crystallographic plane followed by a directional shear of that plane). Another mechanistic category for metal oxide synthesis is ion exchange [20], which is still a relatively unexplored route for solid-state synthesis that plays an as yet unrecognized role in existing solid-state reactions. Finally, the sol-gel technique [21] is derived from a low-temperature method for glass preparation and consists of a series of steps that transform a solution or sol of metal alkoxides to a glass by gel formation. Examples of low-temperature techniques for metal oxide synthesis are summarized in Table 2.1.

Mixed copper-aluminum oxides discussed in this chapter were prepared by the citrate process, a precursor method. The precursor for this technique, developed by Marcilly and coworkers [22], is an amorphous and anhydrous mixed salt between the metal cations of interest and citric acid. The technique is completely general to all transition metals plus aluminum, unlike the aforementioned, low-temperature synthetic routes, which required reactants to possess specific chemical and physical properties. Furthermore, the technique, carefully conducted, will produce a homogeneous and highly dispersed product from any initial stoichiometry of metal cations, even though the product can be polyphasic. The citrate process is important to study because it is a potential source of many new, multicomponent mixed-metal oxides.

The citrate process proceeds through two major stages [23]. In the first stage, low-temperature dehydration of an aqueous solution of the component metal nitrates and citric acid produces a precursor devoid of nitrate ions. Calcination of this precursor to burn away the citric acid constitutes the second stage. Depending on the conditions of the calcination, the oxide product contains a certain amount of copper aluminate with the balance a highly dispersed mixture of CuO and Al₂O₃. Throughout this thesis, the term “mixed oxide” refers to a material containing any mixture of single metal oxides, solid solutions of single metal oxides, metastable phases of single metal oxides, and compound oxides. On the other hand, the phrase “compound oxide” refers specifically to a stoichiometric compound between two or more metal oxides.

2.2 Experimental Techniques

2.2.1. Preparation

The oxide samples were prepared by a complexation technique referred to here as the citrate process. An aqueous solution of copper(II) nitrate hemipentahydrate, aluminum nitrate nonahydrate, and citric acid monohydrate in the desired stoichiometric proportions (1:2:3 unless otherwise stated) was evaporated. The evaporation proceeded first slowly at atmospheric pressure and 70°C until a marked increase in viscosity of the solution was observed, and then rapidly under vacuum at 70°C until an amorphous blue foam was formed. During vacuum evaporation, nitric acid, a by-product of citrate formation, was decomposed and removed as nitrogen-oxide gases. Extra precaution was taken to ensure that all gases formed were condensed in a trap kept cold by a mixture of dry ice and isopropanol. The blue foam was carefully broken up and calcined in a furnace at the chosen temperature under a stream of oxygen to produce the final complex oxide. The temperature of calcination was varied to produce oxides of different compositions. High-temperature calcinations were used to obtain CuAl_2O_4 as the major component and to estimate an activation energy for its formation. Low-temperature calcinations were used to obtain CuO mixed with Al_2O_3 . In both cases, wet chemical analysis and XRD were used to identify and quantify the phases present.

2.2.2. Wet Chemical Analysis

Extraction with hot nitric acid and atomic absorption spectroscopy (AAS) of the extract were used to determine quantitatively the amounts of CuAl_2O_4 , CuO, and Al_2O_3 present in a given sample. It has been reported [8] and con-

firmed in our laboratories that copper oxide in the form of CuAl_2O_4 can not be extracted by hot nitric acid; however, cupric oxide is easily extracted. Subsequent to solubilization of the sample by hot nitric acid, the concentration of copper ions in solution was easily and accurately determined by a modified Varian Techtron Model AA5 atomic absorption spectrometer. The copper ion concentration was proportional to the amount of cupric oxide present in the sample, while insoluble copper oxide represented the concentration of CuAl_2O_4 present. The concentration of Al_2O_3 could then be calculated from the CuO concentration based on initial stoichiometry. Analytical error introduced by preparation of solutions for analysis was found to be negligible in comparison to the instrumental error (estimated from a sample of ultrapure cupric oxide) associated with the concentration measurement by AAS.

2.2.3. X-Ray Diffraction

A Norelco intermittent diffractometer employing Ni-filtered $\text{Cu}(\text{K}\alpha)$ radiation (1.54056 \AA) was used for qualitative chemical analysis of the polycrystalline components present in a sample. The x-ray tube was operated at 45 kV and 20 mA. X-ray powder diffraction patterns in a 2θ range of 30° to 50° (or 20° to 90°) were obtained to detect the presence of CuO , CuAl_2O_4 , and crystalline $\gamma\text{-Al}_2\text{O}_3$. Samples were finely ground and slurried in acetone with a small amount of Duco cement as binder. The slurry was carefully packed into the $21 \times 11 \times 1 \text{ mm}$ depression of a bakelite sample holder. When the available sample size was small (about 30 mg), a specially designed bakelite sample holder with a $11 \times 5 \times 1 \text{ mm}$ depression was used. Spectra were scanned at 0.1° intervals (in 2θ) for 60 seconds per interval.

2.3 High-Temperature Calcination

2.3.1. General Trends

Table 2.2 gives sorbent composition as a function of calcination conditions for various samples prepared by the citrate process. Sorbent compositions were determined by exploiting the difference in solubilities between cupric oxide (CuO) and copper aluminate (CuAl_2O_4) in hot nitric acid (Section 2.2.2). X-ray analysis showed CuAl_2O_4 as the only crystalline phase in precipitates recovered from hot nitric-acid extraction. The content of this compound oxide was found to increase with calcination temperature. For example, the XRD patterns of Figure 2.1 illustrate an increasing CuAl_2O_4 :CuO ratio with calcination temperature for a sample size of about 11 grams and a calcination time of four hours. The results from wet chemical analyses of the samples of Figure 2.1 are included in Table 2.2. The trend of increasing CuAl_2O_4 content with calcination temperature has also been observed for catalysts prepared by impregnation of $\gamma\text{-Al}_2\text{O}_3$ or $\eta\text{-Al}_2\text{O}_3$ with copper nitrate solution [24-27] and for CuAl_2O_4 prepared from the pure component oxides by high-temperature, grinding-heating cycles [8,9].

Examination of several samples of mixed oxide prepared by the citrate process suggested that the yield of CuAl_2O_4 depended primarily on calcination temperature and the conditions of evaporation. There were small variations in compound oxide yield with varying sample size (Table 2.3), probably because of the difficulty in reproducing evaporation conditions for different sample sizes. Maximum conversion to compound oxide at a given calcination temperature was achieved by spreading a small volume (~ 15 ml) of the aqueous solution into a thin film for subsequent evaporation and calcination. Evaporation of larger volumes (> 25 ml) of solution led to lower yields of compound oxide upon cal-

cination at a given temperature. Thus, the rate of evaporation was crucial to the extent of compound-oxide formation. Additional experiments summarized in Figure 2.2 suggested that rapid evaporation produced a foam with a homogeneous dispersion of cations, while comparatively slower evaporation produced a foam with a heterogeneous dispersion. Rapid evaporation apparently preserved the atomic-scale cation mixing established in the initial aqueous solution, and the mixed cations facilitated compound-oxide formation. On the other hand, slow evaporation led to cation segregation, causing preferential formation of the individual oxides over the compound oxide, manifested in Table 2.4 by the different compound oxide yields for partitioned versus unpartitioned precursors as a function of evaporation rate. The smaller the sample size for syntheses using slow evaporation rates (*i.e.*, solution volume ≥ 25 ml), the more pronounced was the heterogeneous cation dispersion of the partitioned precursors.

2.3.2 Activation Energy

Calcination initiates the following two processes: (a) decomposition of the citrate salt complexes formed during evaporation with simultaneous oxidation to form a mixture of cupric oxide (CuO), and alumina (Al₂O₃); and (b) solid-state reaction of the two oxides to form copper aluminate. The gas-solid reactions of process (a) are clearly much faster than the solid-solid reaction of (b); hence, the yield of copper aluminate as a function of calcination time can be used to estimate rate parameters of the solid-solid reaction. The yield data were interpreted by means of the Carter Equation [28], which describes a solid-state reaction between spheres of solid A (*i.e.*, CuO) and a continuous phase of B (*i.e.*, Al₂O₃), assuming a parabolic rate law [29,30]. The parabolic rate law has been derived for a situation in which interdiffusion of metal cations is the rate-

determining step; moreover, this situation has been observed in several spinel systems, including MgAl_2O_4 and ZnAl_2O_4 [31-33].

Figure 2.3 is a plot of a modified form of the Carter equation appropriate for polycrystalline reactants [29,34]. The data of Figure 2.3 were obtained under conditions in which the evaporation proceeded rapidly and homogeneously. Deviation from linearity above a temperature of approximately 750°C may be due to diffusional limitations incurred by CuAl_2O_4 sintering. Cations must diffuse through the growing product layer during the course of reaction; thus, a sintered product layer would lead to a significant retardation of reaction rate. The commencement of CuAl_2O_4 sintering at 750°C is also indicated by crystallite size measurements (Chapter III, Section 3.4). An activation energy of 34 kcal/mol is estimated from the slope of Figure 2.3 for the temperature range 550°C to 750°C . This value is intermediate between the values 23.2 [35] and 51.0 [36] kcal/mol, which have been reported for the reaction of ZnO and $\gamma\text{-Al}_2\text{O}_3$ to ZnAl_2O_4 in the temperature range 800°C to 950°C .

2.4 Low-Temperature Calcination

A series of samples prepared using low-temperature calcinations were studied by XRD to identify the crystalline phases that form initially. A small volume of solution was evaporated to prepare a homogeneous, amorphous precursor containing the stoichiometric ratio of 2 moles of aluminum atoms to 1 mole of copper atoms. Figure 2.4 presents XRD analyses of samples subjected to various calcination conditions. For a sample calcined at 550°C for 5 minutes, the diffractogram shows the presence of metallic copper and Cu_2O in addition to a CuO phase. The presence of metallic copper is evidently due to an initial

reduction of copper cations by reaction with the organic residue of the citrate complexes formed during evaporation. After 10 minutes of calcination at 550°C, metallic copper has disappeared, while CuO has increased and Cu₂O is still detectable. There is no evidence of CuAl₂O₄ formation in the diffractograms of samples calcined at 550°C for 5 or 10 minutes. For calcination lasting 4 hours, XRD provided no evidence for CuAl₂O₄ formation at 350°C or 400°C, but some CuAl₂O₄ is detected at 450°C and 500°C.

In the diffractograms of Figure 2.4, the relative peak intensities of the CuO pattern do not agree with those obtained for a pure reference CuO sample. Specifically, the ratio of the CuO $\langle 002 \rangle$ peak intensity to the CuO $\langle 111 \rangle$ peak intensity is between 1.16 and 1.29 for the samples of Figure 2.4 as compared to values between 0.99 and 1.08 for pure CuO (Figure 2.5). According to Figures 2.1 and 2.4, the CuO $\langle 002 \rangle$ to CuO $\langle 111 \rangle$ peak-intensity ratio is greater than 1.08 for samples calcined between 350°C and 700°C. Furthermore, these peaks broaden symmetrically as the calcination temperature decreases with no measurable shift of CuO peak positions. While the broadening is readily explained by the decrease in CuO crystallite size, the anomalous CuO $\langle 002 \rangle$ peak intensity is more difficult to explain. One possibility is that CuO crystallites assume a preferred orientation along the $\langle 002 \rangle$ direction because of intimate association with alumina. This possibility is unlikely because the sample is in powder form and a powder, by definition, contains randomly oriented crystallites. A second possibility is that CuO forms crystallites with a long dimension along the $\langle 002 \rangle$ direction which is also unlikely according to the same argument as above. A third possibility is that copper cations from (111) planes exchange with aluminum cations at a CuO-Al₂O₃ interface. The higher mass of three copper cations as compared to two aluminum cations results in less scattering power from CuO (111) planes.

Some unexpected results were obtained by dissolving the calcined samples in hot nitric acid and analyzing the solution by AAS. For samples calcined at 450°C and 500°C, the molar ratio of soluble to insoluble copper oxide was 4.5:1 and 5.1:1, respectively. However, the diffraction patterns reveal only a trace of CuAl_2O_4 ; therefore, the insoluble copper oxide must contain microcrystalline CuAl_2O_4 , or some other form of CuO associated with Al_2O_3 , or both. Similarly, the remaining diffractograms in Figure 2.4 did not indicate the presence of CuAl_2O_4 , although the samples contained a certain amount of insoluble copper oxide. Previous work addressing the interaction between NiO and Al_2O_3 [37-39] may offer some indication about the form of the copper oxide that is insoluble in nitric acid but is not identifiable by XRD. NiO- Al_2O_3 and CuO- Al_2O_3 interactions may be quite similar since both NiAl_2O_4 and CuAl_2O_4 are partially inverse spinels, with a fraction of their divalent cations (7-26% of Ni^{+2} and 64-68% of Cu^{+2}) occupying tetrahedral sites [40].

REFERENCES

1. Merrick, D. *Coal Combustion and Conversion Technology* (Elsevier Science Publishing Co., Inc.: New York, 1984).
2. Giner, Inc., "Studies Involving High Temperature Desulfurization Regeneration Reactions of Mixed Oxides for the Fuel Cell Program," Final Report (Argonne National Laboratory, 1981), p.60.
3. Westmoreland, P.R. and Harrison, D.P., "Evaluation of Candidate Solids for High-Temperature Desulfurization of Low-BTU Gases," *Environ. Sci. Technol.*, **10**(7), 659, 1976.
4. MERC Hot Gas Cleanup Task Force, "Chemistry of Hot Gas Cleanup in Coal Gasification and Combustion," Final Report (MERC/SP, 78/2, February, 1978).
5. Bartholomew, C.H., Agrawal, P.K., and Katzer, J.R., "Sulfur Poisoning of Metals," *Adv. Catal.*, **31**, 135, 1982.
6. Westmoreland, P.R., Gibson, J.B., and Harrison, D.P. , "Comparative Kinetics of High-Temperature Reaction Between H₂S and Selected Metal Oxides," *Environ. Sci. Technol.*, **11**(5), 488, 1977.
7. Flytzani-Stephanopoulos, M., Tamhankar, S.S., Gavalas, G.R., Bagajewicz, M.J., and Sharma, P.K., "High-Temperature Regenerative Removal of H₂S by Porous Mixed Oxide Sorbents," *Prepr. Pap. Am. Chem. Soc., Div. Fuel Chem.*, **30**(4), 16, 1985.
8. Paulsson, H. and Rosén, E., "A Study of the Formation of CuAl₂O₄ from CuO and Al₂O₃ by Solid State Reaction at 1000°C and 950°C," *Z. Anorg. Allg. Chem.*, **401**, 172, 1973.

9. Tsuchida, T., Furuichi, R., Sukegawa, T., Furudate, M., and Ishii, T., "Thermoanalytical Study on the Reaction of the CuO-Al₂O₃ (η , γ , and α) Systems," *Thermochim. Acta*, **78**, 71, 1984.
10. Horowitz, H.S., Longo, J.M., and Lewandowski, J.T., "New Oxide Pyrochlores: A₂B_{2-x}A_xO_{7-y} (A= Pb,Bi; B= Ru,Ir)," *Mater. Res. Bull.*, **16**, 489, 1981.
11. Rao, C.N.R., and Gopalakrishnan, J., "Synthesis of Complex Metal Oxides by Novel Routes," *Acc. Chem. Res.*, **20**(6), 228, 1987.
12. Rousset, A., Chassagneux, F., and Paris, J., "Preparation and Properties of Active Submicronic Solids and New Metastable Phases Obtained via a Metal-Organic Precursor Method," *J. Mater. Sci.*, **21**, 3111, 1986.
13. Interrante, L.V., and Williams, A.G., "Design and Synthesis of Polymeric Metal-Organic Precursors to Aluminosilicates," *Polym. Prepr. (Amer. Chem. Soc., Div. Polym. Chem.)*, **25**, 13, 1984.
14. Vidyasagar, K., Gopalakrishnan, J., and Rao, C.N.R., "Synthesis of Complex Metal Oxides Using Hydroxide, Cyanide, and Nitrate Solid Solution Precursors," *J. Solid State Chem.*, **58**, 29, 1985.
15. Longo, J.M., Horowitz, H.S., and Clavenna, L.R., "Solid State Precursors: A Low Temperature Route to Complex Oxides," in *ACS Advances in Chemistry Series 186* (American Chemical Society: Washington , D.C., 1980).
16. Ganapathi, L., Ramanan, A., Gopalakrishnan, I., Rao, C.N.R., "A Study of MoO₃, WO₃ and Their Solid Solutions Prepared by Topotactic Dehydration of the Monohydrates," *J. Chem. Soc., Chem. Commun.*, **62**, 1986.
17. Vidyasagar, K., Gopalakrishnan, J., and Rao, C.N.R., "A Convenient Route for the Synthesis of Complex Metal Oxides Employing Solid-Solution Precursors," *Inorg. Chem.*, **23**, 1206, 1984.

18. Wold, A., "The Preparation and Characterization of Materials," *J. Chem. Education*, **57**(8), 531, 1980.
19. Vidyasagar, K., Reller, A., Gopalakrishnan, J., and Rao, C.N.R., "Oxygen Vacancy Ordering in Superlattices of the Two Novel Oxides, $\text{La}_2\text{Ni}_2\text{O}_5$ and $\text{La}_2\text{Co}_2\text{O}_5$, Prepared by Low Temperature Reduction of the Parent Perovskites," *J. Chem. Soc., Chem. Commun.*, **7**, 1985.
20. England, W.A., Goodenough, J.B., and Wiseman, P.J., "Ion-Exchange Reactions of Mixed Oxides," *J. Solid State Chem.*, **49**, 289, 1983.
21. Sakka, S., "Gel Method for Making Glass" in *Treatise on Materials Science and Technology* (Academic Press, Inc.: New York, 1982), **22**, p.129.
22. Marcilly, C., Courty, P., and Delmon, B., "Preparation of Highly Dispersed Mixed Oxides and Oxide Solid Solutions by Pyrolysis of Amorphous Organic Precursors," *J. Amer. Cer. Soc.*, **53**(1), 56, 1970.
23. Delmon B., and Droguest, J., "Some Mechanistic Features of the Amorphous Citrate Process," in *Fine Particles International Conference Paper, 2nd Meeting Date* ed. by W.E. Kuhn (Electrochemical Society, Inc.: Princeton, N.J., 1973).
24. Ertl, G., Hierl, R., Knözinger, H., Thiele, N., and Urbach, H.P., "XPS Study of Copper Aluminate Catalysts," *Appl. Surf. Sci.*, **5**, 49, 1980.
25. Friedman, R.M., and Freeman, J.J., "Characterization of $\text{CuO}/\text{Al}_2\text{O}_3$ Catalysts," *J. Catal.*, **55**, 10, 1978.
26. Berger, P.A., and Roth, J.F., "Copper Oxide Supported on Alumina. Electron Spin Resonance Studies of Highly Dispersed Phases," *J. Phys. Chem.*, **71**(3), 4307, 1967.
27. Ketchik, S.V., Plyasova, L.M., Seredkin, A.E., Kostov, V.V., and Morozov, L.N., "X-ray Studies of Supported Copper-Aluminum Catalysts," *React.*

- Kinet. Catal. Lett.*, **14**(4), 429, 1980.
28. Carter, R.E., "Kinetic Model for Solid-State Reactions," *J. Chem. Physics*, **34**(6), p.2010, 1961; **35**, 1137, 1961.
 29. Galway, A.K., "Reactions of Solids" in *Chemistry of Solids* (Chapman and Hall Ltd., 1967), p.193.
 30. Armijo, J.S., "The Kinetics and Mechanism of Solid-State Spinel Formation A Review and Critique," *Ox. Metals*, **1**(2), 171, 1969.
 31. Navrotsky, A. and Kleppa, O.J., "Thermodynamics of Formation of Simple Spinel," *J. Inorg. Nucl. Chem.*, **30**, 479, 1968.
 32. Stone, F.S. and Tilley, J.D., "Reactivity Patterns in Spinel Formation," in *Fifth International Symposium on the Reactivity of Solids* ed. by G.M. Scwab (Elsevier Science Publishers: Amsterdam, 1959).
 33. West, A.R. *Solid State Chemistry and its Applications* (John Wiley and Sons: New York, 1984).
 34. Schmalzried, H., *Solid-State Reactions*, Verlag Chemie, Weinheim, 267, 1971.
 35. Kawakami, H., Okada, H., Hashiba, M., Miura, E., Nurishi, Y., and Hibino, T., "Effect of Dispersion of Reactants in Reaction Mixtures on the Kinetics of Formation of Zinc Aluminate," *Yogyo Kyokaishi*, **90**(11), 642, 1982.
 36. Yamaguchi, O., Omaki, H., Takeoka, K., and Shimizu, K., "Thermal Properties of Boehmite Gel Prepared by Alkoxy-Method," *Funtai Oyobi Funtatsuyakin*, **23**(4), 143, 1976.
 37. Gavalas, G.R., Phichitkul, C., and Voecks, G.E., "Structure and Activity of NiO/ α -Al₂O₃ and NiO/ZrO₂ Calcined at High Temperatures," *J. Catal.*, **88**, 54, 1984.
 38. Puxley, D.C., Kitchener, I.J., Komodromas, C., and Parkyns, N.D. "The

Effect of Preparation Method Upon the Structures, Stability and Metal/Support Interactions in Nickel/Alumina Catalysts" in *Preparation of Catalysts III* ed. by Poncelet, G., Grange, P., and Jacobs, A. (Elsevier Science Publishers B.V.: Amsterdam, 1983).

39. Zielinski, J., "Morphology of Nickel/Alumina Catalysts," *J. Catal.*, **76**, 157, 1982.
40. Cooley, R.F., and Reed, J.S., "Equilibrium Cation Distribution in NiAl_2O_4 , CuAl_2O_4 , and ZnAl_2O_4 Spinels," *J. Amer. Cer. Soc.*, **55**(8), 395, 1972.

Table 2.1: Techniques for low-temperature synthesis of mixed metal oxides.

Type of Precursor	Typical Precursors	Typical Products	Ref.
Nitrate Solid Solution	$M_xM'_yPb(NO_3)_{2(x+y+1)}$ $M, M' = Ca, Sr, Ba$	$BaPbO_3, Ba_2PbO_4, SrPbO_4,$ $SrPbO_3, BaSrPbO_4$	1
Hydroxide Solid Solution	$Ln_{1-x}M_x(OH)_3$ $Ln = La, Nd, Y; M = Al, Cr, Co, Ni, Fe$ $Ln_{1-x-y}M'_xM''_y(OH)_3$ $M' = Ni; M'' = Co, Cu$	$LaNiO_3, NdNiO_3,$ $Y_3Fe_2O_{12}, La_2NiO_4$ $LaNi_{1-x}Co_xO_3$ $LaNi_{1-x}Cu_xO_3$	1
Cyanide Solid Solution	$La[Fe_{1-x}Co_x(CN_6)] \cdot 5H_2O$ $La_{1-x}Nd_x[Co(CN)_6] \cdot 5H_2O$	$LaFe_{1-x}Co_xO_3$ $La_{1-x}Nd_xCoO_3$	1
Carbonate Solid Solution	$M_{1-x-y}M'_xM''_yCO_3$ $M = Ca, Mg$ $M', M'' = Mn, Fe, Co, Zn, Ni, Cd$	$M_{1-x-y}M'_xM''_yO$ $CaFeO_{3.5}, CaCo_2O_4$ $CaCo_2O_5, Ca_2FeCoO_5$	2,10
Oxalate Solid Solution	$MCo_2(C_2O_4)_3 \cdot 6H_2O$ $M = Zn, Ni$ $ZnNiM'(C_2O_4) \cdot 6H_2O$ $M' = Co, Mn$	MCo_2O_4 $ZnNiM'O_4$	10
Chromite Metal-Organic	$(NH_4)_2M(CrO_4)_2 \cdot 6H_2O$ $M = Mg, Ni$ $(NH_4)_2M''(CrO_4)_2 \cdot 2NH_3$ $M'' = Cu, Zn$ $M'''Cr_2O_7 \cdot 4C_5H_5N$ $M''' = Co, Mn$	$M'Co_2O_4$ $M' = Mg, Ni, Mn, Co, Cu, Zn, Fe$	11
Oxalate Metal-Organic	$(NH_4)_3[Fe_{0.5}Al_{0.5}(C_2O_4)_3] \cdot 3H_2O$ $(NH_4)_3[Al_{1-x}Cr_x(C_2O_4)_3] \cdot 3H_2O$ $BaTiO(C_2O_4)_2$	$FeAlO_3$ $(Al_{1-x}Cr_x)_2O_3$ $BaTiO_3$	3
Citrate Metal-Organic	$[(NH_4)_3Ln^{III}M^{III}(OH)(C_6H_4O_7)_2] \cdot nH_2O$ $Ln = Y, Al, Nd, La$ $M = Fe, Mn, V, Cr, etc.$	$LnMO_3$	4
Polymeric Metal-Organic	$-[(chel)Al-O-R'_2Si-O-]_n-$ (chel) = β -diketonate, β -diketoester $R' =$ organic substituent	$xAl_2O_3 \cdot ySiO_2$	5
Coprecipitation	Aqueous solution of M and M' nitrates coprecipitated with NH_3OH $M = Pb, Bi; M' = Ru, Ir)$	$M_2[M'_{2-x}M_x]O_{7-y}$ $0 < x \leq 1$ $0 \leq y \leq 0.5$	6
Topotactic Dehydration	$Mo_{1-x}W_xO_3 \cdot H_2O$	$Mo_{1-x}W_xO_3$	7
Topotactic Reduction	$LaMO_3$ $M = Co, Ni$	$La_2M_2O_5$ of homologous series: $La_nM_nO_{3n-1}$	8
Ion-exchange	$\alpha-LiMO_2 + Pd, PdCl_2$ or $+ AgNO_3(l)$ $M = Co, Cr, Ph$ $\alpha-LiFeO_2 + CuCl(l)$ $M''AlO_2$ or $M'''Al_2O_4 + AgNO_3(l)$ $M'' = K, \gamma-Li, \beta-Na; M''' = Sr, Ca$	$MM'O_2$ $M' = Pd, Ag$ $CuFeO_2$ $\beta-AgAlO_2$	9

Table 2.2: Stoichiometric samples (1:2 molar ratio of Cu:Al)
prepared by the citrate process.

Sample	Figures	T _{calc} (°C) (Duration-hrs.)	Yield (grams)	Mole Ratios ^a CuO:CuAl ₂ O ₄ :Al ₂ O ₃
92-1-CA	2.1a,2.3△	900(4)	11.5	2.1:95.8:2.1
86-1-CA	2.1b,2.3△	800(4)	11.5	18.0:64.0:18.0
56-1-CA	2.1c,2.3△	700(4)	11.5	25.8:48.3:25.8
59-1-CA	2.1d,2.3△	600(4)	11.5	45.3:9.4:45.3
72-1-CA	2.1e,2.3△	550(4)	11.5	47.4:5.2:47.4
103-1-CA5	2.3+	550(4)	2.1	44.8:10.4:44.8
108-1-CA5	2.3+	600(4)	2.3	44.8:10.4:44.8
109-1-CA5	2.3+	650(4)	2.2	38.8:22.4:38.8
105-1-CA5	2.3+	700(4)	2.1	29.3:41.4:29.3
111-1-CA5	2.3+	750(4)	2.1	21.0:58.1:21.0
106-1-CA5	2.3+	800(4)	2.0	12.0:76.1:12.0
113-1-CA5	2.3+	850(4)	2.1	9.9:80.2:9.9
107-1-CA5	2.3+	900(14.75)	2.0	7.2:85.5:7.2
45-1-CA6	2.3x	550(4)	1.0	47.1:5.8:47.1
45-2-CA6	2.3x	600(4)	1.0	44.7:10.5:44.7
45-3-CA6	2.3x	700(4)	1.0	34.6:30.8:34.6
45-4-CA6	2.3x	800(4)	1.0	14.9:70.2:14.9
45-5-CA6	2.3x	900(4)	1.0	13.2:73.5:13.2

^a Subject to 1-4% experimental error.

Table 2.3: Effect of sample size on CuAl_2O_4 yield.

Sample	$T_{\text{calc}}(^{\circ}\text{C})$	Duration(hrs)	Sample Size(g)	Mole% $\text{CuAl}_2\text{O}_4^{\text{a}}$
105-1-CA4	550	4	2	11.7
107-1-CA4	550	4	2	8.8
108-1-CA4	550	4	10	7.5
103-1-CA4	550	4	9	7.0
115-1-CA4	550	4	0.4	12.4
117-1-CA4	550	5	2	10.5
72-1-CA	550	4	11.5	5.2
98-2-CA	550	4	2	5.8
54-1-CA2	700	4	4	47.2
54-3-CA2	700	4	2	43.9
56-1-CA	700	4	11.5	48.3
86-1-CA	800	4	11.5	64.0
89-1-CA	800	4	4.3	60.0
44-1-CA	800	4	10	66.6

Table 2.4: Yield of CuAl_2O_4 for partitioned versus unpartitioned precursors.

T_{calc} ($^{\circ}\text{C}$)	Mole% $\text{CuAl}_2\text{O}_4^{\text{a}}$ Partitioned Precursor	Mole% $\text{CuAl}_2\text{O}_4^{\text{a}}$ Unpartitioned Precursor	Rate of Evaporation
600	8.7	9.4	Slow
700	29.8	48.3	Slow
800	37.3	64.0	Slow
900	76.0	95.8	Slow
550	5.8	10.4	Rapid
600	10.5	10.4	Rapid
650		22.4	Rapid
700	30.8	41.4	Rapid
750		58.1	Rapid
800	70.2	76.1	Rapid
850		80.2	Rapid
900	73.5	85.5	Rapid

^a Subject to 1-4% experimental error.

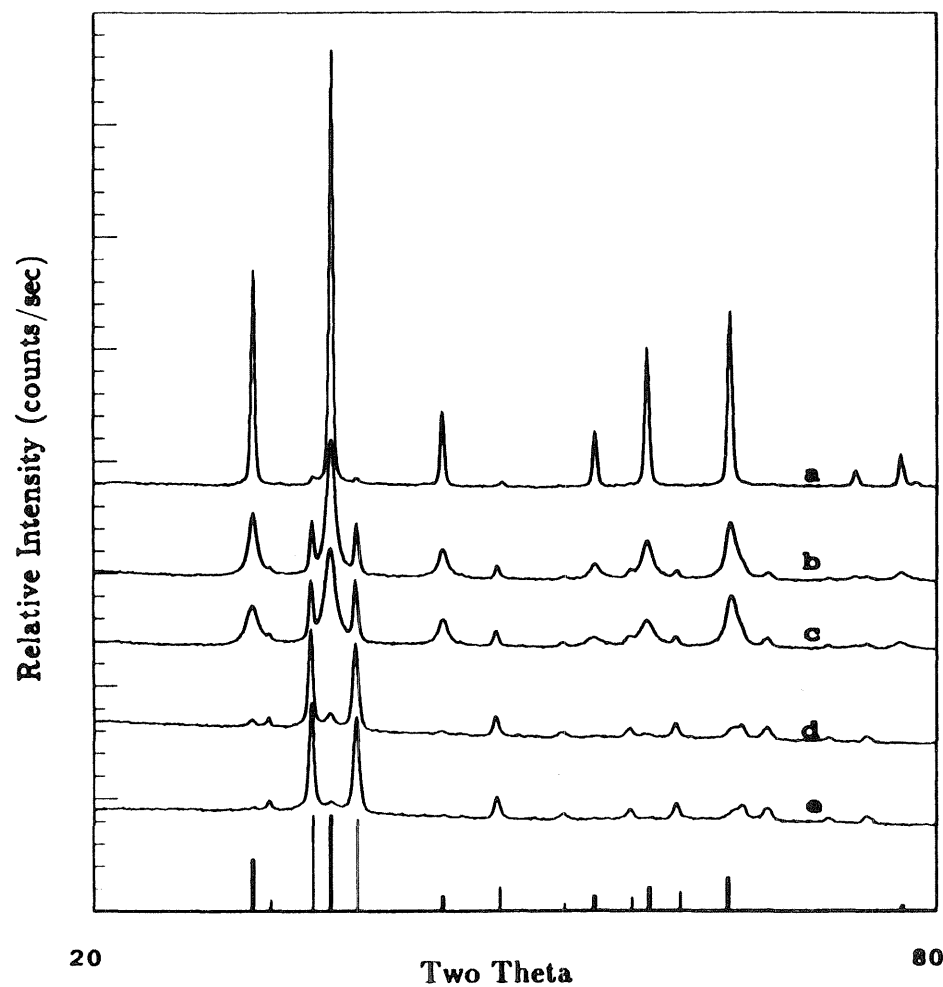


Figure 2.1: XRD patterns of fresh Cu-Al-O samples calcined at different temperatures.

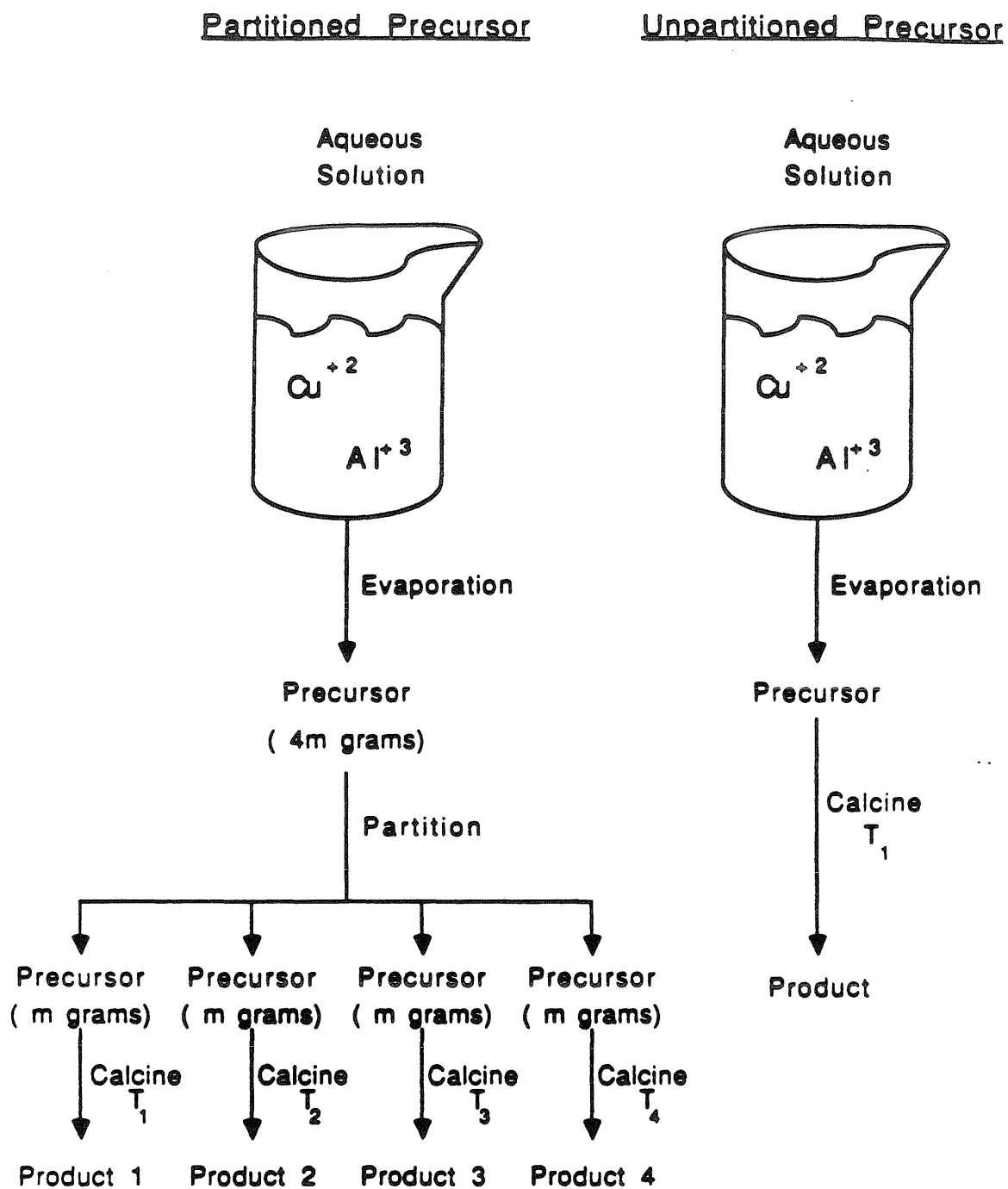
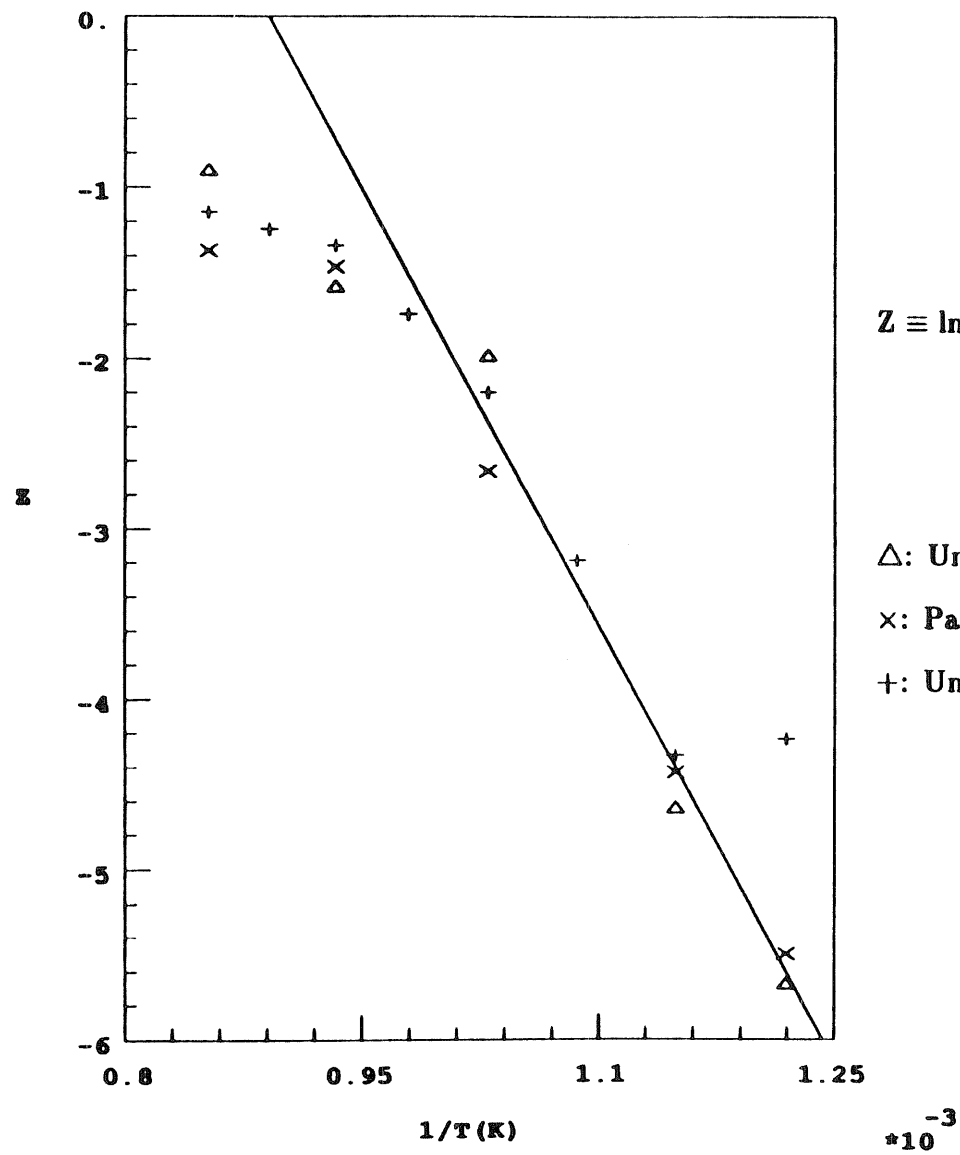


Figure 2.2: Effect of evaporation conditions on the yield of CuAl_2O_4 .



$$Z \equiv \ln \left[\frac{(1 + (z - 1)x)^{\frac{1}{2}} + (z - 1)(1 - x)^{\frac{1}{2}} - z}{1 - z} \right]$$

Δ : Unpartitioned precursors, rapid evaporations

\times : Partitioned precursors, rapid evaporations

$+$: Unpartitioned precursors, rapid evaporations

Figure 2.3.: The Carter equation applied to fresh Cu-Al-O materials.

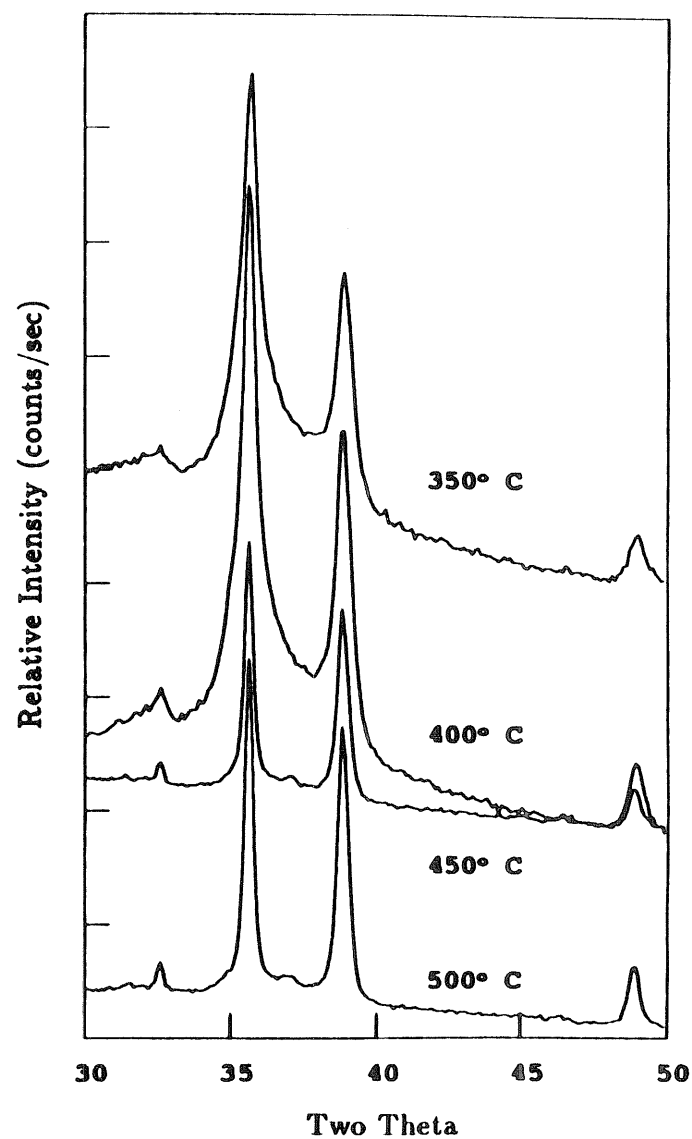
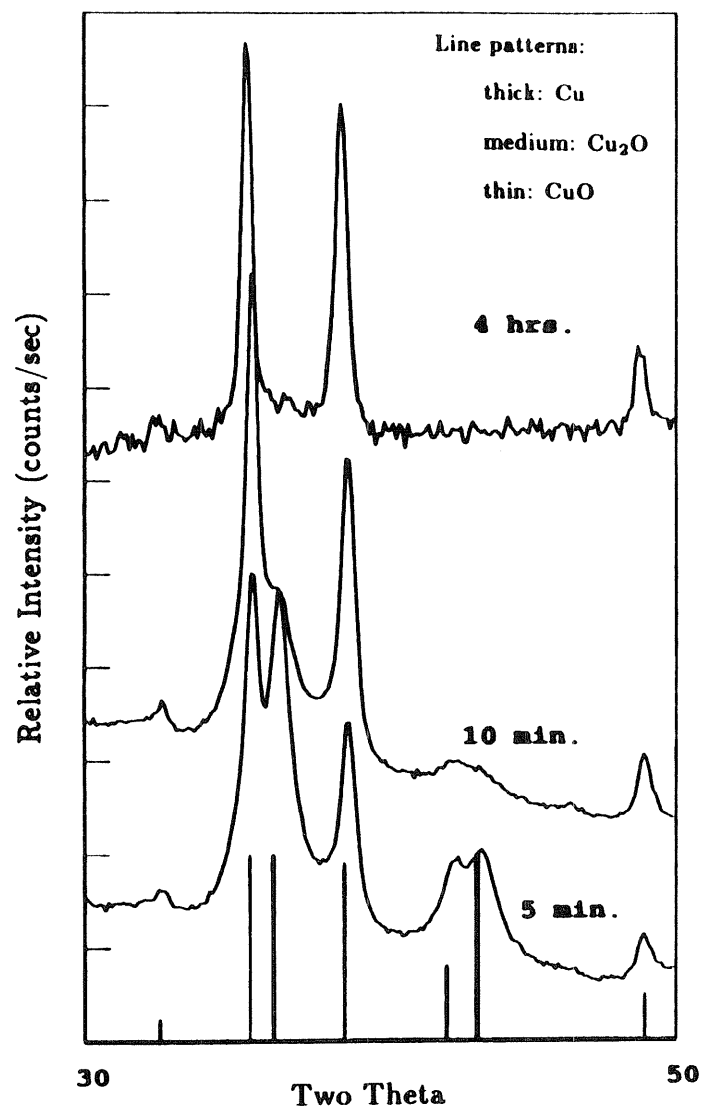
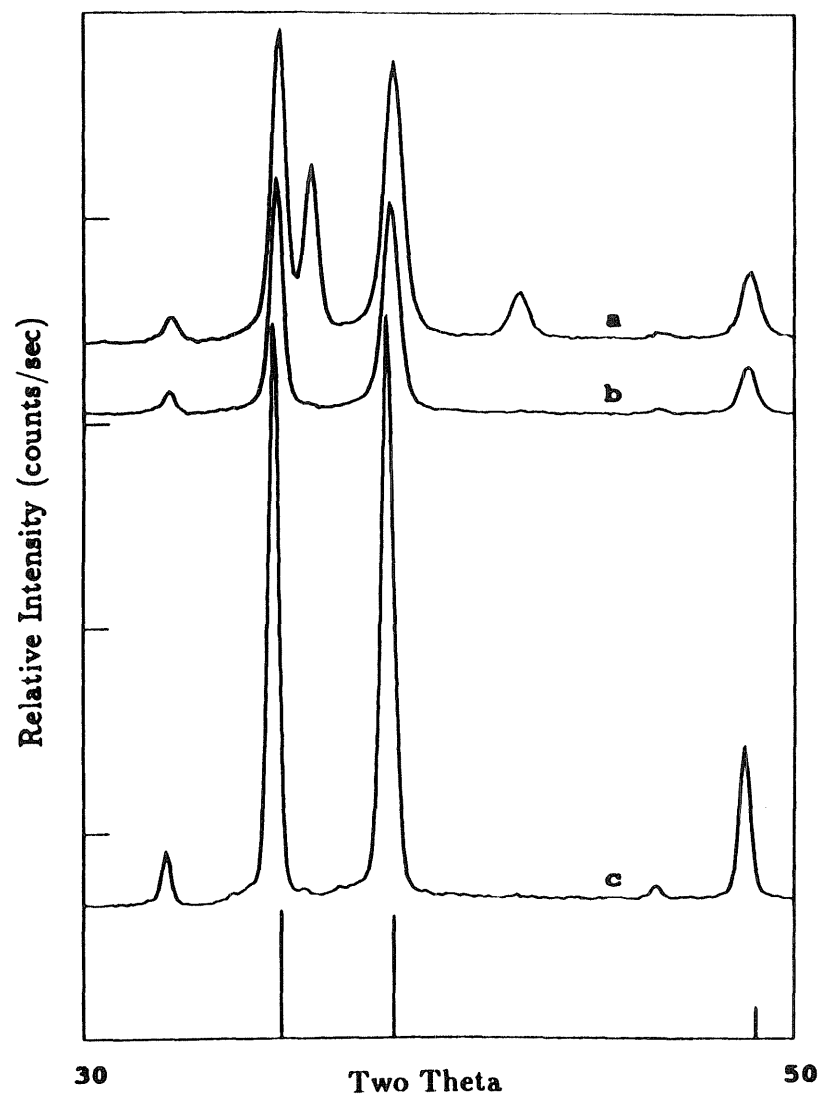


Figure 2.4: XRD patterns of Cu-Al-O materials subjected to various calcination conditions.



a: Calcined at 350°C
b: Calcined at 400°C
c: Calcined at 450°C

Figure 2.5: XRD patterns of CuO prepared by calcination for 4 hours at different temperatures.

CHAPTER III

*Characterization
of
Cu-Al-O Sorbents*

(Portions of this chapter and of the previous chapter have been accepted for publication in the *Journal of the American Ceramic Society*.)

3.1 Background

$\text{CuO}/\text{Al}_2\text{O}_3$ materials have been widely used as catalysts for numerous reactions: hydration, oxidation, and synthesis of hydrocarbons, hydrogenation of aldehydes and ketones, oxidation of CO and reduction of NO for emission control, and methylation of phenols. Typically, the fresh catalyst is prepared by impregnating $\gamma\text{-Al}_2\text{O}_3$ with an aqueous solution of copper nitrate followed by drying and calcining in air. The result is a fresh “supported material” containing only a few mass percent copper (2 to 30% Cu). In contrast, the $\text{CuO}\cdot\text{Al}_2\text{O}_3$ materials under investigation in this chapter have been synthesized by the citrate process (Chapter II), spanning a composition range from 1:5 to 5:1 in molar ratio of CuO to Al_2O_3 . Furthermore, the intended application for this system is as a sorbent for high-temperature removal of H_2S in which the sorbent will undergo bulk chemical reaction with H_2S in contrast to a catalytic application in which the material is not consumed by reaction. The observation that $\text{CuO}\cdot\text{Al}_2\text{O}_3$ materials are superior to CuO as H_2S sorbents, however, has led to interest in the interaction between CuO and Al_2O_3 in these materials [1]. CuO- Al_2O_3 interactions play a variety of roles in catalysis and thus have been extensively studied in $\text{CuO}/\text{Al}_2\text{O}_3$ materials formulated by the method of impregnation. Thus, the techniques used to characterize $\text{CuO}/\text{Al}_2\text{O}_3$ catalysts will be reviewed.

A fresh, calcined catalyst is often subjected to various reduction, oxidation, or REDOX (cyclic reduction-oxidation) pretreatments to improve activity and selectivity. To aid in the selection of an optimum pretreatment schedule, catalysts have been characterized before, during, and after catalytic runs in an attempt to isolate the active species, and to better understand the mechanism of reaction enhancement. Techniques that have been applied to this end

include XRD (x-ray diffraction), diffuse reflectance spectroscopy, PAS (photoacoustic spectroscopy), K-absorption edge shifts, EXAFS (extended x-ray fine structure), XPS (x-ray photoelectron spectroscopy) or ESCA (electron spectroscopy for chemical analysis), ISS (low-energy, ion-scattering spectroscopy), ESR (electron-spin resonance spectroscopy), electron probe microanalysis, and chemisorption. These techniques will be discussed briefly below with an emphasis on information gained about CuO-Al₂O₃ interactions.

The x-ray diffraction pattern of a pure substance has been used as a fingerprint of that material characterizing its crystalline structure and composition. XRD has identified the components in a polycrystalline sample, provided the crystallites are greater than 50 to 75 Å in size [2]. XRD studies of fresh CuO/Al₂O₃ catalysts, for example, included the following major findings: No Cu-containing phases could be detected in samples calcined at 500°C (< 12 hours) and composed of < 1% Cu per 27-30 m²/g of γ-Al₂O₃; CuO was identified in samples calcined at ≤ 600°C containing > 4% Cu per 100 m²/g of γ-Al₂O₃; and both CuAl₂O₄ and α-Al₂O₃ were identified in samples calcined at 900°C regardless of copper content [2,3]. High-temperature XRD detected bulk CuAl₂O₄ and α-Al₂O₃ in a 10.5% Cu catalyst at 700°C [4]. Since the γ-Al₂O₃ to α-Al₂O₃ transition has been reported to occur at 1100°C, it was proposed that the presence of CuAl₂O₄ catalyzes the formation of α-Al₂O₃ at a lower temperature. A closer look at XRD patterns for samples calcined at 500°C containing < 3% Cu per 100 m²/g of γ-Al₂O₃ revealed a larger lattice parameter for γ-Al₂O₃ (7.943 Å) than observed for the pure support (7.920 Å). The increase in the value of the lattice parameter implied insertion of Cu⁺² ions into the γ-Al₂O₃ lattice forming a solid solution [5] as opposed to the formation of bulk CuO at these low copper loadings. In fact, when samples containing

1.1% Cu per 100 m²/g of γ -Al₂O₃ were calcined at 275, 425, 675, and 875 °C, the lattice parameter of the spinel increased from 7.926 Å to 7.932 Å with calcination temperature [6]. This increase was attributed to the formation of a solid solution of CuAl₂O₄ and γ -Al₂O₃, spinels with lattice parameters of 8.078 Å and 7.920 Å, respectively. Finally, it was reported by one investigator that a surface spinel could be detected by XRD for samples calcined at 600°C, containing 3.9, 5.0, 6.4, and 11.5% Cu on γ -Al₂O₃ (surface area not given). This detection was based on the observation of an increase in intensity with copper content of the x-ray lines located at d-spacings of 2.8 Å and 2.4 Å, two strong lines for both γ -Al₂O₃ and CuAl₂O₄.

Additional techniques have helped to further clarify the CuO-Al₂O₃ interaction isolated in catalysts of low copper content ($\leq 4\%$ Cu per 100 m²/g of γ -Al₂O₃) calcined at low temperatures ($< 600^\circ\text{C}$). For example, diffuse reflectance spectroscopy was found to distinguish between copper cations coordinated octahedrally versus tetrahedrally [3,7-9]. For a sample calcined at 500°C containing 2.5% Cu per 100 m²/g of γ -Al₂O₃, bands for both octahedrally and tetrahedrally coordinated Cu⁺² appeared in optical spectra with $\sim 90\%$ of Cu⁺² in octahedral coordination [7]. Since bulk CuAl₂O₄ has 60% Cu⁺² tetrahedrally coordinated and 40% Cu⁺² octahedrally coordinated, this was evidence for a surface CuAl₂O₄ species with Cu⁺² in predominantly octahedral coordination. Alternatively, Cu⁺² could be viewed as occupying octahedral vacancies in the γ -Al₂O₃ spinel structure, thereby forming a solid solution.

The technique of PAS gives the same information as diffuse reflectance spectroscopy with the added advantage of insensitivity to light scattering by the sample [2]. Unfortunately, only octahedrally coordinated cupric ions can be seen because the band for tetrahedrally coordinated Cu⁺² is beyond the range of the

spectrometer. Furthermore, the presence of even a small amount of CuO causes an overall deterioration of the PAS spectrum because of the high absorption coefficient of this species.

The Cu x-ray K-absorption edge for CuAl_2O_4 was found to lie above that for CuO despite the similarity in copper valency for these two compounds [3,10]. For catalysts calcined at 500°C with 1.1-3.5 % Cu per $100 \text{ m}^2/\text{g}$ of $\gamma\text{-Al}_2\text{O}_3$, the Cu K-absorption edge was similar to that for CuAl_2O_4 , even though no bulk CuAl_2O_4 was detected by XRD analysis of these samples [10], suggesting the presence of surface aluminate. For consistency with XRD and diffuse reflectance spectroscopy results, it must be assumed that the value of the Cu x-ray K-absorption edge can distinguish between CuO and aluminate (*i.e.*, copper aluminate, CuAl_2O_4) phases but not between the different cation coordinations within the spinel [3]. A related technique known as EXAFS, however, can provide some information about the two forms of Cu^{+2} coordination in the catalyst samples. EXAFS are the small oscillations in the x-ray absorption coefficient as a function of energy located approximately 50 eV above the characteristic edge of the atom of interest (Cu in this case). The oscillations are caused by the interference between two photoelectron waves, one propagating from the absorption center and one that is elastic backscattering by neighboring atoms of the ejected photoelectron. Transformation of the EXAFS data is complex; however, it has been estimated that a catalyst calcined at 500°C with 2 % Cu per $100 \text{ m}^2/\text{g}$ of $\gamma\text{-Al}_2\text{O}_3$ has a ratio of 50:40 octahedral to tetrahedral Cu^{+2} as compared to a ratio of 40:60 for bulk CuAl_2O_4 [3].

XPS (or ESCA) has provided information similar to that found by measuring Cu x-ray K-absorption edges in that the two phases CuO and CuAl_2O_4 can be distinguished; however, the distribution of Cu^{+2} between octahedral and

tetrahedral sites can not be ascertained [3]. For example, there is a 0.95 eV shift in the Cu 2p_{3/2} binding energy between CuO and CuAl₂O₄ [11,12] and an 0.50 eV shift in the Cu 2p_{1/2} line [11]. A catalyst containing 3.3% Cu per 100 m²/g of γ -Al₂O₃ and calcined at 500°C exhibited the same Cu 2p_{3/2} binding energy as CuAl₂O₄, suggesting the presence of a surface aluminate. The intensity ratio of the Cu 2p_{3/2} peak (including the satellite peak) to the Al 2p peak as a function of copper loading leveled off at a loading of 4.6-5.1% Cu per 100 m²/g of γ -Al₂O₃ for calcination temperatures of 400 and 600°C [2]. This leveling off suggested a change in surface composition at this copper concentration, which was attributed to the segregation of a bulk CuO phase that was due to saturation of vacant octahedral and tetrahedral lattice sites of the support by copper cations. This is consistent with the detection of CuO by XRD in catalysts calcined at 500°C, with > 4% Cu per 100 m²/g of γ -Al₂O₃.

The dependence of the XPS intensity ratio of Cu to Al on copper loading was similar to that found in ISS experiments. For example, a plot of ISS intensity ratio of Cu to Al versus copper loading [2] also leveled off at 4.6-5.1% Cu per 100 m²/g of γ -Al₂O₃; however, a higher sensitivity to calcination temperature was observed for the ISS intensity ratio as compared to the XPS intensity ratio. The discrepant sensitivities to calcination temperature were due to the difference in sampling depth between the two techniques (30 Å for XPS and 3 Å for ISS), because Cu depletion to form bulk CuO is most drastic in the uppermost surface layers.

ESR studies have revealed a significant decrease in the relative intensity of ESR absorption per cupric ion as the copper content of the catalyst increases [3,10,13]. The ESR signal has been attributed to Cu⁺² ions fixed in tetragonally distorted octahedra [14]. Furthermore, since all Cu⁺² ions in supported

catalysts contribute to magnetic susceptibility but only $\sim 2\%$ contribute to the ESR signal [15], it has been concluded that there are two different types of Cu^{+2} centers with the type contributing to the ESR signal being completely isolated. Unfortunately, there is no ESR signal detected for CuAl_2O_4 [3,16] or for tetrahedrally coordinated Cu^{+2} ions. ESR signals, however, have been detected in samples containing up to 21% Cu per 100 m^2/g of $\gamma\text{-Al}_2\text{O}_3$, suggesting the presence of a dispersed phase even at high copper loadings. This is a significant observation, implying that $\text{CuO-Al}_2\text{O}_3$ interactions isolated at low copper concentrations exist in parallel with bulk phases at higher copper contents.

Electron microprobe analysis has a limited resolution of 3 μm and therefore has been used only to a limited extent [17]. The method has the capability of providing concentration profiles for each element with an atomic number greater than 10. Chemisorption is another technique with limited applicability because of problems such as determining the stoichiometry between the adsorbate and the dispersed phase, and accounting for penetration of the adsorbing gas into the bulk phases. While N_2O and O_2 chemisorption have been used to characterize the available surface area and dispersion of Cu^0 in reduced copper catalysts [18,19], no chemisorption techniques have been developed for the characterization of Cu^{+2} to date.

This chapter presents a more extensive characterization of $\text{CuO/Al}_2\text{O}_3$ sorbents than presented in Chapter II. Some of the techniques used to characterize $\text{CuO/Al}_2\text{O}_3$ catalysts have been combined with techniques that have not been used previously to characterize mixed copper-aluminum oxides. The latter techniques include laser Raman spectroscopy, electron microscopy, and temperature-programmed reduction (TPR), using a thermogravimetric analyzer (TGA).

3.2 Experimental Techniques

3.2.1 Preparation

The oxide samples were prepared by the citrate process as described in Section 2.2.1 of Chapter II. Samples referred to in this chapter are summarized in Tables 3.1 and 3.2.

3.2.2 Temperature-Programmed Reduction

A Dupont 951 thermogravimetric analyzer interfaced through an analog-to-digital converter to a microcomputer (Figure 3.1) was used to measure continuously the weight loss accompanying reduction [20]. Typically, a nitrogen-sweep, gas-flow rate of 20 cc/min and a reactant, gas-flow rate of 80 cc/min were used. A mixture containing 5% H₂ in N₂ was used for reduction, while air was used for oxidation. A temperature controller enabled operation under a linear temperature profile at a rate of 1.7°C/min from an initial temperature of 233°C. Typically, a 30 mg sample of particles, 120-170 mesh fraction, was employed. It was verified experimentally that for the range of flow rates and sample sizes employed, the reactions were free of internal and external, mass-transfer effects.

3.2.3 X-Ray Diffraction

A Norelco intermittent diffractometer employing Ni-filtered Cu(K α) radiation (1.54056 Å) was used for qualitative chemical analysis of the polycrystalline components present in a sample. The x-ray tube was operated at 45 kV and 20 mA. X-ray powder diffraction patterns in a 2θ range of 30° to 50° (or 20° to 90°) were obtained to detect the presence of CuO, CuAl₂O₄, Cu₂O, CuAlO₂, Cu, and crystalline γ -Al₂O₃. Samples were finely ground and slurried in ace-

tone with a small amount of Duco cement as binder. The slurry was carefully packed into the $21 \times 11 \times 1$ mm depression of a bakelite sample holder. When the available sample size was small (about 30 mg) as from a TGA experiment, a specially designed bakelite sample holder with a $11 \times 5 \times 1$ mm depression was used. Spectra were scanned at 0.1° intervals (in 2θ) for 60 seconds per interval.

3.2.4 Electron Microscopy

For SEM studies, the samples were examined by an ETEC scanning electron microscope operating at 20 kV with a resolution of 70 Å. The sample was carefully ground and sprinkled on a metal stub containing a light coat of silver paste. This metal stub was then coated with a gold-palladium film 100 Å in thickness prior to observation.

TEM work was performed using an EM301 microscope operating at 100 kV with a resolution of 6 Å. A 120-170 mesh fraction of the powder sample was finely ground in a ceramic mortar and pestle. A small amount of reagent-grade ethanol was added to the mortar to form a dilute solution, which was well stirred and allowed to stand so that larger more dense particles settled to the bottom. A wire loop was used to skim the top of the solution and to place a drop of sample onto the holey carbon side of a standard grid. The grid was allowed to air-dry prior to observation.

3.2.5 Laser Raman Spectroscopy

The laser Raman spectra were recorded using a Spex Model 1401 spectrometer equipped with a Spectra-Physics Model 170 argon ion laser. The 514.5-nm line was used as the exciting source at a power of 450 mW. A double-

monochromator with a 2400 grooves/mm grating received the scattered light. The detector system used a Hamamatsu multialkali-cooled photomultiplier tube to measure the signal that was connected to a Spex Model DPC-2 digital photon counter and electrometer. The Raman spectra were displayed and stored using a Spex Scamp mainframe computer. About 40 mg of sample were packed into a quartz capillary (1.5 mm O.D.), which was placed in the path of the laser beam and analyzed at room temperature. Spectra were recorded for the same position of the capillary as a function of exposure time to the beam (20 to 150 minutes), indicating no apparent sample degradation, for different positions of the capillary, revealing sample homogeneity, and for different aliquots of fresh sample, revealing good reproducibility. The frequency range scanned was 200 to 1230 cm^{-1} , using 10 scans or 43 minutes of accumulation time. The overall spectral resolution was about 6 cm^{-1} .

3.2.6 Diffuse Reflectance Spectroscopy

Spectra in the uv, visible, and near ir region (320 to 2500 nm) were recorded using a Perkin-Elmer type $\lambda 9$ spectrometer equipped with a BaSO_4 -coated integrating sphere. Samples were diluted by an equal mass of LiF [7,21]. The mixture was ground to a uniform color using a mortar and pestle and then packed with care into the $21 \times 11 \times 1$ mm depression of a bakelite or aluminum sample holder to form a smooth flawless surface. The diffuse reflectance, R , from the sample was measured as a fraction of that for the BaSO_4 standard, R_0 . Data were interpreted by the Kubelka-Munk-Schuster function, $F(R) = (1 - R)^2/2R$ [8,21].

3.3 Chemical Properties According to TPR

3.3.1 General Trends

Figure 3.2 shows normalized weight-loss curves for temperature-programmed reduction (TPR) of pure CuO and six mixed-oxide samples prepared under different evaporation and calcination conditions (Table 3.1). TPR of pure CuO (curve g) results in complete conversion to copper metal within 23 minutes, before the temperature has reached 270°C. On the other hand, TPR of sample 92-1-CA (curve a), consisting of 96 mole% CuAl₂O₄, is slow and approaches complete conversion to copper after only 6½ hours, when the temperature has reached 860°C. Sorbents containing a mixture of CuO, CuAl₂O₄, and alumina have reduction curves that resemble a series combination of curves g and a in approximate proportion to their content of CuO and CuAl₂O₄, with the steeply declining section of the weight-loss curve increasing with the CuO:CuAl₂O₄ ratio.

Upon closer examination, however, the steeply declining section of the weight-loss curve is not quite proportional to the amount of CuO present in the sample as determined by wet chemical analysis. The initial reduction periods of four different sorbents shown in Figure 3.3 illustrate that not all the CuO determined by wet chemical analysis is reduced during the initial rapid reduction stage. The fraction of total weight loss for complete reduction of CuO to the metal is in parenthesis adjacent to that which is observed experimentally. Clearly, reduction of a certain fraction of soluble CuO, CuO which dissolved in hot nitric acid during wet chemical analysis, is hindered. Furthermore, this slowly reducing fraction increases with decreasing CuAl₂O₄ content of the sample.

Several phenomena could account for the observed hindering of CuO reduction. Reduction of CuO can be retarded by CuO sintering or through formation of a product Cu diffusion barrier between unreacted CuO and the reactant gas. A second possibility is the existence of a thin shell of nonporous CuAl_2O_4 around CuO crystallites hindering their reduction. A third possibility is that a fraction of CuO at or near an interface with Al_2O_3 reduces more slowly than bulk CuO because of interaction with Al_2O_3 . This possibility is consistent with some previous investigations of impregnated CuO/ Al_2O_3 catalysts in which the supported oxide was reported to be in the form of CuAl_2O_4 [22], or a “surface spinel” consisting of a monolayer of copper ions on a CuO- Al_2O_3 interface [9]. In both cases, association with alumina hindered reduction of copper oxide.

3.3.2 Effect of Sintering

The possible role of CuO sintering in the hindering of CuO reduction was investigated. SEM and x-ray line-broadening analyses of fresh samples provided evidence for the presence of sintered CuO that must form during the calcination step of the synthesis (Section 3.4). The amount of sintered CuO as well as the extent of sintering increased with calcination temperature. Consequently, the sample calcined at the highest temperature should exhibit the highest fraction of CuO hindered from reduction. But in fact, the maximum amount of CuO reducing slowly was observed for a sample calcined at 550°C, and the degree of hindering decreased with increasing calcination temperature. Thus, sintered CuO observed in fresh samples by SEM and x-ray line broadening was not responsible for hindered reduction of CuO.

An additional series of experiments were conducted to examine further the role of sintering. Samples exhibiting the highest (72-1-CA, 5 mole% CuAl_2O_4)

and lowest (11-1-CA3, pure CuO) fraction of CuO hindered from reduction were examined by repeated isothermal reduction-oxidation (REDOX) experiments. As shown in Figure 3.4, each sample was subjected to isothermal REDOX cycles successively at 600°C, 650°C, 700°C, 750°C, and 800°C. Reduction was very fast at all temperatures for both samples, generating similar weight-loss curves in all runs. Oxidation of reduced 72-1-CA was also rapid at all temperatures. Oxidation of the sample obtained by reduction of pure CuO, however, slowed down with successive cycles of increasing temperatures, indicative of Cu sintering. These results confirmed the previous observation that CuO sintering was not responsible for the hindering of CuO reduction. On the other hand, sintering of metallic copper, which was significant in the case of the pure oxide but was suppressed in the sample containing alumina, retarded the reoxidation of reduced samples.

3.3.3 Effect of Copper Aluminate

Six test sorbents were synthesized to investigate the effect of CuAl_2O_4 on CuO reduction with a less than stoichiometric quantity of Al_2O_3 present. These sorbents were prepared by the citrate process using 1.5:1 and 2:1 molar ratios of $\text{CuO}:\text{Al}_2\text{O}_3$. Aqueous solutions of the starting materials were subjected to the usual evaporation and calcination procedures. Table 3.2 summarizes sorbent compositions determined by wet chemical analysis as a function of calcination conditions and starting stoichiometry. All six samples contained free alumina in molar ratio with CuO below 1:2. TPR of all samples revealed an initially rapidly declining weight loss in an amount consistent with the concentration of CuO measured by wet chemical analysis (Figures 3.5 and 3.6). Consequently, CuAl_2O_4 does not appear to play a role in retarding CuO reduction, and Al_2O_3

in the amount employed does not influence CuO reduction.

3.3.4 Effect of Alumina

A set of experiments was performed to investigate further the role of alumina in slowing down the reduction of CuO. Two new samples were prepared by the citrate process using 2:1 and 5:1 molar ratios of Al_2O_3 :CuO. Aqueous solutions of the starting materials were subjected to the usual evaporation and calcination procedures. The 2:1 sorbent (12 mass% Cu) was calcined at 550°C for 2 hours to yield a black sample, while the 5:1 sorbent (31 mass% Cu) was calcined first at 550°C for 4 hours and then at 650°C for 19 hours to yield a blue-green material. The different colors of these samples were consistent with those observed in an earlier study of CuO/ Al_2O_3 prepared by impregnation, showing a blue-green color for 10 to 17% copper loading and a black color for copper loading above 17% [2]. Wet chemical analysis revealed an insoluble fraction of copper in both samples (Table 3.2) even though no CuAl_2O_4 was identified by x-ray analysis, suggesting the presence of microcrystalline CuAl_2O_4 (≤ 50 Å) or regions of CuO in close association with alumina, as postulated previously for samples calcined at low temperatures (Chapter II, Section 2.4). In addition, wet chemical analysis indicated a significant amount of CuO in both samples, even though in XRD patterns no CuO peaks were discerned for sample 21-2-CA3, and low-intensity, broad CuO peaks were observed for sample 6-1-CA3. These XRD patterns indicated that CuO was in the form of very fine crystallites (≤ 50 Å) with the exception of a small fraction of bulk CuO (> 50 Å) in sample 6-1-CA3. The high content of microcrystalline CuO is reasonable since these samples contain excess alumina in a microcrystalline form (≤ 50 Å) with a surface area of ~ 217 m²/g (Table 3.1), which could cause a fine dispersion of

CuO crystallites.

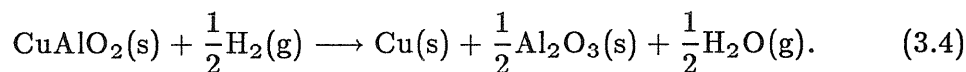
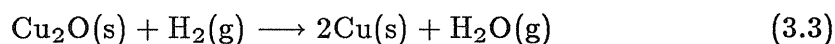
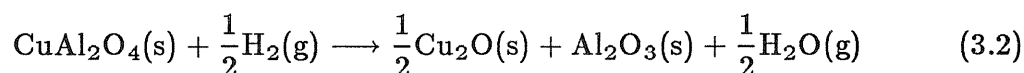
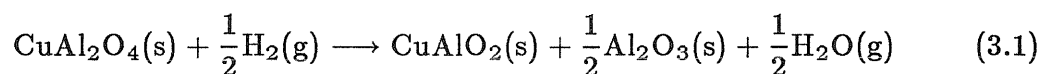
Weight loss during TPR of samples 6-1-CA3 and 21-2-CA3 is compared to that during TPR of samples 11-1-CA3 (pure CuO) and 92-1-CA (96 mole% CuAl₂O₄) in Figure 3.7. The presence of excess alumina in samples 6-1-CA3 and 21-2-CA3 is seen to lower the rate of reduction of CuO. The exact nature of the CuO-Al₂O₃ interaction causing this retardation of reduction still needs to be clarified. In studies of CuO/Al₂O₃ catalysts prepared by impregnation, it was reported that a “surface spinel” species distinct from bulk copper aluminate formed at temperatures below $\sim 700^{\circ}\text{C}$ [2,3], when the loading of copper was low ($< \sim 4\%$ Cu per 100 m²/g of γ -Al₂O₃ support). The “surface spinel” was described as a well-dispersed phase that was not detectable by XRD and that differed from the bulk spinel phase by having copper cations in predominantly octahedral sites as opposed to bulk CuAl₂O₄, which has only 40% copper cations occupying octahedral sites, with the remaining 60% occupying tetrahedral sites. At higher copper loadings and under the same calcination conditions, XRD analysis revealed that the oxide had agglomerated into bulk CuO. Evidence has been provided in this study for the possibility of cation exchange between Cu⁺² and Al⁺³ in samples prepared by the citrate process (Section 2.4); however, the sites involved in this exchange have not been isolated. Formation of a “surface spinel” would require that the exchange between Cu⁺² and Al⁺³ be site selective to octahedral interstices of alumina.

Mixed copper-aluminum oxides prepared by calcination at 350°C and 400°C also exhibited slower rates of reduction than pure CuO (Figure 3.8). For example, the rate of consumption of CuO for $0.4 < W_N < 0.6$ was 0.453 mg/min for sample 11-1-CA3 versus 0.0472 mg/min and 0.0404 mg/min for samples 13-1-CA7 (calcined at 400°C) and 15-1-CA7 (calcined at 350°C), or approximately

one order of magnitude faster for pure CuO. Intensity anomalies in x-ray diffraction peaks for CuO in these samples were postulated to be due to cation exchange between Cu^{+2} and Al^{+3} (Chapter II, Section 2.4), or a preferred orientation of CuO crystallites as a result of an intimate association with alumina. In either case, Figure 3.8 correlates a slow rate of reduction of CuO in samples containing alumina to an interaction between CuO and Al_2O_3 .

3.3.5 Mechanism of Sorbent Reduction

Samples of sorbents 92-1-CA (96 mole% CuAl_2O_4), 72-1-CA (5 mole% CuAl_2O_4), and 56-1-CA (48 mole% CuAl_2O_4) subjected to TPR for different lengths of time were analyzed by XRD to identify intermediate products. Figure 3.9 exemplifies the results obtained from applying this analysis to sample 92-1-CA. The XRD patterns demonstrated the presence of CuAlO_2 and Cu_2O as reaction intermediates. These intermediates are consistent with the following sequence of thermodynamically favorable reactions (Table 3.3):



Thus, thermodynamic and XRD data suggested the simultaneous production of CuAlO_2 and Cu_2O via reactions 3.1 and 3.2, followed by the further reduction of these intermediates to metallic copper through reactions 3.3 and 3.4. The sequence of XRD powder patterns shown in Figure 3.9 revealed that a large amount of CuAlO_2 formed rapidly, initially, and then gradually disappeared.

The broad peaks for temperatures below 540°C were attributed to the formation of small CuAlO_2 crystallites dispersed with high surface area Al_2O_3 , which forms simultaneously via reaction 3.2. Sharp peaks for both Cu and CuAlO_2 observed for temperatures above 630°C were the result of significant crystallite growth. The amount of Cu_2O was difficult to estimate because this phase was present only at low temperatures (below 540°C) and thus the x-ray peaks for Cu_2O were partially obscured by the broad peaks for CuAlO_2 , since these species have similar d-spacings. While a significant fraction of copper maintained a +1 oxidation state up to a temperature of 630°C, the extent of Cu^{+1} that was in association with alumina (as CuAlO_2 or otherwise) was not certain.

TPR of samples 56-1-CA and 72-1-CA was also accompanied by XRD analysis using the same technique (Figures 3.10 and 3.11, respectively). XRD confirmed that the reduction of 56-1-CA began with the rapid conversion of all bulk CuO (*i.e.*, detectable by XRD) to Cu, followed by the conversion of CuAl_2O_4 to CuAlO_2 and Cu_2O , which in turn were reduced to Cu by the mechanism suggested for the reduction of 92-1-CA. Similarly, in TPR of sample 72-1-CA, XRD confirmed the initial rapid conversion of all bulk CuO to Cu; however, the mechanism of the subsequent parallel reduction of CuAl_2O_4 and slowly reducing CuO was undiscernable because of a broad and unresolvable peak in the region of maximum diffraction for CuAl_2O_4 , CuAlO_2 , and Cu_2O species. Close examination of the CuO peaks for 72-1-CA during the initial stage of reduction revealed that a CuO $\langle 002 \rangle$ to CuO $\langle 111 \rangle$ peak-intensity ratio of greater than 1.08 persisted until the end of the steep descent (Figure 3.12), suggesting that a form of CuO in close association with alumina reduced more slowly than bulk CuO (Chapter II, Section 2.4).

XRD data, wet chemical analyses, and reduction studies provide comple-

mentary information for characterizing CuO-Al₂O₃ samples prepared by the citrate process. For example, TPR distinguishes between a fraction of bulk CuO that reduces rapidly and the species which reduce more slowly, namely, the compound oxide CuAl₂O₄, the oxide CuO in close association with Al₂O₃, and a small fraction of bulk CuO. On the other hand, wet chemical analysis can distinguish between bulk CuO, both rapidly and slowly reducing forms, and an insoluble mixture of CuAl₂O₄ and CuO in close association with alumina. Finally, XRD analysis can detect CuO and CuAl₂O₄ crystallites of at least 50 Å in size as well as a fraction of CuO interacting with Al₂O₃, if it is aggregated with large (> 50 Å) CuO crystallites; however, CuAl₂O₄ formed at calcination temperatures ≤ 550°C as well as the slowly reducing form of bulk CuO is not detectable. Therefore, the geometry of the slowly reducing form of bulk CuO is postulated to be small CuO crystallites (< 50 Å) covered by a shell of CuO in close association with alumina. In this geometry, bulk CuO would be hindered from reduction and undetectable by x-rays, but accessible to detection by wet chemical analysis.

The types of chemical species present in CuO·Al₂O₃ mixed-oxide samples prepared by the citrate process depend on the preparation conditions, especially the calcination temperature and the molar ratio of Al₂O₃ to CuO. At low calcination temperatures and high molar ratios of Al₂O₃:CuO, a close association between CuO and Al₂O₃, possibly formed from cation exchange, is maximized. On the other hand, the compound oxide CuAl₂O₄ is maximized at high calcination temperatures and molar ratios of Al₂O₃:CuO lower than unity. For example, for a molar ratio Al₂O₃:CuO of unity, there is evidence for the presence of both bulk CuO and CuO in close association with alumina at calcination temperatures between 350°C and 700°C. In these stoichiometric

samples, the amount of CuO in close association with alumina decreases with increasing calcination temperature, while the amount of CuAl_2O_4 increases as the calcination temperature increases above 550°C . For a molar ratio $\text{Al}_2\text{O}_3:\text{CuO}$ of 5:1 and calcination temperature of 650°C , bulk CuO appears to be totally covered by CuO in close association with alumina. Similarly, for a molar ratio $\text{Al}_2\text{O}_3:\text{CuO}$ of 2:1 and calcination temperature of 550°C , the major fraction of bulk CuO is covered by the CuO- Al_2O_3 interacting species. There is no evidence for bulk CuAl_2O_4 (*i.e.*, $> 50 \text{ \AA}$) in either of these samples. Finally, for molar ratios $\text{CuO}:\text{Al}_2\text{O}_3$ of 1.5:1 and 2:1 at calcination temperatures between 600°C and 800°C , there is no CuO in close association with alumina, but rather a mixture of bulk CuO, Al_2O_3 , and CuAl_2O_4 , with CuAl_2O_4 content increasing with calcination temperature.

3.4 Physical Characterization

X-ray line broadening, SEM, and TEM show that crystallites of CuO and CuAl_2O_4 grow with calcination temperature. In this section, x-ray line broadening and SEM results are compared. The scanning electron micrographs of Figures 3.13 and 3.14 include both fresh and reduced samples of different chemical compositions (Table 3.1). A comparison of fresh and reduced 92-1-CA reveals that reduction is accompanied by the appearance of spheres of metallic copper on the primary brittle structure (micrographs 3.13a and 3.13b). Micrographs 3.13c and 3.13d illustrate how remarkably spherical these copper particles are. A comparison of fresh and reduced micrographs 3.14a and 3.14b of sample 11-1-CA3 (pure CuO) shows extensive sintering of metallic copper. On the other hand, comparison of fresh and reduced micrographs 3.14c and 3.14d of sample

72-1-CA (5 mole% CuAl_2O_4) shows very little difference other than a somewhat higher dispersion in the reduced sample. These observations agree with the conclusion drawn from isothermal REDOX experiments, that sintering of copper was much less during reduction of sample 72-1-CA than during reduction of sample 11-1-CA3 (Section 3.3.2).

The micrographs of Figure 3.15 display a primary porous structure and a secondary texture. The secondary texture is smooth for fresh CuAl_2O_4 (micrographs 3.13a and 3.15d) and globular with inhomogeneities for a mixture of CuO and Al_2O_3 (micrographs 3.14c and 3.15a). Micrographs 3.13b and 3.14d of reduced 92-1-CA and 72-1-CA show that copper is visible in the presence of alumina. Consequently, the size of the globules of fresh 72-1-CA (micrograph 3.15a), fresh 59-1-CA (micrograph 3.15b), fresh 56-1-CA (micrograph 3.15c), fresh 19-1-CA (micrograph 3.15d), and other samples not shown can be used as a rough estimate of CuO domain size. For fresh samples calcined at 550°C (72-1-CA), 600°C (59-1-CA), 700°C (56-1-CA), and 800°C (19-1-CA), the average size of the domains is on the order of 3500, 4100, 6700, and 9000 Å, respectively. In general, SEM shows a trend of increasing CuO domain size with increasing calcination temperature. This sintering phenomenon has been observed previously for other metal oxides prepared by the citrate process [23].

An EM301 transmission electron microscope operating at 100kV was used to estimate the CuAl_2O_4 crystallite size of sample 92-1-CA. The major spots of the observed diffraction patterns were consistent with a $\langle 111 \rangle$ zone axis for the fcc array of oxide ions in the spinel structure (Figure 3.16). Superimposed spots of low intensity were probably due to the cations present in the spinel structure. Variations in spot shapes and intensities were attributed to internal stress or to the presence of crystallites of different orientations. The observation

of a $\langle 111 \rangle$ zone axis was readily explained by cleavage along close-packed planes during grinding. In a typical, bright-field image (Figure 3.17), a particle of the sample had the appearance of thin, overlapping platelets. Some of these platelets were not diffracting (gray areas of dark field image in Figure 3.17), but were thin enough so that features of underlying layers could also be discerned. The complicated fringe patterns of the dark field image (circular, spiral, and curved fringe patterns as magnified in Figure 3.18) suggested diffraction from several layers of crystallites, creating complex interference patterns. Unfortunately, we were not able to perform the necessary dark field work to determine the source of the multiple features seen by close examination of Figure 3.18.

Figure 3.17 reveals various isolated crystallites either diffracting without the interference of other layers, or non-diffracting, that can be used to estimate an average crystallite size. A typical procedure involved a search for a single crystal $\langle 111 \rangle$ zone axis from a particle transmitting electrons by tilting the sample, followed by dark-field imaging of various diffraction spots to illuminate a single crystallite of the particle. This procedure was successfully completed on one occasion (bright- and dark-field images shown in Figure 3.18), revealing a crystallite size of approximately 3100 Å by 1920 Å, which corresponds to a diameter of about 2750 Å for a circle of equal area.

X-ray line broadening showed trends of increasing CuO and CuAl₂O₄ crystallite sizes with calcination temperature. A silicon standard was used to estimate instrumental line broadening (0.00384 radians), and the mean crystallite size was estimated using the Scherrer formula as follows:

$$d = \frac{K\lambda}{\beta(\cos\theta)}, \quad (3.5)$$

where λ = wavelength of Cu(K α) radiation (1.54056 Å)

β = full width at half maximum in radians of maximum intensity

$\langle 002 \rangle$ line for CuO or $\langle 311 \rangle$ line for CuAl_2O_4

K = Scherrer constant (particle shape factor)

θ = Bragg angle of the CuO $\langle 002 \rangle$ line or $\text{CuAl}_2\text{O}_4 \langle 311 \rangle$ line.

For $K=1$, the Scherrer formula predicts a mean CuAl_2O_4 crystallite size of 1910 Å for sample 92-1-CA. A value of 1.4 for K will give a CuAl_2O_4 crystallite size consistent with that observed by transmission electron microscopy. K values between 0.7 and 1.84 have been reported, depending upon several variables, including crystallite morphology and crystallite size distribution [24].

For samples calcined at 550°C, 600°C, 700°C, and 800°C, the Scherrer formula with $K=1.4$ predicts mean CuO crystallite sizes of 540 Å, 690 Å, 800 Å, and 980 Å, respectively, and mean CuAl_2O_4 crystallite sizes of 120 Å, 170 Å, 200 Å, and 790 Å, respectively (Table 3.4). Figure 3.20 shows a linear increase in CuO crystallite size with calcination temperature. The crystallites of CuAl_2O_4 , on the other hand, grow very slowly at low calcination temperatures but rapidly above 800°C. Therefore, CuO crystallites exhibit a steady, sintering rate throughout a temperature range of 550°C to 800°C, while sintering does not become significant for CuAl_2O_4 crystallites up to a temperature between 700°C and 800°C. The transition of the growth of CuAl_2O_4 crystallites from a slow to a rapid rate occurs at approximately the same temperature as the transition of the activation energy for aluminate formation from a high to a low value in the plot of the Carter equation (Figure 2.3). This observation supports the suggestion that the change in activation energy above about 750°C is due to diffusional limitations incurred by CuAl_2O_4 sintering. Below 750°C, crystallites of CuAl_2O_4 form very slowly at the interfaces between CuO and Al_2O_3 grains. Above 750°C, crystallites of CuAl_2O_4 sinter, causing the solid-state reaction to

slow down by hindering interdiffusion of cations.

The domains of CuO observed by SEM were larger than the crystallites identified by x-ray line broadening. This discrepancy suggests that the domains viewed by SEM are actually aggregates of smaller CuO crystallites, whose grain boundaries are invisible at the working magnification. Another possibility in keeping with the trend of increasing domain density with CuO content is that each domain contains several small CuO particles intermingled with Al₂O₃. These possibilities are further supported by comparing scanning electron micrographs of fresh Cu-Al-O samples to those of precipitates recovered from them following hot nitric acid extraction. Since x-ray line-broadening analysis revealed that CuAl₂O₄ crystallites are essentially unaffected by the extraction (Table 3.5), differences detected by SEM between the fresh sample and the recovered solid are assumed to characterize the CuO and Al₂O₃ components. Figure 3.21 shows that leaching CuO from a sample can lead to a filtered precipitate with either no globules or scattered globules of a higher dispersion than in the fresh sample. The former case suggests that CuO is present as clusters of exclusively CuO crystallites, while the latter case suggests that CuO is present in clusters containing CuO, Al₂O₃, and possibly CuAl₂O₄.

3.5 Spectroscopic Studies

3.5.1 Raman Spectroscopy

In situ laser Raman spectroscopy has been recently applied to supported metal oxides [25-28] to investigate the unique state of the supported metal oxide in comparison to the pure, unsupported form of the oxide. The Raman effect occurs when an incident photon perturbs the molecule by an inelastic interaction

that induces a vibrational or rotational transition. The change in polarizability of the molecule associated with the vibration or rotation produces the Raman scattered photon. Laser Raman spectroscopy has been used to investigate bulk, surface, and interfacial structures in supported catalysts. The main advantage of laser Raman spectroscopy over infrared spectroscopy in supported systems is that support materials (typically, titania, silica, and alumina) are poor Raman scatterers but absorb strongly in the infrared.

Figure 3.22 presents laser Raman spectra for (a) ultrapure CuO, (b) a stoichiometric CuO·Al₂O₃ sample (13-1-CA7) subjected to a 4-hour calcination at 400°C and (c) a stoichiometric CuO·Al₂O₃ sample (92-1-CA) subjected to a 4-hour calcination at 900°C. Based on recently reported laser Raman spectra for NiO and NiAl₂O₄ [29], characteristic signals for CuO, CuO·Al₂O₃, and CuAl₂O₄ samples were anticipated to occur at low frequencies (*i.e.*, 200 to 800 cm⁻¹). Signals in this region, however, were intrinsically weak and, in fact, a sample capillary containing water (curve d) revealed a small amount of scattering in the 360-515 cm⁻¹ region. To help improve the strength of the sample signal, the laser was passed through the sample unfiltered, causing the appearance of laser lines at 199.5 cm⁻¹ and 390 cm⁻¹ (Figure 3.22). Sample spectra are the result of 10 accumulated scans, while the background spectrum was recorded after only 2 scans. The constancy of the positions of the laser lines ensures that no overall shift of the spectra occurred between runs.

All three spectra show a strong signal in the region 1020-1130 cm⁻¹. The position of this high-frequency band has values of 1064 cm⁻¹ for pure CuO, 1091 cm⁻¹ for sample 13-1-CA7, and 1124 cm⁻¹ for sample 92-1-CA. Observations in Raman studies of some catalytic systems are noteworthy at this point. A shift towards higher frequencies has been observed for strong Raman bands in the

region $\sim 900 - 1100 \text{ cm}^{-1}$ in alumina-supported vanadium oxide [26], rhenium oxide [28], tungsten oxide [26,31-33], and molybdenum oxide [26,34]. A common feature of these systems has been recognized: The oxidized forms of these metals all possess high oxidation states (V^{+5} , Re^{+7} , W^{+6} , and Mo^{+6}); unlike copper (Cu^{+2}). This strong Raman band has been assigned to the symmetrical stretching mode of the terminal $\text{M}=\text{O}$ ($\text{M}=\text{metal}$) bonds [26,29]. This assignment is not feasible for a Cu^{+2} species because of chemical bonding considerations of the available electrons. Since determination of the particular assignment for this band is beyond the scope of this work, the band will be assumed to characterize some vibrational mode between copper and oxygen.

Frequency shifts of the Raman band corresponding to the symmetrical stretching mode of the terminal $\text{M}=\text{O}$ bonds in alumina-supported metal oxides have been correlated in some cases to increasing coverage up to monolayer coverage and in all cases to surface dehydration. In the case of correlation to increasing coverage, the shift has been attributed to a distortion of the monolayer species by lateral interactions, or the heterogeneity of support adsorption sites, or both. In the case of the removal of coordinated water molecules from the supported metal oxide species, it has been proposed that the interaction of water molecules alters the symmetry of surface bonding and thus affects the symmetric $\text{M}=\text{O}$ stretch.

Dehydration is not believed to play a role in Figure 3.22 because all spectra were recorded at room temperature, so that the state of hydration of the samples should be similar. Furthermore, sample 92-1-CA has very little cupric oxide available ($\leq 1 \text{ mass\% CuO}$) to which water molecules can coordinate. It is difficult to justify that surface coverage (*e.g.*, of CuO on Al_2O_3) is a parameter in these samples, because the ratio of copper to aluminum is the same in each

sample. Rather, the shift of the high-frequency band in Figure 3.22 appears to be correlated to the extent of interaction of cupric oxide with alumina. The lower frequency exhibited by pure CuO is at one extreme, with the higher frequency found for sample 92-1-CA containing CuAl_2O_4 as its major component (identified by XRD) at the other extreme. Sample 13-1-CA7 is at an intermediate extreme because while XRD identifies bulk CuO in this sample, the peaks for CuO display anomalous intensities (Figure 2.5) suggesting, together with TPR studies (Figure 3.8), and wet chemical analysis (Table 3.1), that bulk CuO is at least partially covered by a layer of CuO in close association with alumina.

3.5.2 Diffuse Reflectance Spectroscopy

Diffuse reflectance spectroscopy (DRS) has been used extensively to distinguish between different coordinations of transition metal cations supported on high-surface area materials, and contained in zeolites [35]. For Cu^{+2} supported on $\gamma\text{-Al}_2\text{O}_3$, peak maxima in diffuse reflectance spectra for Cu^{+2} in tetrahedral and octahedral coordinations have been reported at values of 1450 nm and 750 nm [3,8]. The observed bands are broad because both the octahedral and tetrahedral ground states for Cu^{+2} are degenerated and subjected to the Jahn-Teller effect. Furthermore, since tetrahedrally coordinated Cu^{+2} lacks a center of symmetry, the absorption coefficient for the d-d transition is more than an order of magnitude higher than that for octahedrally coordinated Cu^{+2} . A band for octahedrally coordinated Cu^{+2} , therefore, is difficult to distinguish even for CuAl_2O_4 , which contains 60% octahedrally coordinated and 40% tetrahedrally coordinated Cu^{+2} .

DRS was used to obtain spectra for samples 92-1-CA (96 mole % CuAl_2O_4), 72-1-CA (5 mole % CuAl_2O_4), and 13-1-CA7 (no CuAl_2O_4 detected by XRD).

These spectra were compared to those obtained for ultrapure CuO (purchased from Alfa Products) and Al₂O₃ (prepared by the citrate process with calcination at 550°C for 4 hours), and to those reported elsewhere [3,8] for CuAl₂O₄ and octahedrally coordinated Cu⁺² (Figure 3.23). The spectrum obtained for sample 92-1-CA was in excellent agreement with that reported for CuAl₂O₄. Sample 92-1-CA exhibited a strong, broad peak for tetrahedrally coordinated Cu⁺², spanning from 953 nm to 1926 nm with a maximum at 1549 nm; however, no peak was discernable for octahedrally coordinated Cu⁺². Spectra recorded for samples 13-1-CA7 and 72-1-CA displayed a subtle feature indicative of octahedrally coordinated Cu⁺², which was more pronounced for sample 13-1-CA7. A broad band for octahedrally coordinated Cu⁺² in these samples appeared to be partially obscured by the presence of bulk CuO, which exhibits a broad band with a maximum at 675 nm, and extending from 325 nm to 848 nm. The broad band observed for octahedrally coordinated Cu⁺² in a catalyst containing 10% CuO on γ -Al₂O₃, in comparison, exhibited a maximum at 740 nm, and extended from 567 nm to 1017 nm. The spectrum for γ -Al₂O₃, on the other hand, contained no features to obscure peaks for octahedrally or tetrahedrally coordinated Cu⁺². Spectra recorded for samples 72-1-CA and 13-1-CA7 contained no evidence for tetrahedrally coordinated Cu⁺².

DRS revealed the presence of tetrahedrally coordinated Cu⁺² in sample 92-1-CA, and the absence of tetrahedrally coordinated Cu⁺² in samples 72-1-CA and 13-1-CA7. DRS provided qualitative evidence for the presence of octahedrally coordinated Cu⁺² in samples 72-1-CA and 13-1-CA7; however, this observation was partially obscured by the presence of a large quantity of bulk CuO and by the low-absorption coefficient characteristic of octahedrally coordinated Cu⁺². The evidence for octahedrally coordinated Cu⁺² was stronger for

sample 13-1-CA7 than for sample 72-1-CA, which correlates to the amount of CuO-Al₂O₃ interaction characterized by anomolous x-ray diffraction intensities (Chapter II, Section 2.4). These data, combined with information obtained from TPR and Raman spectroscopy, suggest that an interaction between CuO and γ -Al₂O₃ exists and involves Cu⁺² cations in octahedral interstices of γ -Al₂O₃.

REFERENCES

1. Flytzani-Stephanopoulos, M., Tamhankar, S.S., Gavalas, G.R., Bagajewicz, M.J., and Sharma, P.K., "High-Temperature Regenerative Removal of H_2S by Porous Mixed Oxide Sorbents," *Prepr. Pap. Amer. Chem. Soc., Div. Fuel Chem.*, **30**(4), 16, 1985.
2. Strohmeier, B.R., Leyden, D.E., Field, R.S., and Hercules, D.M., "Surface Spectroscopic Characterization of $\text{Cu}/\text{Al}_2\text{O}_3$ Catalysts," *J. Catal.*, **94**, 514, 1985
3. Friedman, R.M., and Freeman, J.J., "Characterization of $\text{CuO}/\text{Al}_2\text{O}_3$ Catalysts," *J. Catal.*, **55**, 10, 1978.
4. Pierron, E.D., Rashkin, J.A., and Roth, J.F., "Copper Oxide on Alumina I. XRD Studies of Catalyst Composition During Air Oxidation of Carbon Monoxide," *J. Catal.*, **9**, 38, 1967.
5. Tsikoza, L.T., Torasova, D.V., Ketchik, S.V., Maskimov, N.G., and Popovskii, V.V., "Physicochemical and Catalyst Properties of Copper-Aluminum Oxide Catalysts," *Kinet. Katal.*, **22**(5), 1300, 1981.
6. Ketchik, S.V., Plyasova, L.M., Seredkin, A.E., Kostov, V.V., and Morozov, L.N., "X-ray Studies of Supported Copper-Aluminum Catalysts," *React. Kinet. Catal. Lett.*, **14**(4), 429, 1980.
7. Freeman, J.J., and Friedman, R.M., "Re-examination of the Diffuse Reflectance Spectra of $\text{Cu}/\text{Al}_2\text{O}_3$ Catalysts," *J. Chem. Soc., Faraday Trans. I.*, **74**, 758, 1978.
8. Hierl, R., Knözinger, H., and Urbach, H.-P., "Surface Properties and Reduction Behavior of Calcined $\text{CuO}/\text{Al}_2\text{O}_3$ and $\text{CuO-NiO}/\text{Al}_2\text{O}_3$ Catalysts," *J. Catal.*, **69**, 475, 1981.

9. Jacono, M.L., Cimino, A., and Inversi, M., "Oxidation States of Copper on Alumina Studied by Redox Cycles," *J. Catal.*, **76**, 320, 1982.
10. Wolberg, A., and Roth, J.F., "Copper Oxide Supported on Alumina. III. X-Ray K-Absorption Edge Studies of the Cu^{+2} Species," *J. Catal.*, **15**, 250, 1969.
11. Wolberg, A., Ogilvie, J.L., and Roth, J.F., "Copper Oxide Supported on Alumina. IV. Electron Spectroscopy for Chemical Analysis," *J. Catal.*, **19**, 86, 1970.
12. Ertl, G., Hierl, R., Knözinger, H., Thiele, N., and Urbach, H.P., "XPS Study of Copper Aluminate Catalysts," *Appl. Surf. Sci.*, **5**, 49, 1980.
13. Matsunaga, Y., "Note on the Electron Spin Resonance of Cupric Oxide-Alumina Catalysts," *Bull. Chem. Soc. Japan*, **34**(9), 1291, 1961.
14. Berger, P.A., and Roth, J.F., "Copper Oxide Supported on Alumina. Electron Spin Resonance Studies of Highly Dispersed Phases," *J. Phys. Chem.*, **71**(3), 4307, 1967.
15. Lumbeck, H., and Voitländer, J., "ESR Investigations of Copper Oxide on Alumina," *J. Catal.*, **13**, 117, 1969.
16. Sventsitskii, E.S., Vorob'ev, V.N., and Talipov, G.Sh., "Electron Spectroscopic and ESR Investigation of the Coordination and Valence States of the Copper Ions in $\text{CuO-Al}_2\text{O}_3$ Catalysts," *Kinet. Katal.*, **18**(1), 201, 1977.
17. Chen, H.-C., and Anderson, R.B., "Concentration Profiles in Impregnated Chromium and Copper on Alumina," *J. Catal.*, **43**, 200, 1976.
18. Parris, G.E., and Klier, K., "The Specific Copper Surface Areas in Cu/ZnO Methanol Synthesis Catalysts by Oxygen and Carbon Monoxide Chemisorption: Evidence for Irreversible CO Chemisorption Induced by the Interaction of the Catalyst Components," *J. Catal.*, **97**(2), 374, 1986.

19. Evans, J.W., Wainwright, M.S., Bridgewater, A.J., and Young, D.I., "On the Determination of Copper Surface Area by Reaction with Nitrous Oxides," *Appl. Catal.*, **7**, 75, 1983.
20. Edelstein, S., *Ph.D. Dissertation*, California Inst. of Tech., 1987.
21. Tandon, S.P., and Gupta, J.P., "Diffuse Reflectance Spectrum of Cupric Oxide," *Spectrosc. Lett.*, **2**(12), 357, 1969.
22. Voge, H.H., and Atkins, L.T., "Uniformity of Supported CuO from Rate of Reduction with Hydrogen," *J. Catal.*, **1**, 171, 1962.
23. Courty, P., Ajot, H., and Marcilly, C., "Mixed Oxides or a Solid Solution of Oxides in a Finely Divided Form Obtained by Thermal Decomposition of Amorphous Precursors," *Powd. Technol.*, **7**, 21, 1973.
24. Klug, H.P., and Alexander, L.R., *X-Ray Diffraction Procedures for Polycrystalline and Amorphous Materials* (John Wiley and Sons: New York, 1954), p.386, 516.
25. Wachs, I.E., Hardcastle, F.D., and Chan, S.S., "Raman Spectroscopy of Supported Metal Oxide Catalysts," *Spectrosc.*, **1**(8), 30, 1988.
26. Chan, S.S., Wachs, I.E., Murrell, L.L., Wang, L., and Hall, K., "In Situ Laser Raman Spectroscopy of Supported Metal Oxides," *J. Phys. Chem.*, **88**, 5831, 1984.
27. Dixit, L., Gerrard, D.L., and Bowley, H.J., "Laser Raman Spectra of Transition Metal Oxides and Catalysts," *Appl. Spectrosc. Rev.*, **22**(2,3), 189, 1986.
28. Anderson, J.R., and Boudart, M., eds., *Catalysis, Science and Technology* (Springer Verlag: New York, 1983), p.97.
29. Chan, S.S., and Wachs, I.E., "In Situ Laser Raman Spectroscopy of Nickel Oxide Supported on γ -Al₂O₃," *J. Catal.*, **103**, 224, 1987.

30. Wang, L., and Hall, W.K., "The Preparation and Properties of Rhenia-Alumina Catalysts," *J. Catal.*, **82**, 177, 1983.
31. Chan, S.S., Wachs, I.E., Murrell, L.L., and Dispenziere, N.C., "Laser Raman Characterization of Tungsten Oxide on Alumina" in *Catalysis on the Energy Scene* ed. by S. Kaliaguine and A. Mahay (Elsevier Science Publishers B.V.: The Netherlands, 1984), p.259.
32. Chan, S.S., Wachs, I.E., Murrell, L.L., and Dispenziere, N.C., "Laser Raman Characterization of Tungsten Oxide Supported on Alumina: Influence of Calcination Temperatures," *J. Catal.*, **92**, 1, 1985.
33. Iannibello, A., Villa, P.L., and Marengo, S., "Interaction of Tungsten(VI) and γ -Al₂O₃. A Chromatographic and Spectroscopic Investigation," *Gazz. Chim. Ital.*, **109**, 521, 1979.
34. Stampfl, S.R., Chen, Y., Dumesic, J.A., Niu, C., and Hill, G.G. Jr., "Interactions of Molybdenum Oxide with Various Oxide Supports: Calcination of Mechanical Mixtures," *J. Catal.*, **105**, 445, 1987.
35. Schoonheydt, R.A., "Diffuse Reflectance Spectroscopy" in *Characterization of Heterogeneous Catalysts* ed. by F. Delannay (Marcel Dekker, Inc.: New York, 1984), p.125-160.
36. Jacob, K.T., and Alcock, C.B., "Thermodynamics of CuAlO₂ and CuAl₂O₄ and Phase Equilibria in the System Cu₂O-Cu-Al₂O₃," *J. Amer. Cer. Soc.*, **58**(5-6), 192, 1975.
37. Zalanskii, A.G., Balakirev, V.F., Chebotaev, N.M., and Chufarov, G.I., "Thermodynamic Analysis of the Reduction, Dissociation, and Formation from the Elements and Oxides of Copper(I) Aluminate (CuAlO₂), Chromate(III) (CuCrO₂), and Ferrate(III) (CuFeO₂)," *Russ. J. Inorg. Chem.*, **14**(3), 326, 1969.

Table 3.1: Stoichiometric samples (1:2 molar ratio of Cu:Al)
prepared by the citrate process for TPR studies.

Sample	Figures	$T_{\text{calc}}(^{\circ}\text{C})$ (Duration-hrs.)	Yield (grams)	Mole Ratios ^a $\text{CuO}:\text{CuAl}_2\text{O}_4:\text{Al}_2\text{O}_3$	BET ^b (m^2/g)
92-1-CA	3.2a,3.7c,3.9,3.13a,3.16 3.17,3.18,3.19	900(4)	11.5	2.1:95.8:2.1	2.7(0.4)
19-1-CA	3.2b,3.15d,3.19	800(3.75)	7.6	10.4:79.1:10.4	5.6(0.8)
56-1-CA	3.2c,3.3a,3.10,3.15c	700(4)	11.5	25.8:48.3:25.8	33(5)
15-1-CA	3.2d,3.3b	550(4)	4.2	33.3:33.3:33.3	
59-1-CA	3.2e,3.3c,3.15b,3.19	600(4)	11.5	45.3:9.4:45.3	86(5)
72-1-CA	3.2f,3.3d,3.4,3.11,3.12 3.14c,3.15a,3.19	550(4)	11.5	47.4:5.2:47.4	120(8)
11-1-CA3	3.2g,3.4,3.7a,3.8a,3.14a	550(4)	8.3	Pure CuO	1.1(0.5)
14-1-Al3		550(4)	3.4	Pure Al_2O_3	217(15)
15-1-CA7	3.8c	350(4)	2.5		
13-1-CA7	3.8b	400(4)	2.4		

^a Subject to 1-4% experimental error.

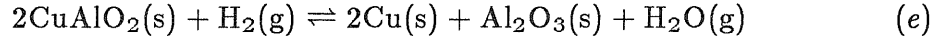
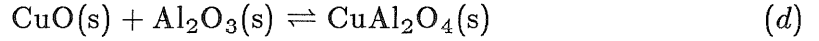
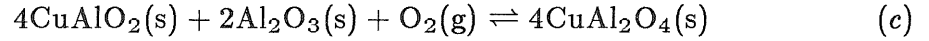
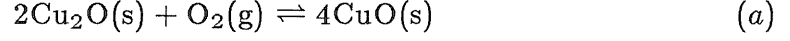
^b Overall surface area determined by physical adsorption of N_2 .

Table 3.2: Nonstoichiometric Cu-Al-O sample prepared by the citrate process.

Sample	Figure	Mole Ratios $\text{CuO}:\text{Al}_2\text{O}_3$	$T_{\text{calc}}(^{\circ}\text{C})$ (Duration-hrs.)	Mole Ratios ^b $\text{CuO}:\text{CuAl}_2\text{O}_4:\text{Al}_2\text{O}_3$
17-1-CA8	3.5a	1.5:1	600(13)	54:9.9:36
19-2-CA8	3.5b	1.5:1	700(25)	52:13:35
19-4-CA8	3.5c	1.5:1	800(14)	35:41:24
14-1-CA8	3.6a	2:1	600(8)	61:8.5:30
19-1-CA8	3.6b	2:1	700(18)	59:12:29
19-3-CA8	3.6c	2:1	800(19)	46:30:23
6-1-CA3	3.7b	1:2	550(2)	31:7.5:62**
21-2-CA3	3.7d	1:5	650(19)	15:8.8:76**

^b Subject to 6-10% experimental error.

Table 3.3: Gibbs' free energies of formation for various Cu, Al, and Cu-Al containing species.



Reaction	ΔG_f° (cal/mol)	Temperature (K)	Ref.
a	$-62354 + 44.89T (\pm 100)$	973-1473	36
b	$-5670 + 2.49T (\pm 300)$	973-1473	36
c	$-33400 + 20.02T (\pm 300)$	973-1473	36
d	$+4403 - 4.97T (\pm 350)$	973-1473	36
e	$+6310 - 21.0T$	973-1273	37

Table 3.4: CuO and CuAl₂O₄ crystallite sizes in fresh Cu-Al-O samples.

Sample	CuO:CuAl ₂ O ₄	SEM	XRD(d,Å)	XRD(d,Å)	
	T _{calc} (°C)	(mole ratios)	(Å)	CuO	CuAl ₂ O ₄
11-1-CA3	550	100:0		1400	
72-1-CA	550	47.5:5	3500	540	120
59-1-CA	600	45:10	4100	690	170
56-1-CA	700	26:48	6700	800	200
19-1-CA	800	10:80	9000	980	790

Table 3.5: CuAl_2O_4 crystallite size estimated before and after hot nitric-acid extraction.

Sample	Description	Location in 2θ of $\langle 311 \rangle$ peak	FWHM ^a (degrees)	Crystallite Size (\AA)
19-1-CA	Calcined at 800°C, 4 hrs, contains 80 mol% CuAl_2O_4	36.810	0.378	424.0
104-1-FCA	Precipitate from nitric acid extraction of 19-1-CA	36.830	0.382	417.4
56-1-CA	Calcined at 700°C, 4 hrs, contains 48 mol% CuAl_2O_4	36.765	0.878	153.3
107-1-FCA	Precipitate from nitric acid extraction of 56-1-CA	36.942	0.787	172.6
92-1-CA	Calcined at 900°C, 4 hrs, contains 96 mol% CuAl_2O_4	36.840	0.328	535.8
24-2-FCA2	Precipitate from nitric acid extraction of 92-1-CA	36.759	0.330	529.9
59-1-CA	Calcined at 600°C, 4 hrs, contains 10 mol% CuAl_2O_4	36.708	0.718	190.6
109-1-FCA	Precipitate from nitric acid extraction of 59-1-CA	36.436	0.648	213.6

^a Full width at half-maximum intensity.

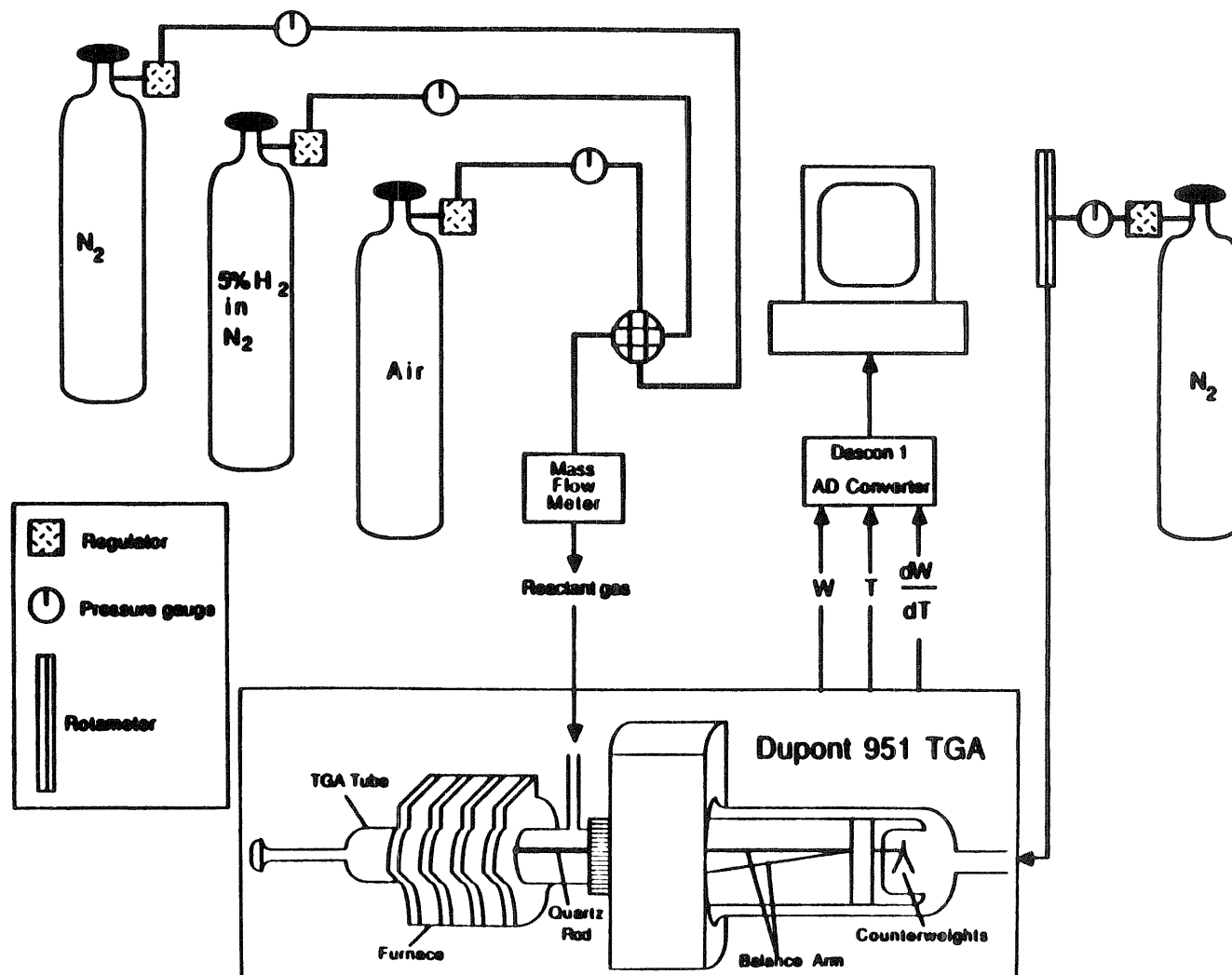


Figure 3.1: Schematic of the thermogravimetric system used for TPR experiments.

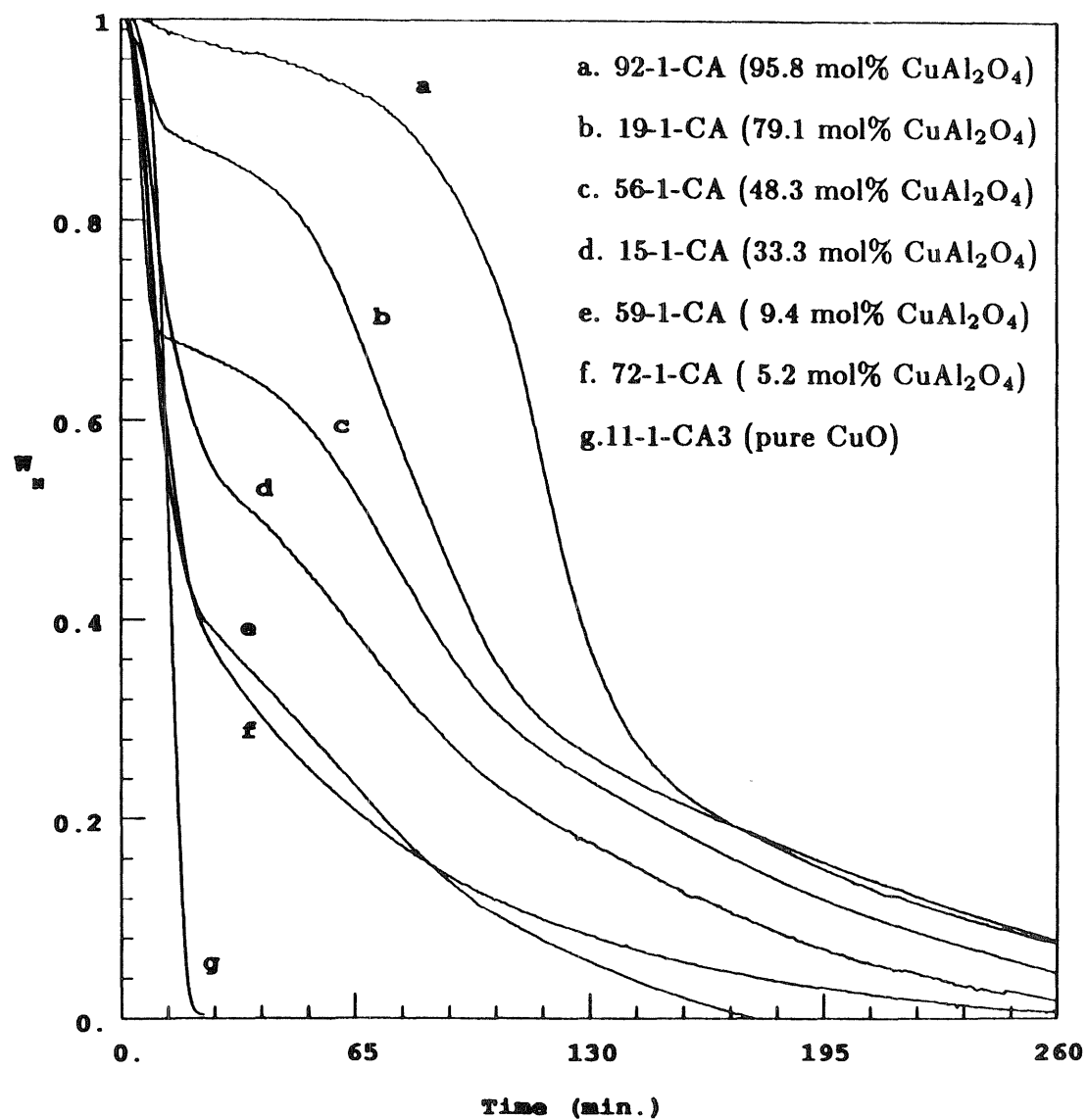


Figure 3.2: Normalized weight-loss curves for TPR of CuO and Cu-Al-O samples.

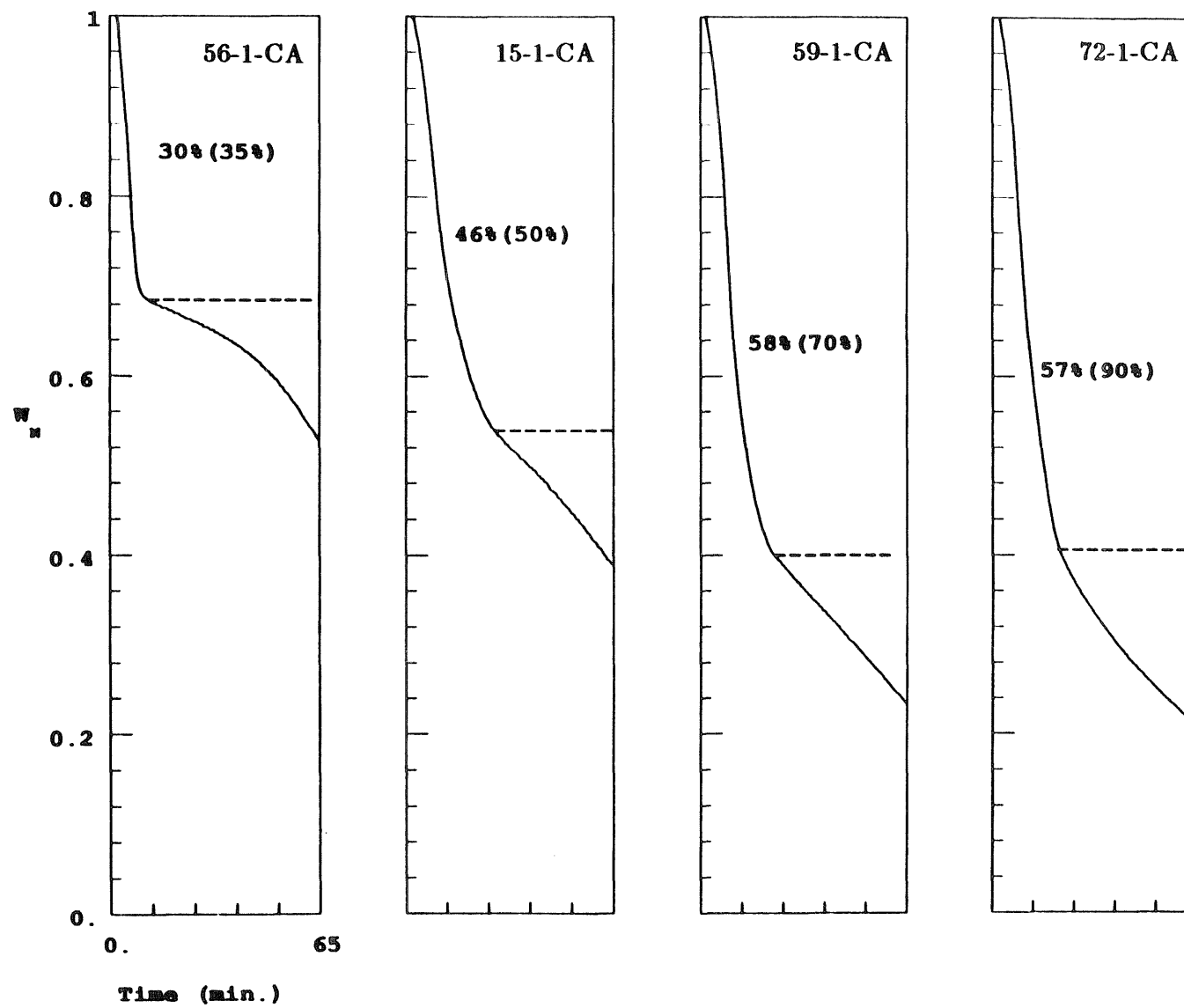


Figure 3.3: Enlargement of the initial reduction periods for 4 of the 7 curves depicted in Figure 3.2.

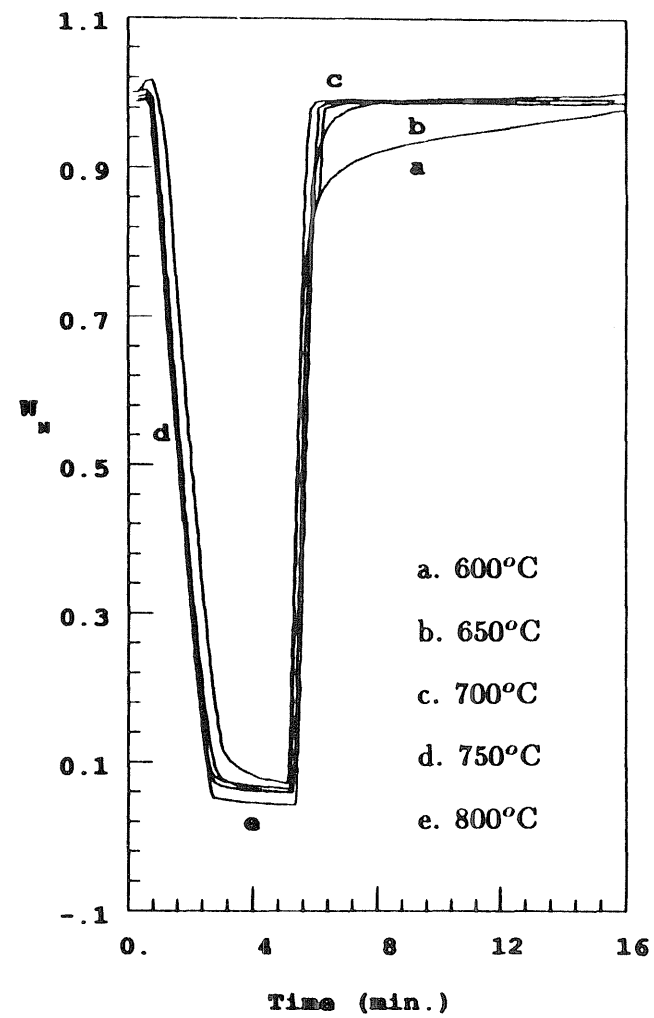
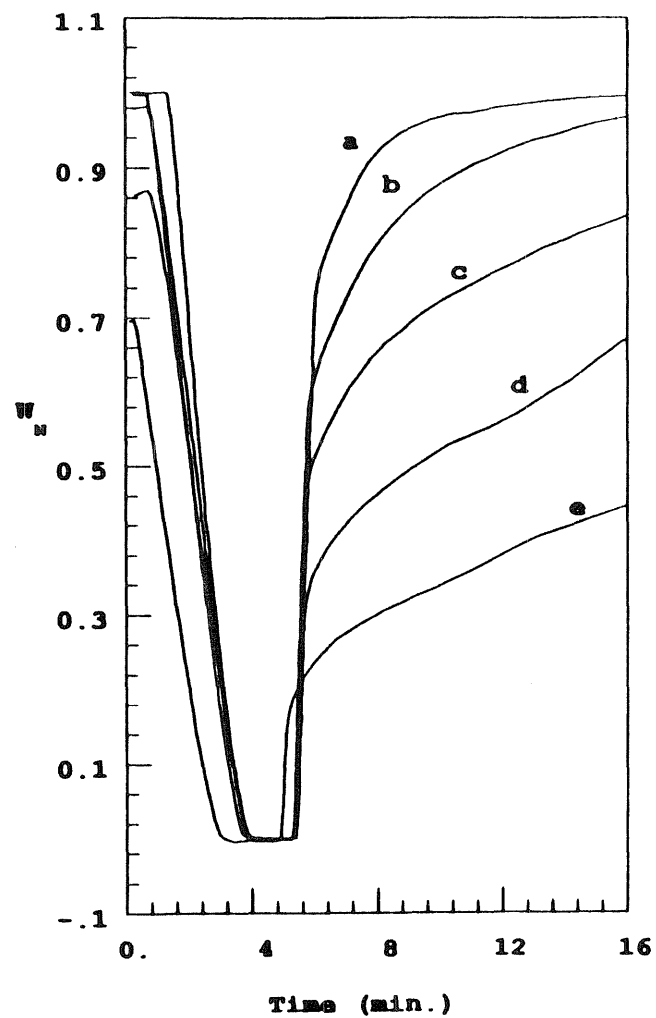


Figure 3.4: Normalized weight-loss curves for repeated isothermal REDOX of 11-1-CA3 (right) and 72-1-CA (left).

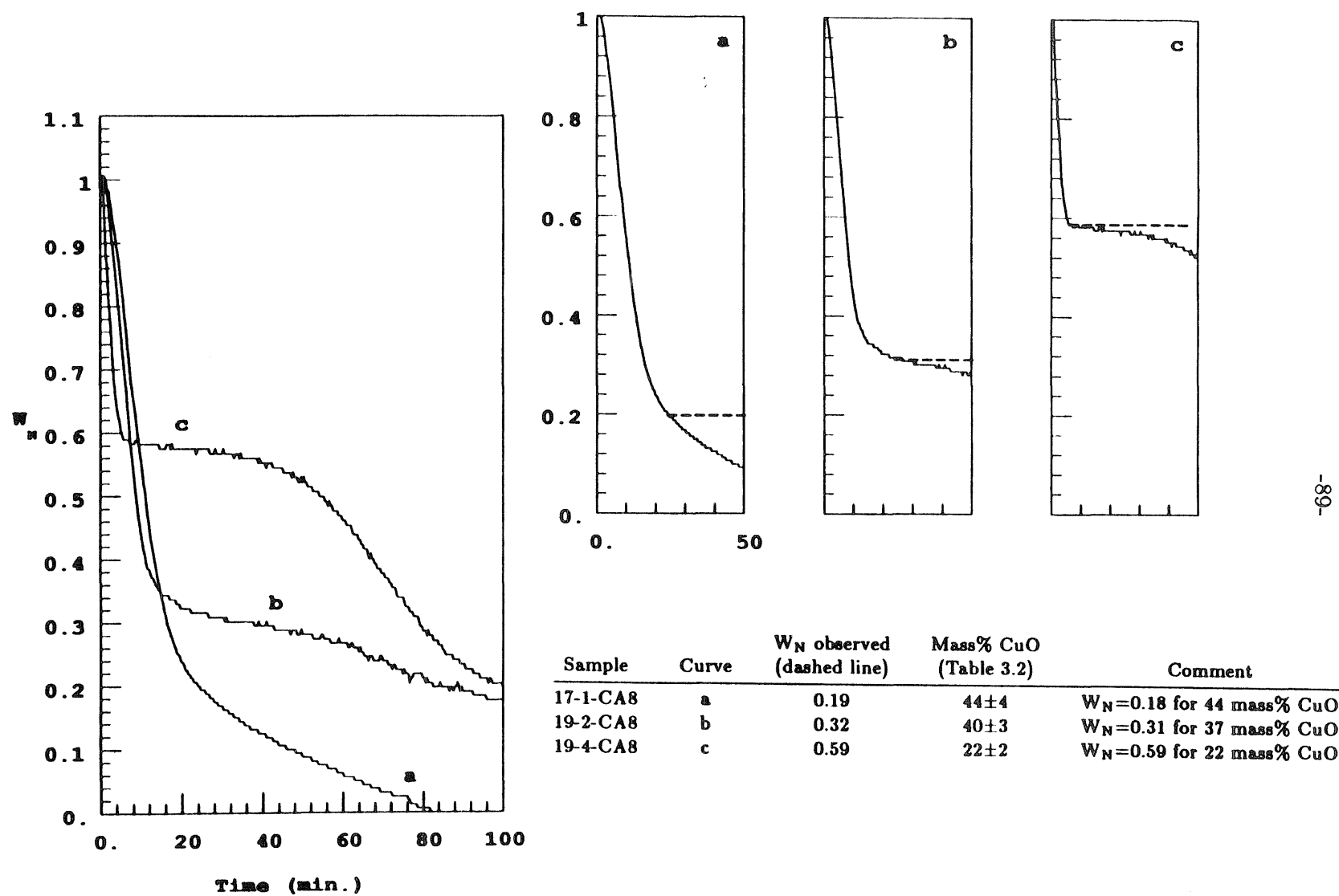


Figure 3.5: Normalized weight-loss curves for TPR of Cu-Al-O samples prepared with a molar ratio Cu:Al₂ of 3:2.

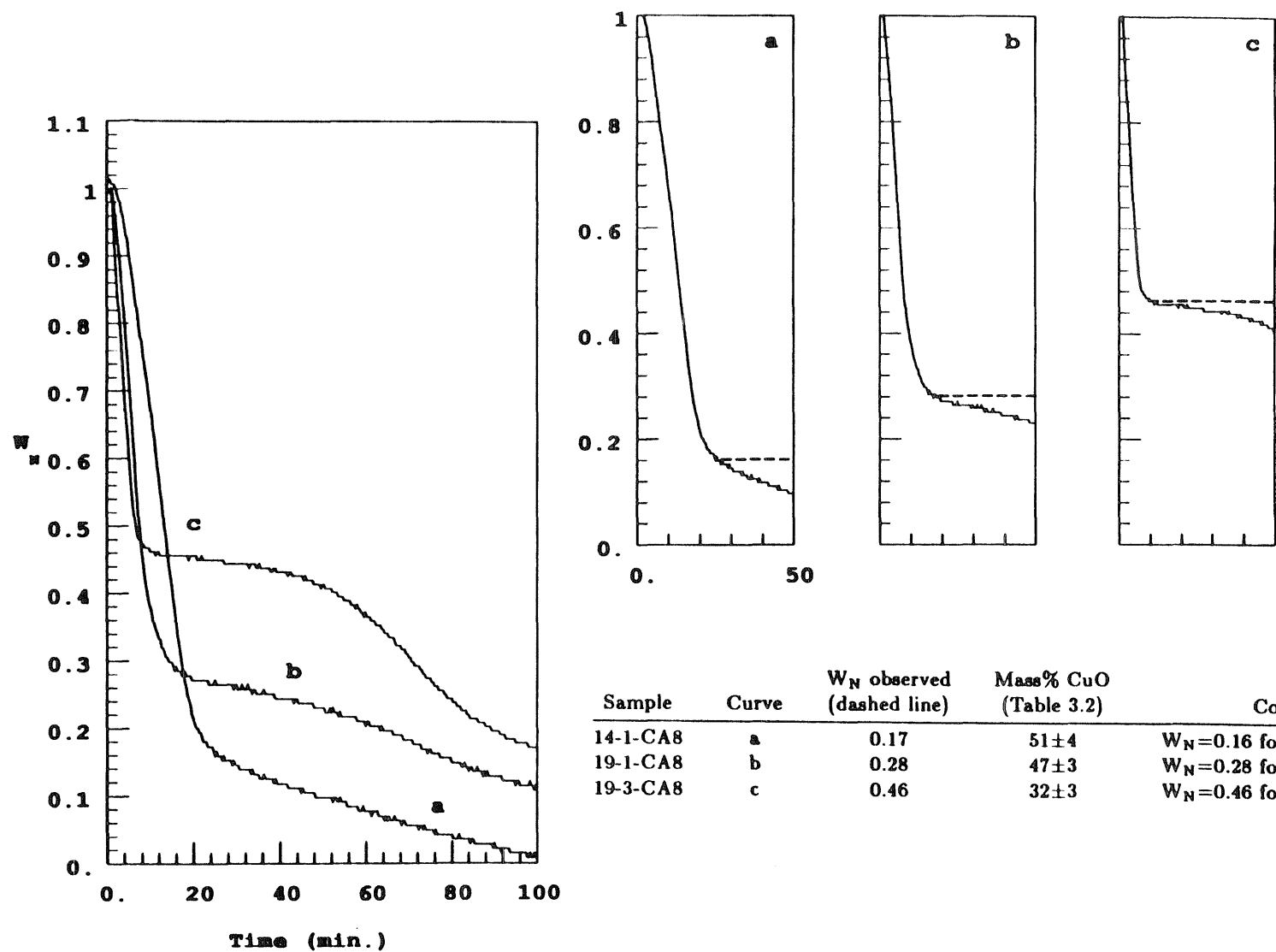


Figure 3.6: Normalized weight-loss curves for TPR of Cu-Al-O samples prepared with a molar ratio Cu:Al₂ of 2:1.

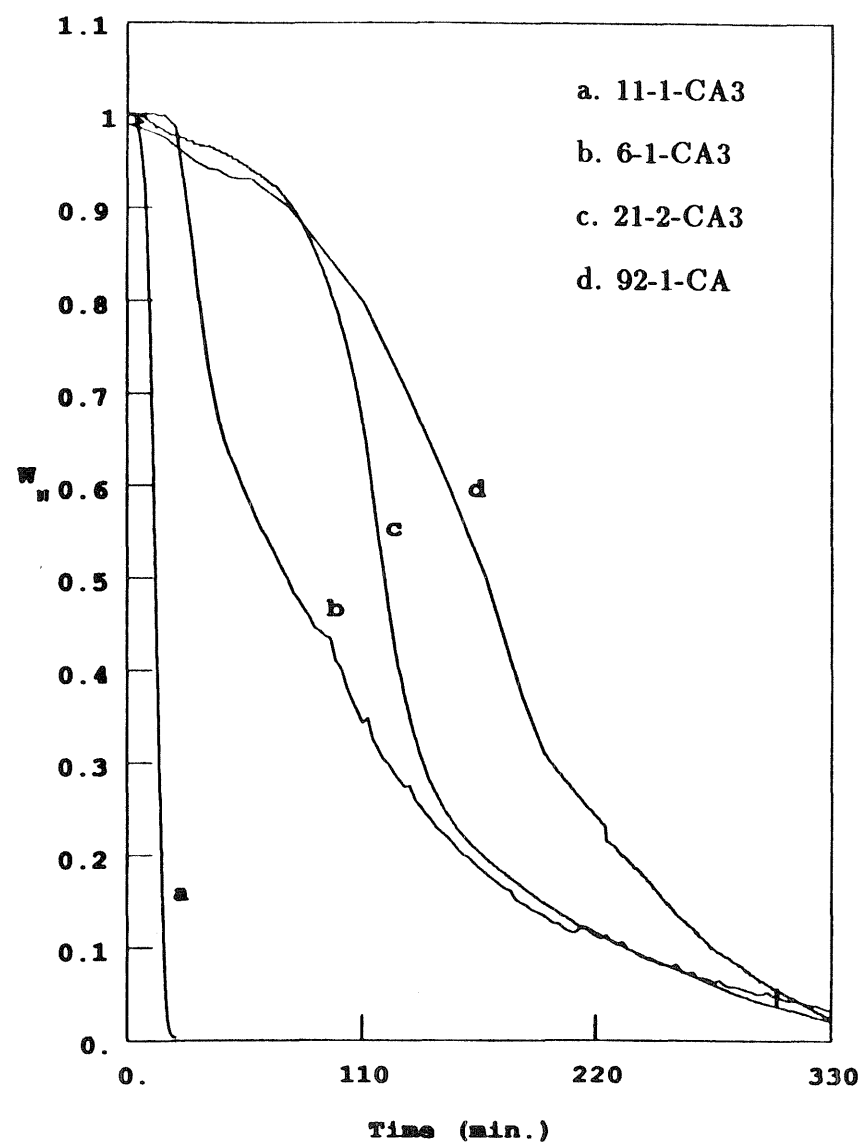


Figure 3.7: Normalized weight-loss curves for TPR of CuO (11-1-CA3, a), CuAl_2O_4 (92-1-CA, c), and samples prepared with a molar ratio $\text{Cu}:\text{Al}_2 < 1$ (b,d).

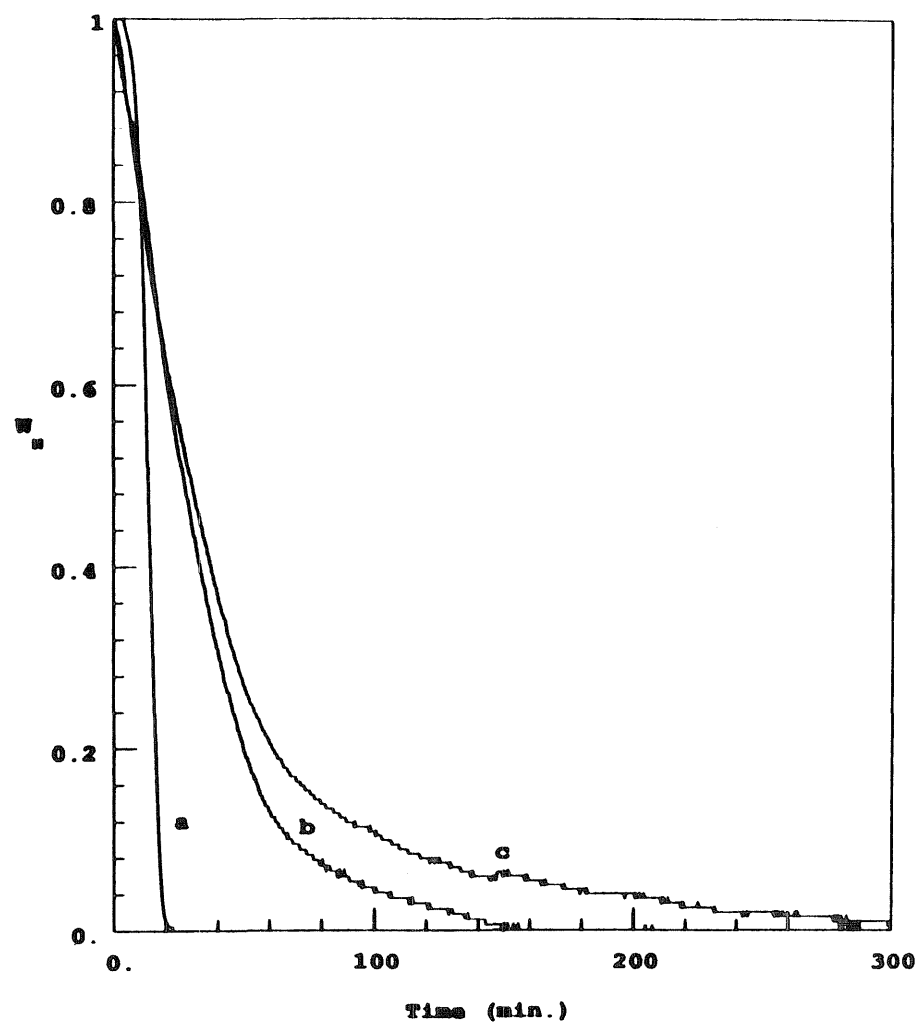


Figure 3.8: Normalized weight-loss curves for TPR of CuO (11-1-CA3, a), and Cu-Al-O samples calcined at 350°C (c) and 400°C (b).

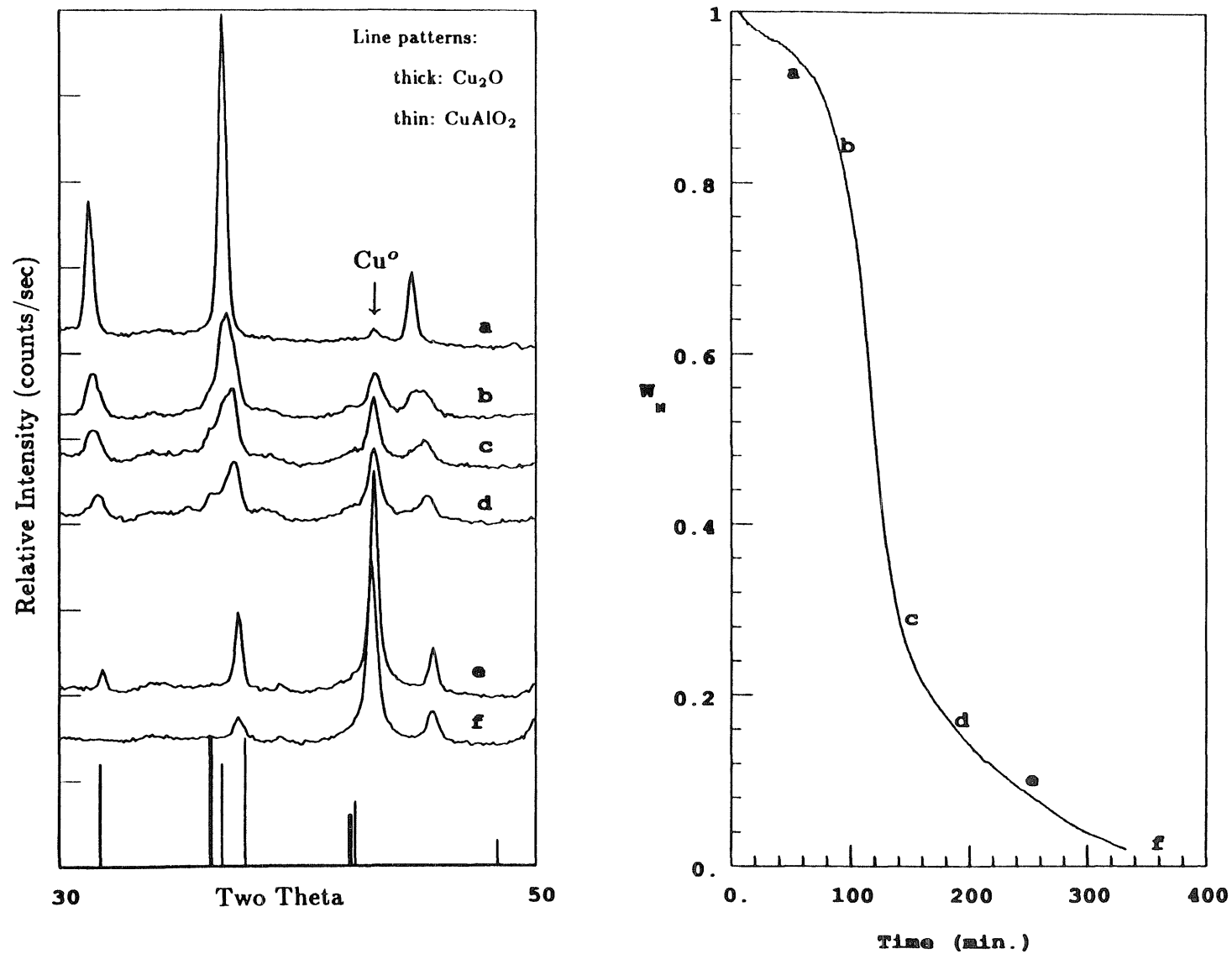


Figure 3.9: XRD patterns of partially reduced 92-1-CA after quenching separate TPR experiments as indicated.

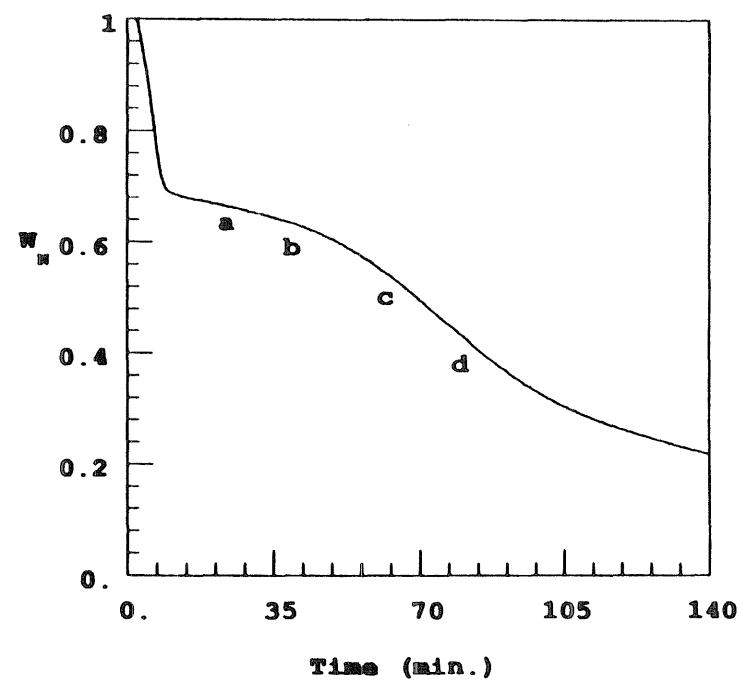
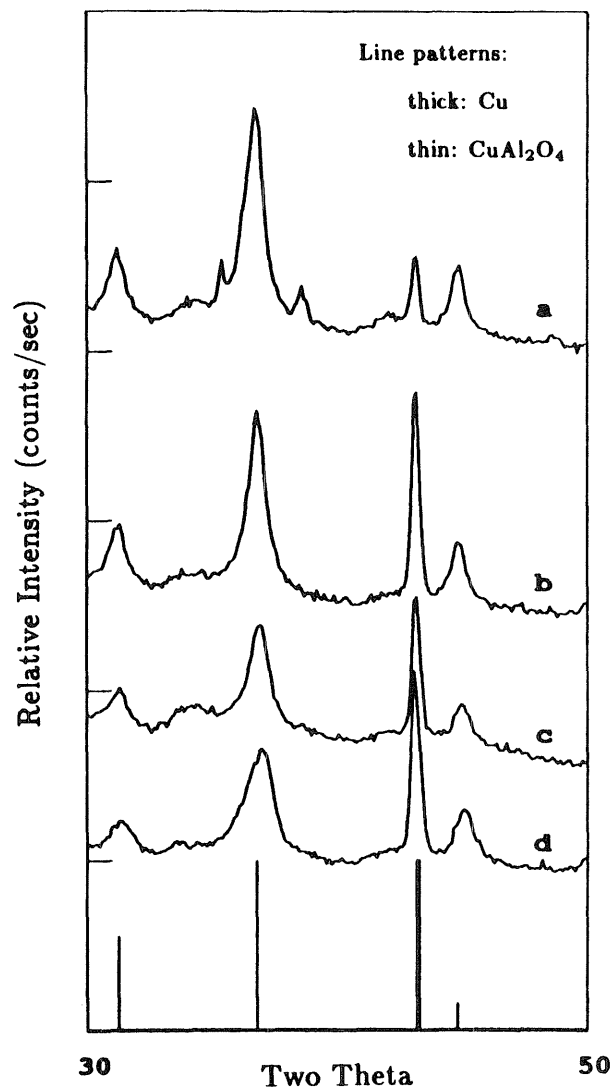


Figure 3.10: XRD patterns of partially reduced 56-1-CA after quenching separate TPR experiments as indicated.

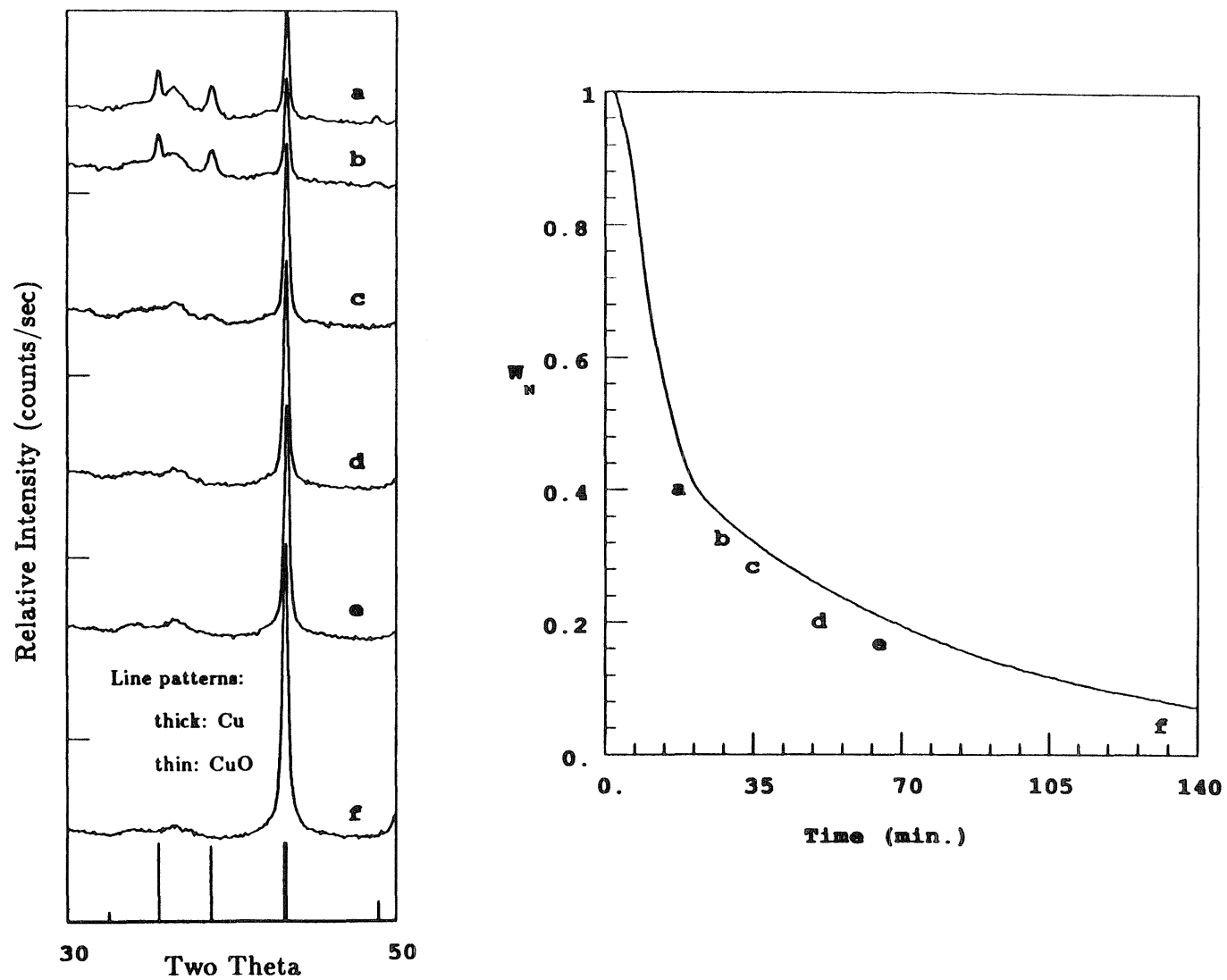


Figure 3.11: XRD patterns of partially reduced 72-1-CA after quenching separate TPR experiments as indicated.

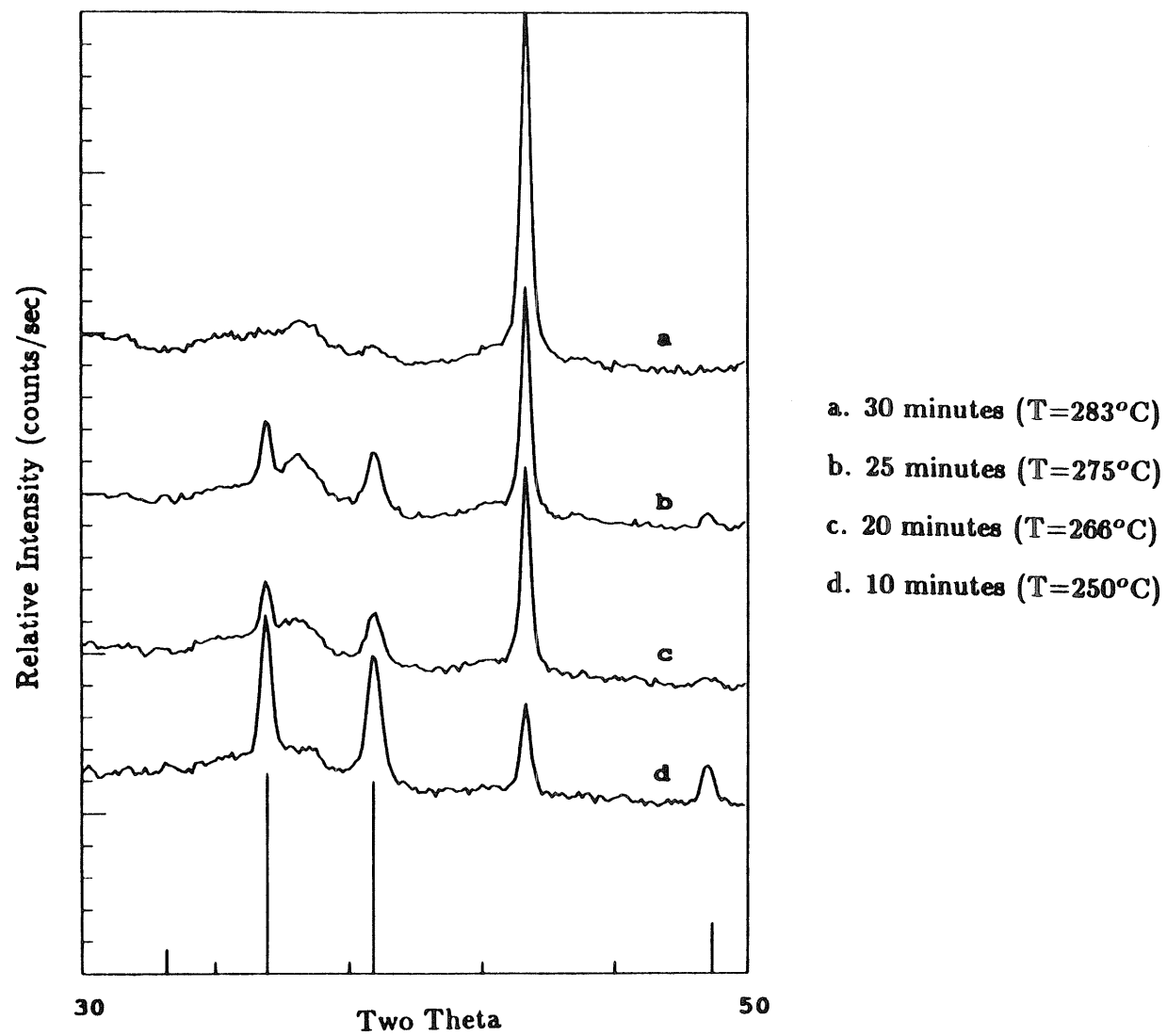
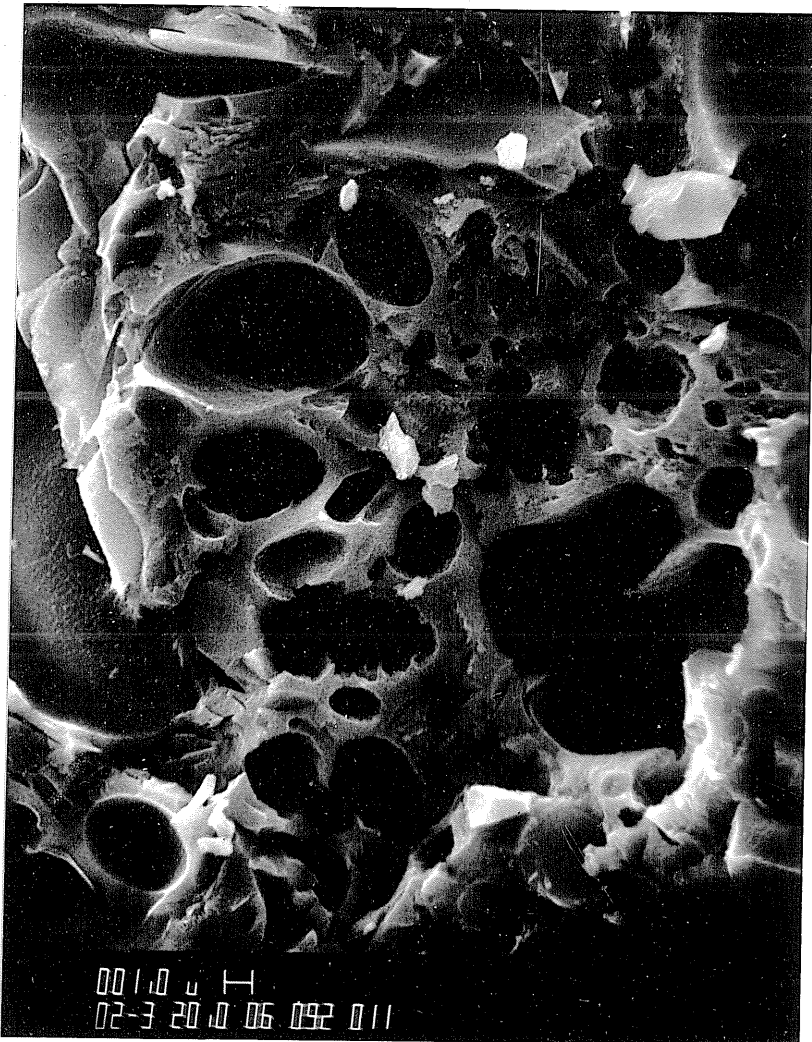


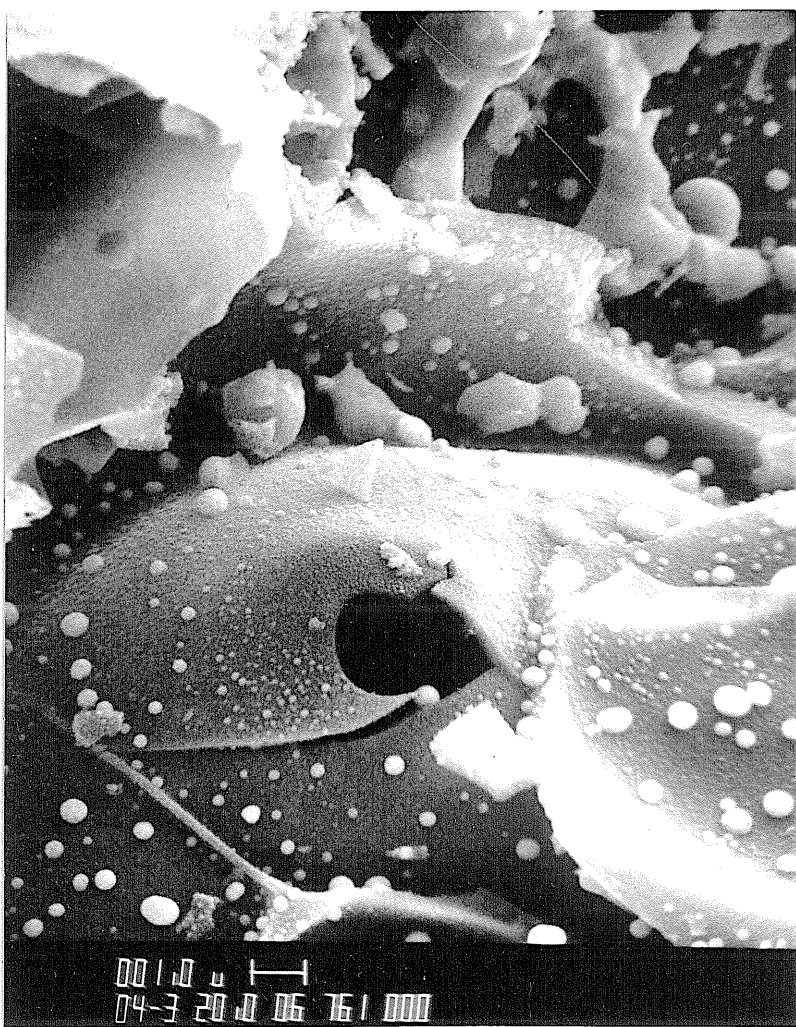
Figure 3.12: Maximum intensity CuO peaks in XRD patterns of 72-1-CA reduced for short times by TPR.



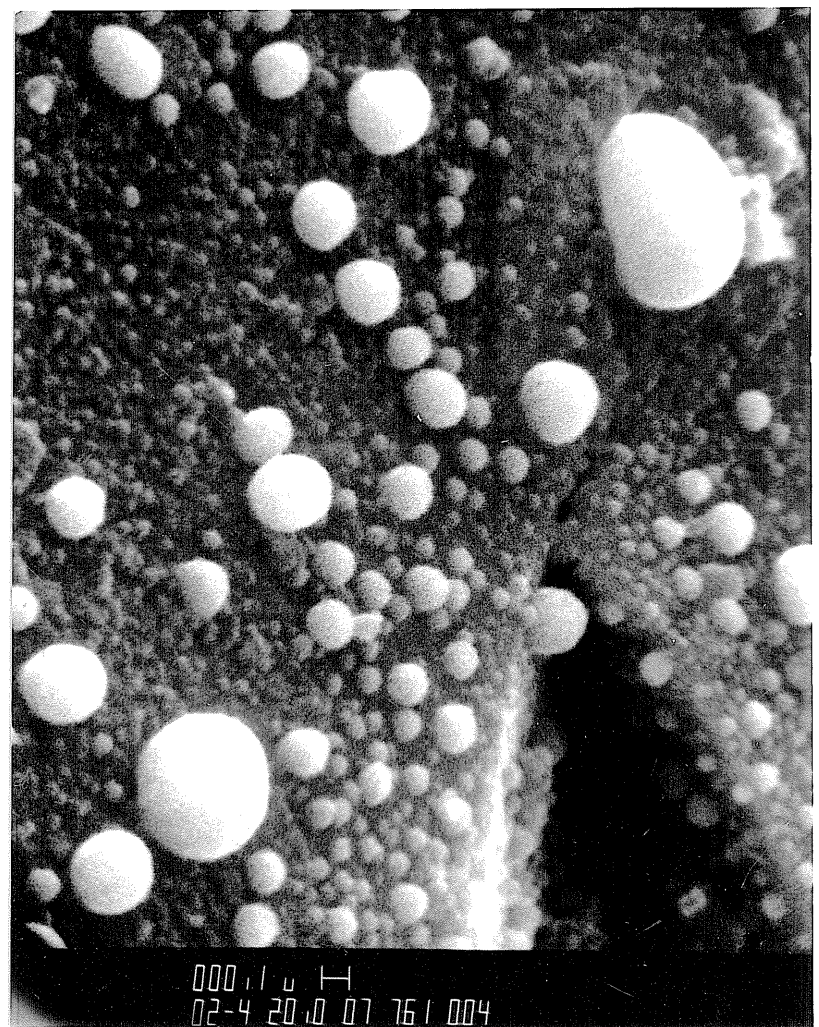
(a) Fresh at 2000×



(b) Reduced at 2000×

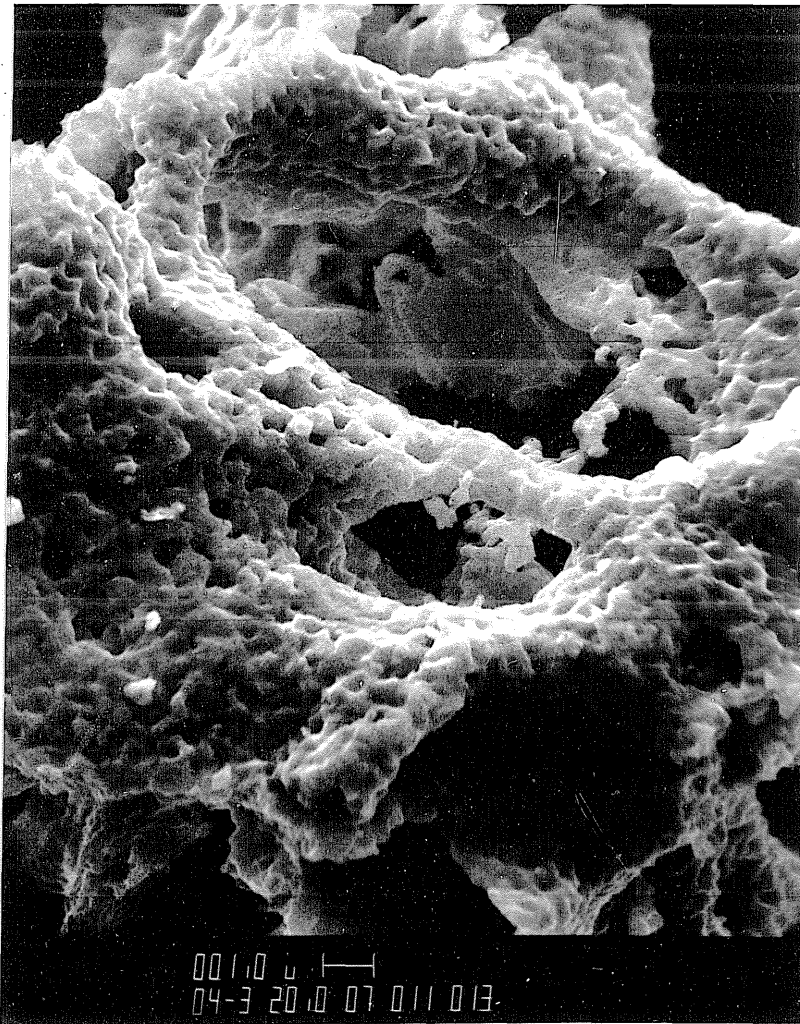


(c) Reduced at 4000×

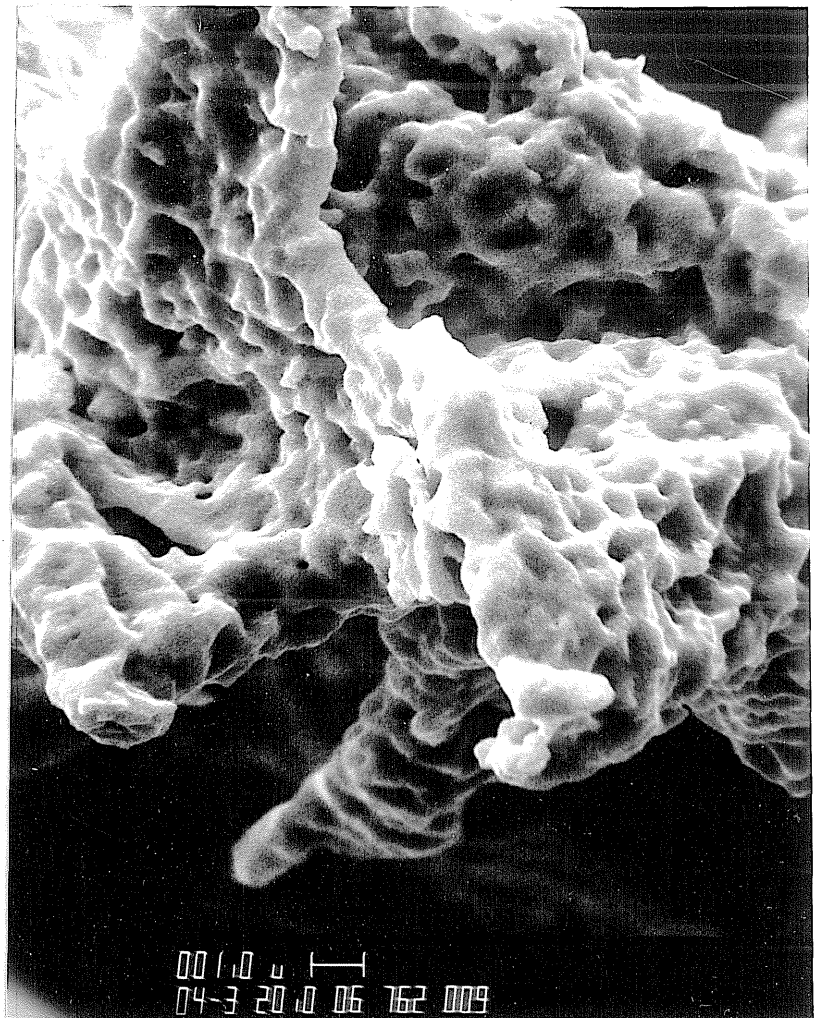


(d) Reduced at 20000×

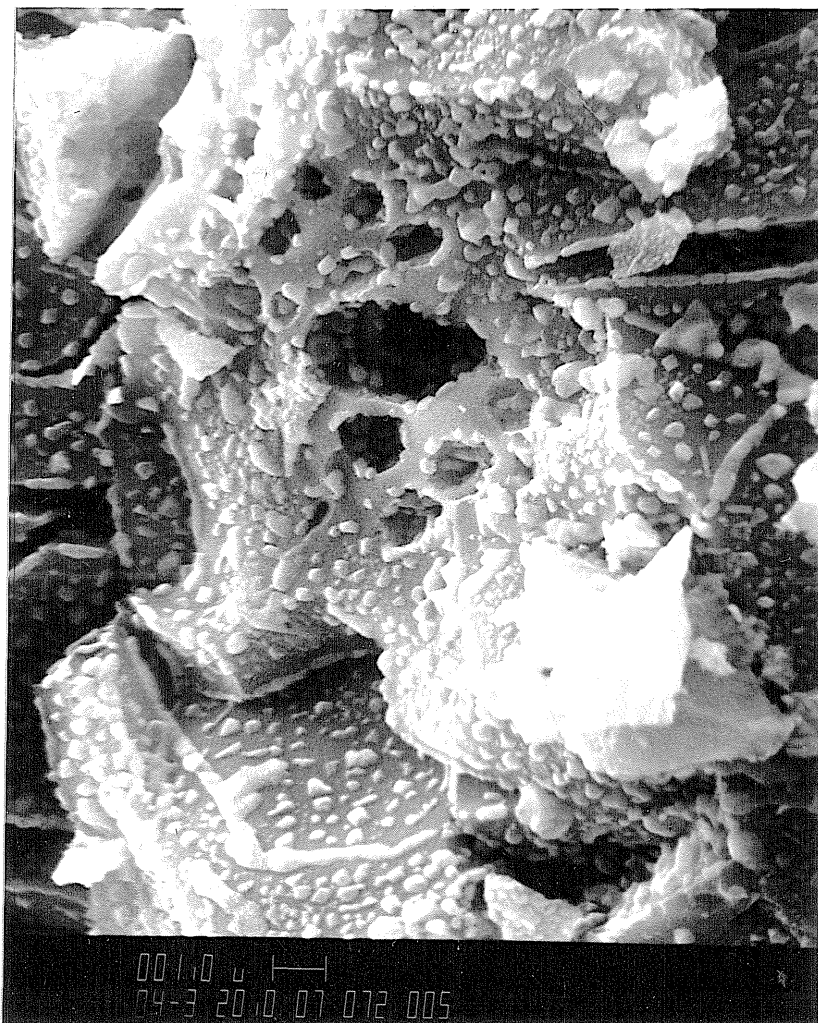
Figure 3.13: Scanning electron micrographs (markers are 1 μ m) of fresh versus reduced 92-1-CA.



(a) Fresh at 4000 \times



(b) Reduced at 4000 \times



(c) Fresh at 4000 \times



(d) Reduced at 4000 \times

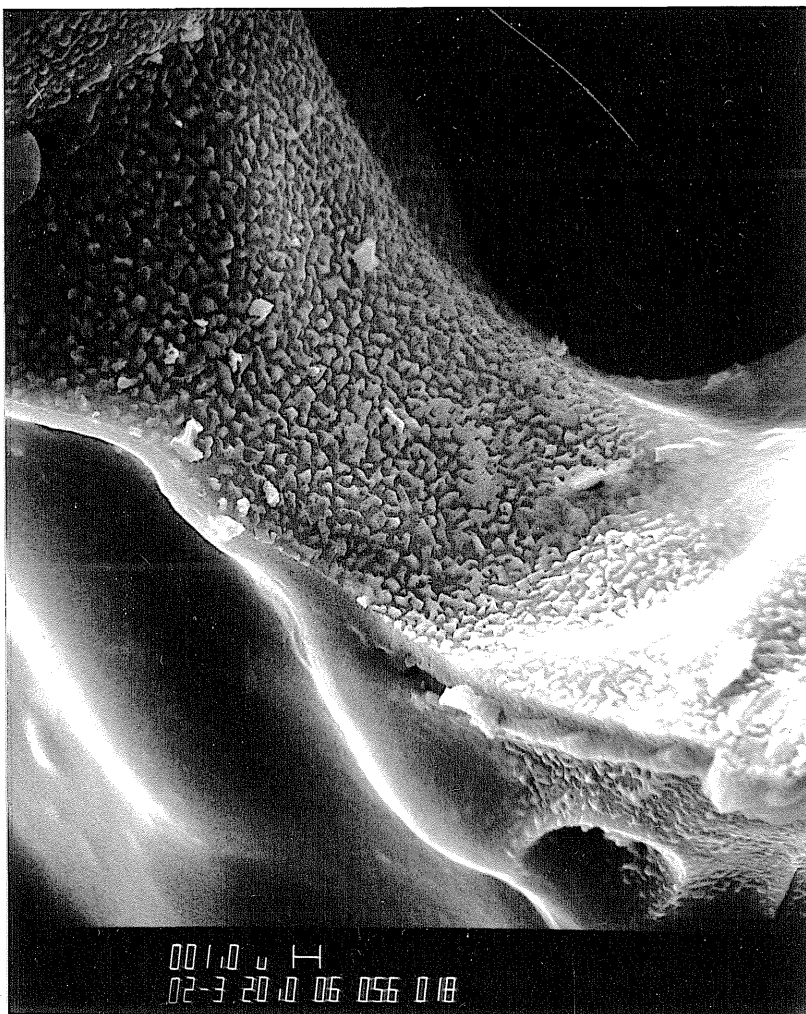
Figure 3.14: Scanning electron micrographs (markers are 1 μ m) of fresh versus reduced 11-1-CA3 (a and b) and 72-1-CA (c and d).



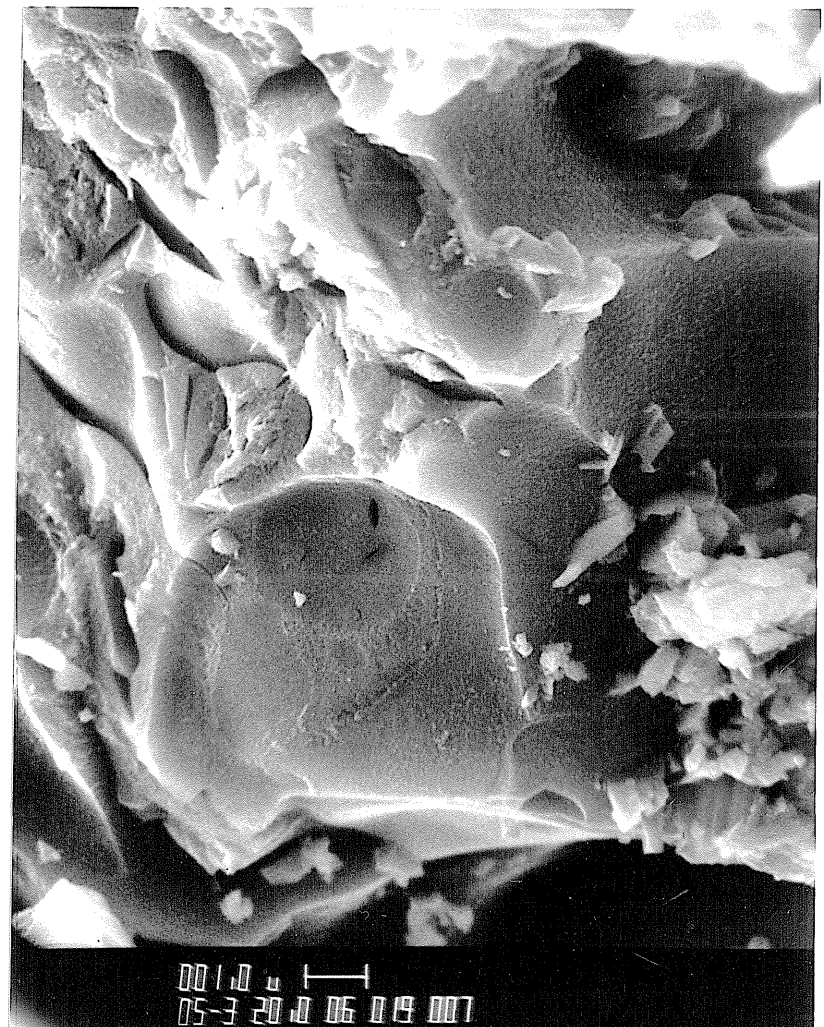
(a) Fresh at 5000×



(b) Fresh at 5000×



(c) Fresh at 2000×



(d) Fresh at 5000×

Figure 3.15: Scanning electron micrographs (markers are 1 μ m) of fresh Cu-Al-O samples: 72-1-CA (a, 5 mol% CuAl₂O₄), 59-1-CA (b, 10 mol% CuAl₂O₄), 56-1-CA (c, 48 mol% CuAl₂O₄), and 19-1-CA (d, 80 mol% CuAl₂O₄).

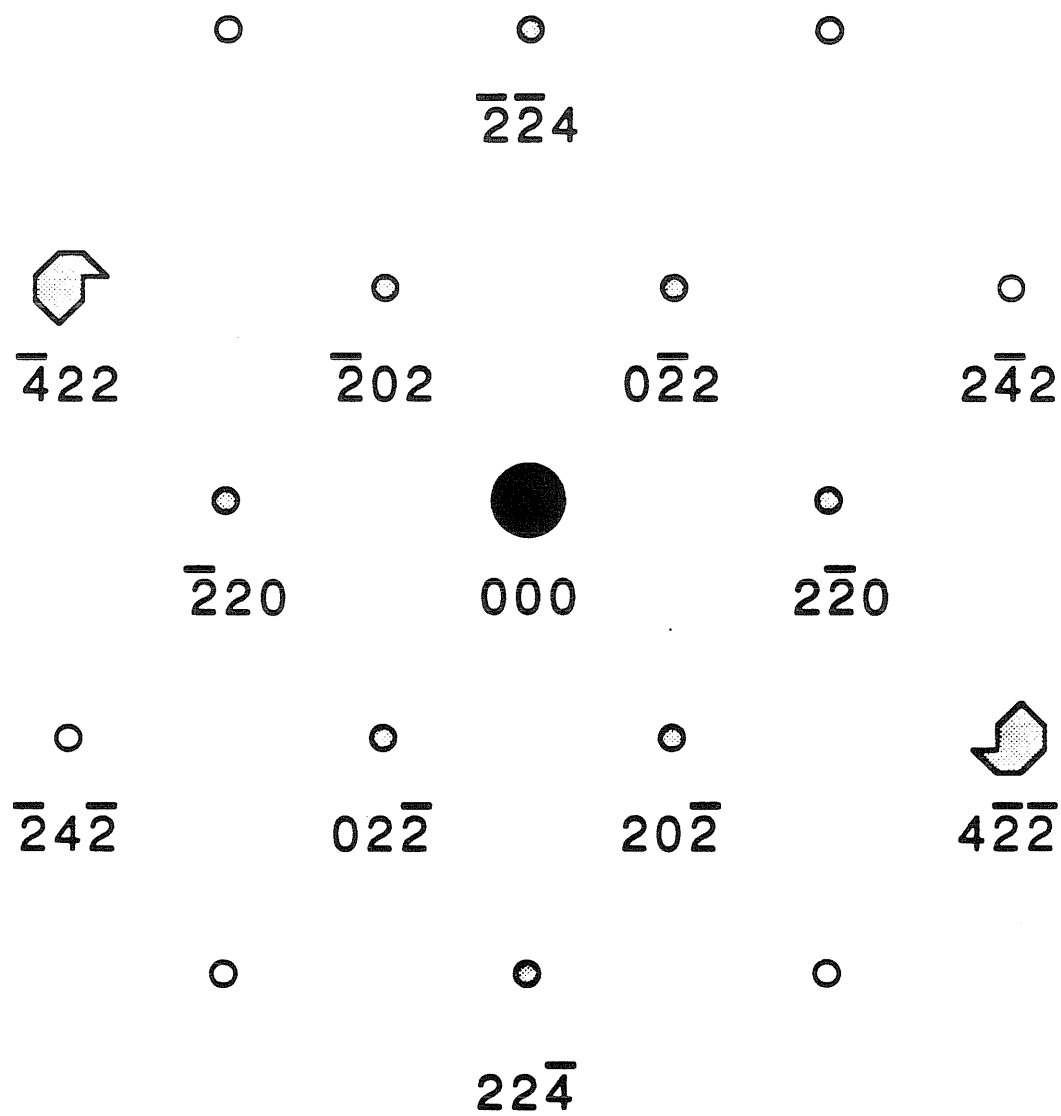
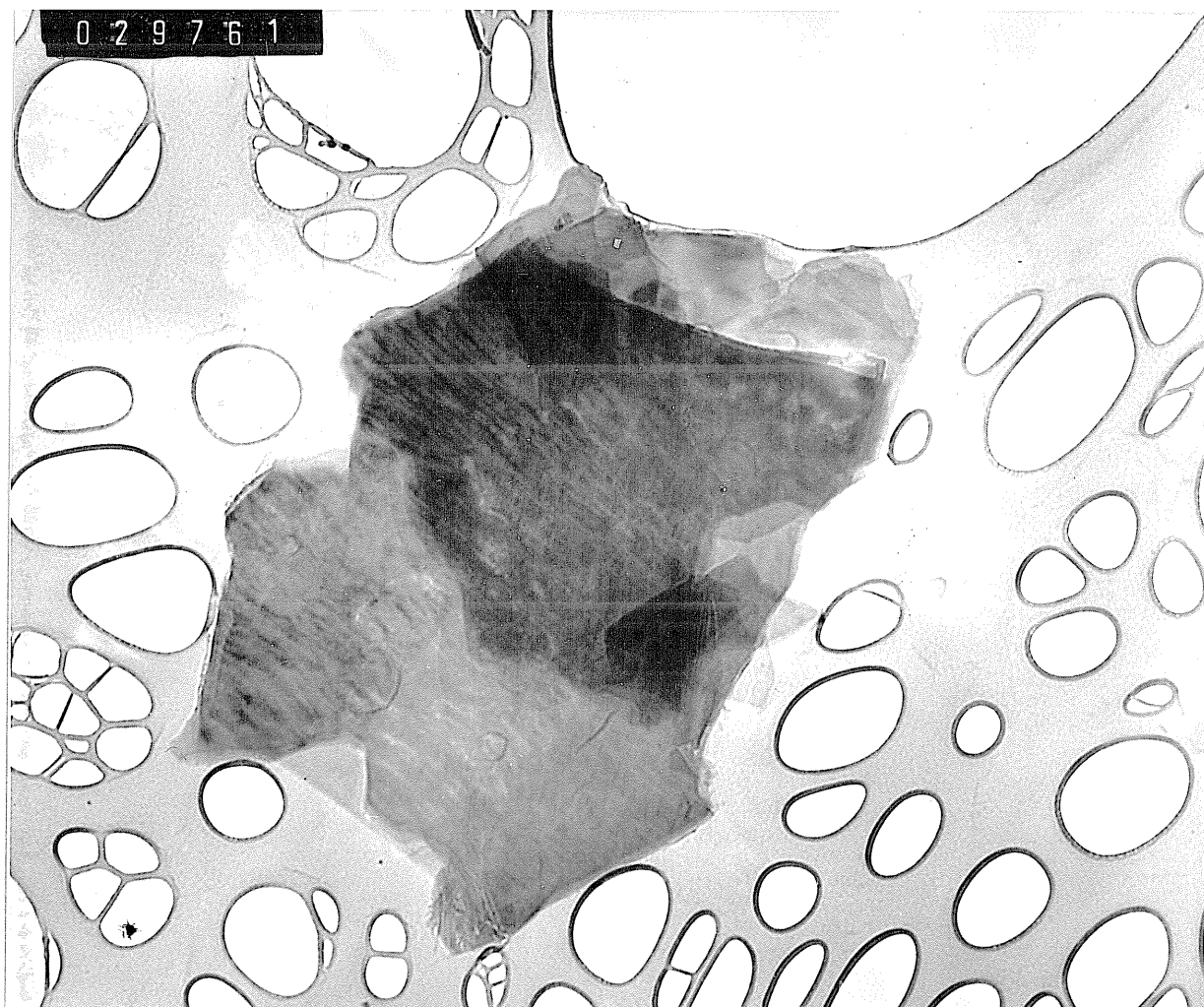
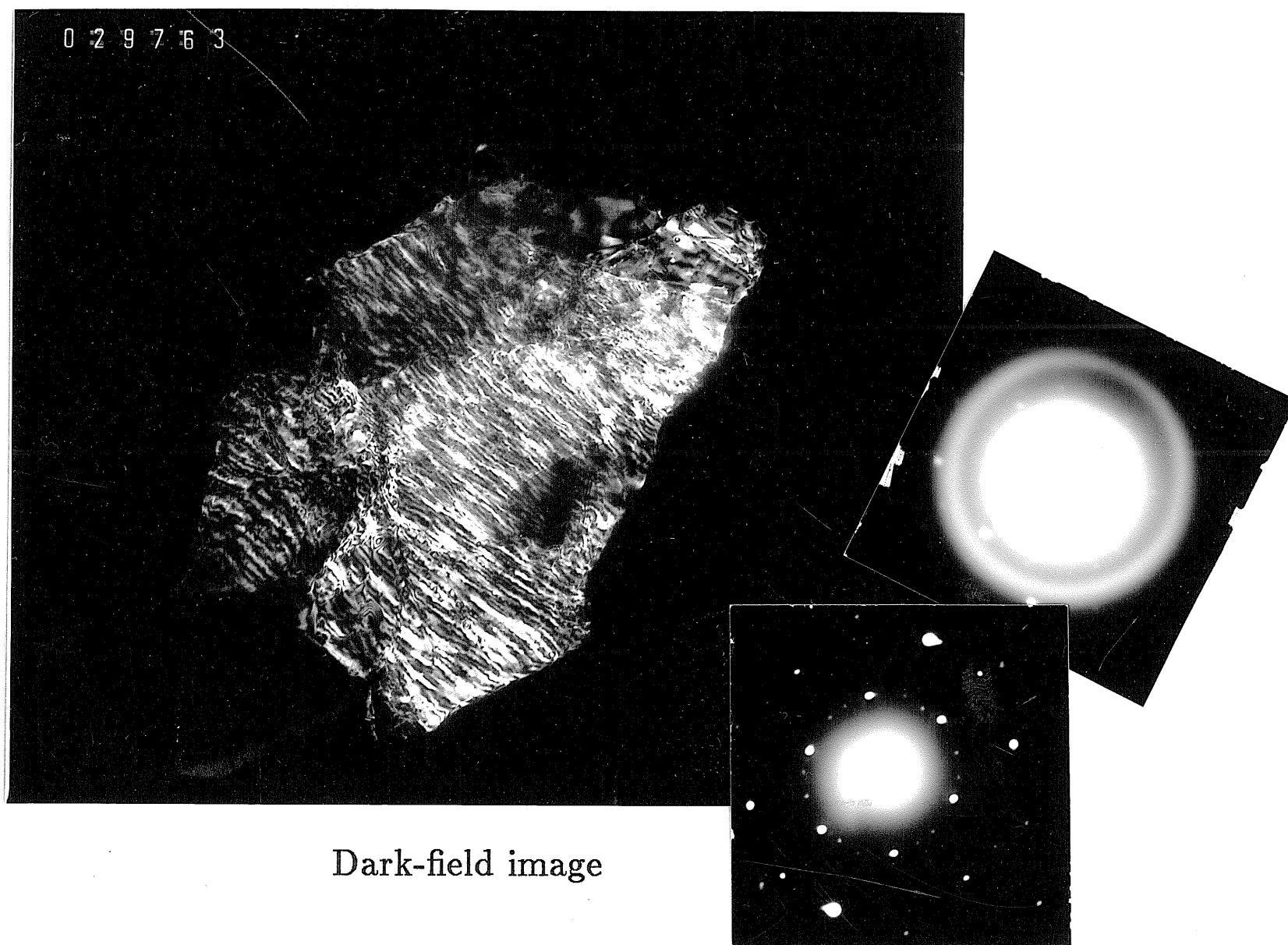


Figure 3.16: Schematic of the diffraction pattern observed for a sample of 92-1-CA by TEM (Figure 3.17) with indexing according to a $\langle 111 \rangle$ zone axis for an fcc array.

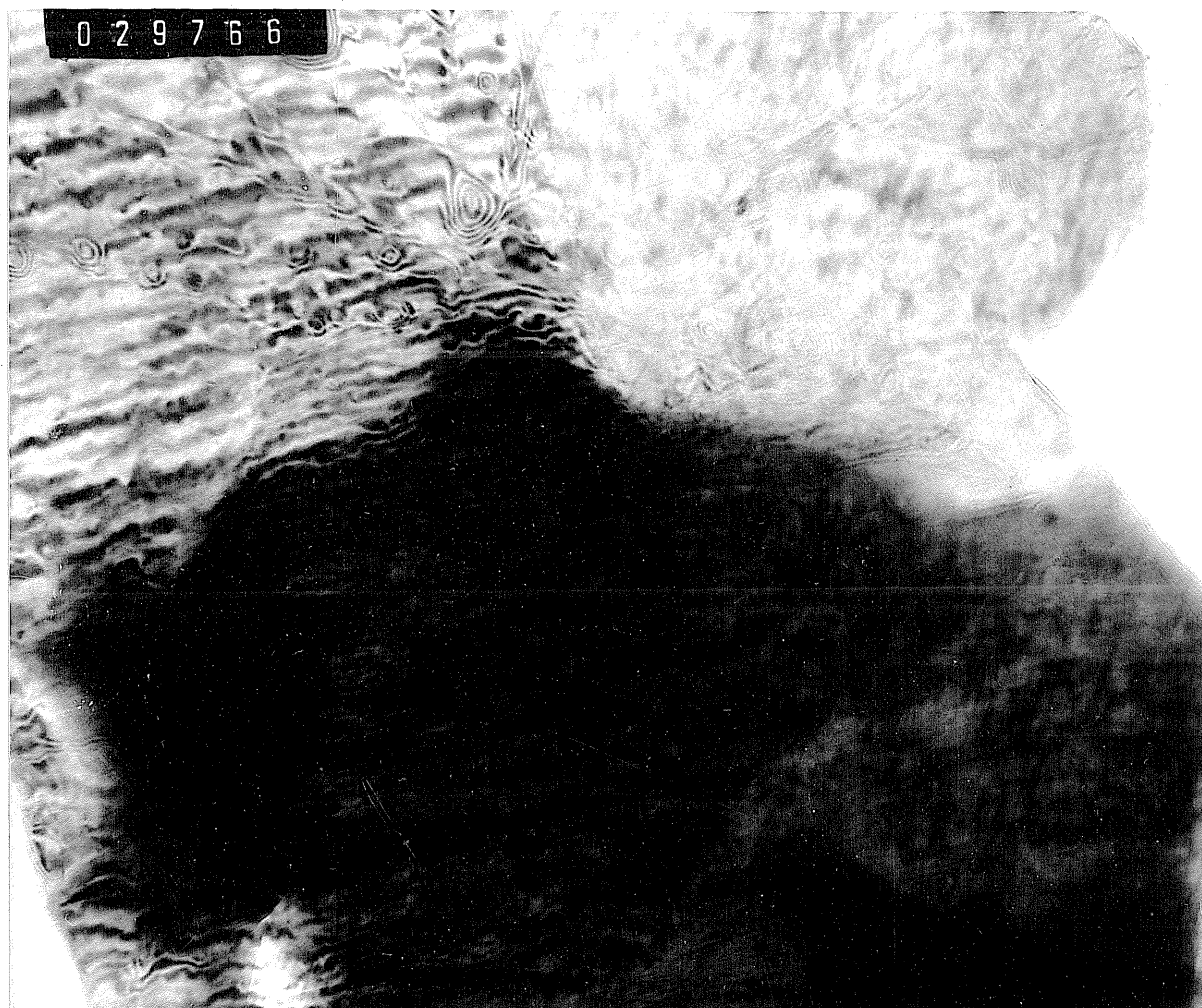


Bright-field image

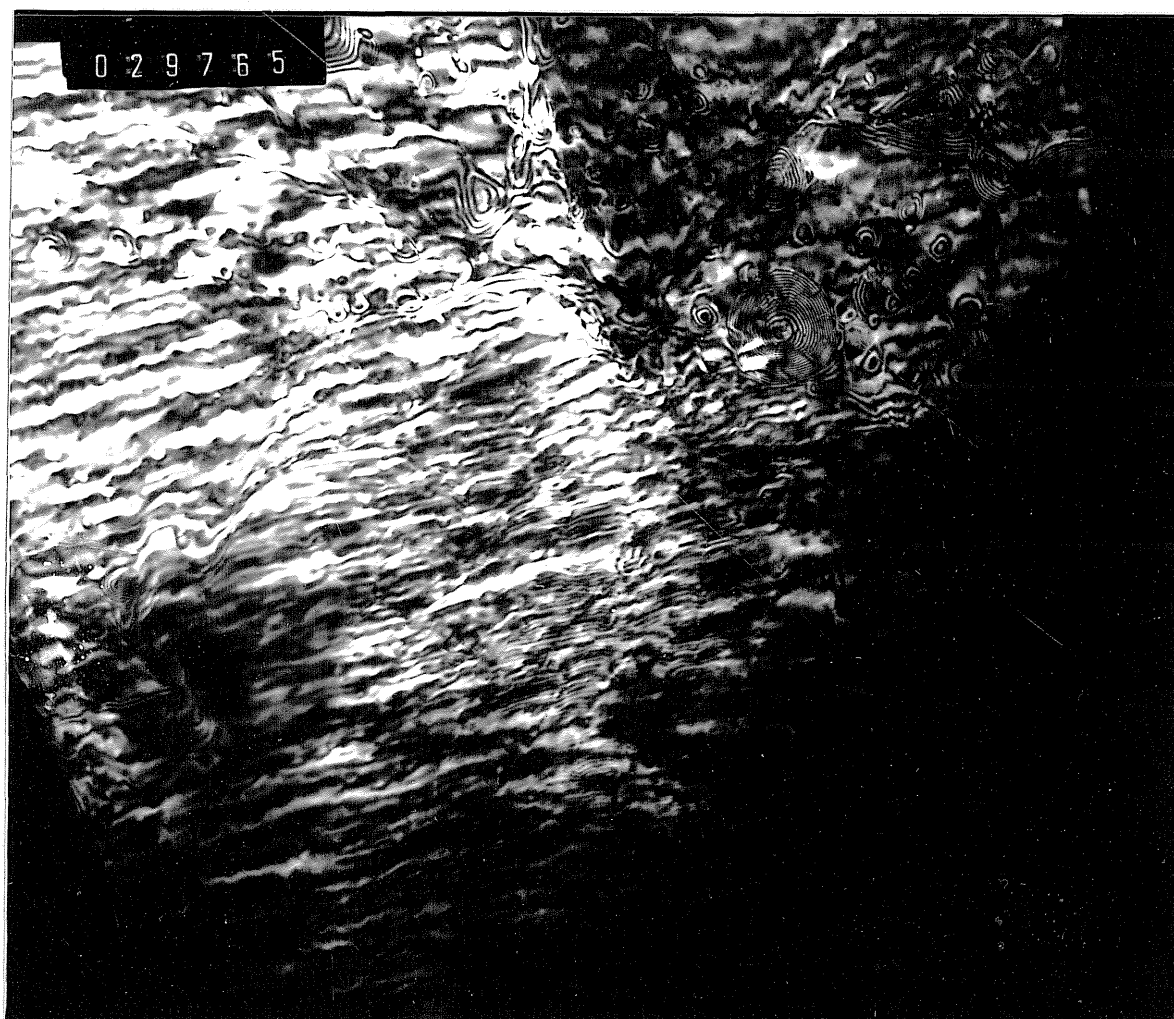


Dark-field image

Figure 3.17: TEM bright-field image and corresponding dark-field image for the indicated diffraction spot for a sample of 92-1-CA.

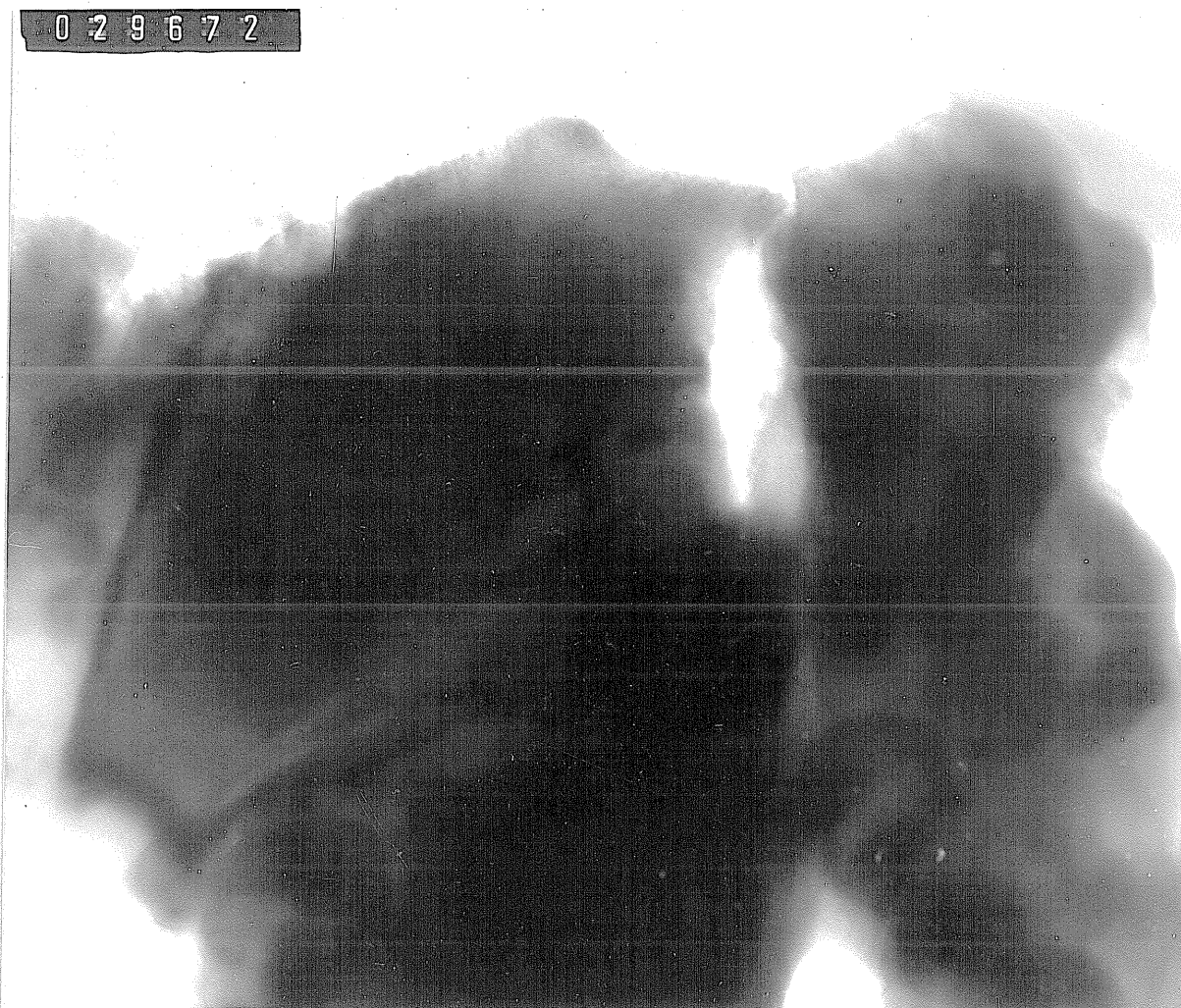


Bright-field image

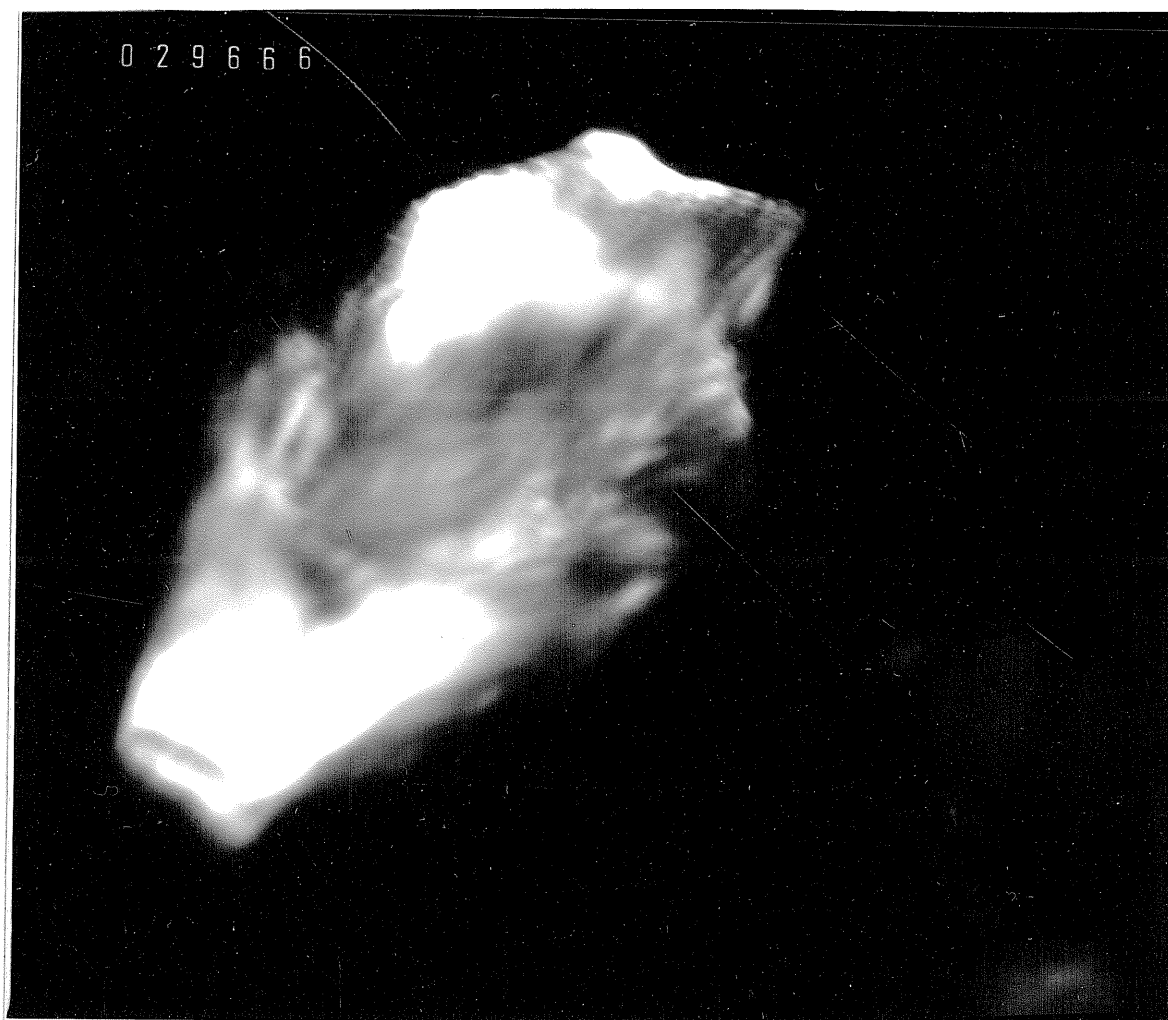


Dark-field image

Figure 3.18: Enlargement of a portion of the bright-field and corresponding dark-field images in Figure 3.17 (see arrow).



Bright-field image



Dark-field image

Figure 3.19: TEM bright-field image and corresponding dark-field image in poor focus showing an isolated CuAl_2O_4 crystallite.

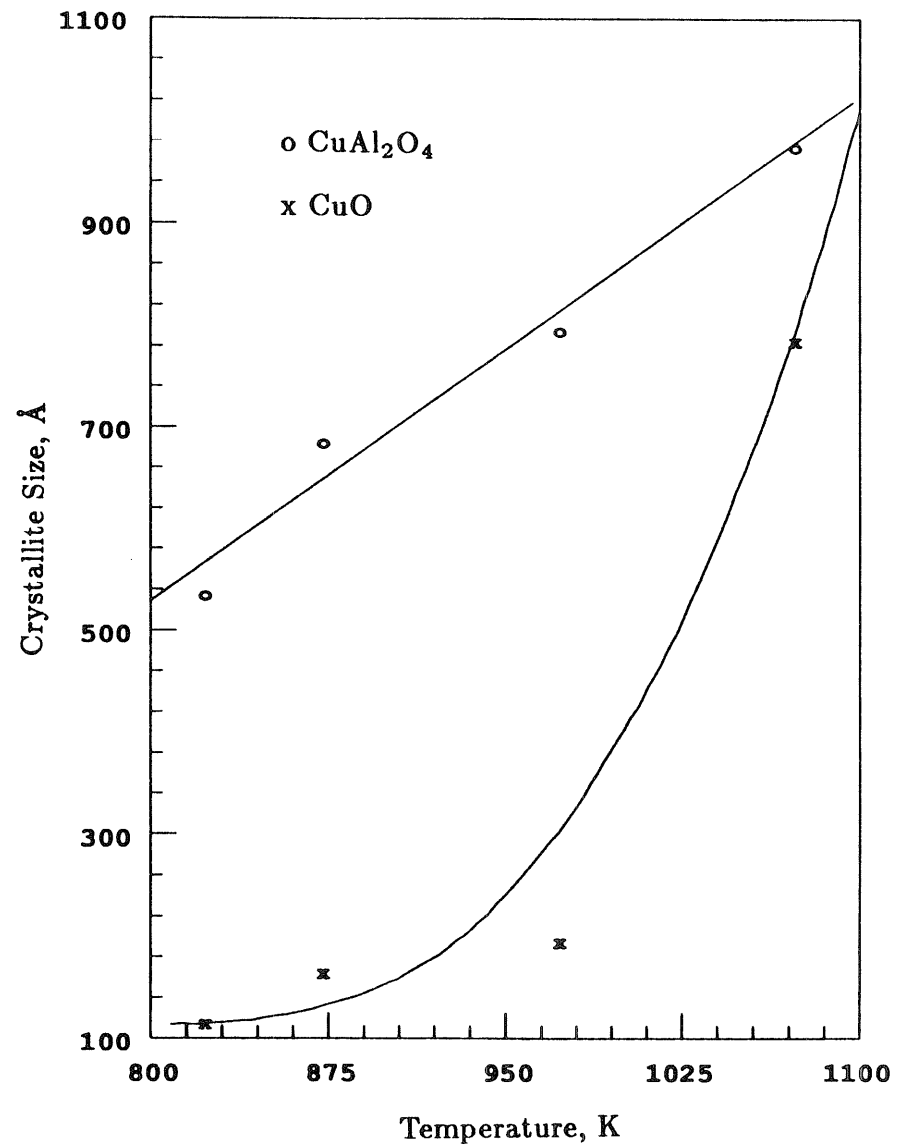
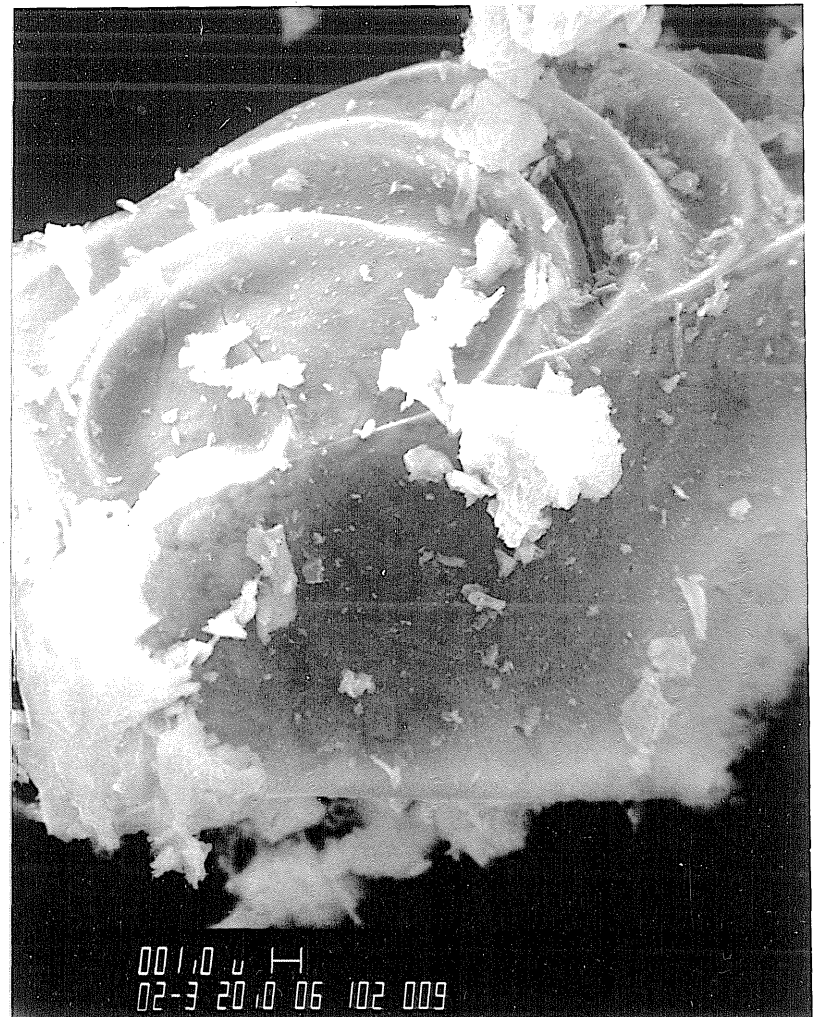


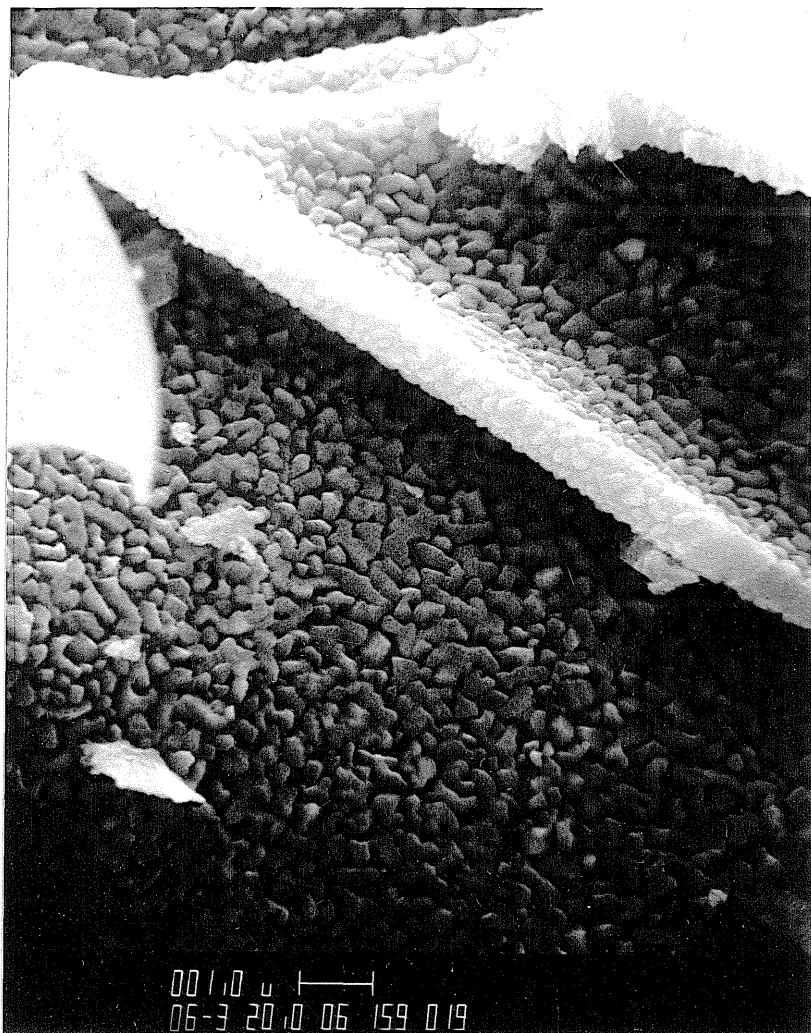
Figure 3.20.: CuO and CuAl₂O₄ crystallite sizes in fresh Cu-Al-O samples as a function of calcination temperature (Table 3.3).



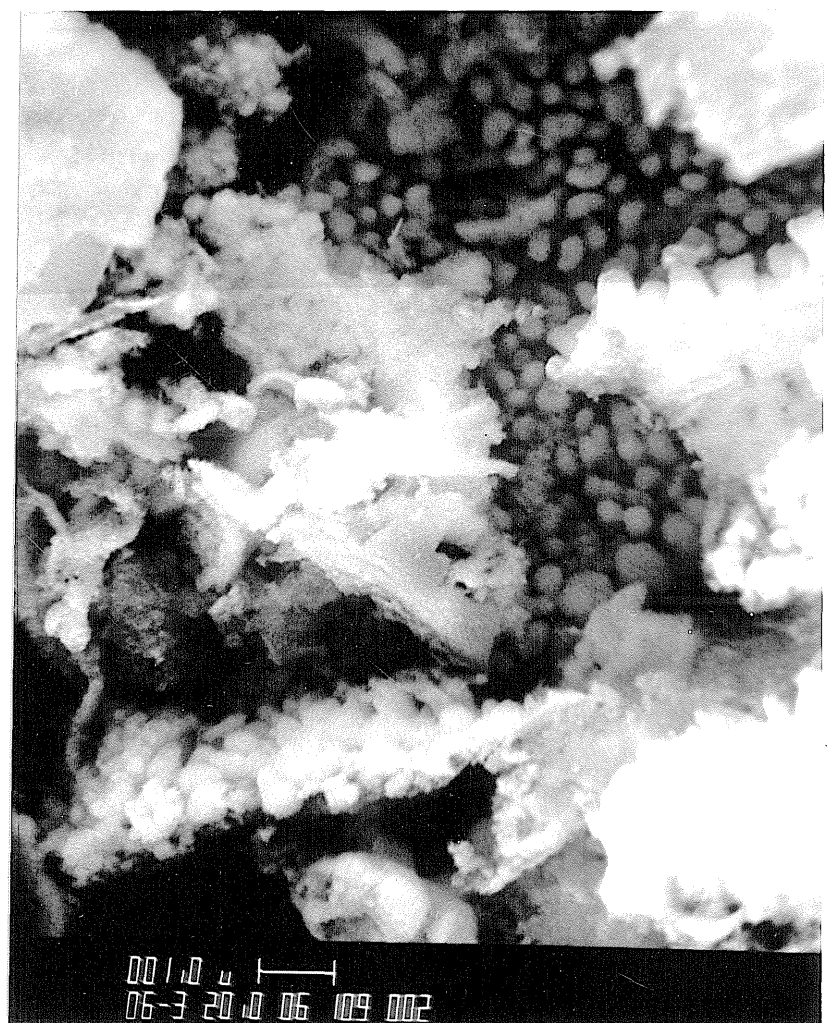
(a) Fresh at 2000×



(b) Extracted at 2000×



(c) Fresh at 6000×



(d) Extracted at 6000×

Figure 3.21: Scanning electron micrographs (markers are $1\mu\text{m}$) of fresh versus extracted Cu-Al-O samples: 15-1-CA (a and b), and 59-1-CA (c and d).

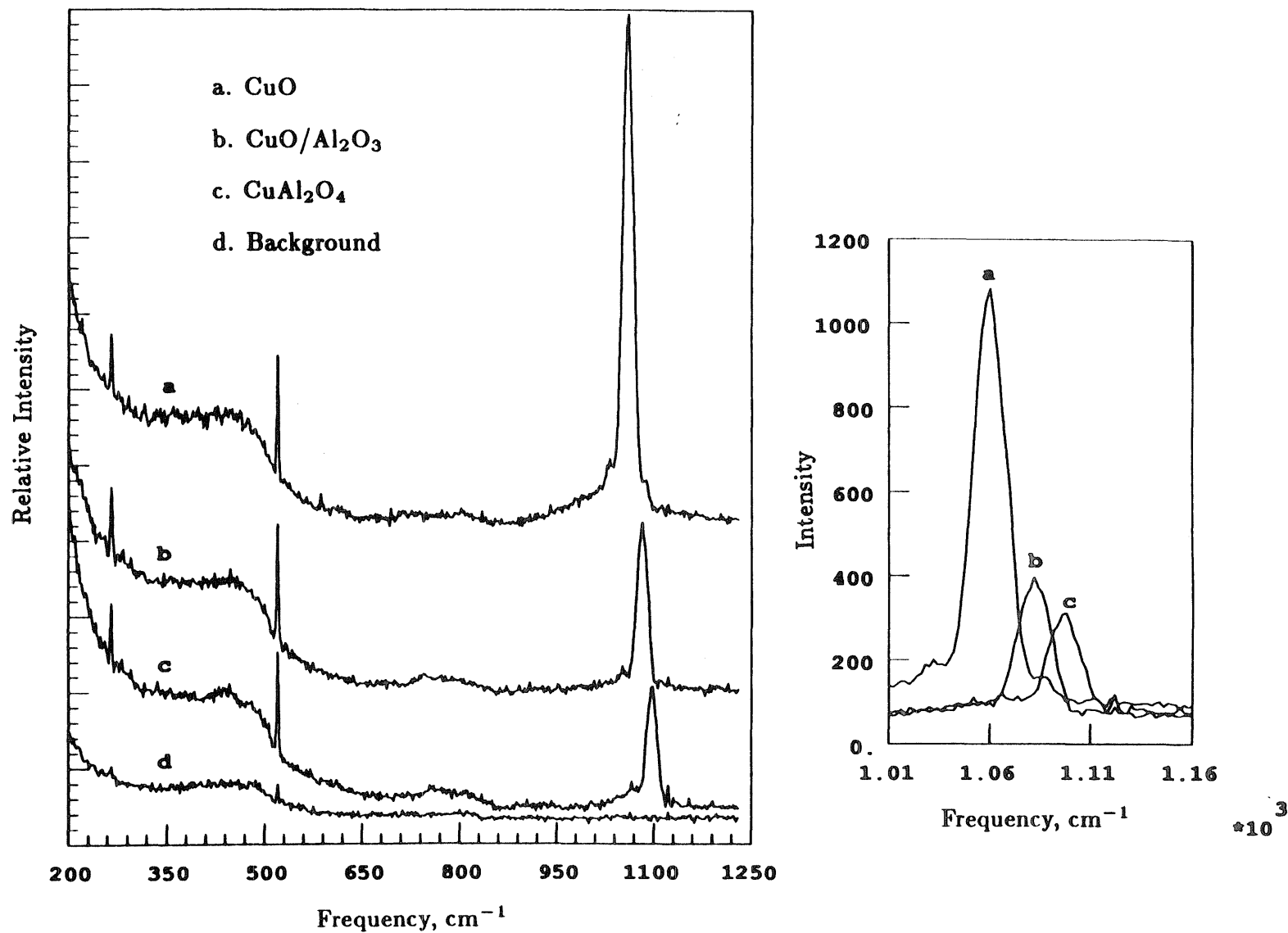


Figure 3.22: Laser Raman spectra of ultrapure CuO and two fresh Cu-Al-O samples.

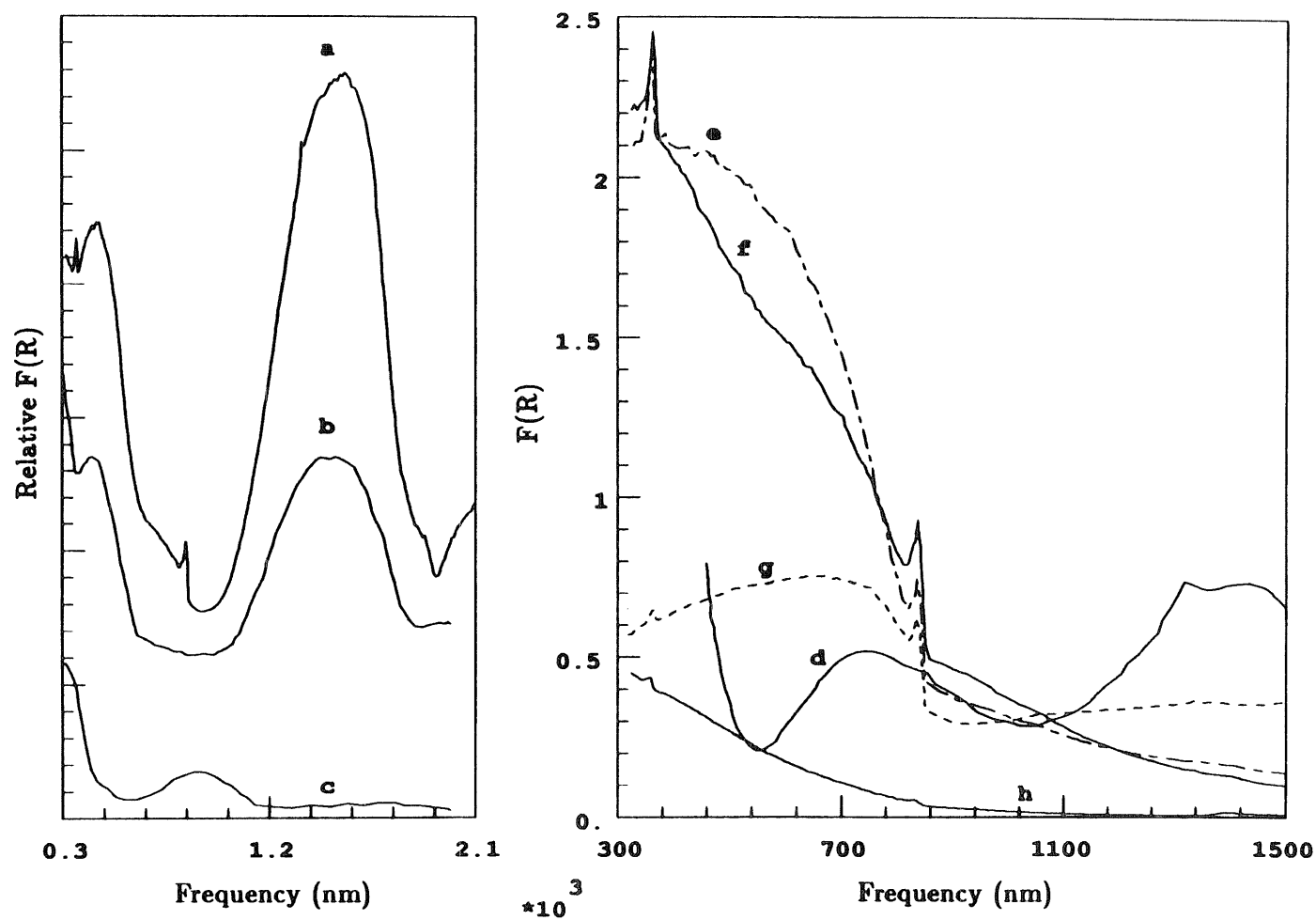


Figure 3.23: Diffuse reflectance spectra of sample 92-1-CA (a), CuAl_2O_4 reported in [3] (b), octahedrally coordinated Cu^{+2} reported in [3] (c), 10 wt% CuO on Al_2O_3 reported in [8] (d), sample 72-1-CA (e), sample 13-1-CA7 (f), ultrapure CuO (g), and Al_2O_3 (h).

CHAPTER IV

*Reduction and Oxidation Studies
of
Copper and Mixed Copper-Aluminum Oxides*

(Includes additional interpretation of TPR data presented in Chapter III, and new, more recent experiments.)

4.1 Background

Temperature-programmed reduction (TPR) has been a powerful technique for characterizing the reducible components on the surface of a catalyst [1,2]. In this application, the measured TPR profile is the change in H_2 concentration between the entrance and exit of the reaction chamber as a function of temperature. Monitoring H_2 consumption provides the high sensitivity needed to identify the small concentration of reducible components (typically 2-20%) which, together with the carrier (*e.g.*, Al_2O_3 , TiO_2 , SiO_2 , *etc.*), comprise the catalyst. The TPR profile identifies components by the temperature at which they reduce. Furthermore, if the TPR peak for a component of a supported material is different from that for the same component in an unsupported, pure state, then the difference characterizes interactions between the supported component and the carrier, or between the supported component and another supported component [3-5].

Experimentally, a TPR profile is simple to measure, but theoretically, a TPR profile is complex to interpret. For example, in measuring H_2 consumption to characterize the reduction of a supported metal oxide, there may be additional processes occurring that mask the true TPR spectrum [6]. These processes include adsorption of hydrogen on the reduced metal, spillover of chemisorbed hydrogen from the reduced metal to the support, desorption of hydrogen from the reduced metal, and desorption of hydrogen from the support. Depending on the relative rates of these processes in comparison to reduction, the resultant TPR profile will be identical to or significantly altered from the true TPR profile, which reflects only reduction. Another process that could lead to faulty interpretation of a TPR profile is the emission of a gas other than H_2 from

the sample. This causes dilution of the H_2 gas stream, which results in the measurement of an apparent H_2 consumption [5,7].

The aforementioned complexities in interpreting TPR profiles obtained by H_2 -concentration measurements are not present in TPR profiles obtained by gravimetric measurements. The decrease in complexity is, however, at the expense of a decrease in sensitivity. While rendering the technique impractical for metal-supported materials, the low sensitivity of gravimetric TPR is suitable for bulk metal oxides (Chapter III, Section 3.3) Since gravimetric TPR is best suited for solids undergoing significant changes in mass ($> 1\%$) during reduction, H_2 adsorption and desorption causing negligibly small changes in sample mass will be undetectable relative to the larger changes in sample mass that are due to reduction. It is conceivable, however, that an extraneous weight loss that is due to a process other than reduction (*e.g.*, the emission of water from the sample) may be present to confound the interpretation of a gravimetric TPR profile. Usually, the effect can be eliminated by sample pretreatment, or the data can be corrected to account for the extraneous weight loss by incorporation of additional experimental data. In Chapter III, for example, weight loss from alumina in samples containing an excess of this component (Section 3.3.4) was corrected by using a TPR profile for pure alumina prepared in the same manner as the original sample. The correction was based on the assumption that weight loss from alumina and weight loss from reduction of the remainder of the sample occurred independently, in parallel.

There are additional complexities inherent in both types of TPR. For example, the temperature at which the rate of reduction is a maximum for a given species, T_{max} , is a function of hydrogen flow rate and the heating rate [2,8]. Typically, an increase in the hydrogen flow rate, or a decrease in the heating

rate results in a decrease of T_{\max} . For example, reported values for T_{\max} corresponding to TPR of bulk CuO range from 222 to 367°C (Table 4.1). In addition, the mass of a sample has been reported to affect the resolution of a step-wise reduction [8]. Finally, while multiple peaks in TPR plots of reaction rate versus time or temperature are most commonly assigned to the reduction of different reacting species, they can also be caused by the presence of a multimodal size distribution, because particle size affects the shape of the TPR plot, or by the presence of a mixed-control mechanism, because the rate-controlling step for the reaction affects the shape of the TPR plot [9]. An interpretation of a TPR profile, consequently, must be substantiated by independent experiments.

While most TPR studies of CuO-supported materials contain TPR profiles of bulk CuO [1,7,10], there is very limited TPR data for bulk mixed oxides such as CuAl_2O_4 . This chapter summarizes temperature-programmed and isothermal TGA studies of the reduction and oxidation of copper and mixed copper-aluminum oxides. The two modes of TGA analysis, temperature-programmed mode and isothermal mode, provide complementary mechanistic and kinetic information.

4.2. Reduction of Porous CuO

Both isothermal and temperature-programmed investigations suggest that the reduction of CuO by hydrogen consists of three stages: induction, autocatalysis or acceleration, and decay. Furthermore, reduction occurs on certain nuclei generated during the induction period. Acceleration of reduction has been observed when an initial fraction of copper metal is added to a CuO sample [11]. Addition of copper metal to a CuO sample, on the other hand, has been reported

to have no measurable effect on subsequent reduction [12]. According to these conflicting results, while copper nuclei appear to be sites for reaction, they must form at specific active sites within the bulk of the solid. Since chemisorbed hydrogen is more active than molecular hydrogen, it is conceivable that CuO in the presence of copper metal, depending on quantity and configuration, reduces faster than pure CuO because of chemisorption and subsequent spillover of hydrogen from the copper metal. Spillover hydrogen, in addition, can migrate to active sites on CuO for nucleation of Cu^o. The reaction is accelerated at the various Cu-CuO interfaces by this same mechanism in the stage following induction. When CuO particles become totally covered by Cu, further reduction is controlled by diffusion of H₂ to the reaction site or of H₂O away from the reaction site and thus, the reaction rate slows down during the final stage following acceleration.

4.2.1. Temperature-Programmed Studies

Reduction of CuO prepared by the citrate process using a calcination temperature of 550°C (sample 11-1-CA3, Table 3.1), was studied by gravimetric TPR. X-ray diffraction (XRD) analysis of partially reduced samples provided complementary information. For an initial temperature of 193°C, a heating rate of 1.7°C/min, and a sample mass of ~ 20 mg, no Cu^o product was observed by XRD until a temperature of ~ 235°C. Furthermore, no Cu₂O was determined by XRD as an intermediate to the reduction of CuO. These data agree with the observations that reduction of CuO involves an induction period and proceeds at Cu-CuO interfaces. The small amounts of CuO and Cu₂O observed for a completely reduced sample (Figure 4.1) were due to oxidation of Cu^o, while the reduced sample was quenched from ~ 268°C to room temperature under flowing

N₂ for subsequent XRD analysis. X-ray peaks for CuO and Cu₂O disappeared when the sample was quenched under the reducing gas (5% H₂ in N₂).

A comparison of a series of TPR curves obtained for CuO (sample 11-1-CA3) reveals subtle differences. A TPR curve is here defined as a plot of nondimensional weight loss, W_N , versus time, in which W_N is equivalent to $1-\alpha$ with α symbolizing the fractional conversion of CuO to copper metal. Theory predicts that a plot of $\frac{d\alpha}{dT}$ versus temperature, T , consists of a single symmetric peak for a gas-solid reaction occurring by the mechanism of nucleation. Transforming the TPR curves for CuO to plots of $\frac{d\alpha}{dT}$ versus T , however, reveals a range of temperatures, 224 to 289°C, for which $\frac{d\alpha}{dT}$ is a maximum, and a variety of peak contours (Figure 4.2). When the reduction of CuO is characterized by a smooth symmetric peak, a high maximum rate is attained relative to that attained for a peak exhibiting splitting (curves d and e of Figure 4.2) or a shoulder (curves b and c of Figure 4.2). The value of the maximum rate is a function of the peak shape because the area enclosed by a plot of $\frac{d\alpha}{dT}$ versus T is equal to 1, assuming complete conversion to copper metal ($\alpha=1$). Curve shape, in addition, is correlated with sample mass. For example, a sample mass of 17.5 mg appears to be a critical value in determining peak shape below which a broad shoulder is observed, and above which peak splitting is observed. On the other hand, a correlation between T_{\max} , temperature at which the rate of reduction is a maximum, and sample mass does not exist. For example, for sample masses of 17.5, 17.2, and 21.9 mg, a value of $254 \pm 2^\circ\text{C}$ is observed for T_{\max} .

Since variations in T_{\max} and curve shape are related to masses both above and below a critical value, the variations can not be accounted for by mass transfer effects alone. Consideration of thermal effects, however, appears only to muddle the interpretation of these variations. For example, modelling the

TGA reaction chamber as a plug flow reactor, and considering a macroscopic control volume containing the sample, there are three terms in the resulting energy balance: the enthalpy difference between gas flowing in and gas flowing out of the control volume, the heat-generation term, and the accumulation term. The heat-generation term is the heat added to the control volume by the electric furnace, and is a function of time. The accumulation term is the time rate of change of the enthalpies summed over all the components present in the control volume. The presence of these two time-dependent terms results in an unwieldy equation. Alternatively, perhaps the observed variation in T_{\max} reflects a sensitivity of CuO reduction to the physical state of the sample. Sample inhomogeneity, differences in loading the sample into the reaction chamber, and differences in heating the sample prior to reaction could all affect the physical nature of the sample. Fortunately, the observed variations, though poorly understood, are small and seemingly rectifiable by the proper choice of sample mass.

4.2.2. Isothermal Studies

The effects of temperature in a range of 400 to 600°C and H_2 partial pressure in a range of 0.05 to 0.30 atm on the reduction of CuO (sample 11-1-CA3) were examined by isothermal TGA studies. Typical data transformed to plots of reaction rate, $\frac{d\alpha}{dt}$, versus conversion, α , are shown in Figure 4.3.

Three models have been used to interpret isothermal reduction data for CuO: Johnson-Mele-Avrami, Roginskii-Shul'ts, and Prout-Tompkins. The main hypothesis differentiating these models is the method of nuclei formation. Copper seeds are hypothesized to form solely in the bulk for the Johnson-Mele-Avrami model, solely on the surface for the Roginskii-Shul'ts model, and both

in the bulk and on the surface for the Prout-Tompkins model [13]. The models are represented mathematically as follows:

Johnson-Mele-Avrami:

$$-\ln(1 - \alpha_i) = (k_i t)^{m_i}, \quad (4.1)$$

where

$i = 1, 2, \text{ or } 3$ for different stages of CuO reduction

$\alpha_i =$ fractional conversion of CuO to Cu in stage i

$$m_i = a_i + b_i T; \quad a \text{ and } b \text{ are constants} \quad (4.2)$$

$$k_i = k_{i_0} \exp \left[\frac{-E_i}{RT} \right] p_{H_2}^{n_i} \quad (4.3)$$

Roginskii-Shul'ts:

$$1 - (1 - \alpha)^{\frac{1}{3}} = kt \quad (4.4)$$

Prout-Tompkins:

$$\ln \left(\frac{\alpha}{1 - \alpha} \right) = kt + C. \quad (4.5)$$

The Johnson-Mele-Avrami equation was resorted to by one group of investigators, who found that Equations 4.4 and 4.5 both gave satisfactory descriptions of reduction data for CuO with the fastidious choice of 2 or 3 constants, k [13].

An attempt to fit the data of Figure 4.3 to the Roginskii-Shul'ts equation, Equation 4.4, results in quadratic curvature rather than linearity (Figure 4.4). These results indicate that the Roginskii-Shul'ts equation underpredicts the reaction rate over a large portion of the reduction curve. This underprediction

is due to a failure to account for a random seed-forming process during the induction stage. The Roginskii-Shul'ts equation describes reduction of CuO as follows: Seeds of Cu^o form on the specimen surface, the seeds grow and coalesce to form a continuous film of product Cu^o, and then the thickness of the Cu^o film increases with time as reaction proceeds at the Cu-CuO interface. The formation of seeds in the bulk and continued seed formation beyond the induction stage are not accounted for.

The Prout-Tompkins equation, Equation 4.5, gave a satisfactory fit of reduction data for CuO obtained at temperatures between 400 and 500°C (Figure 4.5). The equation was obeyed from approximately 15 to 95% conversion with one constant, k, being adequate to describe the data which exhibited a slight sinusoidal curvature in some cases. The Prout-Tompkins equation was derived based on the assumption that the maximum rate of reaction occurs at a conversion of approximately 50% (*i.e.*, $\alpha=0.5$). From Figure 4.3, the maximum rate of reaction occurs at conversions of between 0.438 and 0.721 with an average value of 0.62 for 14 of the 20 sets of data used. Equation 4.5 can be modified to accommodate a conversion of other than 0.5 at the maximum rate of reduction; however, for values greater than 0.5, the modified equation is applicable only to a dramatically reduced range of conversions. For example, when the maximum rate of reduction occurs at a conversion of 0.72, the modified version of equation 4.5 is applicable to only 62% of the data.

Values of k estimated by fitting the data of Figure 4.5 to Equation 4.5 were found to vary linearly with the partial pressure of hydrogen (Figure 4.6). Because Equation 4.5 is derived from the following rate expression,

$$\frac{d\alpha}{dt} = k\alpha(1 - \alpha), \quad (4.6)$$

and because k varies linearly with partial pressure of hydrogen, then reaction rate is first order with respect to partial pressure of hydrogen as follows:

$$\frac{d\alpha}{dt} = k' p_{H_2} \alpha (1 - \alpha), \quad (4.7)$$

where

$$k = k' p_{H_2}. \quad (4.8)$$

An Arrhenius plot of k' (Figure 4.6) results in the following expression:

$$k' (s^{-1} atm^{-1}) = 498 \exp \left[\frac{-25.9 \text{ kJ/mol}}{RT} \right]. \quad (4.9)$$

The apparent activation energy is approximately half that estimated from experiments performed at temperatures between 112 and 227°C (Table 4.2).

The measurement of a different activation energy in a high-temperature regime, 400 to 500°C, than in a low-temperature regime, 112 to 227°C, implies that different rate-controlling mechanisms operate in each regime. A discrepancy by a factor of two is significant because it suggests that diffusion of hydrogen to CuO is the rate-controlling step in the high-temperature regime. This conclusion can be derived by modelling the solid, CuO, as spherical particles undergoing reduction, and calculating the concentration profile. The reaction is assumed to be first order with respect to species A, hydrogen, in agreement with experimental findings. Furthermore, the diffusivity of hydrogen in CuO, and the dimensions of the CuO particles are assumed to remain constant with conversion of CuO to Cu. The resulting mass balance:

$$\mathcal{D}_e \left[\frac{\partial^2 c_A}{\partial r^2} + \frac{2}{r} \frac{\partial c_A}{\partial r} \right] = a k_s c_A \quad (4.10)$$

$$c_A(r = R) = c_{A_o} \quad (4.11)$$

$$\frac{\partial c_A}{\partial r}(r = 0) = 0, \quad (4.12)$$

where

R = radius of the sphere

$a = (1 - \epsilon)\rho S_g, \text{ cm}^{-1}$

ρ = density of CuO, g/cm³

ϵ = void fraction of CuO

S_g = specific surface area of CuO, cm²/g

c_A = concentration of hydrogen, mol/cm³

\mathcal{D}_e = effective diffusivity for hydrogen in CuO, cm²/s

can be solved to arrive at the following concentration profile:

$$\frac{c_A}{c_{A_o}} = \frac{\sinh\left[\phi\left(\frac{r}{R}\right)\right]}{\sinh\phi} \quad (4.13)$$

$$\phi = R\sqrt{\frac{ak_s}{\mathcal{D}_e}}, \quad (4.14)$$

in which from Equations 4.7 and 4.10:

$$ak_s = k'p_T\alpha(1 - \alpha), \quad (4.15)$$

where

$$c_A = \frac{p_A}{RT}$$

p_T = total pressure, atm.

The Thiele modulus, ϕ , defined by Equation 4.14, is a measure of the relative rates of diffusion and chemical reaction. In addition, an effectiveness factor, η , is defined to quantify the relationship between a measured reaction rate and the

intrinsic reaction rate as follows:

$$\eta = \frac{\text{Observed reaction rate}}{\text{Reaction rate when diffusion is fast}} = \frac{k_{\text{obs}}}{k_{\text{act}}} = \frac{k'p_T\alpha(1-\alpha)}{ak_s}. \quad (4.16)$$

From Equations 4.13, 4.14, and 4.16:

$$\eta = \frac{3}{\phi^2} [\phi \coth \phi - 1]. \quad (4.17)$$

From Equations 4.14 and 4.17, if diffusion of hydrogen is rate-controlling, then $\phi \rightarrow \infty$ and $\eta \rightarrow \frac{3}{\phi}$; however, if chemical reaction is rate-controlling, then $\phi \rightarrow 0$ and $\eta \rightarrow 1$. If diffusion of hydrogen is rate-controlling, then the observed activation energy, E_{obs} , is computed to be half of the intrinsic activation energy, E_{act} , from Equations 4.14 and 4.16 as follows:

$$k_o\alpha(1-\alpha)\exp\left[\frac{-E_{\text{obs}}}{RT}\right] = \frac{3\mathcal{D}_e^{\frac{1}{2}}}{R}k_{s_o}^{\frac{1}{2}}\exp\left[\frac{-E_{\text{act}}}{2RT}\right]$$

$$E_{\text{obs}} = \frac{E_{\text{act}}}{2} \quad (4.18)$$

$$\alpha(1-\alpha)k'_o = \frac{3\mathcal{D}_e^{\frac{1}{2}}k_{s_o}^{\frac{1}{2}}}{R}, \quad (4.19)$$

where

$$k'p_T = k_o\exp\left[\frac{-E_{\text{obs}}}{RT}\right]$$

$$k_sa = k_{s_o}\exp\left[\frac{-E_{\text{act}}}{RT}\right].$$

This derivation is only approximate because the reduced sample is observed to be more compact than the fresh sample, in contradiction with starting assumptions. In particular, particle size decreases with increasing conversion of CuO to Cu,

and simultaneously, effective diffusivity, \mathcal{D}_e , decreases with increasing conversion which are both due to loss of porosity.

Adherence of data to the Prout-Tompkins equation for both low- and high-temperature regimes suggests that this equation adequately describes the mechanism of autocatalysis or acceleration. Specifically, the Prout-Tompkins equation is based on the growth of active nuclei by a branched-chain mechanism, which appears to be the case for both regimes. The only difference between the two regimes, thus, is the mechanism governing the growth rate of the active nuclei. Proposed rate-controlling mechanisms for the low-temperature regime include adsorption of hydrogen to copper [13], diffusion of H_2O through copper [14], and surface removal of oxygen from the oxide lattice [15]. On the other hand, diffusion of hydrogen to CuO is proposed as the rate-controlling step for the high-temperature regime. Resistance to hydrogen diffusion is due, primarily, to sintering of the solid mass at these high temperatures, which causes pore blockage, and, secondarily, to increased hydrogen desorption at these high temperatures.

4.3. Reduction of Cu-Al-O Materials by TPR

The TPR curves of Figure 3.2 have been reproduced in Figure 4.7 after a transformation to the coordinates $\frac{d\alpha}{dT}$ and temperature, T . Pure CuO (curve g, sample 11-1-CA3) exhibited a sharp, symmetric peak centered at 256°C , while CuAl_2O_4 (curve a, sample 92-1-CA containing 96 mole% CuAl_2O_4) exhibited a broad, symmetric peak centered at 430°C . The remaining samples of Figure 4.8 contained different molar ratios of $\text{CuO}:\text{CuAl}_2\text{O}_4$ with the balance Al_2O_3 and therefore exhibited both a low-temperature, sharp peak characteristic of the

reduction of CuO, and a high-temperature, broad peak characteristic of the reduction of CuAl_2O_4 . Table 4.3 summarizes the temperatures corresponding to the peak maxima, T_{max} , for each sample of Figure 4.7. For the broad, noisy peaks assigned to the reduction of CuAl_2O_4 , the value of T_{max} was estimated graphically at the midpoint of the peak width corresponding to approximately half the maximum rate. For the sharp peak assigned to the reduction of CuO, the value of T_{max} was estimated at the highest point of the peak. Samples containing ≥ 10 mole% Al_2O_3 exhibited reduction peaks for CuO and CuAl_2O_4 components at T_{max} values, notably lower than those measured for the pure components. In particular, denoting sample 11-1-CA3 as pure CuO, sample 92-1-CA as pure CuAl_2O_4 , and samples 72-1-CA, 59-1-CA, 15-1-CA, 56-1-CA, and 19-1-CA as mixed oxides, the mixed oxides displayed a T_{max} for CuO that was 3-5% lower than that for pure CuO and a T_{max} for CuAl_2O_4 that was 15-19% lower than that for pure CuAl_2O_4 .

While the variation in T_{max} for CuO is random, T_{max} for CuAl_2O_4 increases linearly with the CuAl_2O_4 content of the mixed oxide (Figure 4.8). An increase in T_{max} with increasing calcination temperature has been reported for the reduction of CuO by TPR [14]. No explanation for this finding was reported, however, and no such correlation was found in the experiments reported here (Figure 4.8). The variation in T_{max} for the CuO peak of the mixed oxides is attributed to thermal effects as described in Section 4.2.1. On the other hand, the variation in T_{max} for the CuAl_2O_4 peak of the mixed oxides is attributed to the simultaneous reduction of a slowly reducing CuO species. Evidence has been presented in Chapter III that the slowly reducing form of CuO is CuO that possesses an intimate interaction with Al_2O_3 in the sample. It has been postulated that this interaction could be an intermediate phase to the formation of

CuAl_2O_4 . A shift of the peak for CuAl_2O_4 reduction to lower temperatures with decreasing CuAl_2O_4 content is due to an increased amount of slowly reducing CuO , consistent with the results presented in Chapter III.

The plots of Figure 4.8 for the mixed oxides revealed features that were difficult to detect in similar plots reported for $\text{CuO}/\gamma\text{-Al}_2\text{O}_3$ materials prepared by the technique of impregnation. For example, for reduction using 10% H_2 in Ar of a $\text{CuO}/\gamma\text{-Al}_2\text{O}_3$ material containing 6% Cu and calcined at 600°C for 4 hours, a plot of H_2 consumption versus temperature contained a sharp peak at 175°C with a broad shoulder at 339°C [15]. The broad peak at 339°C could be due to a slowly reducing CuO species in intimate association with $\gamma\text{-Al}_2\text{O}_3$, in agreement with data reported here; however, no attention was addressed to this feature. The appearance of a CuO peak at 175°C is difficult to justify since there was no plot reported for pure CuO . Furthermore, values of T_{max} reported in Table 4.1 are 28 to 110% higher than this value. Since the values of T_{max} recorded in Table 4.1 were measured for reducing gases containing H_2 and N_2 , while a value of 175°C was measured for a reducing gas containing H_2 and Ar, the difference was due to the content of the reducing gas. Specifically, reagent grade N_2 contained a higher O_2 content than Ar. The presence of O_2 retarded the induction step of CuO reduction by combining with H_2 to form H_2O which competed with H_2 for adsorption to the specimen surface [11]. For a $\text{CuO}/\gamma\text{-Al}_2\text{O}_3$ material containing 19% Cu and calcined at 327°C for 2 hours, a plot of H_2 consumption versus temperature contained a peak at 144°C with a low-temperature shoulder [10]. The gas mixture used was 66% H_2 in Ar and the observed value of T_{max} was slightly lower than that measured for a mixture of 10% H_2 in Ar because of the higher H_2 content. On the other hand, no high-temperature broad peaks were observed for this sample. The 6% Cu sample

composed of 4.5% Cu per 100 m²/g of γ -Al₂O₃ should contain an interaction between Cu⁺² and γ -Al₂O₃, while the 19% Cu sample composed of 9.7% Cu per 100 m²/g of γ -Al₂O₃ should contain mostly bulk CuO and little or no interaction with γ -Al₂O₃ (Chapter III, Section 3.1), consistent with the interpretation that the high-temperature shoulder in the case of the 6% Cu sample was due to reduction of a Cu⁺² species interacting strongly with γ -Al₂O₃.

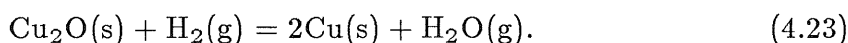
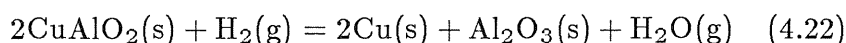
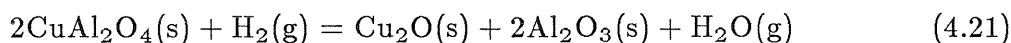
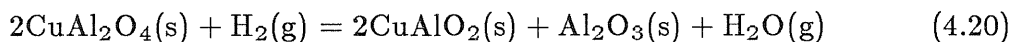
4.4. REDOX of Cu-Al-O Materials

The mechanism for the reduction of Cu-Al-O materials was investigated by a temperature-programmed technique in Chapter III, Section 3.3.5. In this technique, the samples were partially reduced by TPR, and subsequently, reduction intermediates were identified by XRD. The impact of the heating rate used during TPR and of the quenching process used to prepare the sample for subsequent XRD analysis on the results of these experiments was not determined. This section describes a technique that while being devoid of these potential limitations, provides similar mechanistic data for the reduction of Cu-Al-O materials.

Samples of CuAl₂O₄ are first reduced with 5% H₂ in N₂ at a fixed temperature, second, oxidized with air at the same temperature, and third rapidly cooled to room temperature under air for subsequent XRD analysis. Rapidly quenching an oxidized sample to room temperature under air will not alter the chemical phases present in the oxidized sample at the temperature of oxidation. Figure 4.9, together with Table 4.4, summarizes the normalized weight-loss curves for reduction-oxidation (REDOX) of sample 92-1-CA (containing 96 mole% CuAl₂O₄) at 463, 506, 636, and 774°C. X-ray diffraction patterns of the

oxidized samples from the experiments described in Table 4.4 appear in Figure 4.10.

Peaks for CuAlO_2 are detected in XRD patterns of samples subjected to REDOX at 463 and 506°C. This detection indicates that the free energy of formation for the oxidation of CuAlO_2 to CuAl_2O_4 is positive for temperatures up to at least 506°C and, moreover, that CuAlO_2 is an intermediate to the reduction of CuAl_2O_4 . TPR experiments also determined CuAlO_2 as an intermediate with the added information that CuAlO_2 is present at all stages of reduction (Chapter III, Section 3.3.5). The presence of Cu_2O , on the other hand, can not be ascertained. This is because Cu_2O is reported to oxidize to CuO at temperatures as low as 250°C [16]; thus, its presence as an intermediate to the reduction of CuAl_2O_4 would be destroyed during the subsequent oxidation. Cu_2O is also difficult to detect in TPR experiments because Cu_2O has d-spacings close to those reported for CuAlO_2 , and thus, the broad x-ray peaks observed for CuAlO_2 may have obscured the presence of Cu_2O (Chapter III, Section 3.3.5). While the presence of Cu_2O is inconclusive, a single peak in the TPR profile for CuAl_2O_4 (Figure 4.8a) indicates that Cu_2O is not important to the kinetics of the reaction. For example, multiple reactions must occur in parallel to generate both Cu_2O and CuAlO_2 by thermodynamically feasible means as follows:



The one-stage reduction indicated by TPR suggests that reaction 4.22 is the rate-determining step, while reactions 4.20, 4.21, and 4.23 occur rapidly by comparison. This interpretation is consistent with the observation of CuAlO_2 at all stages of reduction in TPR experiments (Chapter III, Section 3.3.5).

REDOX of CuAl_2O_4 at 636 or 774°C results in a mixture of CuO and CuAl_2O_4 , with the balance being Al_2O_3 . The relative amounts of CuO and CuAl_2O_4 , approximated by the relative intensities of the CuO $\langle 002 \rangle$ peak ($2\theta \sim 35.5^\circ$) and the CuAl_2O_4 $\langle 113 \rangle$ peak ($2\theta \sim 36.8^\circ$), correspond, qualitatively, to the relative amounts of CuO and CuAl_2O_4 expected for samples calcined at these temperatures (Figure 4.10). This correspondence suggests that the dispersion of copper is relatively unaffected by REDOX. The weight-loss curve for reduction at 774°C (Figure 4.9), however, exhibits a discontinuity at a conversion of 87%, which is believed to be the result of CuAl_2O_4 sintering, which according to previous evidence (Chapter III, Sections 3.3.1 and 3.4) becomes prominent at a temperature between 700 and 800°C.

REDOX of samples prepared using different calcination temperatures provides information about the physicochemical properties of the original samples. TPR experiments of samples prepared by calcination temperatures of 550, 700, and 900°C were followed by temperature-programmed oxidation (TPO) in air. The cooled samples were examined by XRD. For sample 15-1-CA calcined at 550°C and containing 33.3 mole% CuAl_2O_4 , the CuAl_2O_4 :CuO ratio was higher in samples exposed to TPR and TPO (Table 4.5) than in the fresh sample, according to the intensity ratio observed for these components by XRD (Figure 4.11). Furthermore, of the three experiments conducted, the CuAl_2O_4 :CuO ratio was lowest for the experiment with the lowest temperatures during TPO. These observations suggested an increase in CuAl_2O_4 content with increasing

temperature of oxidation, which resulted because a good dispersion of copper and aluminum was maintained during oxidation.

Similarly, for sample 56-1-CA calcined at 700°C and containing 48 mole% CuAl_2O_4 , no CuO was detected in samples exposed to TPR and TPO. Temperatures during TPO were between 905 and 912°C for sample 56-1-CA, and between 745 and 857°C for sample 15-1-CA. The absence of CuO implied that a good dispersion of copper and aluminum was present at the conclusion of TPR and maintained during TPO. Furthermore, while a temperature of 857°C was not high enough, a temperature of 905°C was high enough for complete conversion to CuAl_2O_4 , provided an adequate dispersion of copper and aluminum prevailed.

In contrast, for sample 92-1-CA calcined at 900°C and containing 96 mole% CuAl_2O_4 , the CuAl_2O_4 :CuO ratio was lower in samples exposed to TPR and TPO than in the fresh sample. Since observations for samples 15-1-CA and 56-1-CA suggested that dispersion of copper and aluminum was not significantly affected during TPO, the dispersion of metallic copper on alumina at the conclusion of TPR determined the relative amounts of CuAl_2O_4 and CuO formed during TPO for a given temperature range. Therefore, TPR of 15-1-CA or of 56-1-CA lead to a higher dispersion of copper than TPR of 92-1-CA. This is partly rationalized by considering that the BET surface areas of samples 15-1-CA and 56-1-CA are 13% higher than that of sample 92-1-CA, reflecting the presence of high surface area alumina. High surface area alumina present in the fresh sample leads to a good dispersion of copper metal upon TPR. TPR of CuAl_2O_4 , however, does not lead to as good a dispersion of copper metal. This may be related to the different nature of alumina produced in the two cases: Alumina produced by the reduction of CuAl_2O_4 is liable to have a higher crystallinity

and lower surface area than free alumina that is largely amorphous in the fresh sample and heated to a high temperature during TPR.

The results of isothermal REDOX experiments reiterated the conclusions drawn from the above temperature-programmed REDOX experiments. Two samples prepared by the citrate process using calcination temperatures of 550°C (sample 72-1-CA with 5 mole % CuAl_2O_4) and 900°C (sample 33-1-CA6 with 96 mole % CuAl_2O_4) were subjected to isothermal REDOX at 600, 700, and 800°C. In each case, following REDOX, the sample was rapidly cooled to room temperature in air and then examined by XRD (Figure 4.12). Reduction and oxidation were each conducted for 10 minutes, producing a partial conversion, α_{red} , following reduction, and complete conversion following oxidation. Conversions, α_{red} , were lower for sample 33-1-CA6 than for sample 72-1-CA because of the slower reduction kinetics of CuAl_2O_4 as compared to CuO (Table 4.6). REDOX at temperatures of 600 and 700°C therefore resulted in a higher CuAl_2O_4 : CuO ratio for sample 33-1-CA6 than for 72-1-CA because of the presence of unreacted CuAl_2O_4 at the onset of oxidation. At a temperature of 800°C, however, α_{red} for the two samples was comparable and REDOX led to a higher CuAl_2O_4 : CuO ratio for sample 72-1-CA than for sample 33-1-CA6. This was in keeping with the conclusion that reduction of CuAl_2O_4 resulted in a lower dispersion of copper metal than does reduction of a sample containing a mixture of the pure oxides, CuO and Al_2O_3 . In further support of the different dispersions of copper resulting from the reduction of different samples, copper particles viewed by SEM for reduced CuAl_2O_4 (reduced 92-1-CA or reduced 33-1-CA6) were on the average larger than those viewed for reduced 72-1-CA for both temperature-programmed (micrographs 3.13d and 3.14c), and isothermal (micrographs 5.11b and 5.6b) modes of reduction. Good dispersion of copper metal upon reduction

has been observed for samples containing between 5 and 48 mole % CuAl_2O_4 with the balance an equimolar mixture of CuO and Al_2O_3 .

REFERENCES

1. Jenkins, J.W., McNicol, B.D., and Robertson, S.D., "Characterized Catalysts via Temperature-Programmed Reduction," *Chem. Technol.*, **7**, 316, 1977.
2. Hurst, N.W., Gentry, S.J., and Jones, A., "Temperature Programmed Reduction," *Catal. Rev.-Sci. Eng.*, **24**(2), 233, 1982.
3. Brito, J., and Laine, J., "Characterization of Supported MoO₃ by Temperature-Programmed Reduction," *Polyhedron*, **5**(1/2), 179, 1986.
4. Houalla, M., LeMaitre, J., and Delmon, B., "Influence of the Lithium Content on the State, Dispersion, and Reducibility of Nickel Oxide Supported on γ -Al₂O₃," *J. Chem. Soc. Faraday Trans. I*, **78**, 1389, 1982.
5. Arnoldy, P., and Moulijn, J.A., "Temperature-Programmed Reduction of CoO/Al₂O₃ Catalysts," *J. Catal.*, **93**, 38, 1985.
6. Huang, Y.-J., Xue, J., and Schwarz, J.A., "Analysis of Temperature-Programmed Reduction Profiles from Metal-Supported Catalysts," *J. Catal.*, **111**, 59, 1988.
7. Robertson, S.D., McNicol, B.D., deBaas, J.H., and Kloet, S.C., "Determination of Reducibility and Identification of Alloying in Copper-Nickel-on-Silica Catalysts by Temperature-Programmed Reduction," *J. Catal.*, **37**, 424, 1975.
8. Gentry, S.J., Hurst, N.W., and Jones, A., "Temperature Programmed Reduction of Copper Ions in Zeolites," *J. Chem. Soc. Faraday I*, **75**, 1688, 1979.
9. LeMaitre, J.L., "Chapter 2: Temperature Programmed Methods" in *Characterization of Heterogeneous Catalysis* ed. by F. Delannay (Marcel Dekker,

- Inc.: New York, 1984), p.29.
10. Matulewicz, E.R.A., deKeijser, M.S., Mol, J.C., and Kapteijn, F., "Characterization of CuO-ZnO-Al₂O₃ Methanol-Synthesis Catalysts Using Temperature-Programmed Reduction and Thermal Stability," *Thermochim. Acta*, **72**, 111, 1984.
 11. Pease, R.N., and Taylor, H.S., "The Reduction of Copper Oxide by Hydrogen," *J. Amer. Chem. Soc.*, **43**, 2179, 1921.
 12. Bond, W.D., "Thermogravimetric Study of the Kinetics of Reduction of Cupric Oxide by Hydrogen," *J. Phys. Chem.*, **66**, 1573, 1962.
 13. Naumov, Y.B., Pavlov, Y.L., Vasilevich, A.A., Alekseev, A.M., Novikov, É.A., and Shihibrya, G.G., "Kinetic Model of the Process for Reduction by Hydrogen of Oxide Systems Containing Copper," *Kinet. Katal.*, **27**(4), 818, 1986.
 14. Wang, H.-P., and Yeh, C.-T., "On the Reduction of Copper Oxide," *J. Chinese Chem. Soc.*, **30**, 139, 1983.
 15. Oates, W.A., and Todd, D.D., "Kinetics of the Reduction of Oxides," *Australian Institute of Metals Journal*, **7**, 109, 1962.
 16. Paryjczak, T., Rynkowski, J., and Krzyzanowski, K., "Temperature-Programmed Reduction of CuO-NiO/Al₂O₃ Catalysts," *React. Kinet. Catal. Lett.*, **21**(3), 295, 1982.
 17. Lupu, A., "Thermogravimetry of Copper and Copper Oxides (Cu₂O and CuO)," *J. Thermal Anal.*, **2**, 445, 1970.
 18. Gentry, S.J., Hurst, N.W., and Jones, A., "Study of the Promoting Influence of Transition Metals on the Reduction of Cupric Oxide by Temperature Programmed Reduction," *J. Chem. Soc., Faraday Trans. I*, **77**, 603, 1981.

Table 4.1: T_{\max} measured for the reduction of CuO by the method of TPR.

$T_{\max} (^{\circ}\text{C})$	Gaseous Reactant	Flow Rate (cc/min)	Heating Rate ($^{\circ}\text{C}/\text{min}$)	Preparation of CuO	Ref.
332.85	10% H_2 in N_2	?	13	Decomposition of copper nitrate at 752°C .	18
350	5% H_2 in N_2	20	?	Decomposition of copper nitrate at 500°C .	1
367	6% H_2 in N_2	10	6.5	Decomposition of copper nitrate at 500°C .	7
280	10% H_2 in N_2	20	6.5	?	2
224	5% H_2 in N_2	80	1.7	Citrate process with calcination at 550°C .	this work
254 ± 2	5% H_2 in N_2	80	1.7	Citrate process with calcination at 550°C .	this work
289	5% H_2 in N_2	80	1.7	Citrate process with calcination at 550°C .	this work

Table 4.2: Activation energies measured for the reduction of CuO.

Apparent Activation Energy (kJ/mole)	Temperature Range ($^{\circ}\text{C}$)	Technique	Ref.
40.6, 47.7, 64.5	145-220	Isothermal gravimetry	13
67	?	Isothermal monitor of $\Delta[\text{H}_2]$	18
54.5	144-227	Isothermal monitor of $\Delta[\text{H}_2]$	14
51.5-61.5	112-227	Isothermal gravimetry	12

Table 4.3: T_{\max} for CuO and CuAl_2O_4 peaks in Figure 4.7.

Sample	Mole Ratios ^a CuO: CuAl_2O_4 : Al_2O_3	$T_{\text{calc}}(^{\circ}\text{C})$ [Duration-hrs]	$T_{\max}(^{\circ}\text{C})$ CuO peak	$T_{\max}(^{\circ}\text{C})$ CuAl_2O_4 peak	Sample Size (mg)
11-1-CA3	100:0:0	550[4]	256.0	none	17.461
92-1-CA	2.1:95.9:2.1	900[4]	none	430.2	35.622
72-1-CA	47.5:5:47.5	550[4]	246.6	none	31.733
59-1-CA	45:10:45	600[4]	247.6	350.0	35.355
15-1-CA	33.3:33.3:33.3	550[4]	247.4	352.9	32.680
56-1-CA	26:48:26	700[4]	243.2	362.7	36.379
19-1-CA	10:80:10	800[4]	245.8	365.7	25.519

^a Subject to 1-4% experimental error.

Table 4.4: Experimental parameters for Figures 4.9 and 4.10.

Temp. ($^{\circ}\text{C}$)	Fig. 4.10	Sample Mass(mg)	t_{R}^{a} (min)	W_{N} at t_{R}	t_{O}^{b} (min)	W_{N} at t_{O}
463	a	30.169	630	0.32	267.5	0.81
506	b	29.916	690	0.26	185	0.86
636	c	30.104	516	0.18	76	1.00
774	d	29.307	98.5	0.07	66	1.00

^a Total time of exposure to the reducing gas.

^b Total time of exposure to the oxidizing gas.

Table 4.5: Conditions of TPR and TPO for the XRD patterns of Figure 4.11.

Sample	$T_{\text{calc}}(^{\circ}\text{C})$ [Duration-hrs]	Fig. 4.12	Heating rate ($^{\circ}\text{C}/\text{min}$)	Length of TPR(min)	Length of TPO(min)	$T_{\text{fr}}^{\text{a}} = T_{\text{io}}^{\text{b}}$ ($^{\circ}\text{C}$)	T_{fo}^{c} ($^{\circ}\text{C}$)
56-1-CA	700[4]	b	1.7	395.5	50	912	912
		c	1.7	420	158.5	912	912
		d	1.7	433	113	905	912
15-1-CA	550[4]	f	1.7	301	15.5	745	758
		g	1.7	305	23.5	752	771
		h	8.3	65.5	9.3	780	818
92-1-CA	900[4]	j	1.7	390.5	67.5	897	912
		k	1.7	420	9.5	912	912

^a Temperature at the completion of reduction (initial temperature is 233°C).

^b Temperature at the onset of oxidation.

^c Temperature at the completion of oxidation.

Table 4.6: Conditions of isothermal REDOX for the XRD patterns of Figure 4.12.

Sample	$T_{\text{calc}}(^{\circ}\text{C})$ [Duration-hrs]	Mole Ratios $\text{CuO}:\text{CuAl}_2\text{O}_4:\text{Al}_2\text{O}_3$	Temperature of REDOX($^{\circ}\text{C}$)	$\alpha_{\text{R}}^{\text{a}}$	Sample Mass(mg)
72-1-CA	550[4]	47.5:5:47.5	600	1.00	43.200
			700	0.99	25.075
			800	0.96	41.525
33-1-CA6	900[4]	2:96:2	600	0.43	33.675
			700	0.77	32.125
			800	0.93	30.500

^a Conversion of Cu^{+2} to Cu° immediately before oxidation.

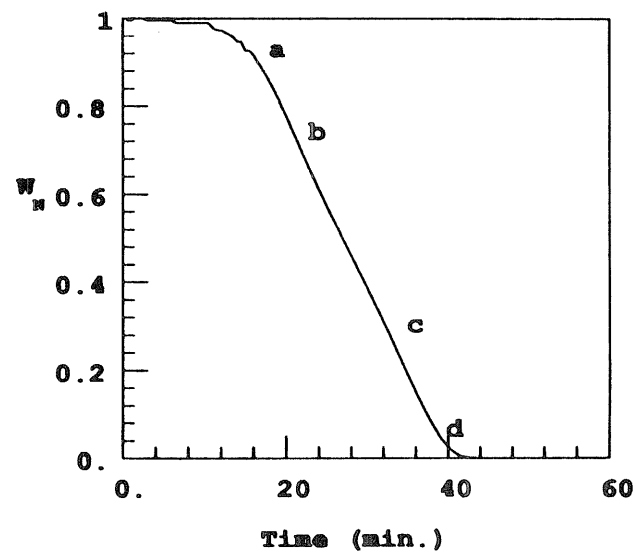
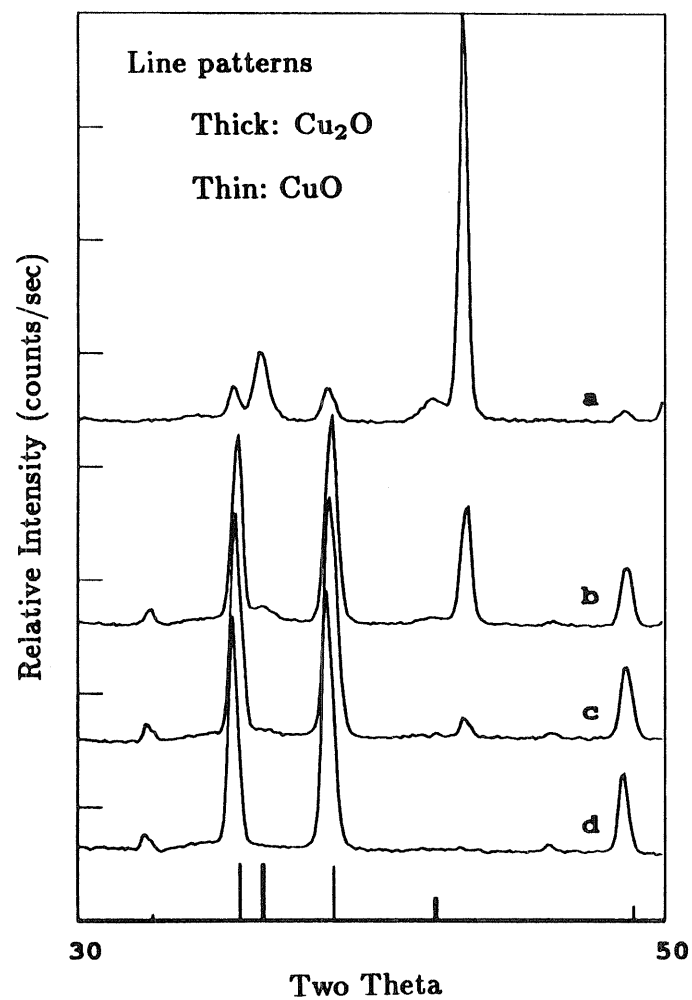


Figure 4.1: Identification of reduction intermediates for TPR of 11-1-CA3 (pure CuO) by XRD.

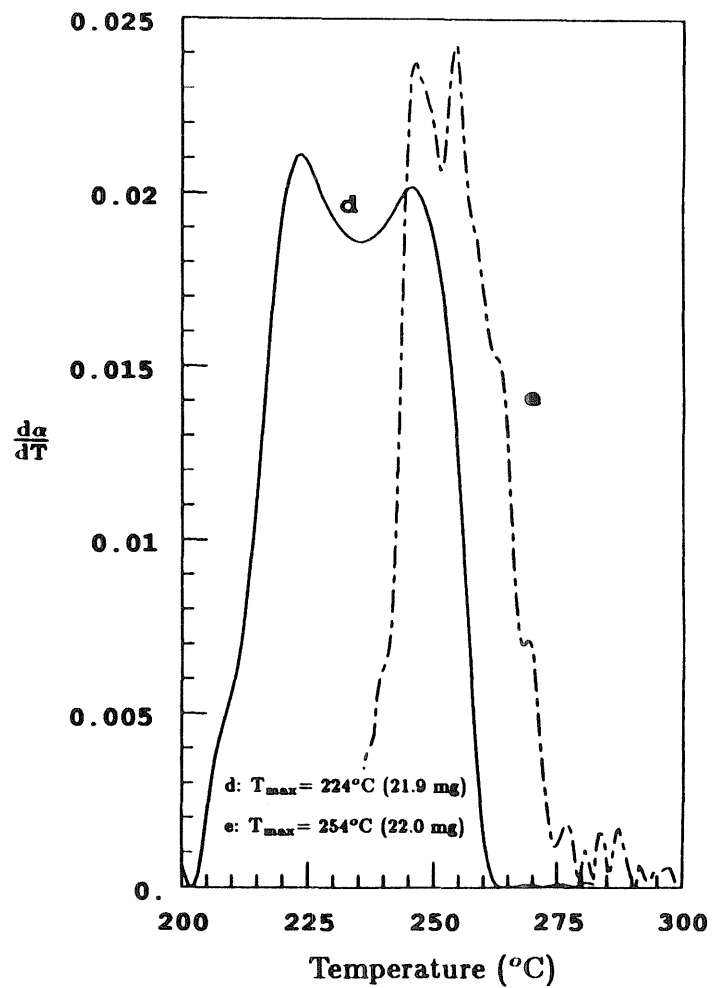
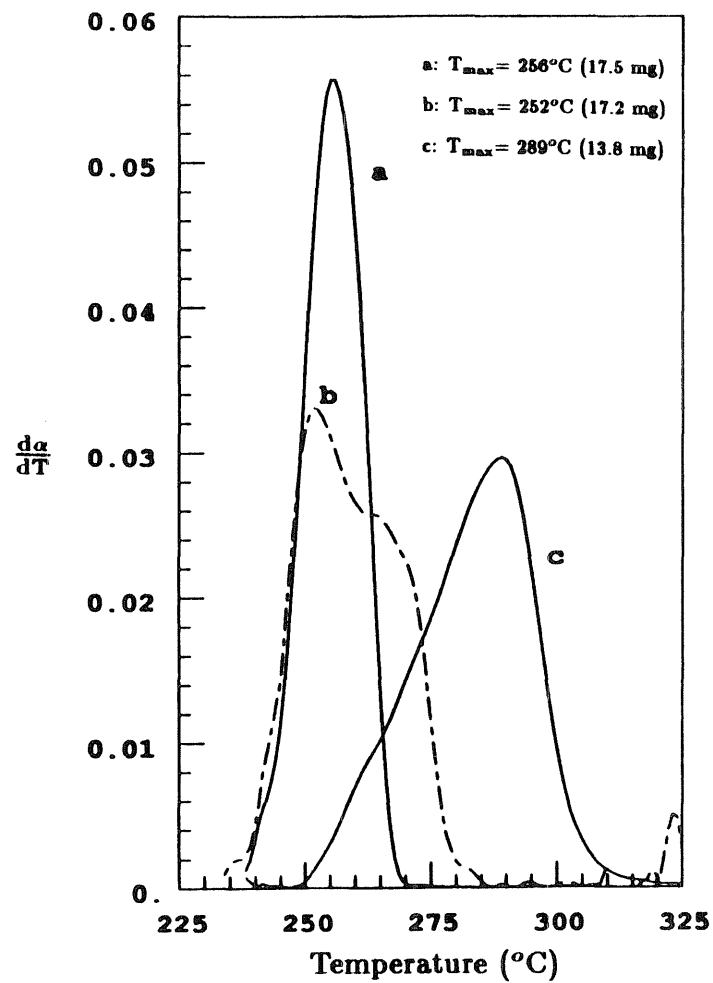


Figure 4.2: Reaction rate versus temperature for different TPR runs of CuO, sample 11-1-CA3.

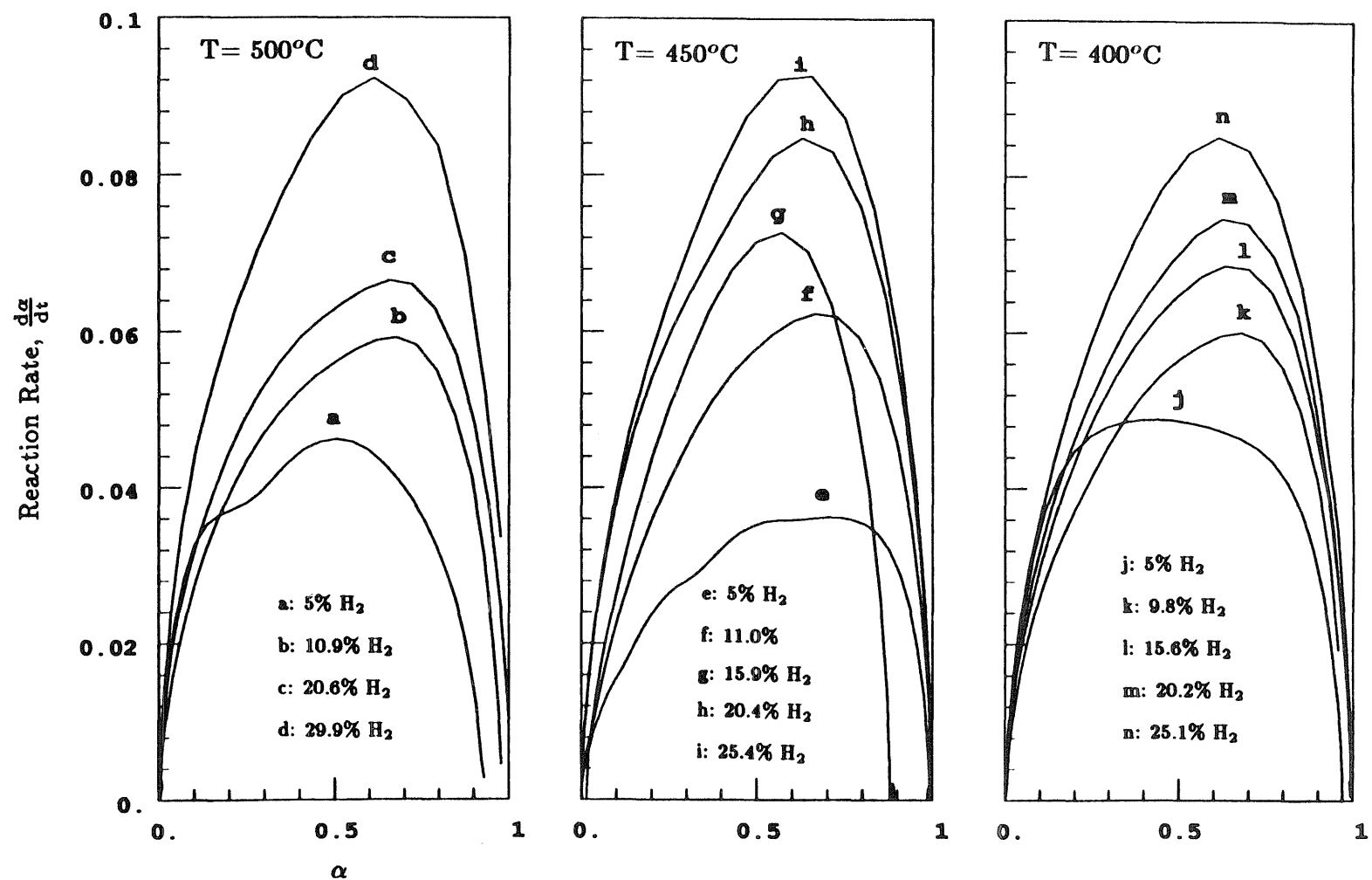


Figure 4.3: Reaction rate as a function of conversion for the isothermal reduction of CuO, sample 11-1-CA3.

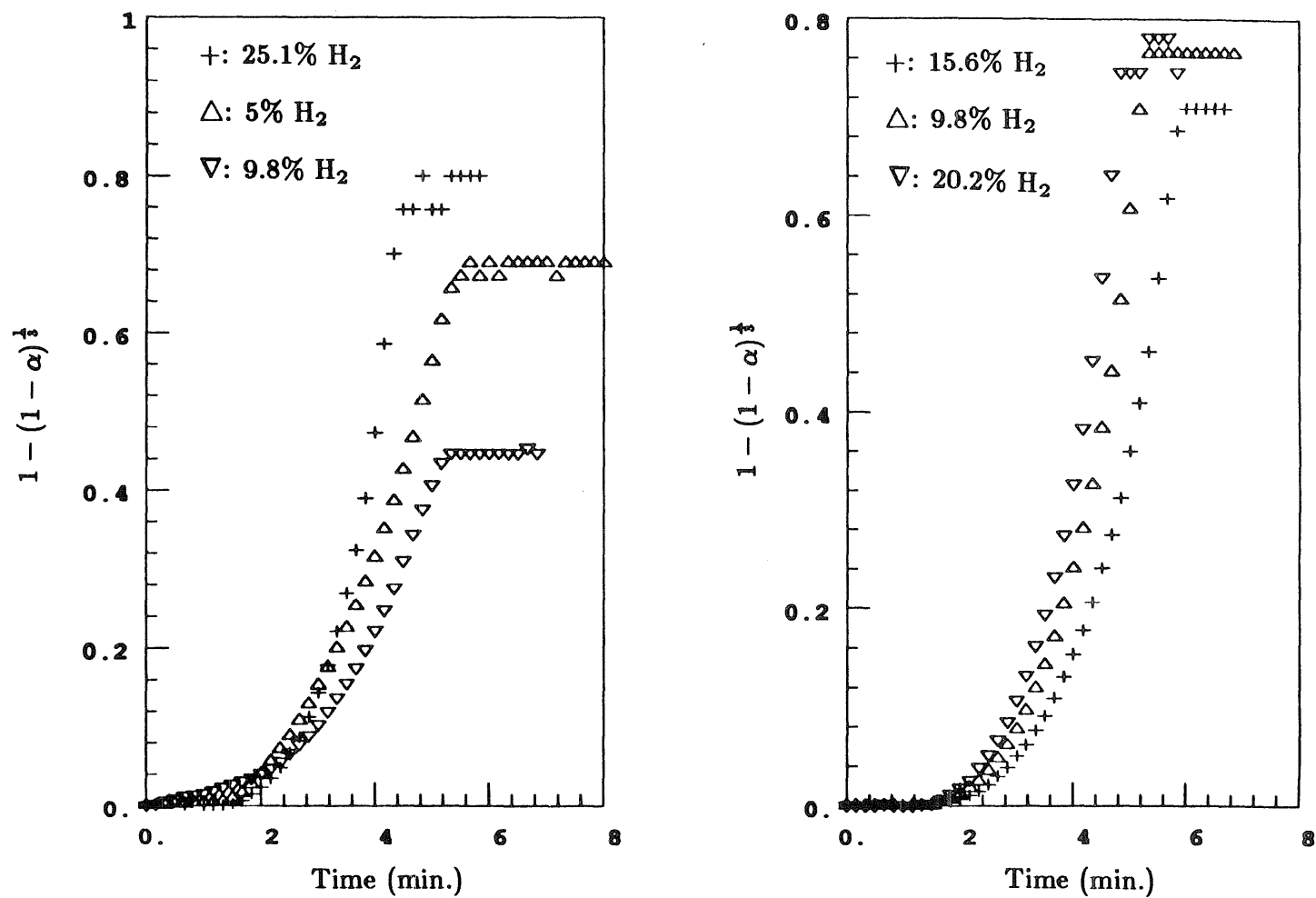


Figure 4.4: Roginskii-Shul'ts plots for isothermal reduction of CuO, sample 11-1-CA3, at 400°C.

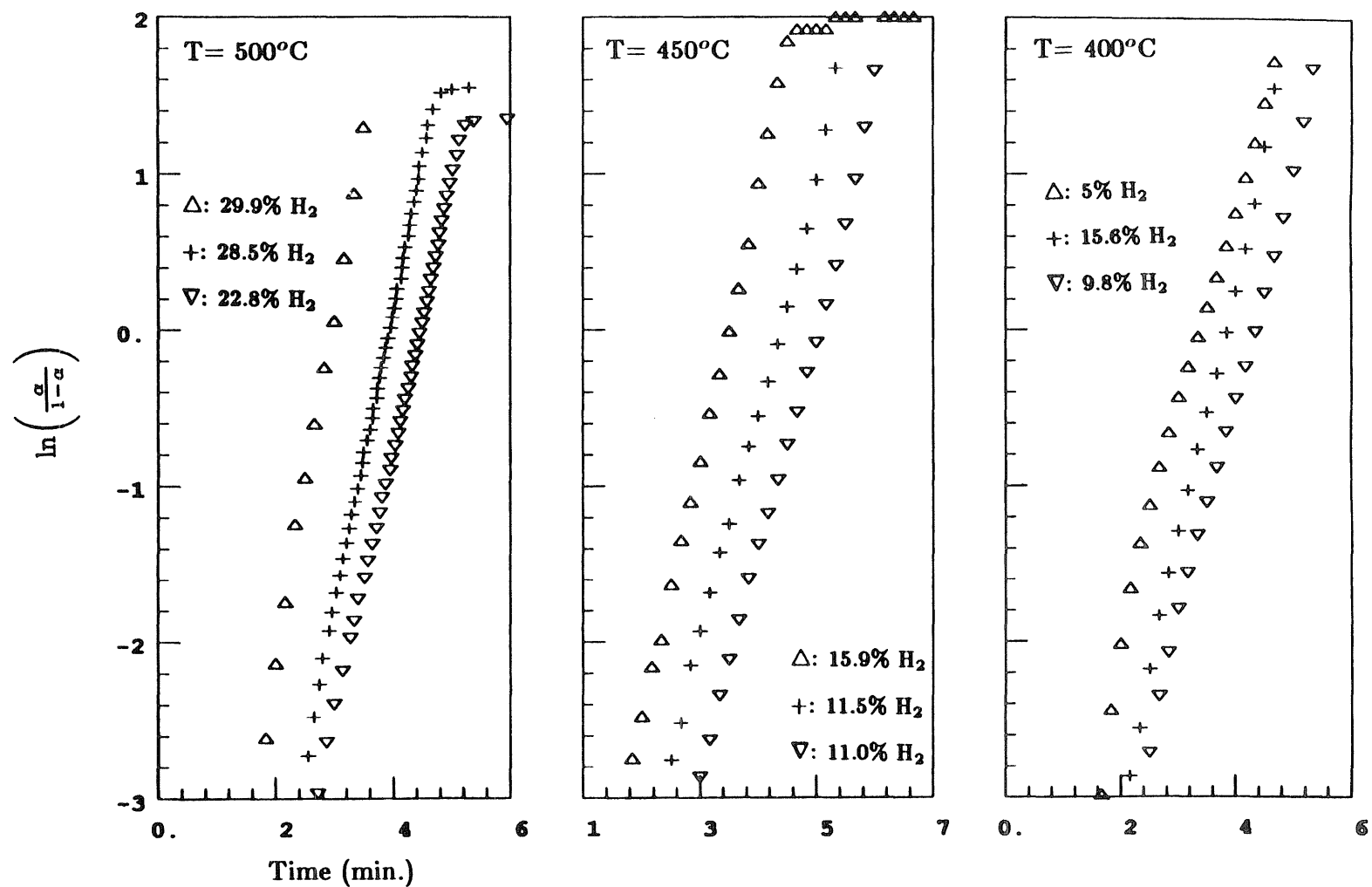


Figure 4.5: An example of some Prout-Tompkins plots for the isothermal reduction of CuO, sample 11-1-CA3.

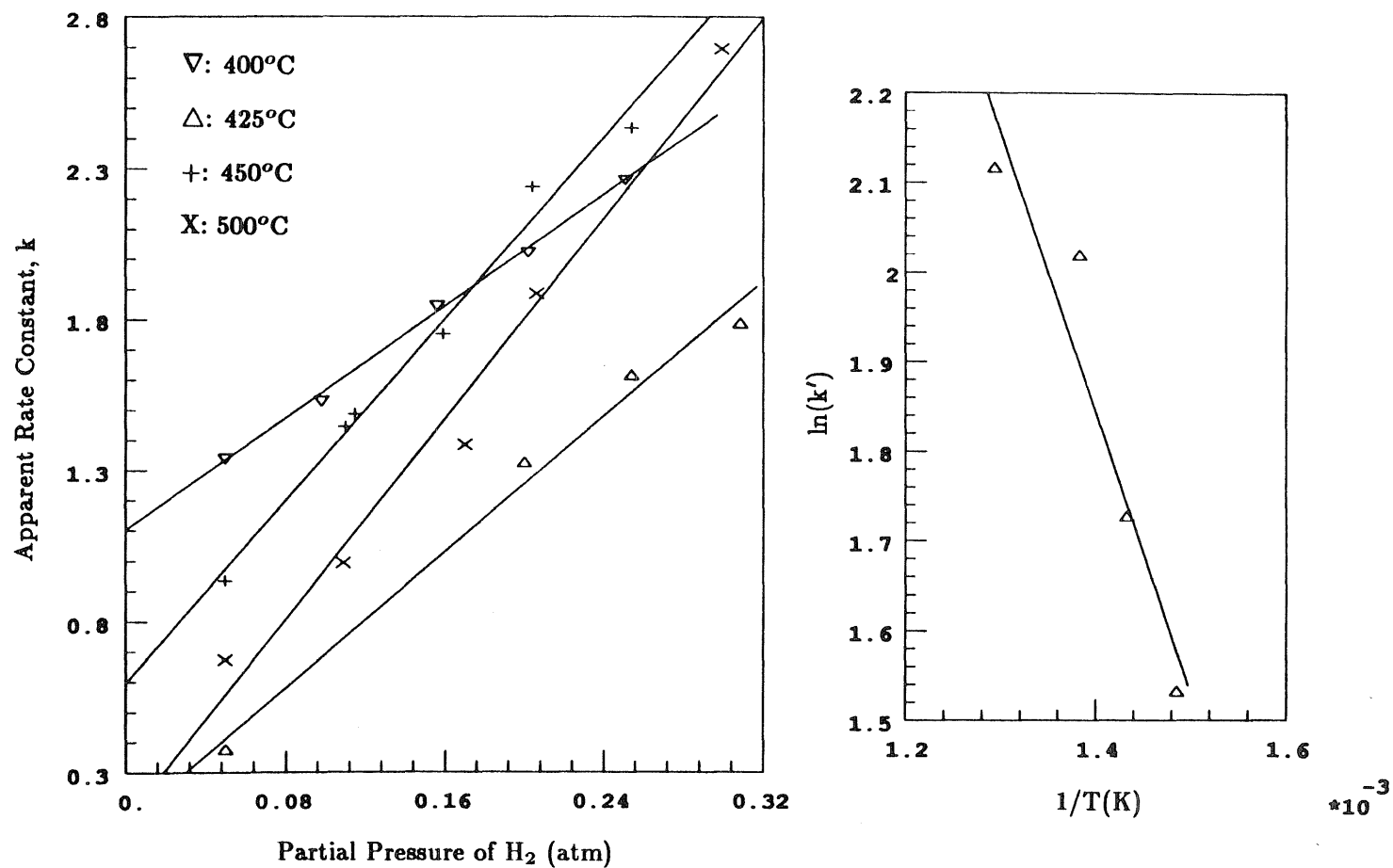


Figure 4.6: H_2 partial pressure dependence of apparent reaction rate constant (left) and temperature dependence of the true reaction rate constant (right) for the reduction of CuO, sample 11-1-CA3.

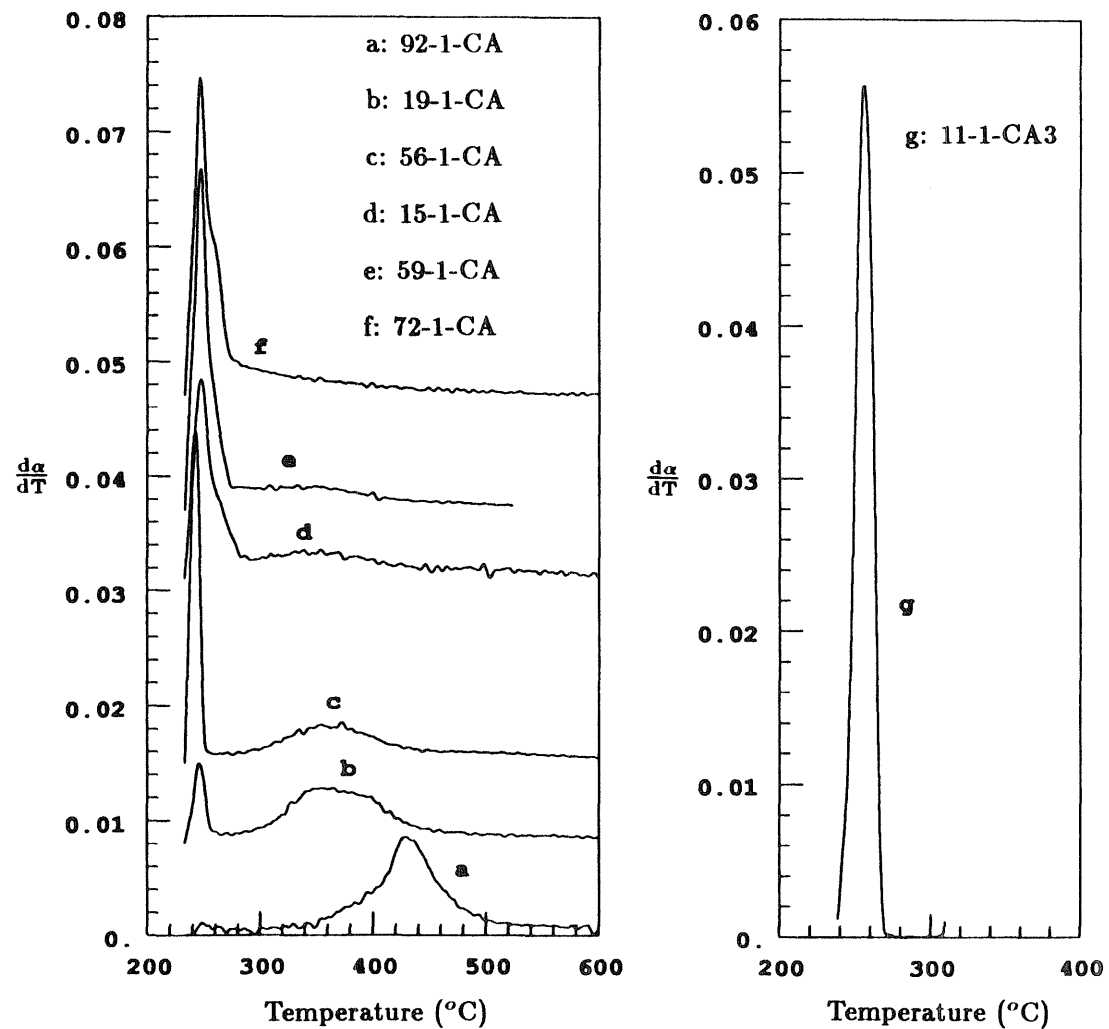


Figure 4.7: Reaction rate versus temperature for six Cu-Al-O samples (left) and CuO (right) prepared by the citrate process.

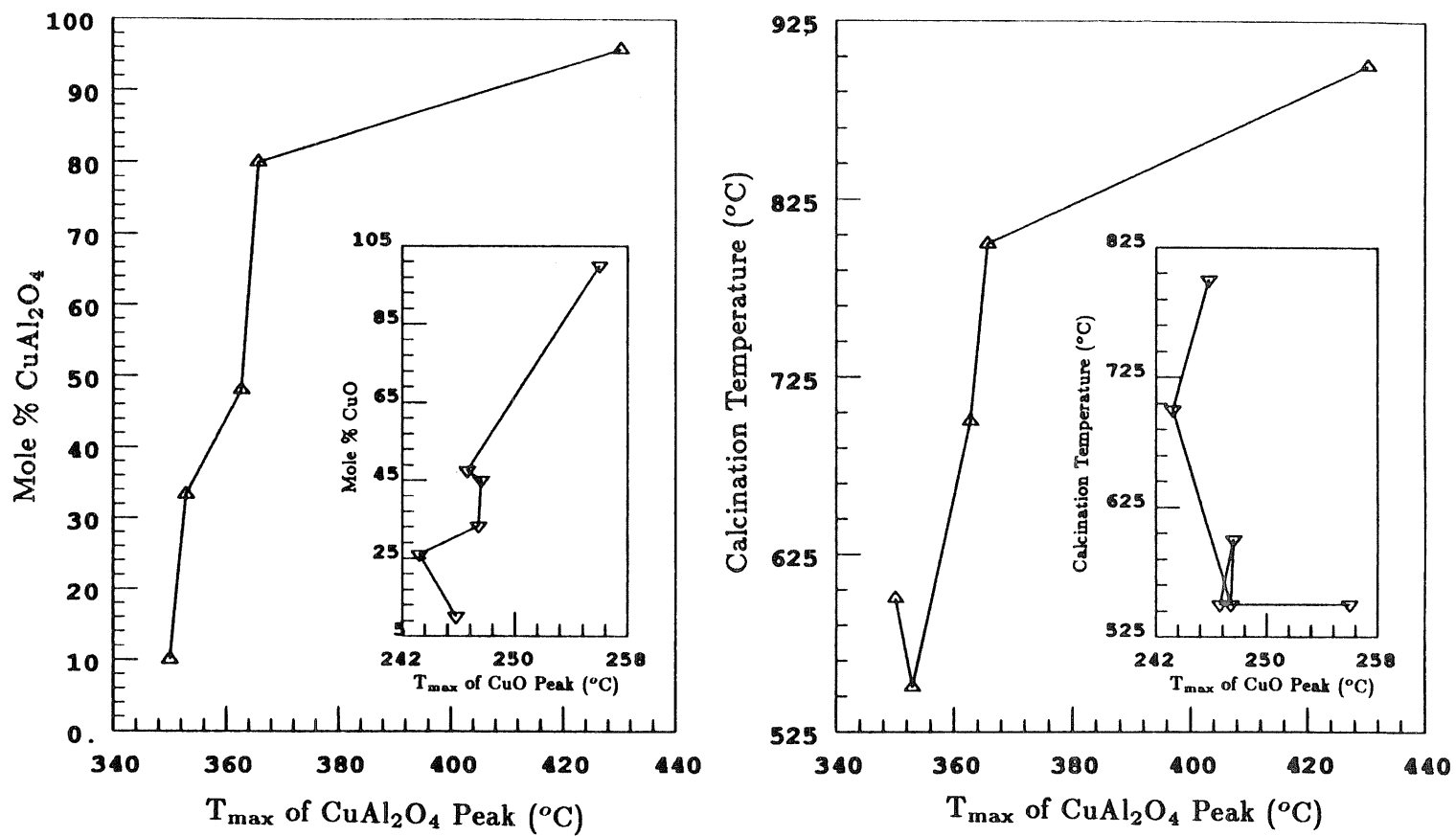


Figure 4.8: Values of T_{\max} estimated from Fig. 4.8 for CuO and CuAl_2O_4 as a function of concentration (left) and calcination temperature (right).

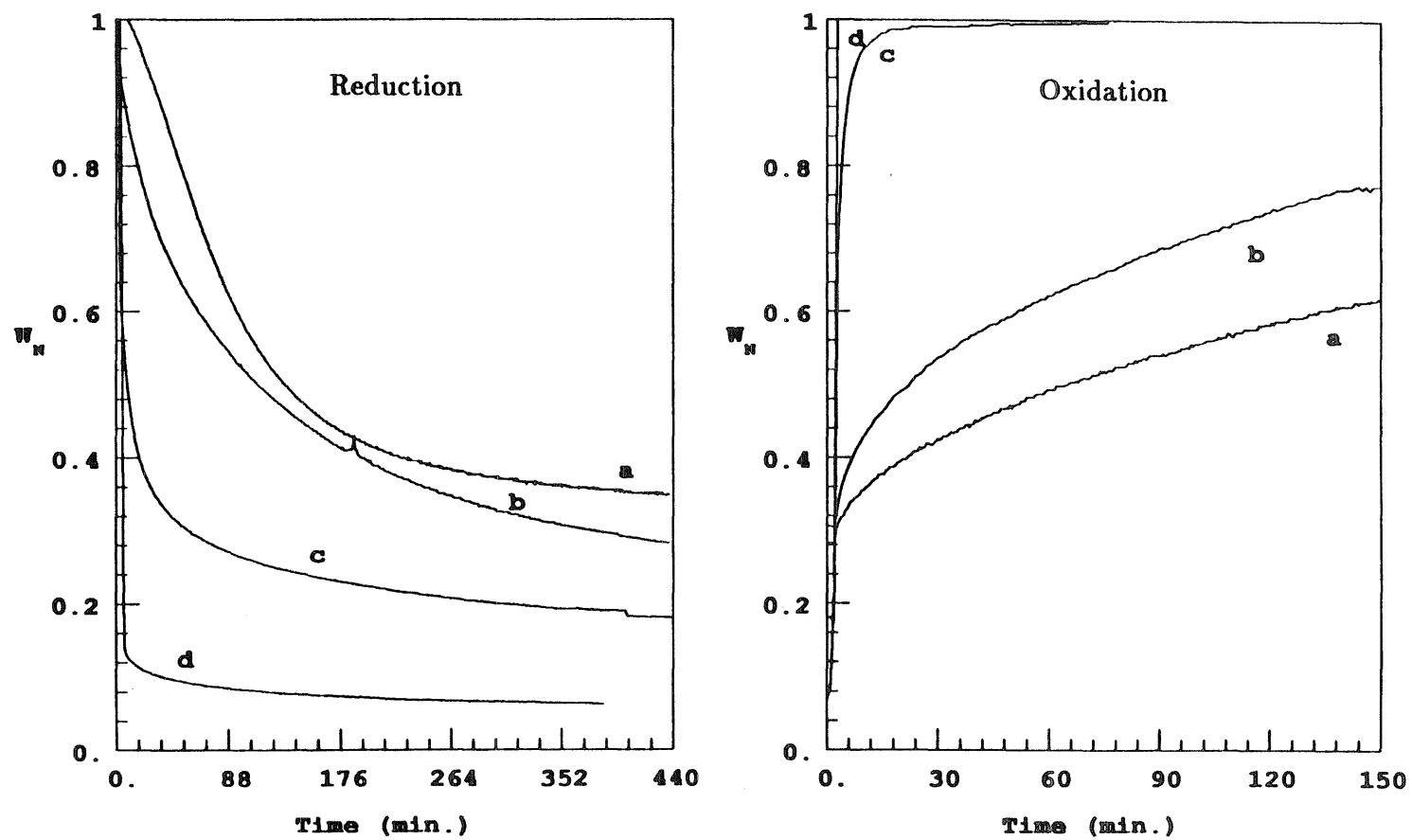


Figure 4.9: Isothermal REDOX of CuAl_2O_4 (sample 92-1-CA) at (a) 463°C , (b) 506°C , (c) 636°C , and (d) 774°C .

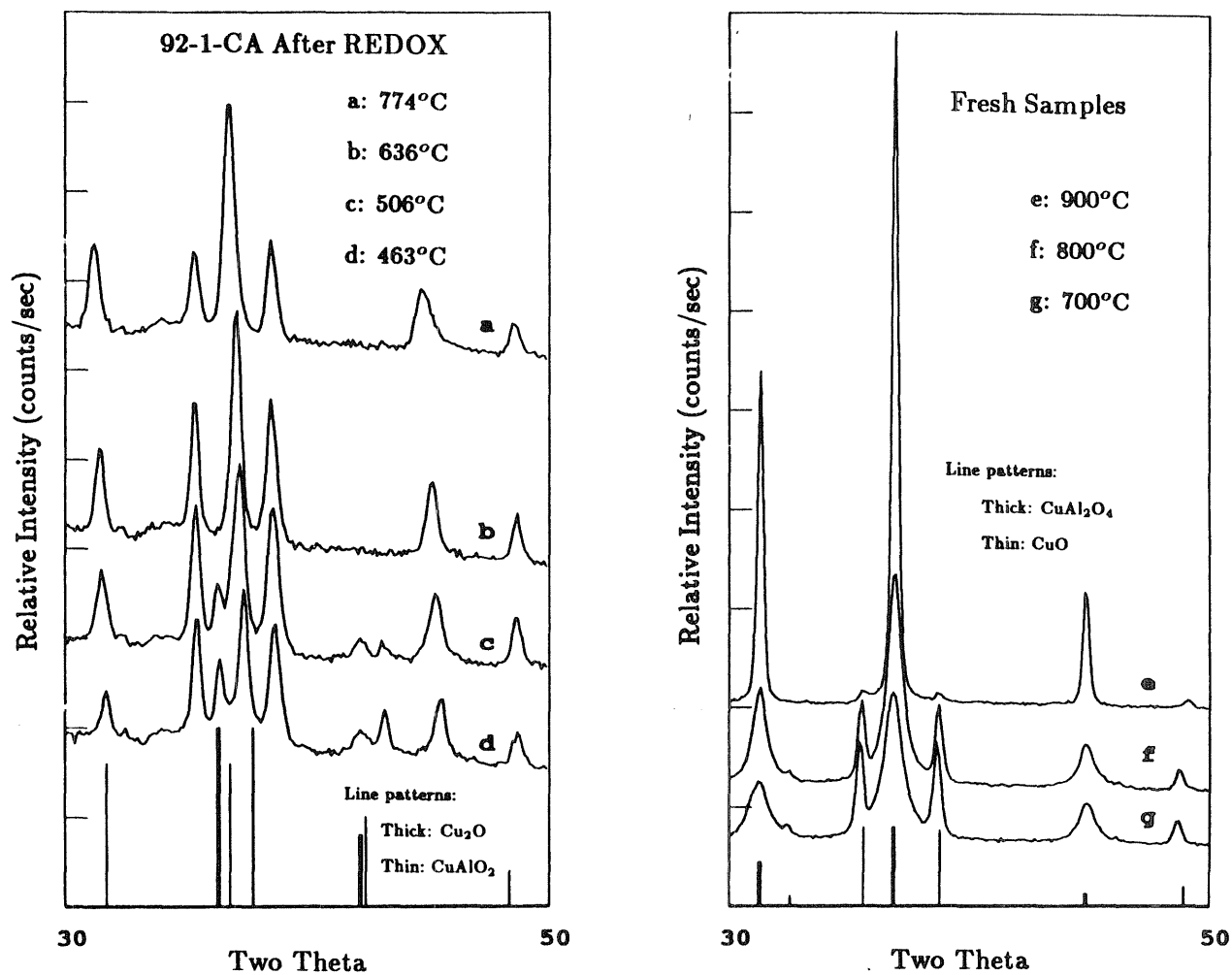


Figure 4.10: XRD patterns accompanying Figure 4.9 (left) compared to fresh Cu-Al-O samples (right) prepared by calcination at different temperatures.

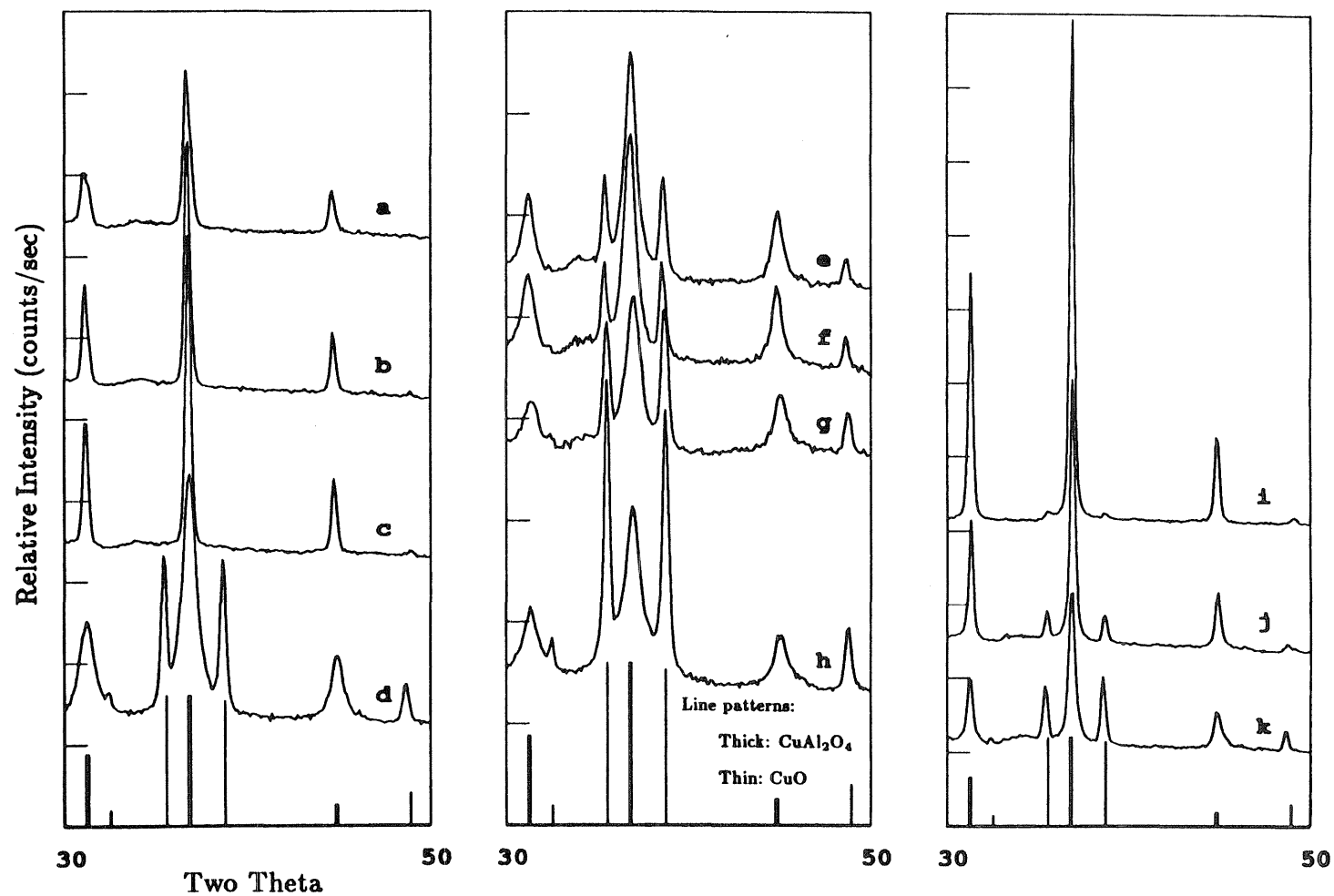


Figure 4.11: Xrd patterns for 56-1-CA (left), 15-1-CA(middle), and 92-1-CA (right) oxidized by TPO following TPR.

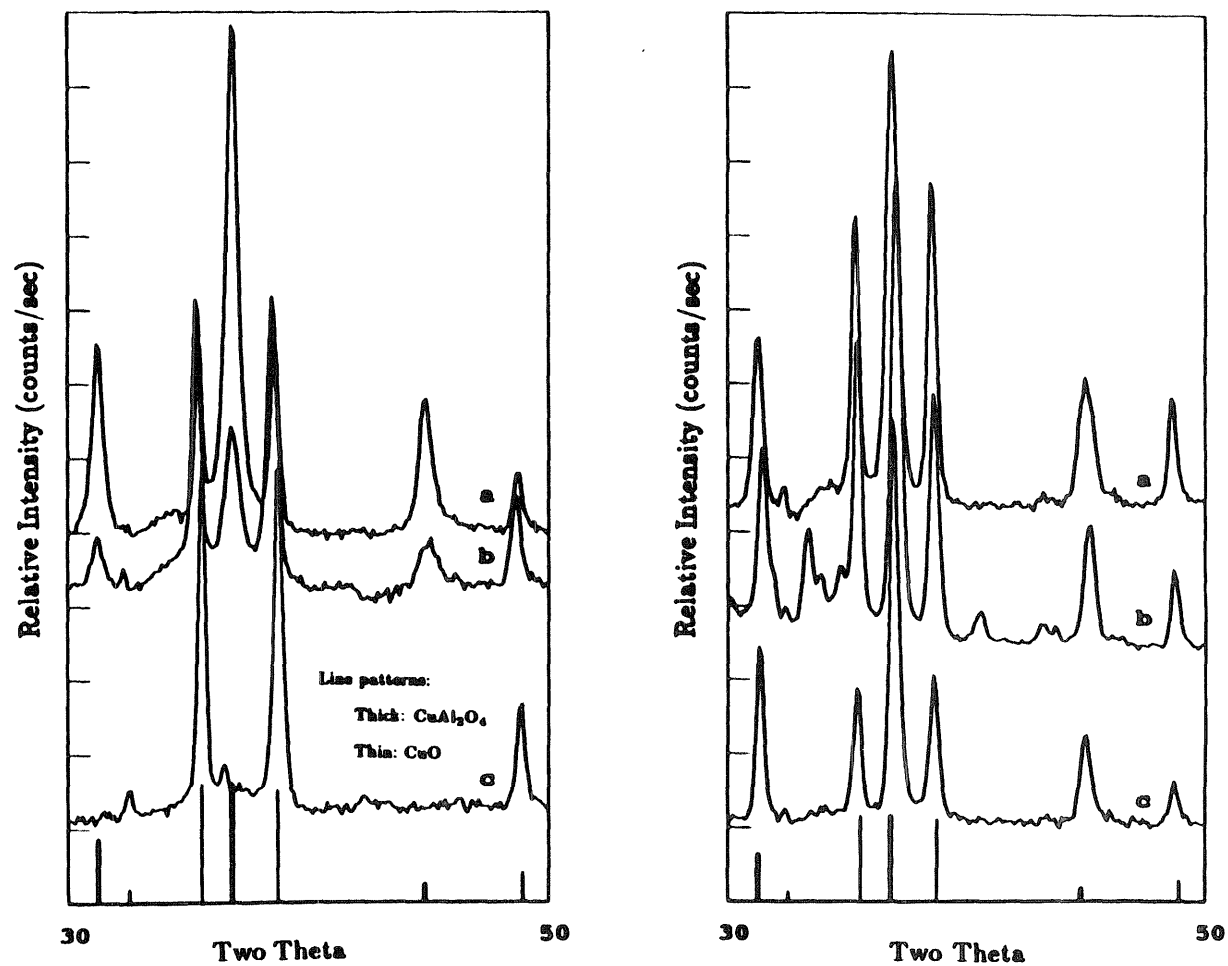


Figure 4.12: XRD patterns for 72-1-CA (left) and 33-1-CA6 (right) following isothermal REDOX at 600°C (a), 700°C (b), and 800°C (c).

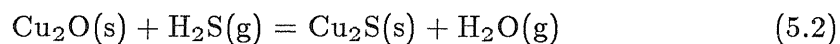
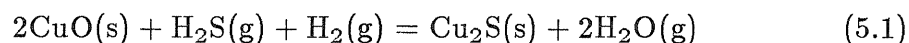
CHAPTER V

Reduction, Sulfidation, and Regeneration of Cu-Al-O Powders and Pellets

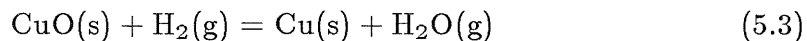
(Portions of this chapter, together with independent microreactor experiments performed at JPL, have been accepted for publication in *Ind. Engrng. Chem. Res.*)

5.1 Background

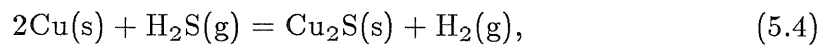
Among the most promising new technologies of power generation from coal are coal gasification integrated with a mechanical conversion process, combined cycle (gas turbine in series with a steam turbine), and coal gasification integrated with a chemical conversion process, molten-carbonate fuel cell. Both technologies require removal of H_2S (and COS) from the fuel gas prior to combustion. While this removal can be carried out at ambient temperatures by established technology, removal at high temperatures offers considerable improvement in process economics [1]. In the original research on hot gas desulfurization, pure metal oxides were tested, including those of zinc and iron [2]. Recent work has focused on mixed metal oxides, especially zinc ferrite (ZnFe_2O_4). Above about 650°C , however, sorbents containing zinc oxide lose zinc by reduction to the volatile metal. Iron and copper oxides are not subject to this limitation, but do not possess sufficiently large equilibrium constants for sulfidation to provide the required level of sulfur removal. In the case of copper oxide, the equilibria:



are very favorable. In the fuel gas atmosphere, however, the reaction



progresses rapidly so that sulfidation proceeds by reaction with metallic copper



which does not have sufficiently high equilibrium constant for the desired purification.

We have recently found that when copper oxide is employed in association with aluminum oxide, or iron oxide, or both, the level of sulfur removal is much higher than that obtained with pure copper oxide. Such behavior was exhibited by the binary and ternary oxides $\text{CuO-Al}_2\text{O}_3$, $\text{CuO-Fe}_2\text{O}_3$, and $\text{CuO-Fe}_2\text{O}_3\text{-Al}_2\text{O}_3$, and was attributed to the retardation of copper reduction to the metallic form engendered by the association with iron or aluminum oxides [3].

Previous work on the copper-containing, mixed-oxide sorbents involved measurements of breakthrough curves in a packed bed reactor and x-ray diffraction (XRD) analysis of fresh, sulfided, and regenerated sorbents to determine crystalline phases present [4]. The purpose of the present study was to obtain more detailed mechanistic and kinetic information about the sulfidation and regeneration of the binary $\text{CuO-Al}_2\text{O}_3$ sorbent. To this end we have used extensively thermogravimetric analysis (in isothermal or temperature-programmed mode) combined with XRD and scanning electron microscopy.

5.2 Experimental Techniques

5.2.1 Sorbent Preparation

The citrate method, described in Chapter II (Section 2.2.1), was used to synthesize the mixed oxide sorbents in a highly dispersed state. The complexing agent (citric acid), equimolar to total metal cations, was added to an aqueous solution of metal nitrates of the desired stoichiometric proportions. An amorphous citrate precursor was prepared by evaporation of this solution. This evaporation proceeded first rapidly at atmospheric pressure and 70°C until a marked

increase in viscosity of the solution was observed, and then, for several hours (3-24) in a vacuum oven at 70°C, until an amorphous solid foam formed. The foam was carefully broken up and and calcined at the desired temperature (between 550°C and 900°C) in air either under static conditions or under flow to produce the final mixed oxide. Hot nitric acid extraction coupled with atomic absorption spectroscopy (AAS) was used to determine quantitatively the amounts of CuAl_2O_4 , CuO , and Al_2O_3 present in a given sample as described in Chapter II (Section 2.2.2).

5.2.2 X-Ray Diffraction

A Siemens D400 intermittent diffractometer employing Ni-filtered $\text{Cu(K}\alpha\text{)}$ radiation (1.54056 Å) was used for qualitative chemical analysis of the polycrystalline components present in a sample. The x-ray tube was operated at 40kV and 30mA. X-ray powder diffraction patterns in a 2θ range of 25° to 60° (or 30° to 50°) were obtained that could detect the presence of CuO , CuAl_2O_4 , Cu_2O , CuAlO_2 , Cu , crystalline $\gamma\text{-Al}_2\text{O}_3$, Cu_2S , CuS , and other copper sulfides. Samples were finely ground and spread out evenly (*i.e.*, so as to avoid preferred orientations) over a piece of double-stick tape adhered to a glass slide. Spectra were scanned at 0.1° intervals (in 2θ) for 60 seconds per interval.

5.2.3 Scanning Electron Microscopy

The samples were examined by an ETEC corporation scanning electron microscope operating at 20 kV with a resolution of 70 Å. The sample was carefully ground and sprinkled on a metal stub containing a light coat of silver paste. This metal stub was then coated with a gold-palladium film 100 Å in thickness prior to observation.

5.2.4 Thermogravimetric Analysis

A Dupont 951 thermogravimetric analyzer interfaced through an analog to digital converter to a microcomputer served to measure the sample weight continuously. The quartz housing and flow path of the TGA were modified (Figure 5.1) to accommodate corrosive gases such as H_2S [5]. A gas flow rate of 80 cc/min was used for both the protective N_2 backflow gas and the reactant gas. Gas chromatography was used to determine the reactant gas concentration profile for these flow rates. The analysis showed that the reactant gas concentration over the sample was identical to that at the entrance to the reaction chamber, and, moreover, that no reactant gas was contaminating the mechanism of the instrument. The reactant gas mixtures were 5% H_2 in N_2 for the reduction runs, 4.2% H_2S in N_2 for the sulfidation runs, and air for the regeneration runs. A temperature programmer enabled either isothermal operation or operation under a linear temperature profile. Typically, a 30 mg sample of particles, 120-170 mesh fraction, was employed. It was verified experimentally that for the range of flow rates and sample sizes employed, the reactions were free of internal and external mass-transfer effects.

The TGA experiments described in this study, and the packed-bed microreactor experiments described in other studies [3,4] each have distinct advantages and disadvantages and provide complementary information. Packed-bed reactor experiments are suitable for obtaining overall sorbent performance under conditions similar to those of an industrial reactor. These experiments can provide information about sulfur-removal efficiency and can generate large samples for solid analysis. They are not well suited, however, to kinetic and mechanistic studies because of the intrinsic gradients of gas and solid composition along the

reactor. TGA runs, on the other hand, involve uniform gas and solid composition and are better suited for kinetic investigations. However, the small sample size that must be used to avoid mass transfer limitations may not be sufficient for certain analytical procedures.

TGA results are discussed in terms of normalized weight (W_N) versus time. Normalized weight is the ratio of the instantaneous weight change (relative to W_f) to the maximum weight loss expected ($W_i - W_f$). For example, following complete reduction of a sample of pure CuO to Cu, the final weight gives $W_N=0$. Subsequent sulfidation of this Cu to exclusively Cu_2S results in $W_N=1$ as a final weight.

5.3 Sorbent Characterization

Two amorphous citrate precursors were prepared and exposed to 4 hour-long calcinations. One precursor was calcined at $900^{\circ}C$ to yield predominantly compound oxide ($CuAl_2O_4$, sample 33-1-CA6), while the other was calcined at $550^{\circ}C$ to yield a mixture of oxides (CuO and Al_2O_3 , sample 72-1-CA). For comparison, a sample of pure CuO was prepared by the same procedure and calcined in air at $550^{\circ}C$ for 4 hours (sample 11-1-CA3). Components present in crystalline form were identified by XRD analysis (Figure 5.2), while quantitative chemical compositions (Table 5.1) were determined by atomic absorption spectroscopy (AAS). SEM analysis showed the markedly different microstructures possessed by these three materials (Figure 5.3). The micrographs displayed both a primary porous structure and a superimposed secondary texture. The secondary texture was smooth in the case of $CuAl_2O_4$ (sample 33-1-CA6); homogeneous and coarse for pure CuO (sample 11-1-CA3); and inhomogeneous

with granules for a mixture of oxides (sample 72-1-CA). Consequently, the presence of free alumina created the appearance of crystallites on the surface of fresh sorbents.

The three sorbents were characterized by temperature-programmed reduction (TPR) as shown in Figure 5.4. The major observation was that the reduction rate of CuAl_2O_4 (sample 33-1-CA6) was more than one order of magnitude lower than that of pure CuO (sample 11-1-CA3) proceeding through CuAlO_2 and Cu_2O as intermediates. Furthermore, independent TGA experiments revealed that for a sorbent containing a mixture of CuAl_2O_4 , CuO and inert Al_2O_3 , the major fraction of the pure oxide, CuO , reduced rapidly, while a smaller fraction of the CuO and the compound oxide, CuAl_2O_4 , reduced very slowly (Chapter III, Section 3.3). For sample 72-1-CA, 37 mass% of the CuO was observed to reduce more slowly than pure CuO . The association of CuO with Al_2O_3 was believed to be responsible for retarding reduction of this species [6]. This phenomenon has been reported for $\text{NiO}/\text{Al}_2\text{O}_3$ [7] and $\text{CuO}/\text{Al}_2\text{O}_3$ [8,9] prepared by impregnation.

5.4 Isothermal TGA Experiments

5.4.1 Reduction and Sulfidation Experiments

Desulfurization of coal gas by CuO or $\text{CuO}\cdot\text{Al}_2\text{O}_3$ involves simultaneous reduction and sulfidation of the sorbent (reactions 5.1 to 5.4). However, for the purpose of mapping out the reaction network and measuring reaction rates, it is useful to separate reduction and sulfidation. Therefore, in the TGA experiments, reduction and sulfidation were carried out consecutively.

Isothermal reduction and sulfidation of sample 72-1-CA were performed in

the modified TGA system for temperatures of 600°C, 700°C, 800°C, and 900°C (Figure 5.5). Consistent data were obtained by careful reproduction of sorbent heating procedures. Reduction was carried out with 5% H₂ in N₂ for the first ~5 minutes, followed by sulfidation with 4.2% H₂S in N₂ for the next ~35 minutes. XRD analysis of a sample following sulfidation at 700°C identified Cu_{1.8}S (digenite) as the dominant crystalline phase, while SEM analysis of the same sample revealed large crystals (5 to 12.5 μm) composed of interlocking malformed octahedra. In the majority of the octahedral building blocks, 2 of the 8 faces predominated, creating flat, hexagonal plates. This same crystal morphology was observed by Donnay and coworkers [10] in scanning electron micrographs of digenite crystals grown from a mixture containing ratios between 9:5 and 2:1 copper to sulfur, and at temperatures of 500°C to 775°C. Since for both Donnay's study and this study, SEM was performed on samples cooled to room temperature, the observed phase is a low-temperature form of digenite, low digenite. There exists a high-temperature form of digenite, high digenite, that forms from low digenite at temperatures greater than approximately 83°C [11].

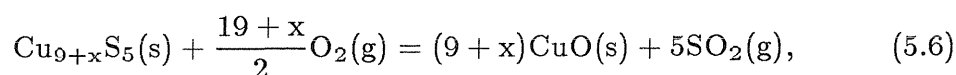
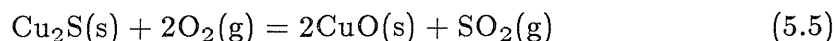
High and low digenite both have sulfur atoms in approximate cubic close packing, and are solid solutions of formula Cu_{9+x}S₅. On the other hand, the composition range of low digenite ($-0.166 < x < 0.125$) is narrower than that of high digenite ($-0.35 < x < 1.00$) [12], and low digenite has been isolated in the form of various polymorphs or superstructures of high digenite. For example, high digenite has a cubic cell of lattice parameter 5.56 Å, while, low digenite has a pseudocubic cell with lattice parameter (.56Å) · N, where N has been found to take on both integral (*e.g.*, N=5, 6) and nonintegral (*e.g.*, N= 5.2, 5.5, 5.7, 5.8) values [13-15]. While the method of powder XRD enables the distinction

between high digenite and low digenite, the method of single-crystal XRD is required for identification of a particular superstructure of low digenite [16].

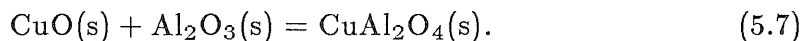
The succession of scanning electron micrographs shown in Figure 5.6 exhibits the marked structural changes accompanying consecutive reduction and sulfidation of sample 72-1-CA at 700°C. The fresh 72-1-CA having inhomogeneous grainy texture is converted upon reduction to a dispersion of spherical copper particles on alumina. Subsequent sulfidation produces a bimodal dispersion of large (2 to 6 μm), octahedral crystals and small ($< 0.3\mu\text{m}$), irregular crystals of digenite. The weight gain during sulfidation of 72-1-CA suggests that the amount of nonstoichiometric sulfur increases with reaction temperature. Since a value $W_N = 1$ corresponds to total conversion of copper to stoichiometric Cu_2S , nonstoichiometric sulfur produces weight gain $W_N > 1$. However, sulfidation at 900°C exhibits unexpected behavior, suggesting decomposition of the nonstoichiometric sulfides that have formed.

5.4.2 Regeneration Experiments

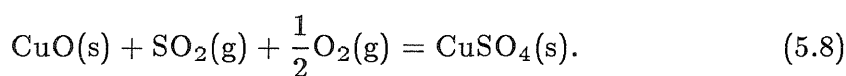
Regeneration of sulfided sorbents in air was also investigated to assess the extent of physicochemical modifications to the fresh sorbent as a result of sulfidation and regeneration. Regeneration was carried out in air for ~ 40 minutes following sulfidation. The ideal course for regeneration of the sorbent (without considering composition of the product gas) was the formation of copper oxide directly from the sulfide via the reactions



followed by the solid-state reaction,



The CuO:CuAl₂O₄ ratio will, of course, depend on the regeneration temperature. Production of SO₂ in reactions 5.5 and 5.6, however, can lead to the simultaneous formation of sulfate by the following side reaction:



Isothermal regeneration of sulfided 72-1-CA at 600°C, 700°C, 800°C, and 900°C is included in Figure 5.5. Regeneration at 600°C is rapid and yields both CuO and a significant fraction of CuSO₄ (corresponding to about one-third of the copper), which decomposes slowly. At 700°C, less sulfate is formed (about 8% of the copper) and decomposition is rapid. At 800°C and 900°C, there is no evidence of sulfate formation during regeneration. XRD analysis shows a higher content of CuAl₂O₄ in the regenerated as compared to the fresh sorbent, in keeping with the fact that the regeneration temperatures are greater than the calcination temperature (550°C) used in sorbent preparation. The sample regenerated at 900°C contained some crystalline CuAlO₂ in disagreement with reported thermodynamic data [16]. The implication is that CuAl₂O₄ formed through CuAlO₂ as an intermediate during regeneration, and that sintering of CuAl₂O₄ prevented complete oxidation of CuAlO₂ to CuAl₂O₄. Independent experiments have provided evidence for sintering of CuAl₂O₄ at temperatures in excess of 700°C (Chapter III, Sections 3.3.1 and 3.4).

5.4.3 Sulfur Chemisorption on Alumina

The sulfidation curves of Figure 5.5 pose a contradiction: Weight gain exceeds $W_N=1.1$, but $W_N=1.1$ corresponds to complete conversion of copper to Cu_9S_5 , which is the most sulfur-rich form of the only sulfide product identified by XRD. One possible explanation is that the alumina component of the sorbent contributes directly to sulfur retention.

To test the role of alumina during sulfidation, a sample of pure Al_2O_3 (prepared by the citrate process using calcination at $550^\circ C$) was exposed to isothermal reduction and sulfidation at different temperatures (Figure 5.7) as in the case of sample 72-1-CA (Figure 5.5). The final weight (W_f) used in the expression for W_N in Figure 5.7 was determined experimentally in a separate TPR experiment [17]. During sulfidation, the alumina showed significant weight gain, which increased with temperature. Reduction and sulfidation in succession of an empty platinum pan at $700^\circ C$ and $800^\circ C$, however, revealed no weight change; thus, chemisorption of sulfur on the platinum pan or formation of platinum sulfides was negligible. Since alumina is inert to sulfidation, these observations indicated the adsorption of a sulfur-containing species on alumina. In an attempt to eliminate the adsorbing species, the experiments for pure Al_2O_3 were repeated using a quartz boat in place of the standard platinum pan. While reduction was accompanied by a small weight loss as previously, subsequent sulfidation produced a flat profile indicative of no chemisorption on alumina. It has been reported that H_2S irreversibly adsorbs on $\gamma-Al_2O_3$; however, the quantity irreversibly adsorbed was small enough to be beyond detection by gravimetric analysis [18]. Therefore, the platinum pan is proposed to have catalyzed the decomposition of H_2S to elemental sulfur which, in turn, chemisorbed readily on alumina. This conclusion is supported by the well-known catalytic activity

of platinum in H_2S decomposition [19-21].

5.5 TGA Experiments in the Absence of Sulfur Deposition

5.5.1 Reduction and Sulfidation Experiments

Consecutive reduction and sulfidation of samples were repeated at 700°C and 800°C using a quartz boat in place of the standard platinum pan to eliminate the influence of sulfur chemisorption on alumina during sulfidation. While the basic trends of the weight cycle were similar to those observed with the platinum pan, the weight excursion above $W_N = 1$ is drastically reduced. It will be recalled that this weight excursion was significant only for the alumina-containing samples. With both the quartz and platinum pans, the weight gain following sulfidation increased with temperature. But in contrast to what was observed with the platinum pan, the weight gain during sulfidation was higher for pure CuO than for the alumina-containing sorbents (Figures 5.8 and 5.9).

Low digenite ($\text{Cu}_{9+x}\text{S}_5$) was again identified by XRD in cooled samples, suggesting that high digenite was the major sulfidation product at 700°C and 800°C (Figure 5.10) for all three samples. In addition, a large quantity of unreacted CuAl_2O_4 was identified in sample 33-1-CA6 after sulfidation at 700°C . This observation was consistent with the extent of reduction to metallic copper which, at 700°C , is nearly 100% for both 72-1-CA and 11-1-CA3, but only 70% for 33-1-CA6 (Figure 5.8). Copper oxide, CuO , and products of reduction, Cu_2O , CuAlO_2 , and Cu , were not identified at the end of sulfidation. Evidently, these compounds react more rapidly with H_2S to form the sulfide $\text{Cu}_{9+x}\text{S}_5$ than does CuAl_2O_4 . In a separate study [18], it was found that CoAl_2O_4 was unsulfidable at 400°C , and this stability was correlated to the presence of Co^{+2} in

tetrahedral sites. Both CoAl_2O_4 and CuAl_2O_4 possess spinel structures; however, the distribution of cations in each compound is different. CoAl_2O_4 is a normal spinel, with Co^{+2} occupying tetrahedral sites and Al^{+3} occupying octahedral sites [22], while CuAl_2O_4 is a partially inverse spinel with Cu^{+2} occupying both tetrahedral (tet) and octahedral (oct) sites such that $x=0.4$ in the formula $[\text{Cu}_{1-x}\text{Al}_x]_{\text{tet}}[\text{Cu}_x\text{Al}_{2-x}]_{\text{oct}}\text{O}_4$. Since CoAl_2O_4 with 100% of Co^{+2} occupying tetrahedral sites was found to be unsulfidable at 400°C , and CuAl_2O_4 with 60% of Cu^{+2} occupying tetrahedral sites was found to sulfide slowly at 800°C , tetrahedrally coordinated divalent cations indeed appear to be resistant to sulfidation by H_2S .

The XRD patterns of sulfided 33-1-CA6 reveal that the peaks of CuAl_2O_4 are about twice as intense as those of $\text{Cu}_{9+x}\text{S}_5$. In view of the sharpness of these peaks, the intensities are approximately proportional to the content of the crystalline compounds. Comparing the weight loss during reduction with the weight gain during sulfidation (Figure 5.8), however, shows that the content of the sulfide is actually higher than the content of unreacted CuAl_2O_4 . Thus, the XRD intensity relations can be explained only by assuming that the sulfide is predominantly in an amorphous state or a microcrystalline (*i.e.*, $\leq 50\text{\AA}$) state as opposed to a crystalline form. Furthermore, the XRD intensities for $\text{Cu}_{9+x}\text{S}_5$ formed by sulfidation of 11-1-CA3 are 2 to 3 times greater than those for $\text{Cu}_{9+x}\text{S}_5$ formed by sulfidation of alumina-containing samples, suggesting that a high fraction of copper sulfided in the presence of alumina forms amorphous or microcrystalline sulfide.

The scanning electron micrographs (Figures 5.6 and 5.11) of sulfided alumina-containing samples (sulfided 72-1-CA and 33-1-CA6) show large (2 to 6 μm), octahedral crystals, and small ($< 0.3\mu\text{m}$), irregular crystallites of $\text{Cu}_{9+x}\text{S}_5$.

The scanning electron micrographs (Figure 5.12) of sulfided CuO (sulfided 11-1-CA3), however, show exclusively large (8 to 16 μm) crystals of sulfide. Apparently, the presence of alumina hinders crystallite growth of digenite ($\text{Cu}_{9+x}\text{S}_5$). Furthermore, the bimodal dispersion of $\text{Cu}_{9+x}\text{S}_5$ in alumina-containing samples is consistent with the previous conclusion that the sulfide is present in both amorphous and crystalline forms. The sulfided CuO sample, on the other hand, is well crystallized as evidenced both by sharp, high-intensity peaks in XRD patterns and large crystals in scanning electron micrographs. The presence of alumina also plays a role in the weight attained following sulfidation at 700°C (Figure 5.8). While 11-1-CA3 sulfided at 700°C approaches a final weight $W_N = 1.1$, the alumina-containing samples (72-1-CA and 33-1-CA6) approach final weights $W_N < 1$. This means that reduction and sulfidation of 11-1-CA3 at 700°C results in nearly complete conversion to digenite ($\text{Cu}_{9+x}\text{S}_5$) while for 72-1-CA and 33-1-CA6 conversion is partial, leaving behind the unreacted reduction intermediates Cu, Cu_2O , and CuAlO_2 . These reduction intermediates are not identified by x-ray diffraction, suggesting that they must be present as a fine dispersion ($< 50 \text{ \AA}$ crystallites). An attempt was made to identify these reduction intermediates by x-ray photoelectron spectroscopy; however, extensive charging that was due to the presence of alumina rendered the technique futile. It is possible that the reduction intermediates are hindered against sulfidation because of association with alumina. A similar effect was observed for a certain fraction of CuO during reduction of these sorbents.

The effect of the extent of reduction on the kinetics of sulfidation was investigated to obtain additional mechanistic information. Sample 72-1-CA was exposed to 5% H_2 in N_2 for a time, t_R , and then the 5% H_2 in N_2 gas mixture was replaced by a 4.2% H_2S in N_2 mixture. Experiments were performed

using different values of t_R , which created samples with different conversions of Cu^{+2} to Cu^0 , α_R , for subsequent sulfidation. A temperature of 400°C was maintained because it was less than 550°C , the calcination temperature used in preparing sample 72-1-CA; therefore, physicochemical changes to the sample, which were due to processes other than the reactions of interest, were eliminated. The maximum rate of sulfidation achieved decreased with decreasing α_R for $0.37 < \alpha_R \leq 1$, and was constant for $\alpha_R \leq 0.37$ (Figure 5.13). To interpret these data, the small amount of CuAl_2O_4 (~ 5 mole %) present in the sample was neglected because reduction kinetics and sulfidation kinetics for this component were anticipated to be much slower than for CuO , based on previous results. Furthermore, CuO , Cu , and Al_2O_3 were assumed to be the only components present following reduction of the sample because Cu_2O was not identified by XRD analysis of partially reduced samples (Figure 3.11). Since XRD of the samples sulfided here revealed digenite as the only crystalline phase, both Cu and CuO were sulfidable at 400°C . The large sulfidation rate observed for a completely reduced sample was due to the sulfidation of Cu . The intermediate sulfidation rate observed for a sample with $\alpha_R=0.67$ was due to the sulfidation of a smaller fraction of Cu combined with the sulfidation of a more slowly reacting CuO phase. For example, the maximum reaction rates for the reduction of CuO in samples containing between 0 and 100 mole% CuO initially were $\sim 0.056 \text{ min}^{-1}$ for a sample containing 100 mole% CuO , $\sim 0.026 \text{ min}^{-1}$ for samples containing between 26 and 47.5 mole% CuO , and $\sim 0.007 \text{ min}^{-1}$ for a sample containing 10 mole% CuO . The constant maximum rate of sulfidation observed for conversions of $\alpha_R \leq 0.37$ was due to control of the maximum rate of sulfidation by the sulfidation of CuO . Since the maximum rate of sulfidation attributed to Cu was only 32% higher than that attributed to CuO , the slower

sulfidation kinetics of CuO was due to mass-transfer limitations caused by larger particles and a lower dispersion for CuO as compared to Cu in the sample.

5.5.2 Regeneration Experiments

Sulfate formation during regeneration was found to depend on the alumina content of the sorbents. Regeneration of sorbent 11-1-CA3 (no alumina) yielded sulfate at 600°C (14% of the copper) but not at 700°C. By contrast, regeneration of the alumina-containing sorbents 72-1-CA and 33-1-CA6 yielded sulfate at both 600 and 700°C (Figures 5.8a and 5.8c), and the amount of sulfate was higher for sorbent 72-1-CA, which has the larger content of alumina. Moreover, a 1:1 mechanical mixture of γ -Al₂O₃ to 11-1-CA3 (pure CuO) by mass produced sulfate at 700°C, implying that alumina-chemisorbed SO₂ produced by reaction 5.5, and the SO₂ then migrated and spilled over onto CuO to form sulfate by reaction 5.8. The presence of alumina as discrete particles caused sulfate formation by sample 11-1-CA3 at 700°C, which suggests a high mobility of SO₂ on the alumina surface.

A related observation concerning the role of alumina can be made by comparing sulfate formation in experiments using a quartz pan to that in experiments using a platinum pan. For both sorbents, 72-1-CA and 33-1-CA6, more sulfate is formed with the quartz pan (Figures 5.8a, 5.8c, 5.9a, 5.9c). We have no convincing explanation for this behavior although it is possible that the sulfur chemisorbed on alumina during sulfidation in the presence of the platinum pan may hinder the catalytic role of alumina in sulfate formation. In particular, if chemisorption of SO₂ to alumina is the key to the formation of sulfate as suggested above, then the presence of chemisorbed sulfur reduces the number of sites available for chemisorption of SO₂.

The ratio of CuO to CuAl₂O₄ in the regenerated 33-1-CA6 and 72-1-CA materials depends, as expected, on the regeneration temperature. In the case of 33-1-CA6, the content of CuAl₂O₄ is less than that in the original sample, while for sample 72-1-CA, the content of CuAl₂O₄ is higher than in the original sample. The difference in chemical composition between regenerated and fresh materials is easily explained by the different calcination and regeneration temperatures.

5.5.3 Reduction and Sulfidation of Cu-Al-O Pellets

Mixed copper-aluminum oxide was prepared in the form of an extrusion by Miretta Flytzani-Stephanopoulos of M.I.T. [23]. The mixed oxide was synthesized by the citrate process with calcination at 700°C for 5 hours. Following calcination, the sample was crushed to a fine powder, and mixed with 5 wt% bentonite in dry form. A paste was then prepared by adding de-ionized water, formic acid (diluted to $\geq 10^{-3}$ moles/l, pH=1.7), aluminum formate (diluted to 0.05 moles/l), or formic acid and aluminum formate. The paste was extruded through a die containing $\frac{1}{8}$ th inch holes, and the moist cylindrical strands were dried in an oven at 120°C for 16 hours under air flow. The dried strands were cut into pellets of ~ 0.025 inch in length, and calcined in air at 850°C for 5 hours.

Scanning electron micrographs of partially reacted pellets showed some of the same features observed for bulk powders. A single pellet, after exposure to reaction conditions in the TGA, was cooled to room temperature under the reactant-gas mixture, and then snapped in half so that the pellet cross section could be viewed by a scanning electron microscope. A pellet, partially reduced to a conversion of 79% at 700°C, showed regions containing individual

clumps of metallic copper (Figure 5.12c) as seen in reduced samples of 33-1-CA6 (Figure 5.11b) and 72-1-CA (Figure 5.6b). Similarly, a pellet, reduced to a conversion of 76% followed by sulfidation at 700°C, showed crystals of digenite (Figure 5.12d) scattered about, of the same morphology as observed for samples 33-1-CA6 (Figure 5.11c,d) and 72-1-CA (Figure 5.6c,d). Micrographs a and b of Figure 5.14 gave a perspective of the large channels present in reduced and sulfided forms of the pellet with the outer edge of the pellet visible in micrograph b. The same types of channels were observed in fresh pellets (micrographs not shown), suggesting preservation of the channel network during reduction and sulfidation. Micrographs c and d of Figure 5.14 are enlargements of regions of micrograph b, revealing the copper sulfide crystals that have preferentially formed along the inner channels and outer surfaces of the sulfided pellet.

The effect of repeated reduction-sulfidation-regeneration cycles on reaction rates was examined for the pellets at temperatures of 700°C and 725°C. A typical cycle involved reduction with 5% H₂ in N₂ for the first ~ 10 minutes, sulfidation with 4.2% H₂S in N₂ for the next ~ 30 minutes, and regeneration with air for the next ~ 20 minutes. Three cycles were performed at each temperature in which the pellet was crushed to a fine powder prior to the third and final cycle. Profiles of normalized weight, W_N ($W_N = 1 - \alpha$ where α is the conversion of Cu⁺² to Cu^o), showed an increase in the conversion during reduction, α_R ($\alpha_R = \alpha$), but a decrease in the conversion during sulfidation, α_S ($\alpha_S = W_N(9 + x)/10.02$), from the first cycle to the second cycle (Figure 5.15). Crushing the pellet eliminated the internal mass transfer limitations to the gaseous reactant and products, and thus resulted in faster reaction rates during all three stages. In addition, the increase in α_R and decrease in α_S were much smaller between the second and third cycles than between the first and second cycles. The changes in α_S between

cycles were smaller at 725°C than at 700°C, and furthermore, a difference in conversions between the second and third cycles was undetectable at 725°C. The curves of Figure 5.16 revealed higher maximum rates of reduction (first peak) and sulfidation (second peak) at 725°C than at 700°C, and a larger difference in maximum rate between the crushed and intact pellet at 725°C than at 700°C. For example, for a temperature of 725°C, the sulfidation rate was 50% lower for the intact pellet as compared to the crushed pellet, and the reduction rate was 49% lower, while for a temperature of 700°C, the sulfidation rate was 88% lower, and the reduction rate was 75% lower.

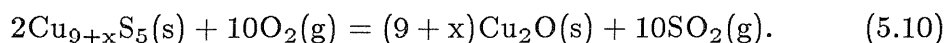
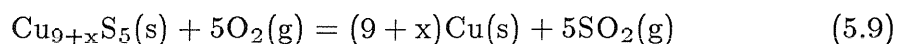
The decrease in α_S between the first and second cycles was not characteristic of a Cu-Al-O sorbent in a pelletized form, because an identical decrease in α_S was observed for a crushed pellet in a separate experiment. Furthermore, the decrease in α_S between the first and second cycles was not characteristic of a chemical interaction between CuO and Al₂O₃, because a similar decrease in α_S was observed for a mechanical mixture of sample 11-1-CA3 (pure CuO) and γ -Al₂O₃. Since sulfate was formed during regeneration in all cases, perhaps the reduction in α_S with repeated cycles was due to the presence of residual sulfate at the start of the next cycle (*i.e.*, the TGA was rezeroed and the sample mass reweighed between runs).

5.5.4 Simultaneous Reduction-Sulfidation

Figure 5.17 compares the step-wise reduction-sulfidation of pure CuO (sample 11-1-CA3) at 700°C and 800°C to the reaction of pure CuO with a gas mixture containing 13% H₂, 4% H₂S, and balance N₂. For a temperature of 700°C, the initial portion of the simultaneous reduction-sulfidation curve decreases at a slower rate than the reduction stage of the step-wise curve because

of the simultaneous sulfidation accompanying reduction. Similarly, the upward sloping portion of the simultaneous reduction-sulfidation curve increases at a slower rate than the sulfidation stage of the step-wise curve, presumably because of continued reduction accompanying sulfidation. A lower value of W_N is attained at a time of 30 minutes for reaction with an H_2 - H_2S mixture as compared to reaction in separate stages, implying that either unsulfided Cu in the former case, or the product sulfide, $Cu_{9+x}S_5$, contains a different stoichiometry (*i.e.*, different value of x) in each case. For reaction in separate stages, a value $W_N = 1.06$ is attained after 30 minutes and implies that $x=0.45$ in the product sulfide, $Cu_{9+x}S_5$, assuming complete sulfidation of copper. If it is assumed that $x=0.45$ for the product sulfide that is formed by the reaction of 11-1-CA3 with an H_2 - H_2S mixture, then 4 mole% of the total copper is present as unreacted metallic copper after 30 minutes. Alternatively, if it is assumed that copper is completely sulfided after 30 minutes of reaction with an H_2 - H_2S mixture, then $x=0.82$ in the product sulfide (corresponding to $W_N=1.02$). The same general features are observed for a temperature of $800^\circ C$, except that the indicated differences between step-wise and simultaneous reduction-sulfidation are less than those observed for a temperature of $700^\circ C$.

The attainment of a lower value of W_N during air regeneration of the sample exposed to an H_2 - H_2S mixture as compared to air regeneration of the sample exposed to step-wise reduction and sulfidation suggests the existence of product sulfides with different stoichiometries. For example, the initial weight loss during air regeneration is due to the following reactions:



The subsequent increase in weight during regeneration is due to the oxidation of Cu and Cu_2O to CuO . Assuming that only reaction 5.9 occurs at the onset of regeneration, more weight loss per mole of copper occurs for $x=0.82$ than for $x=0.452$.

Samples 72-1-CA (contains 5 mole % CuAl_2O_4 , Figure 5.18) and 33-1-CA6 (contains 96 mole % CuAl_2O_4 , Figure 5.19) exhibited the same differences as sample 11-1-CA3 (pure CuO) between step-wise and simultaneous reduction-sulfidation. Time trajectories of the rates of reduction (first peak) and rates of sulfidation (second peak) for samples 72-1-CA, 33-1-CA6, and 11-1-CA3 are shown in Figures 5.20 and 5.21 for temperatures of 700°C and 800°C . The solid curves correspond to step-wise reduction-sulfidation, while the dashed curves correspond to simultaneous reduction-sulfidation. For step-wise reduction-sulfidation at both temperatures, maximum rates of both reduction and sulfidation are highest for sample 72-1-CA, and lowest for sample 11-1-CA3. This difference is attributed to sintering of copper, which occurs in sample 11-1-CA3 but is absent in sample 72-1-CA, in agreement with independent experiments (Chapter III, Section 3.3.2). The intermediate reduction and sulfidation rates exhibited by sample 33-1-CA6 are due to the slower reduction and sulfidation kinetics of CuAl_2O_4 as compared to CuO . The largest discrepancy between the maximum rate of sulfidation for consecutive reduction-sulfidation and simultaneous reduction-sulfidation is observed for sample 33-1-CA6 for a temperature of 700°C , while the smallest discrepancy is observed for sample 11-1-CA3 at both 700°C and 800°C (Table 5.2), suggesting that CuO is more sulfidable than CuAl_2O_4 .

REFERENCES

1. Marqueen, T.J., Carbone, D.J., and Ligammari, J., "Coal Gasification Combined Cycle Systems—Technical Horizons," *Proc. Amer. Power Conf.*, **48**, 235, 1986.
2. MERC Hot Gas Cleanup Task Force, "Chemistry of Hot Gas Cleanup in Coal Gasification and Combustion," Final Report (MERC/SP 78/2, February, 1978).
3. Tamhankar, S.S., Bagajewicz, M., Gavalas, G.R., Sharma, P.K., and Flytzani-Stephanopoulos, M., "Mixed-Oxide Sorbents for High-Temperature Removal of Hydrogen Sulfide," *IEEG Proc. Des. Develop.*, **25**, 429, 1986.
4. Flytzani-Stephanopoulos, M., Tamhankar, S.S., Gavalas, G.R., Bagajewicz, M.J., and Sharma, P.K., "High-Temperature Regenerative Removal of H_2S by Porous Mixed Oxide Sorbents," *Prepr. Pap. Amer. Chem. Soc., Div. Fuel Chem.*, **30**(4), 16, 1985.
5. Ruth, L.A., Squires, A.M., and Graff, R.A., "Desulfurization of Fuels with Half-Calcined Dolomite: First Kinetic Data," *Environ. Sci. Technol.*, **6**(12), 1009, 1972.
6. Patrick, V., and Gavalas, G.R., "Structure and Reduction of Mixed Copper-Aluminum Oxides," accepted for publication in *J. Amer. Cer. Soc.*
7. Puxley, D.C., Kitchener, C., Parkyns, N.D., and Komodromas, C., "The Effect of Preparation Methods on the Structure, Stability, and Metal Support Interactions in Nickel/Alumina Catalysts," in *Preparation of Catalysts III* ed. by G. Poncelet, P. Grange, and P.A. Jacobs (Elsevier Science Publishers B.V.: Amsterdam, 1983), p.237.
8. Friedman, R.M., and Freeman, J.J., "Characterization of Cu/Al_2O_3 Cata-

- lysts," *J. Catal.*, **55**, 10, 1978.
9. Strohmeier, B.R., Leyden, D.E., Field, R.S., and Hercules, D.M., "Surface Spectroscopic Characterization of Cu/Al₂O₃ Catalysts," *J. Catal.*, **94**, 514, 1985.
 10. Donnay, G., Donnay, J.D.H., and Kullerud, G., "Crystal and Twin Structure of Digenite, Cu₉S₅," *Amer. Mineral.*, **43**, 228, 1958.
 11. Craig, J.R., "The Cu-S System," in *Sulfide Mineralogy* ed. by P.H. Ribbe (Southern Printing Co.: Virginia, 1974), **1**, p. CS-58.
 12. Roseboom, E.H., Jr., "An Investigation of the System Cu-S and Some Natural Copper Sulfides Between 25°C and 700°C," *Econ. Geol.*, **61**(4), 641, 1966.
 13. Morimoto, N., and Kullerud, G., "Polymorphism in Digenite," *Amer. Mineral.*, **48**, 110, 1963.
 14. Morimoto, N., and Koto, K., "Phase Relations of the Cu-S System at Low Temperatures: Stability of Anilite," *Amer. Mineral.*, **55**, 106, 1970.
 15. Morimoto, N., and Gyobu, A., "The Composition and Stability of Digenite," *Amer. Mineral.*, **56**, 1889, 1971.
 16. Jacob, K.T., and Alcock, C.B., "Thermodynamics of CuAlO₂ and CuAl₂O₄ and Phase Equilibria in the System Cu₂O-CuO-Al₂O₃," *J. Amer. Cer. Soc.*, **58**(5-6), 192, 1974.
 17. Thomas, R., deBeer, V.H.J., and Moulijn, J.A., "A Temperature Programmed Reduction Study of γ -Al₂O₃ Supported Molybdenum and Tungsten Oxide," *Bull. Soc. Chim. Belg.*, **90**(12), 1349, 1981.
 18. Chung, K.S., and Massoth, F.E., "Studies on Molybdenum-Alumina Catalysts VIII. Effect of Cobalt on Catalyst Sulfiding," *J. Catal.*, **64**, 332, 1980.
 19. Fukuda, K., Dokiya, M., Kameyama, T., and Kotera, Y., *Ind. Engng.*

- Chem. Fundam.*, **17**, 243, 1978.
20. Worell, W.L., and Kaplan, H.I., *Heterogeneous Kinetics at Elevated Temperatures* (Plenum Press: New York, 1979), p.113.
 21. Bartholomew, C.H., and Agrawal, P.K., "Sulfur Poisoning of Metals," *Adv. Catal.*, **31**, 135, 1982.
 22. Navrotsky, A., and Kleppa, O.J., "Thermodynamics of Formation of Simple Spinels," *J. Inorg. Nucl. Chem.*, **30**, 479, 1968.
 23. Flytzani-Stephanopoulos, M., Gavalas, G.R., Jothimurugesan, K., Lew, S., Sharma, P.K., Bagajewicz, M.J., and Patrick, V., "Detailed Studies of Novel Regenerable Sorbents for High-Temperature Coal-Gas Desulfurization," Final Report (DE-FC21-85MC22193, September, 1987).

Table 5.1: Fresh Cu-Al-O sorbents used for sulfidation-regeneration studies.

Sample	Mole % CuO:CuAl ₂ O ₄ :Al ₂ O ₃	BET Surface Area
72-1-CA	47.5:5:47.5	120 m ² /g
33-1-CA6	2:96:2	2.72 m ² /g
11-1-CA3	100:0:0	1.11 m ² /g

**Table 5.2: Maximum rates of reduction and sulfidation accompanying
Figures 5.21 and 5.22.**

Sample	Gaseous Feed	Temp. (°C)	r _{m,red} ^c (min ⁻¹)	r _{m,sulf} ^d (min ⁻¹)
72-1-CA	H ₂ -H ₂ S ^a	700	0.0443	0.0261
		800	0.0540	0.0322
	H ₂ then H ₂ S ^b	700	0.0923	0.0701
		800	0.0815	0.0697
33-1-CA6	H ₂ -H ₂ S	700	0.0254	0.0160
		800	0.0348	0.0273
	H ₂ then H ₂ S	700	0.0611	0.0519
		800	0.0664	0.0631
11-1-CA3	H ₂ -H ₂ S	700	0.0373	0.0245
		800	0.0432	0.0284
	H ₂ then H ₂ S	700	0.0537	0.0467
		800	0.0389	0.0324

^a A mixture of 13% H₂, 4% H₂S, and balance N₂.

^b First exposed to 5% H₂ in N₂, and then to 4% H₂S in N₂.

^c Maximum rate of reduction.

^d Maximum rate of sulfidation.

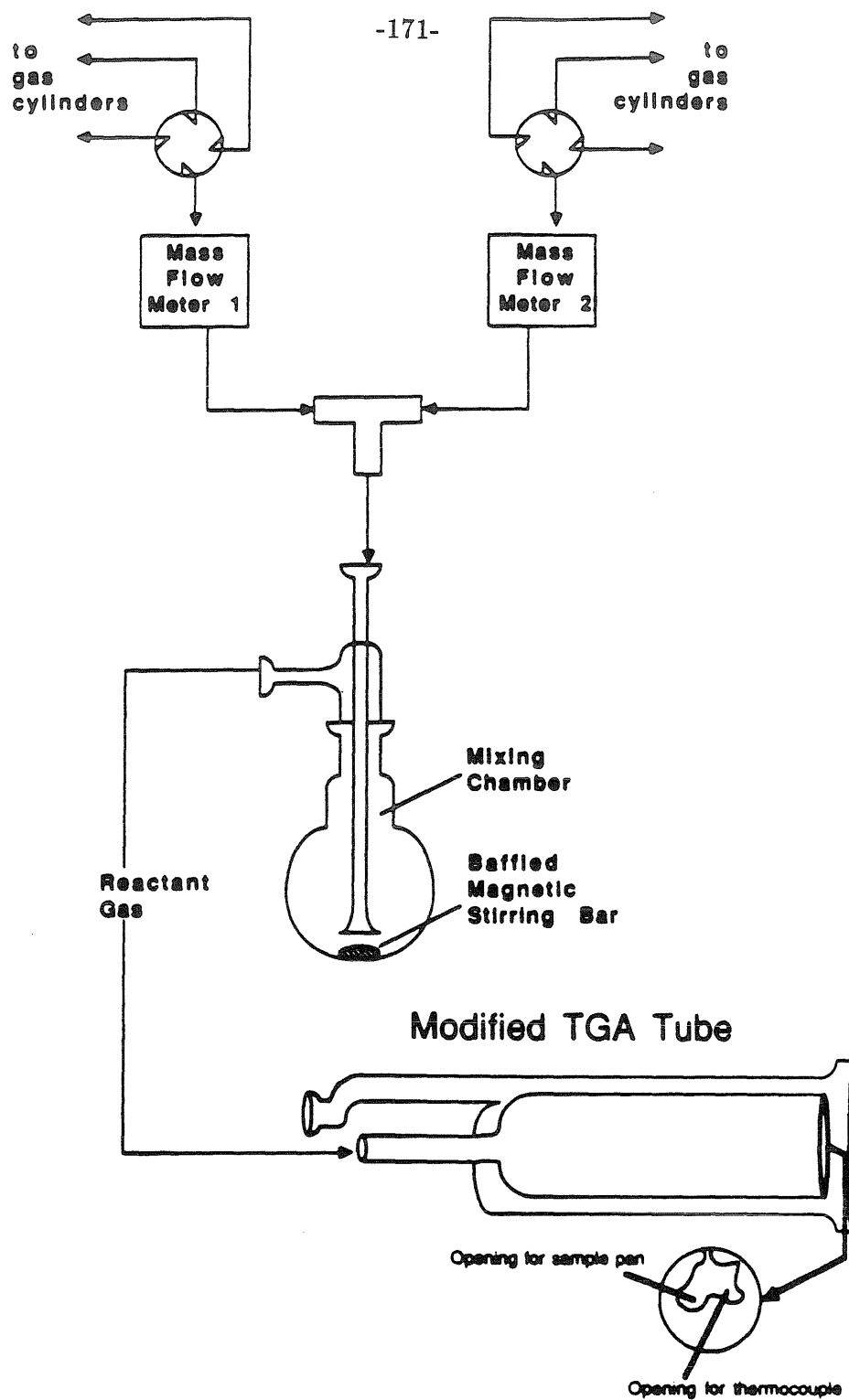


Figure 5.1: Schematic of the thermogravimetric system used for experiments requiring the use of corrosive gases, or of mixtures containing more than one reactive component, or both.

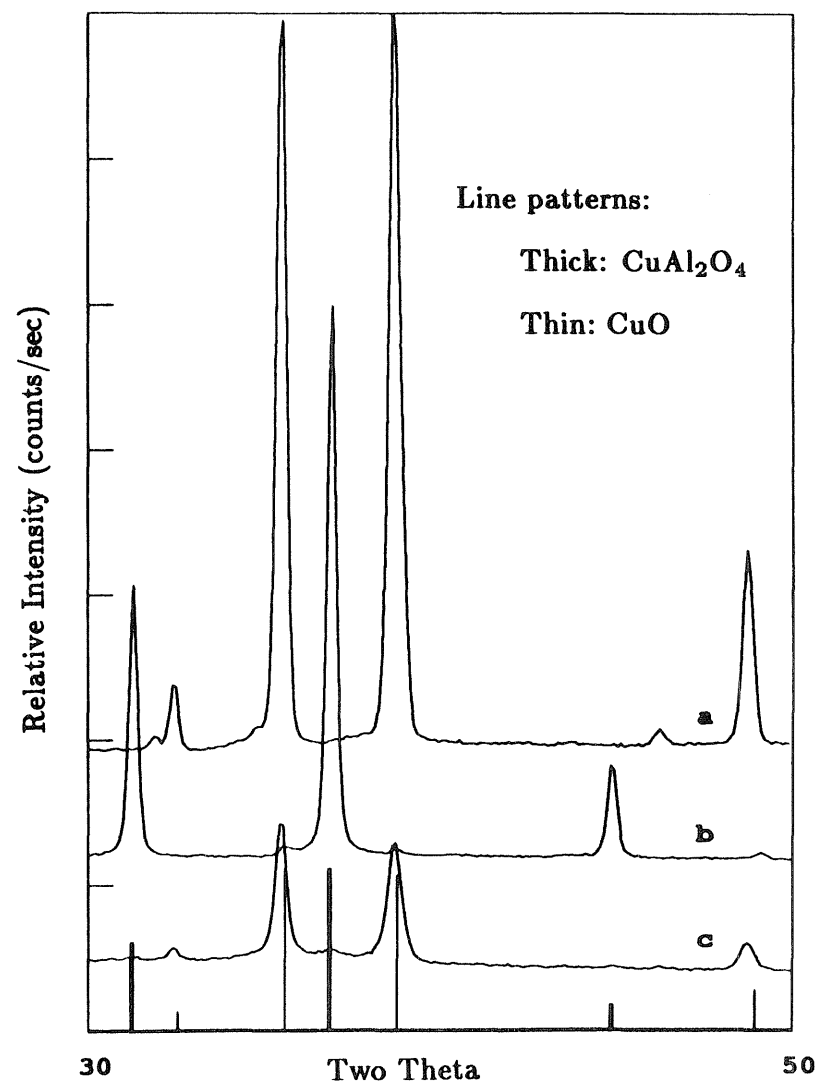
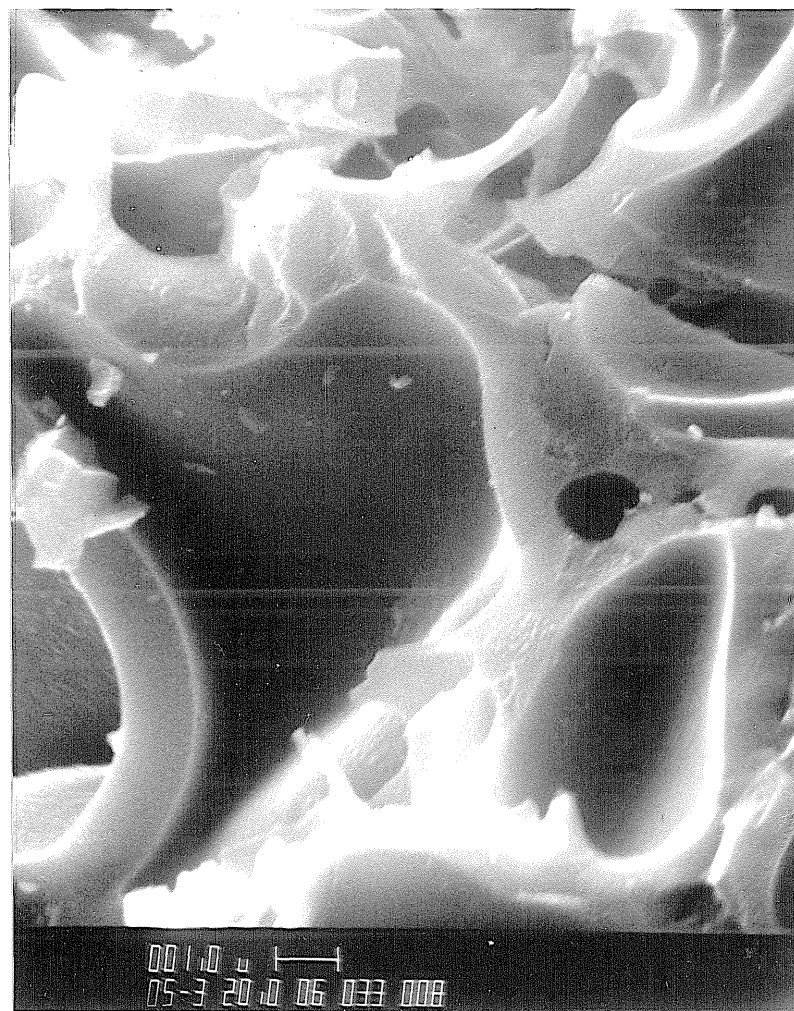


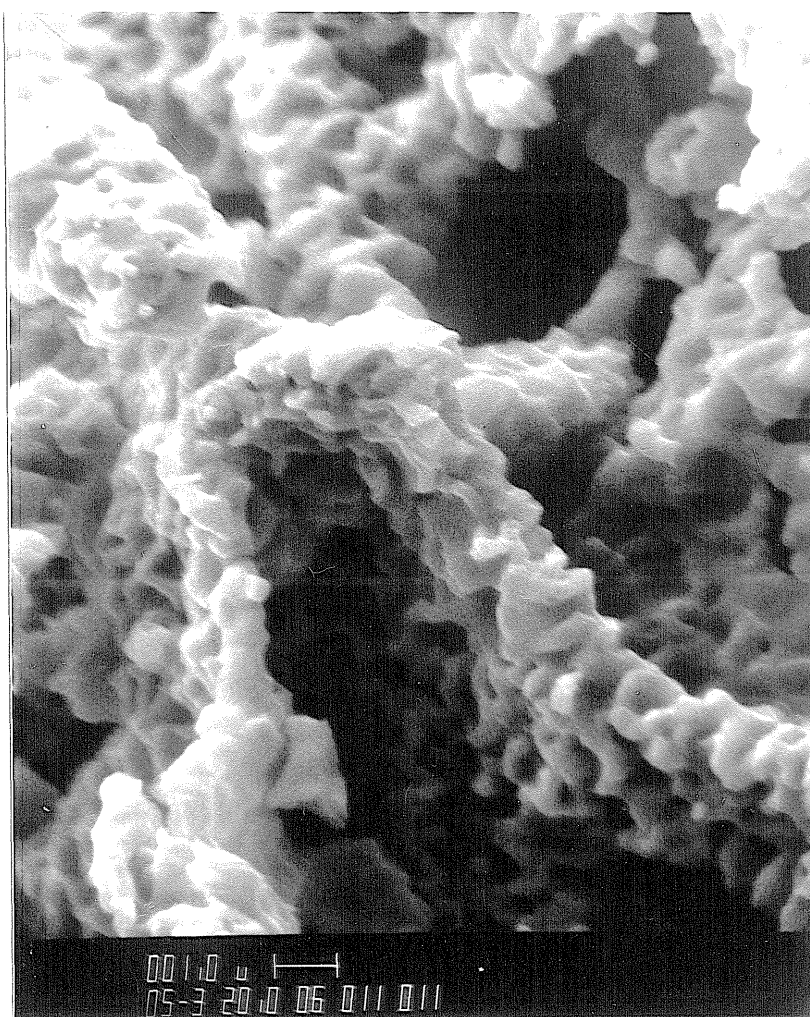
Figure 5.2: XRD patterns of samples 11-1-CA3 (a), 33-1-CA6 (b), and 72-1-CA (c).



(a) 72-1-CA at 5000×



(b) 33-1-CA6 at 5000×



(c) 11-1-CA3 at 5000×

Figure 5.3: Scanning electron micrographs (markers are 1 μ m) of fresh Cu-Al oxides prepared by the citrate process.

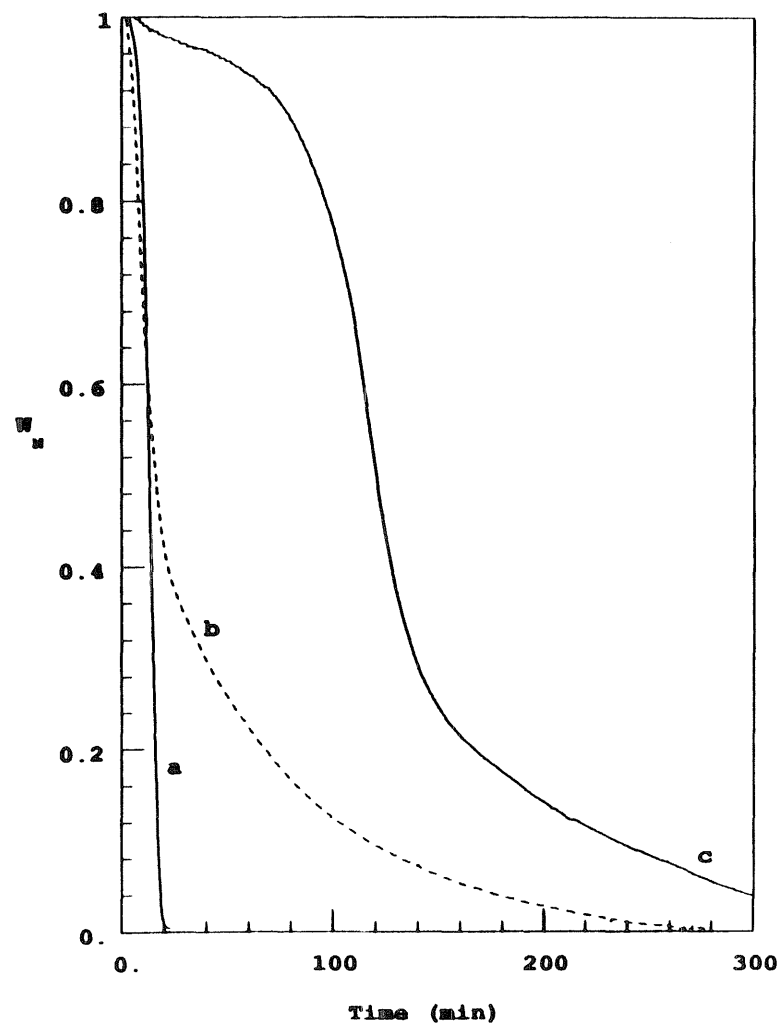


Figure 5.4: Normalized weight-loss curves for TPR of 11-1-CA3 (a), 72-1-CA (b), and 33-1-CA6 (c) using a heating rate of 1.7°C/min from 233°C to 912°C.

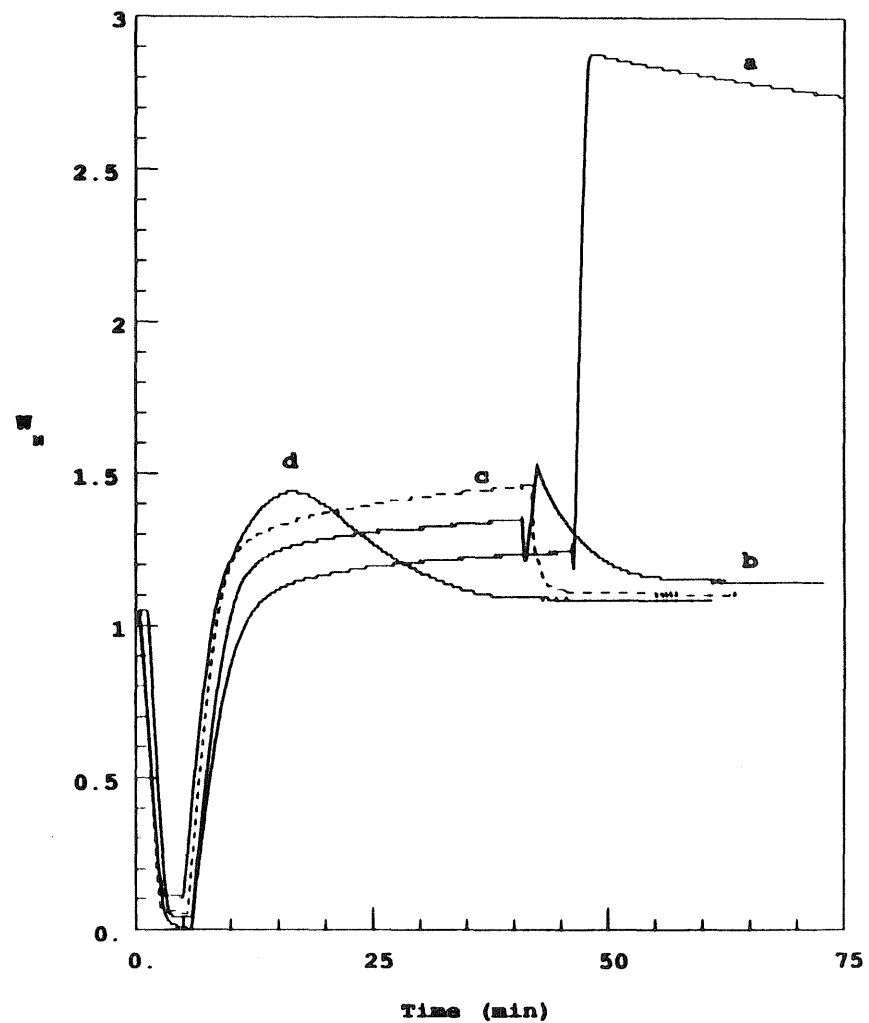
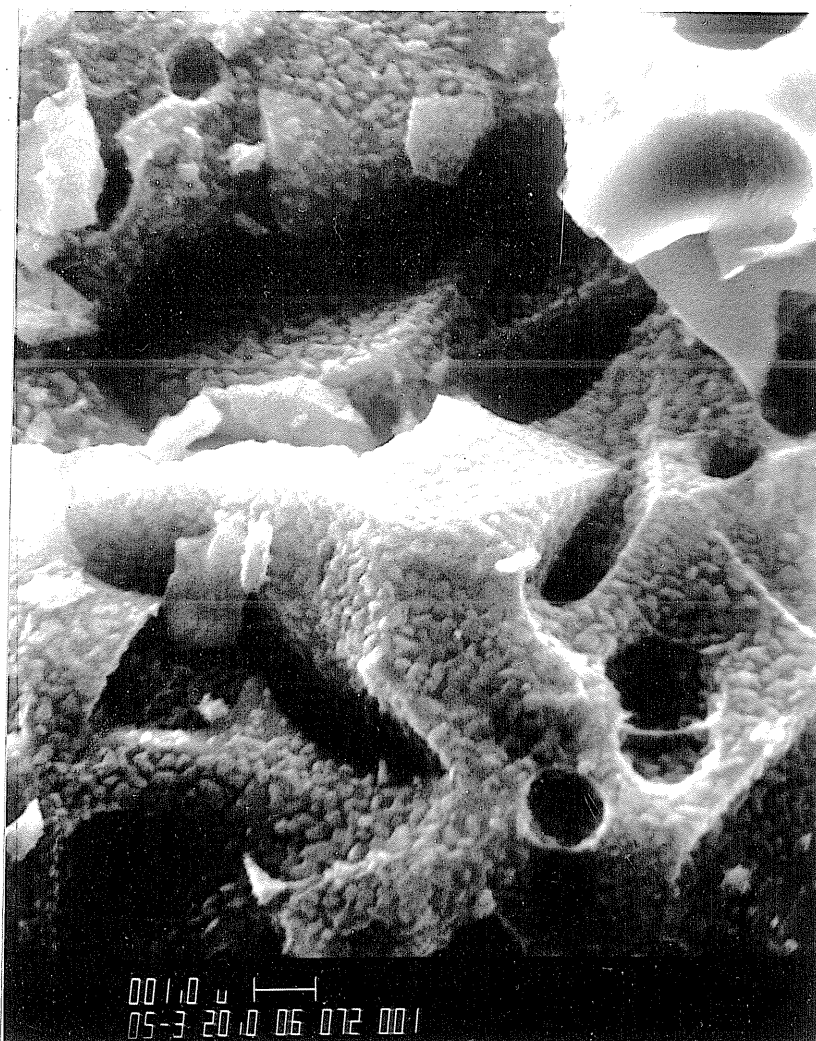
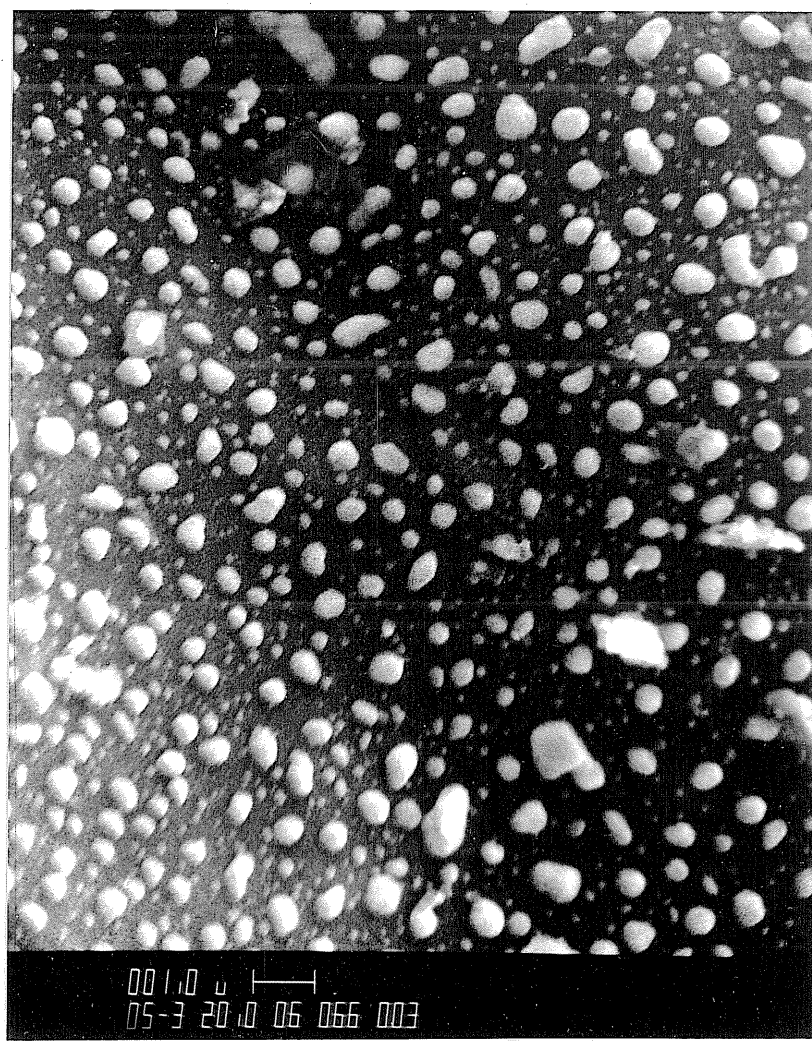


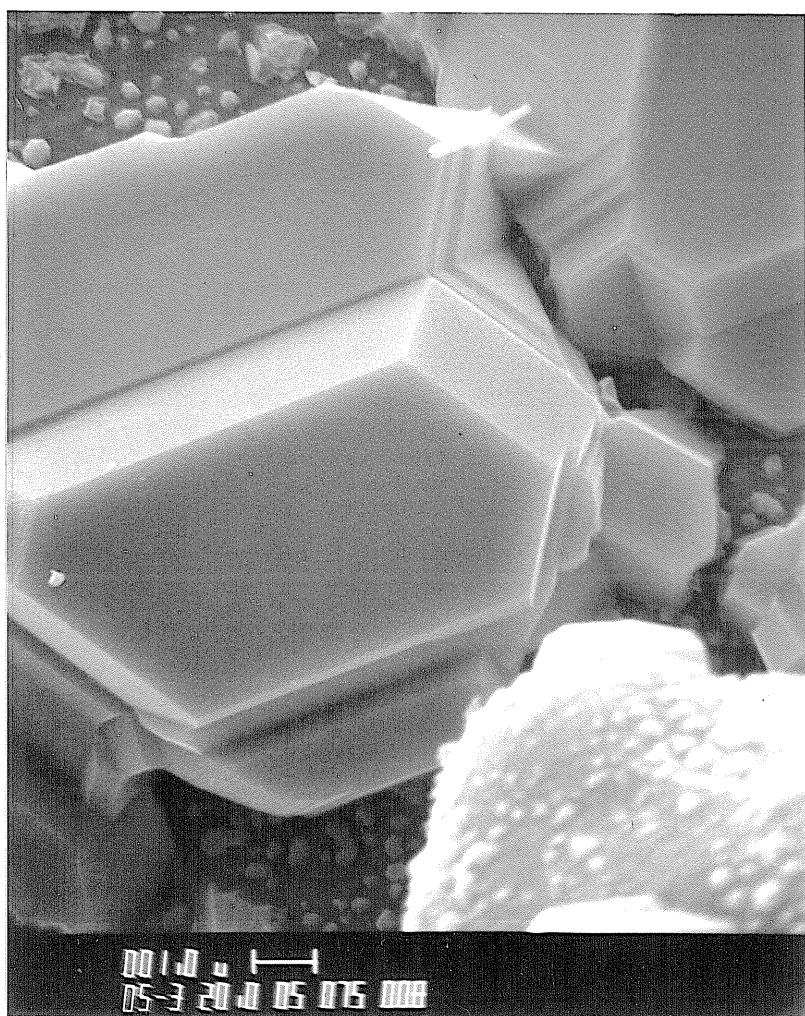
Figure 5.5: Normalized weight-loss curves for reduction, sulfidation, and air regeneration, in series, of sample 72-1-CA at 600°C (a), 700°C (b), 800°C (c), and 900°C (d).



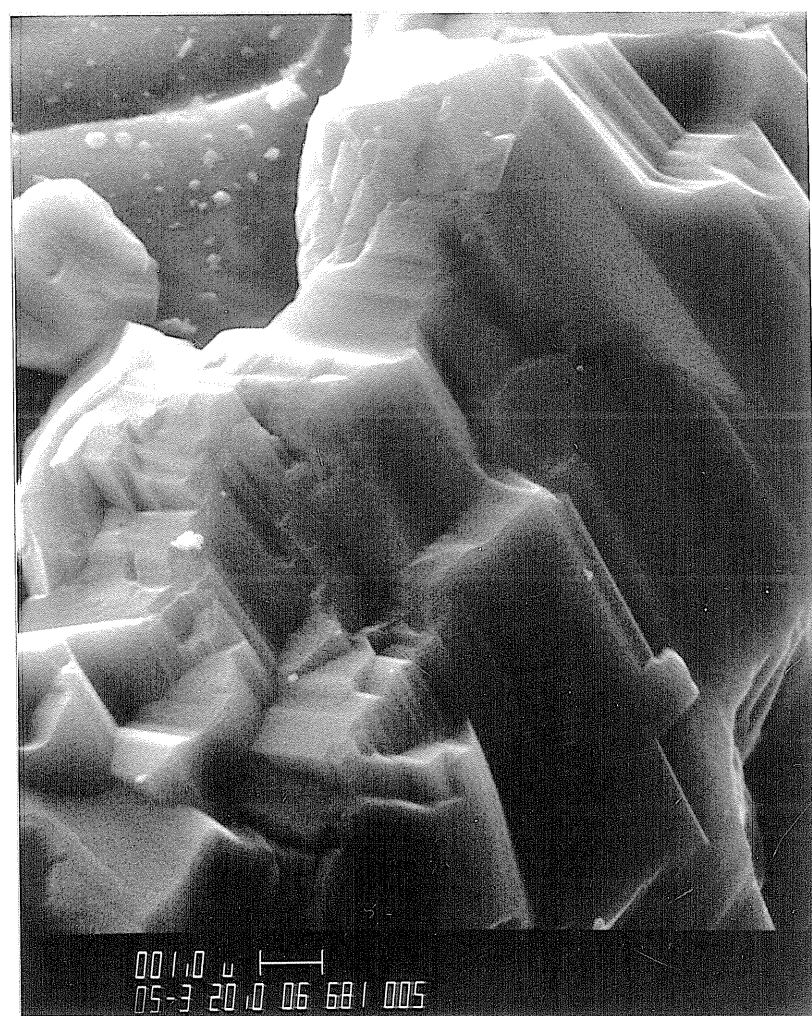
(a) Fresh at 5000×



(b) Reduced at 5000×



(c) Sulfided at 5000×



(d) Sulfided at 5000×

Figure 5.6: Scanning electron micrographs of sample 72-1-CA (markers are $1\mu\text{m}$) in a fresh state (a), after reduction at 700°C (b), and after step-wise reduction-sulfidation at 700°C in a platinum pan (c), and in a quartz pan (d).

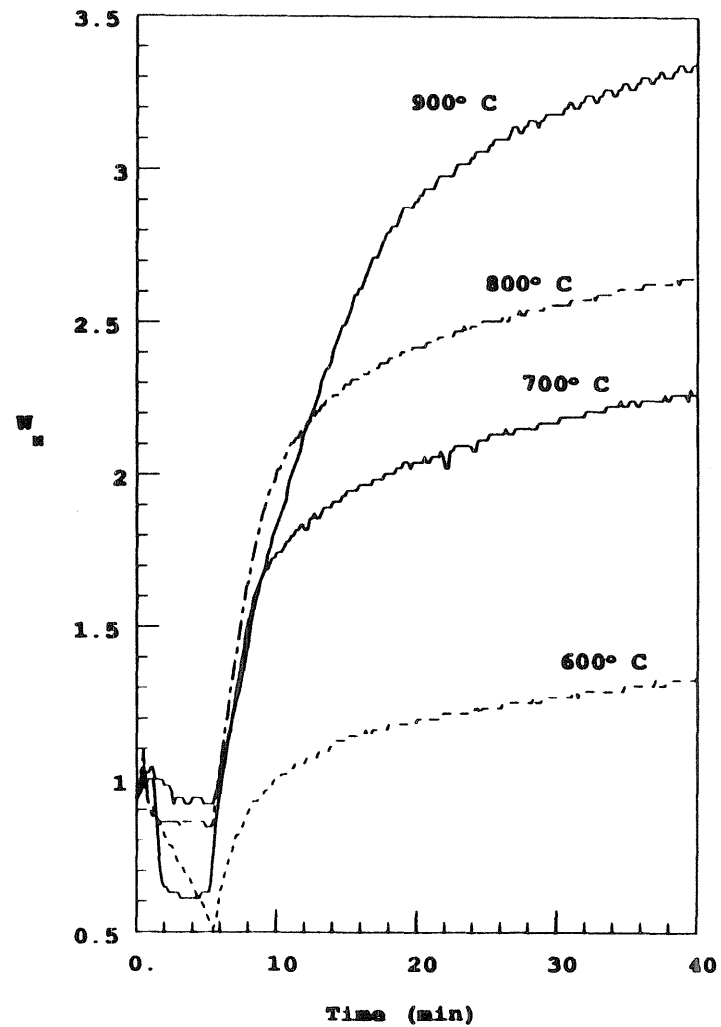


Figure 5.7: Normalized weight-loss curves for reduction followed by sulfidation of pure Al_2O_3 contained in a platinum pan at different temperatures.

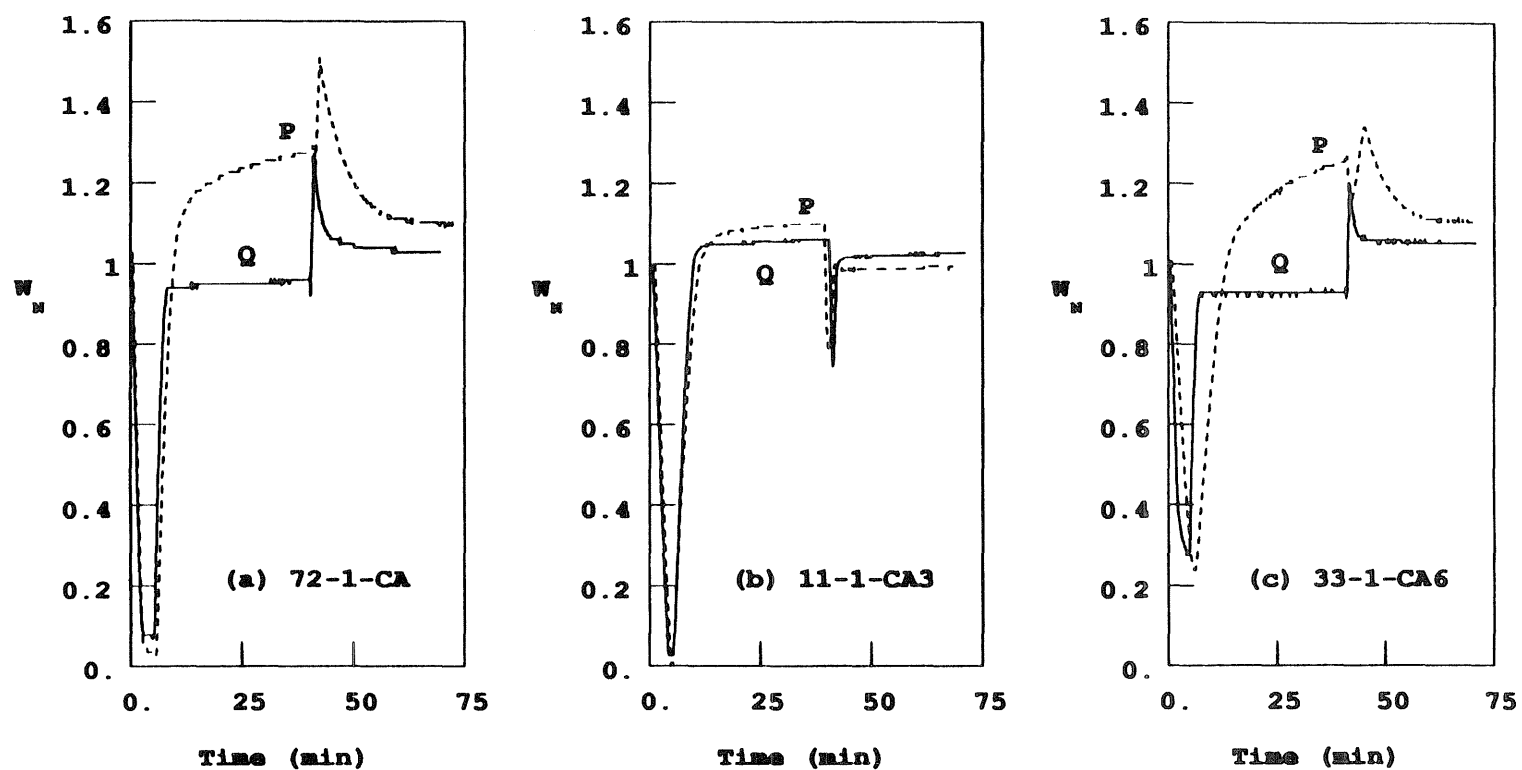


Figure 5.8: Normalized weight-loss curves for reduction, sulfidation, and regeneration, in series, of different samples at 700°C contained in a platinum (P) and a quartz (Q) pan.

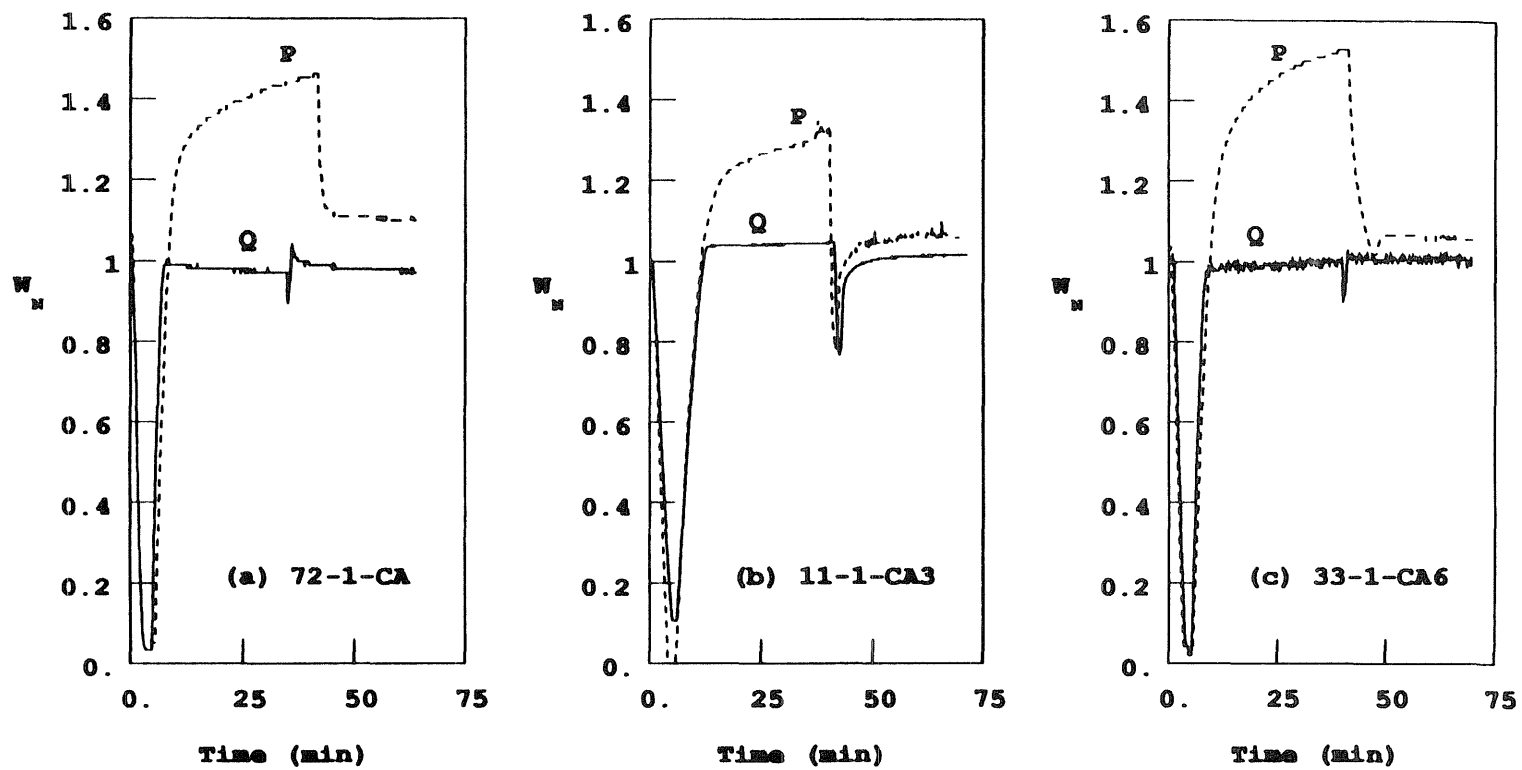


Figure 5.9: Normalized weight-loss curves for reduction, sulfidation, and regeneration, in series, of different samples at 800°C contained in a platinum (P) and a quartz (Q) pan.

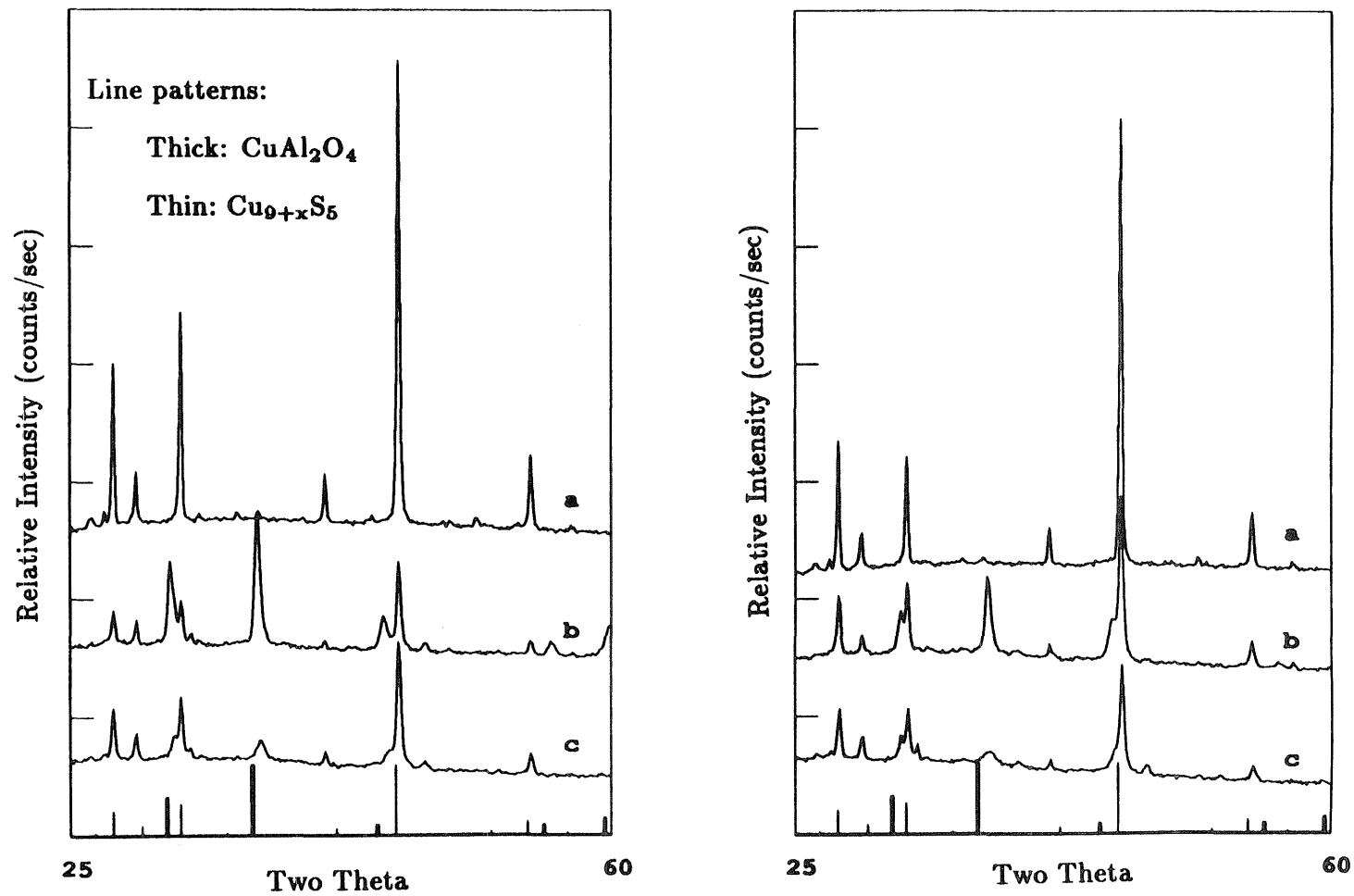
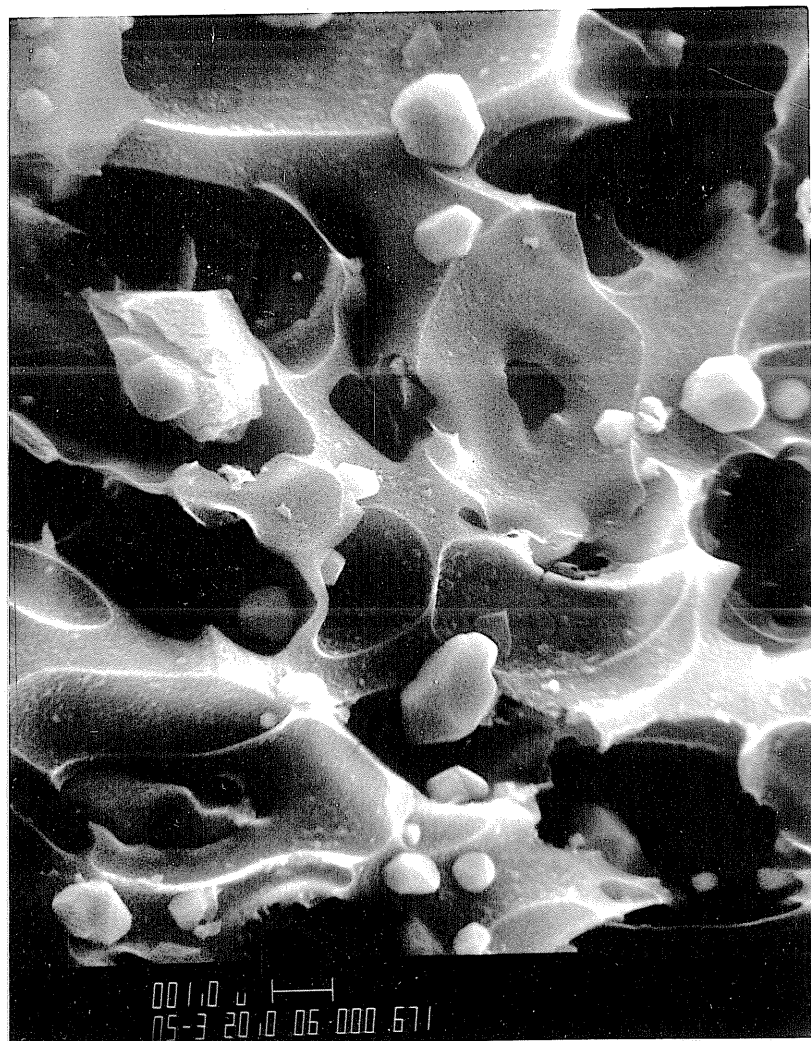


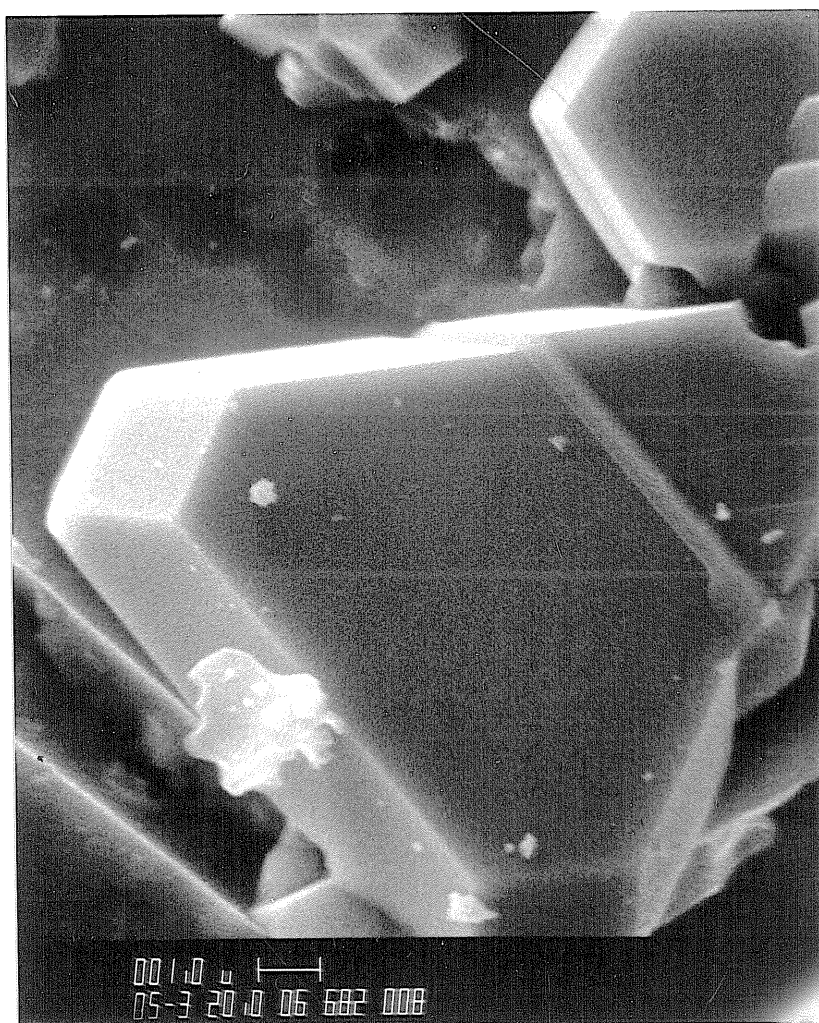
Figure 5.10: XRD patterns of samples 11-1-CA3 (a), 33-1-CA6 (b), and 72-1-CA (c) cooled following sulfidation at 700°C (left) and 800°C (right).



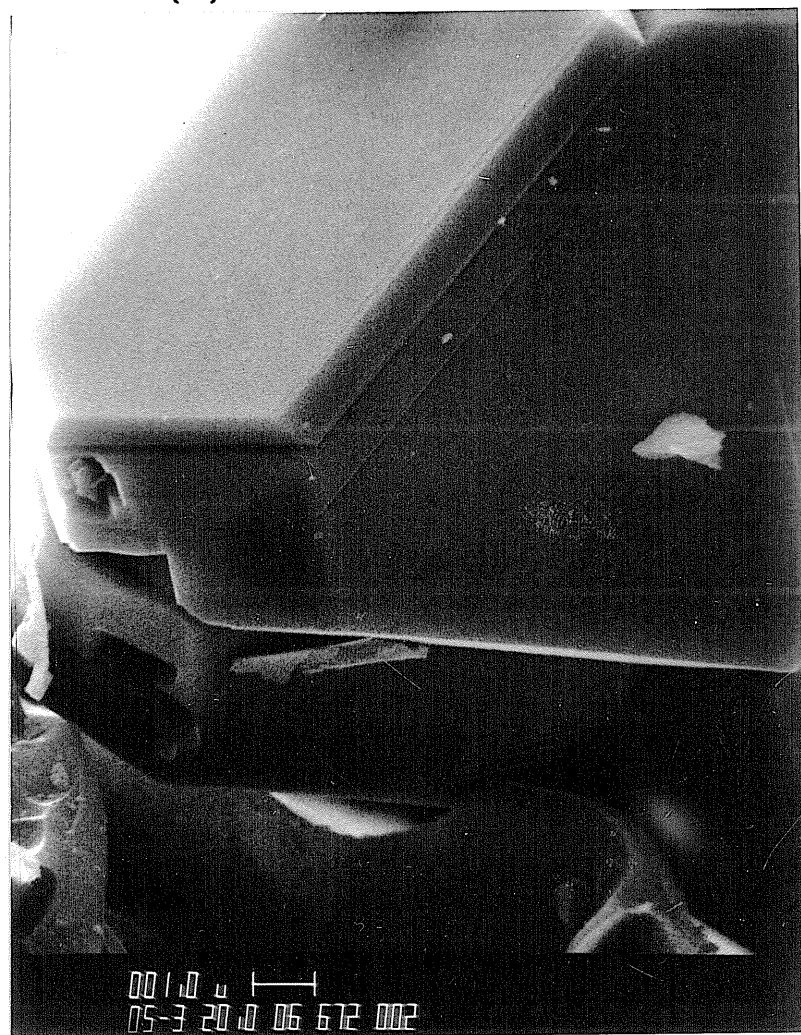
(a) Fresh at 5000×



(b) Reduced at 5000×

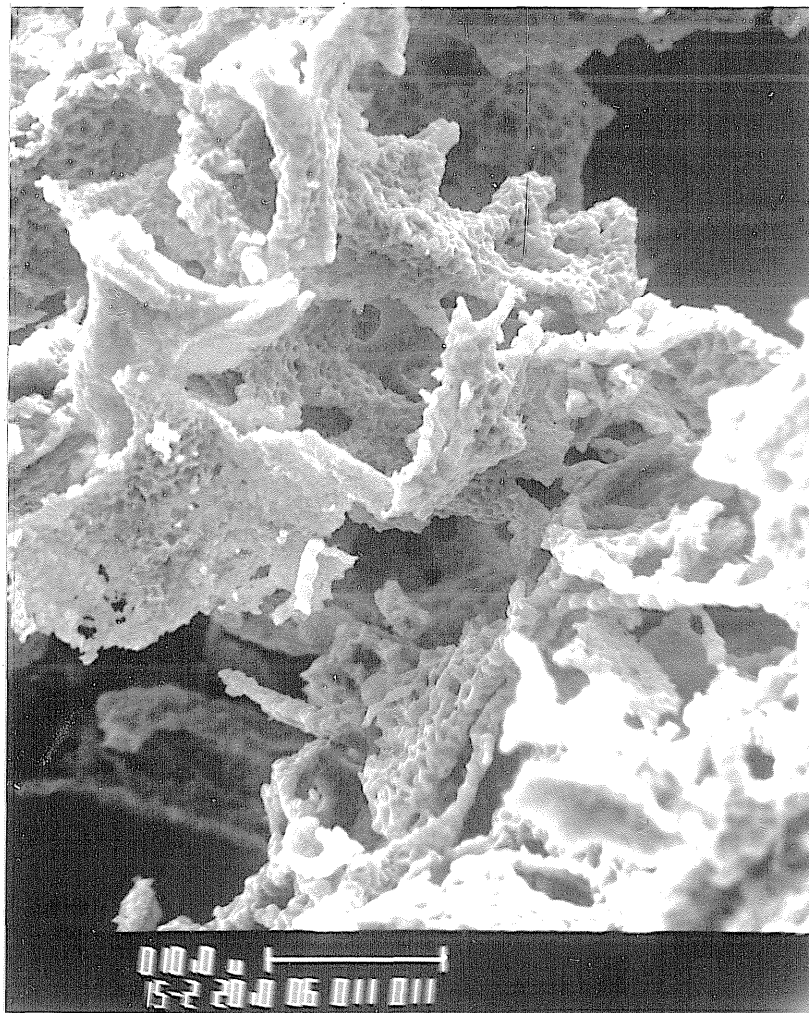


(c) Sulfided at 5000×

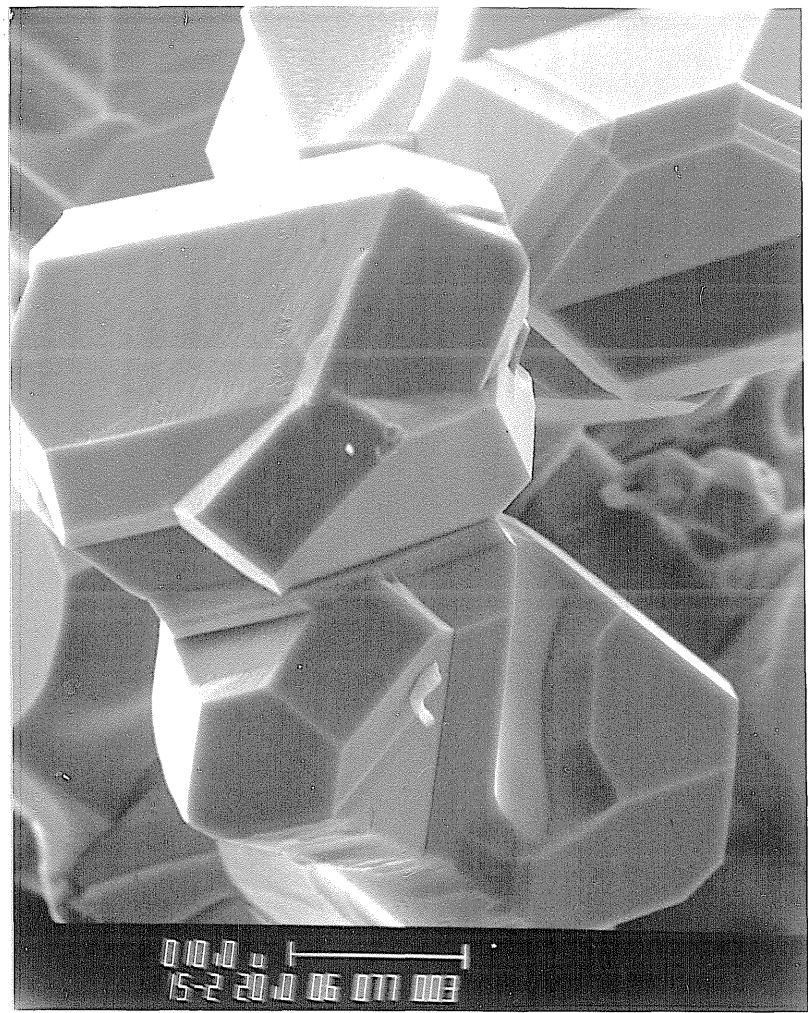


(d) Sulfided at 5000×

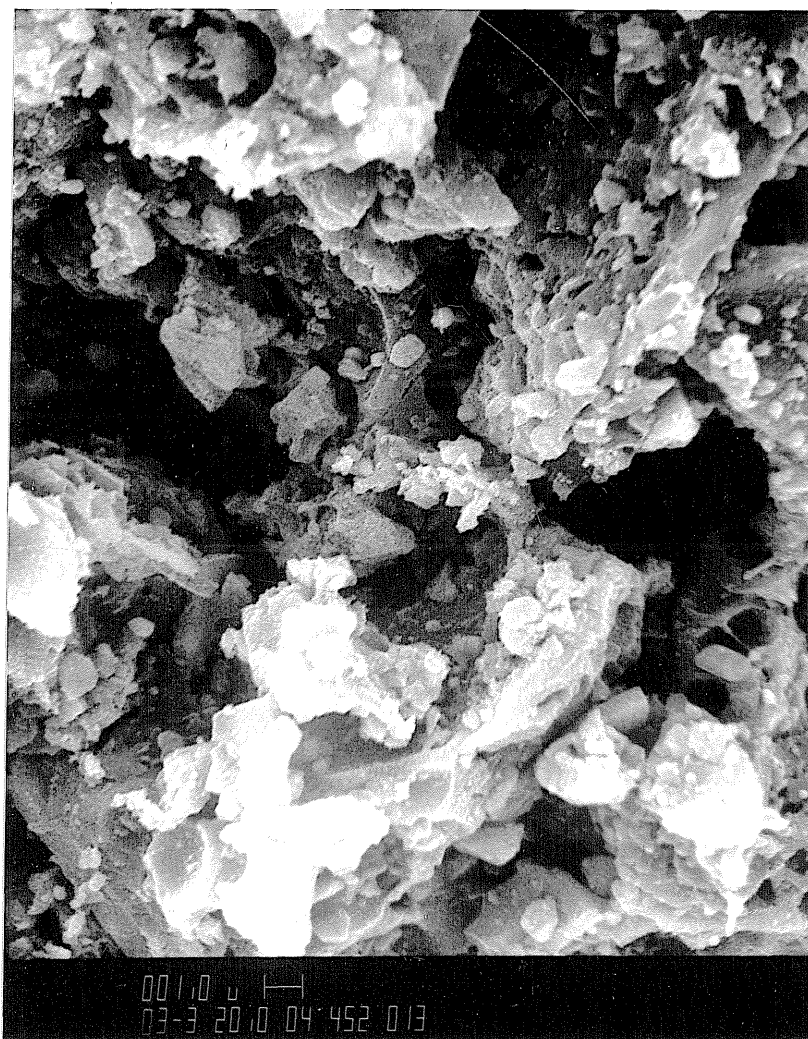
Figure 5.11: Scanning electron micrographs of sample 33-1-CA6 (markers are $1\mu\text{m}$) in a fresh state (a), after reduction at 700°C (b), and after step-wise reduction-sulfidation at 700°C in a platinum pan (c), and in a quartz pan (d).



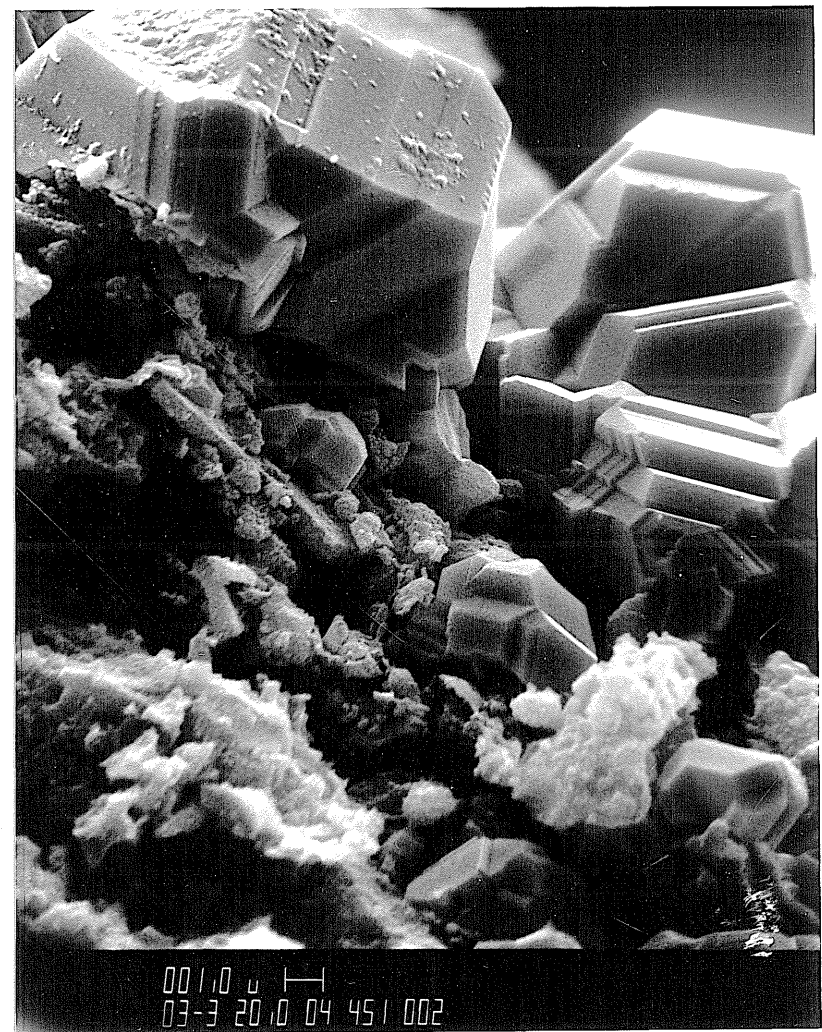
(a) Fresh at 5000×



(b) Sulfided at 5000×



(c) Reduced at 3000×



(d) Sulfided at 3000×

Figure 5.12: Scanning electron micrographs of 11-1-CA3 (markers, 10 μ m) in a fresh state (a), and after step-wise reduction-sulfidation at 700°C (b), and of a pellet (markers, 1 μ m) reduced (c), and reduced, then sulfided at 700°C (d).

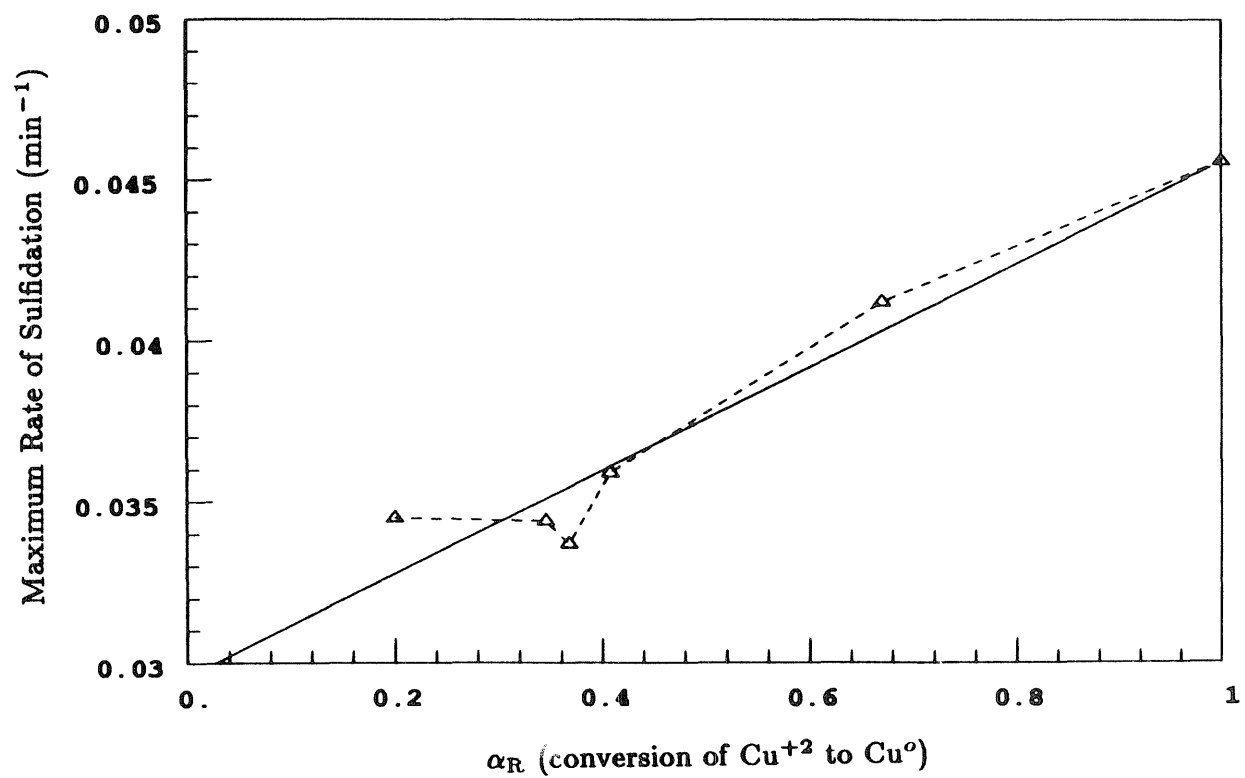
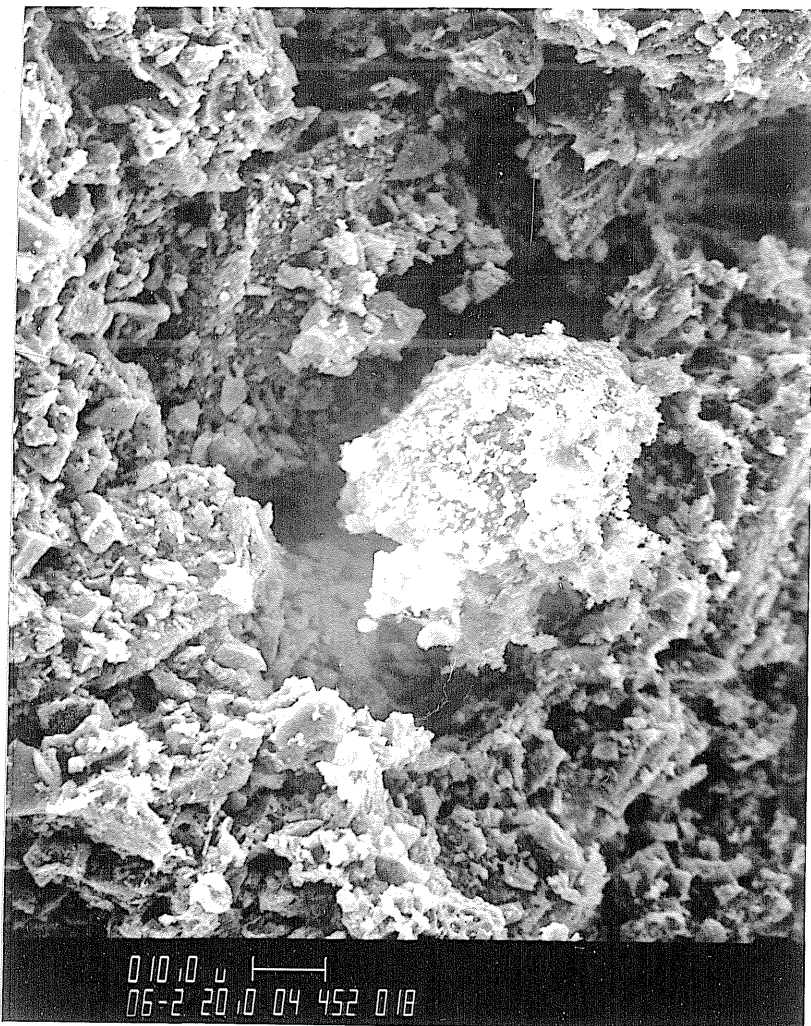
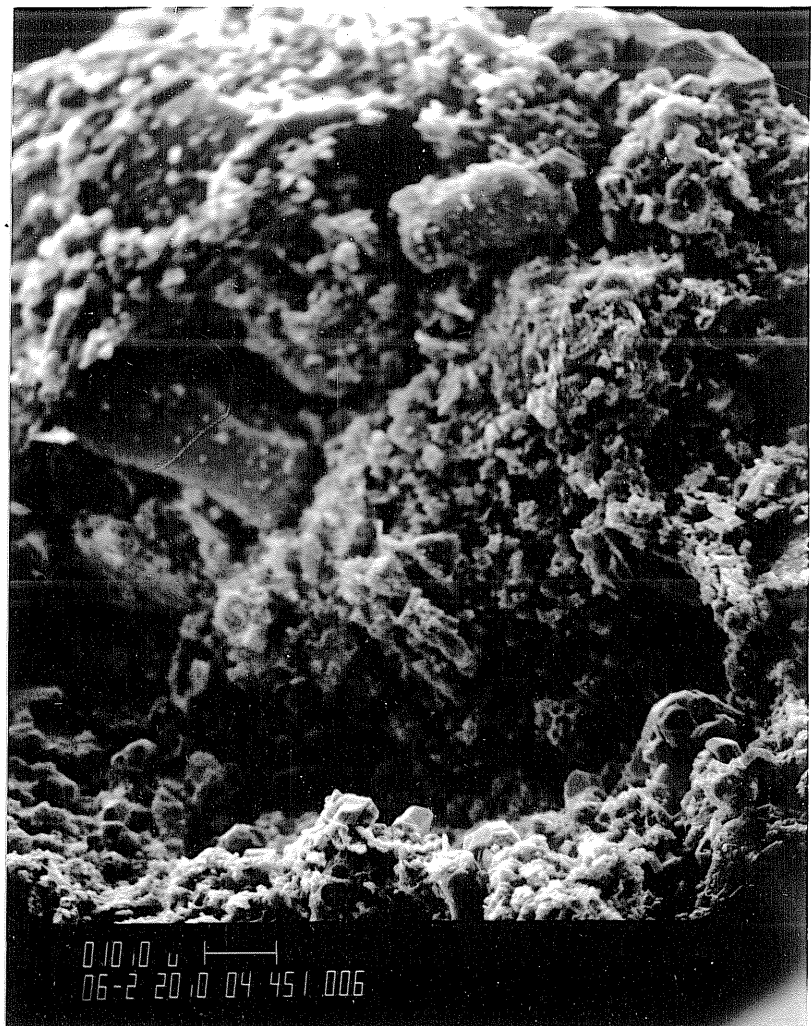


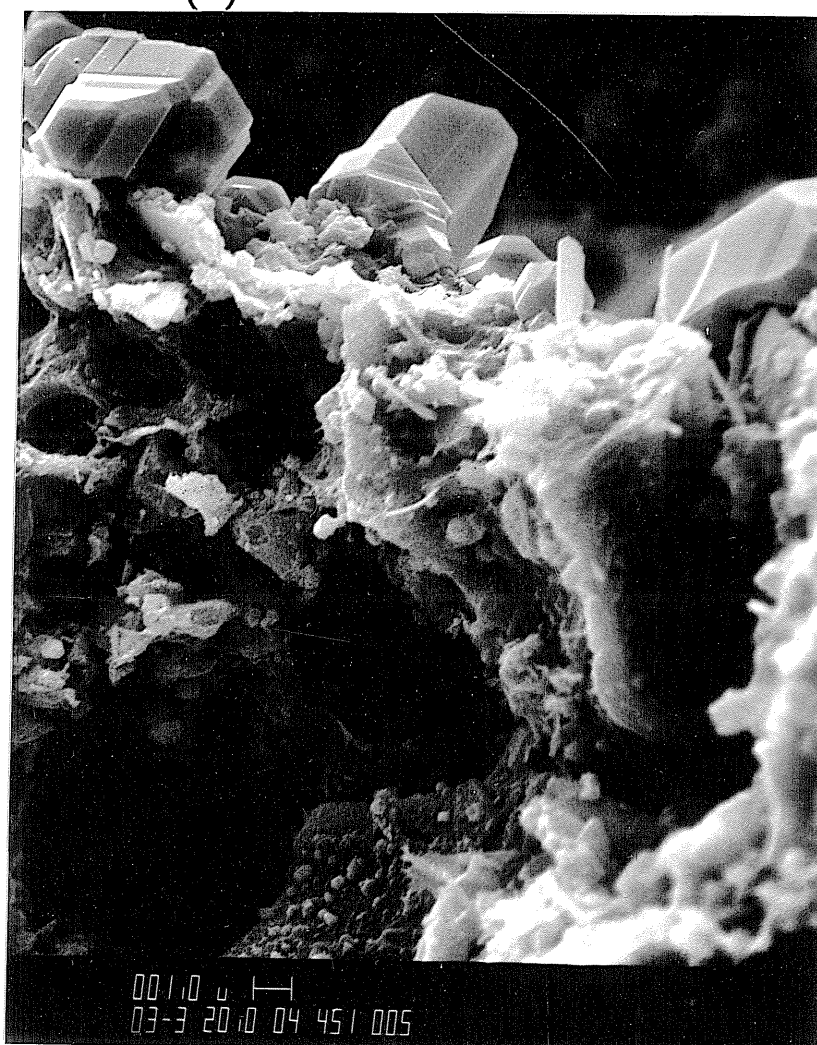
Figure 5.13: Maximum rate of sulfidation as a function of the extent of reduction at 400°C for sample 72-1-CA.



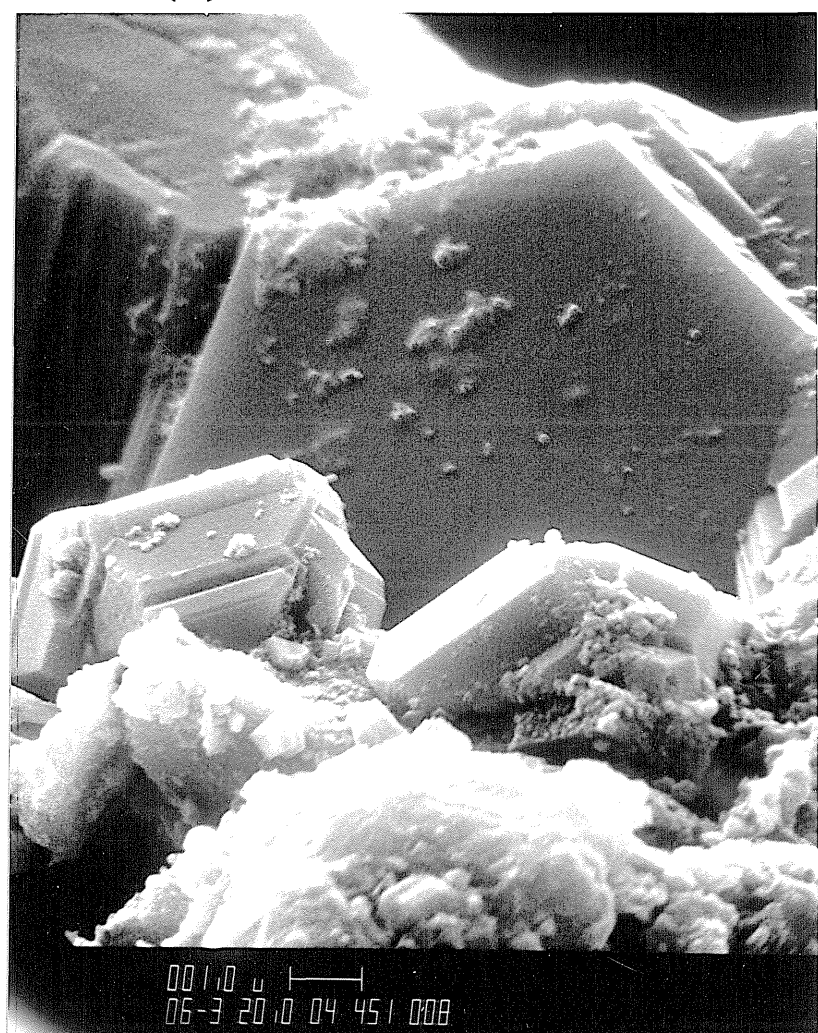
(a) Reduced at 600 \times



(b) Sulfided at 600 \times



(c) Sulfided at 3000 \times



(d) Sulfided at 6000 \times

Figure 5.14: Scanning electron micrographs of a pellet (markers are 10 μm) reduced at 700 $^{\circ}\text{C}$ (a), and reduced then sulfided at 700 $^{\circ}\text{C}$ (b) with enlargements (markers are 1 μm) of the bottom center (c) and upper right (d) of micrograph b.

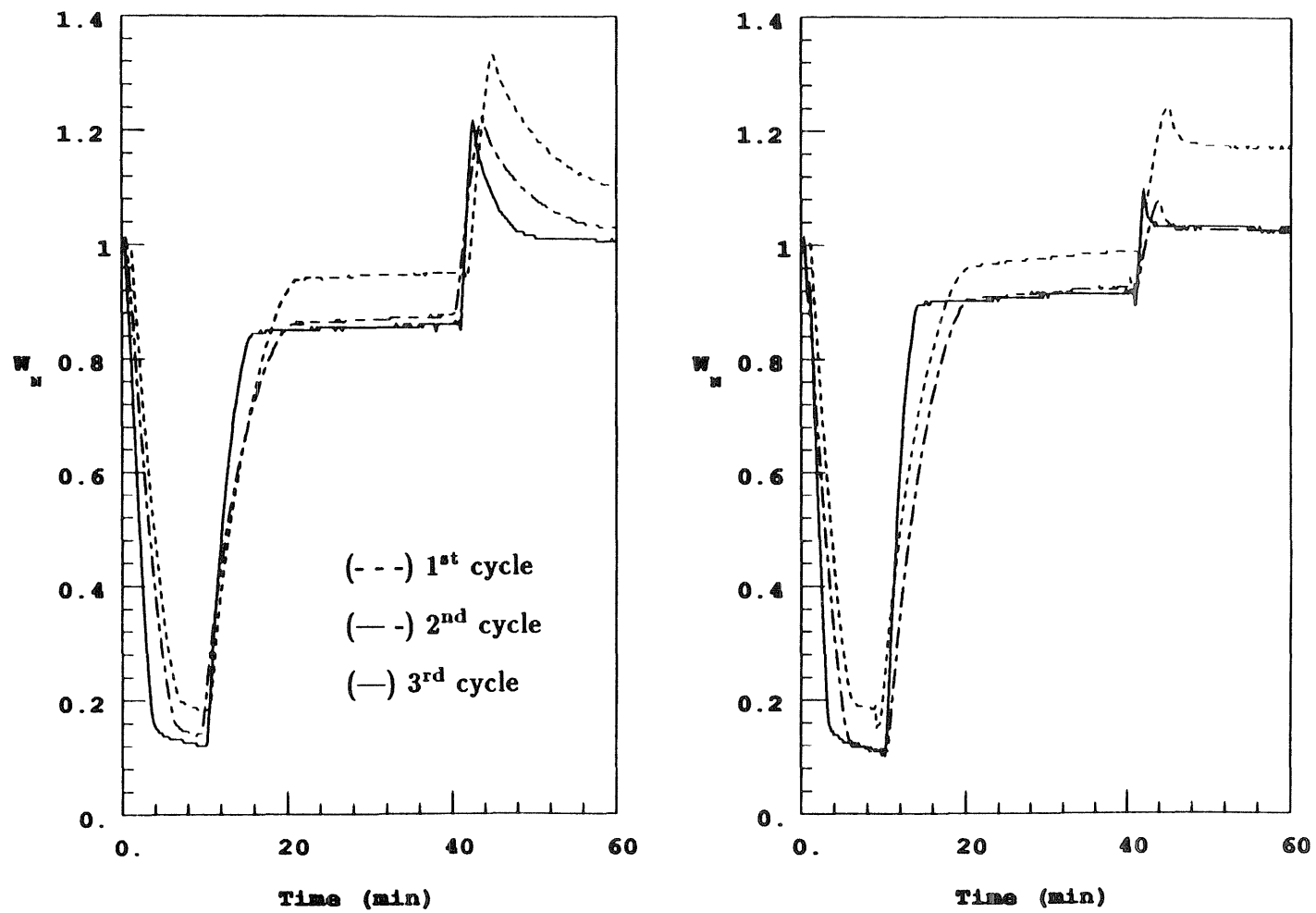


Figure 5.15: Normalized weight-loss curves for consecutive reduction-sulfidation-regeneration of Cu-Al-O pellets at 700°C (left) and 725°C (right).

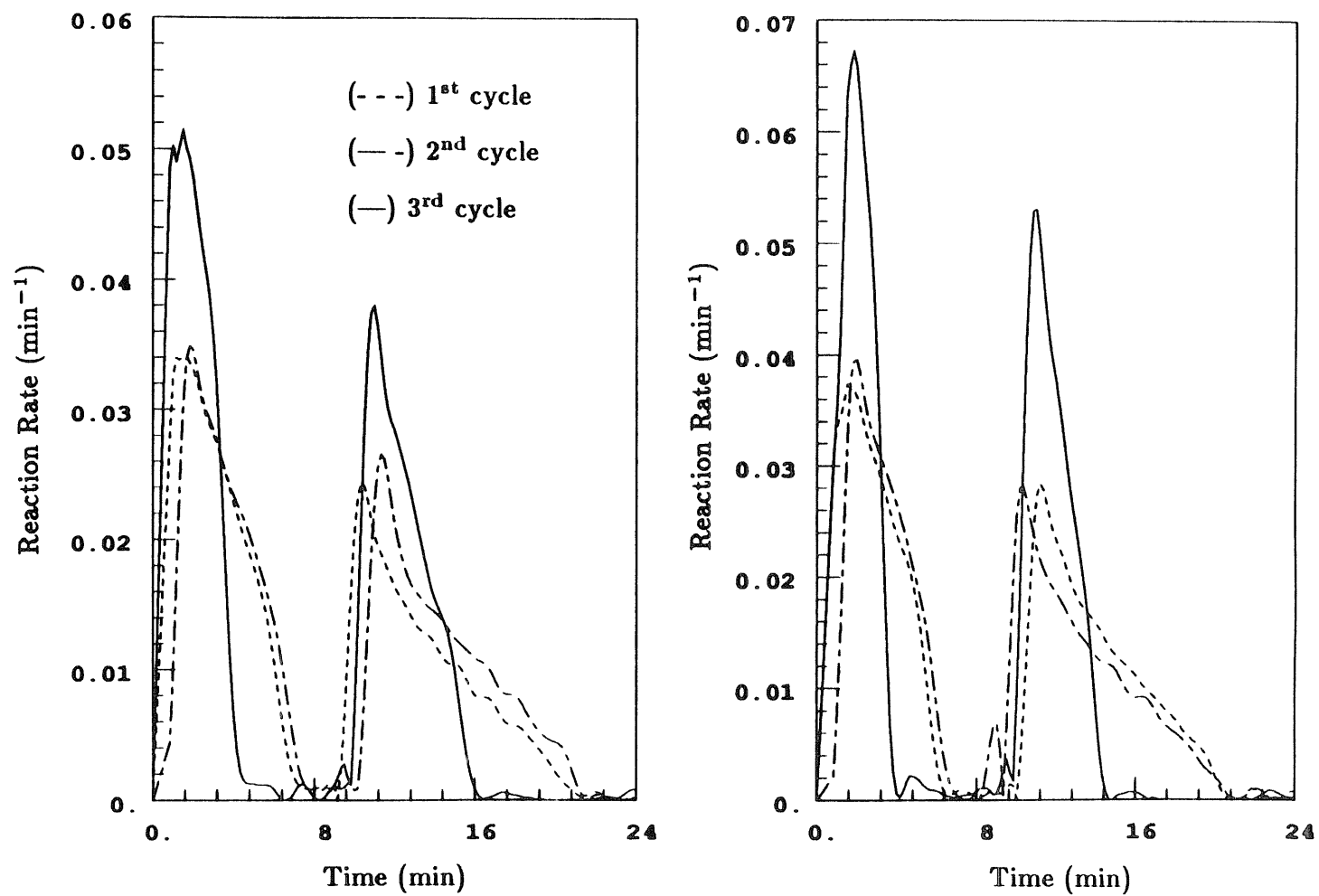


Figure 5.16: Plots of reaction rate, $\frac{da}{dt}$, versus time, t , obtained by transformation of the data contained in Figure 5.15.

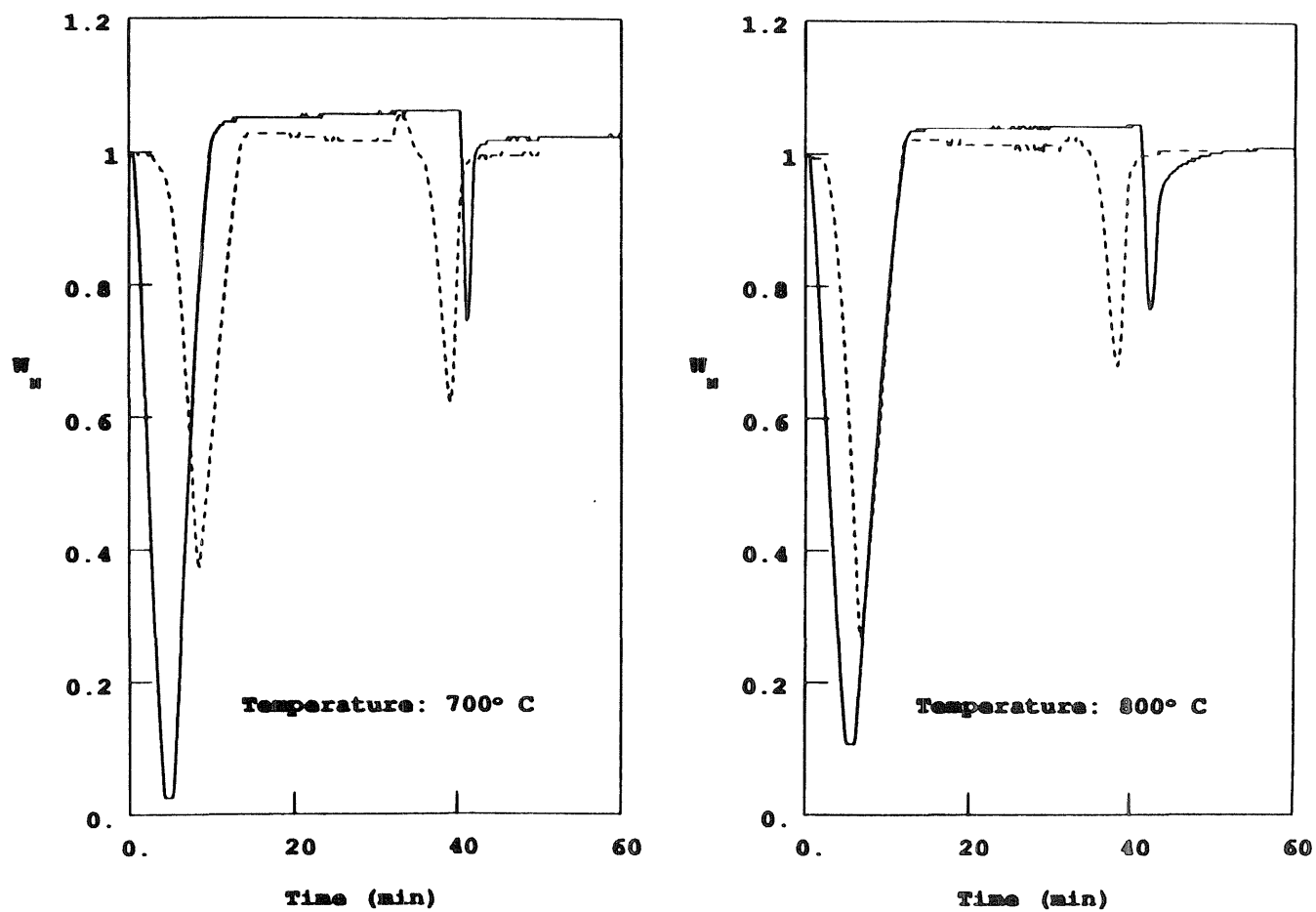


Figure 5.17: Normalized weight-loss curves for the isothermal reaction of sample 11-1-CA3 with a mixture of 13% H_2 , 4% H_2S , and balance N_2 (---), and the step-wise reduction-sulfidation (—) of sample 11-1-CA3, both followed by regeneration in air.

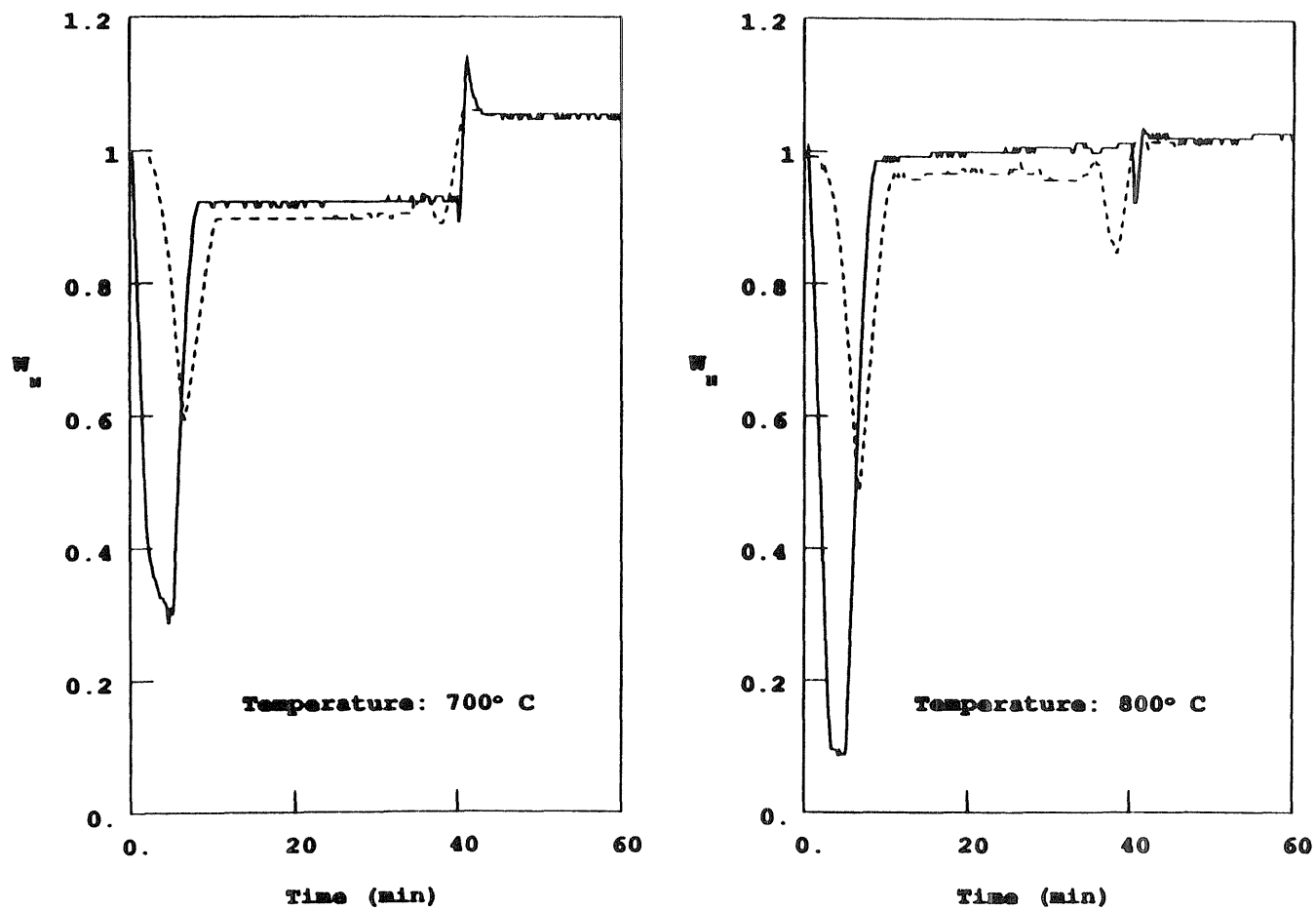


Figure 5.18: Normalized weight-loss curves for the isothermal reaction of sample 72-1-CA with a mixture of 13% H_2 , 4% H_2S , and balance N_2 (---), and the step-wise reduction-sulfidation (—) of sample 72-1-CA, both followed by regeneration in air.

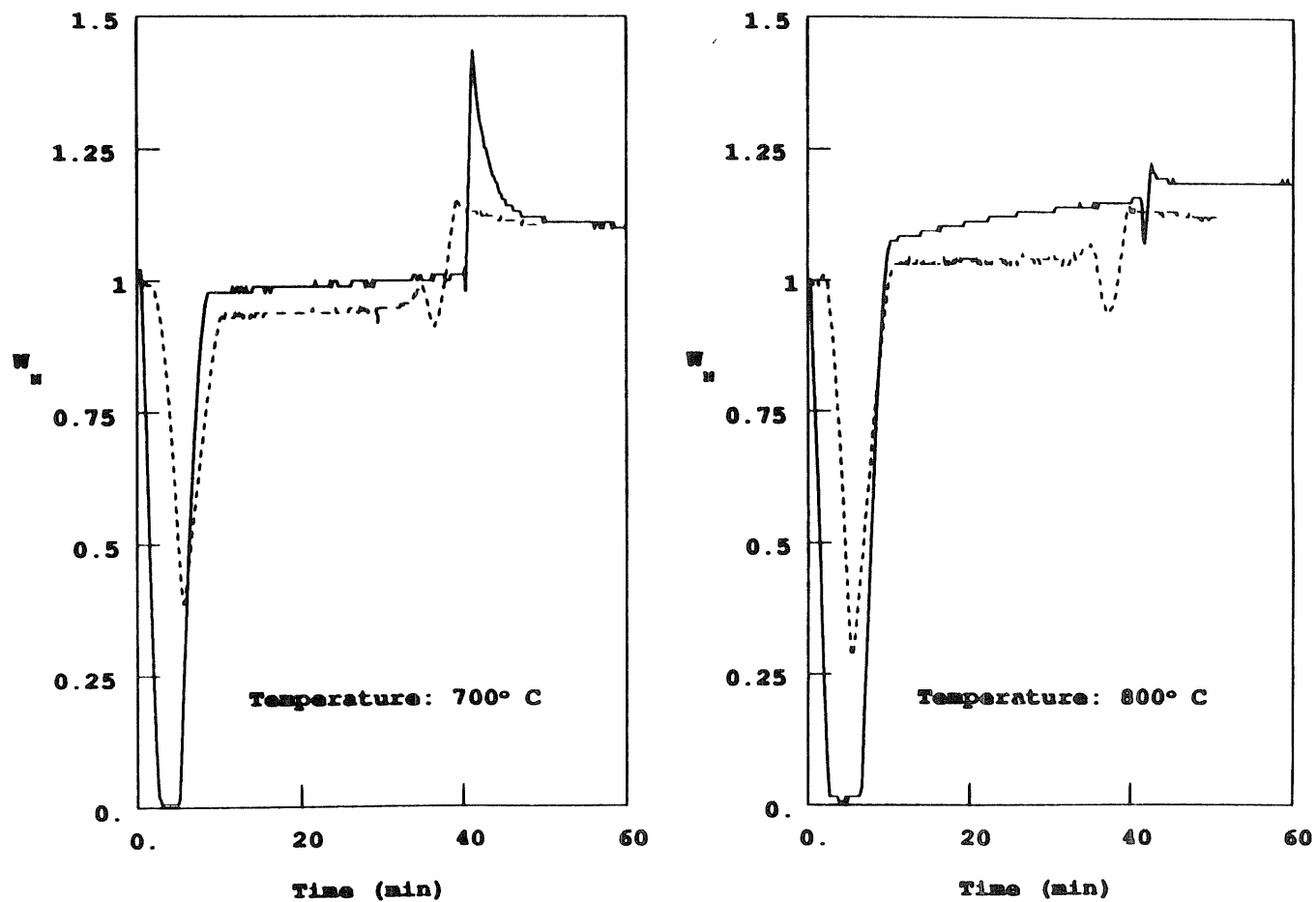


Figure 5.19: Normalized weight-loss curves for the isothermal reaction of sample 33-1-CA6 with a mixture of 13% H_2 , 4% H_2S , and balance N_2 (---), and the step-wise reduction-sulfidation (—) of sample 33-1-CA6, both followed by regeneration in air.

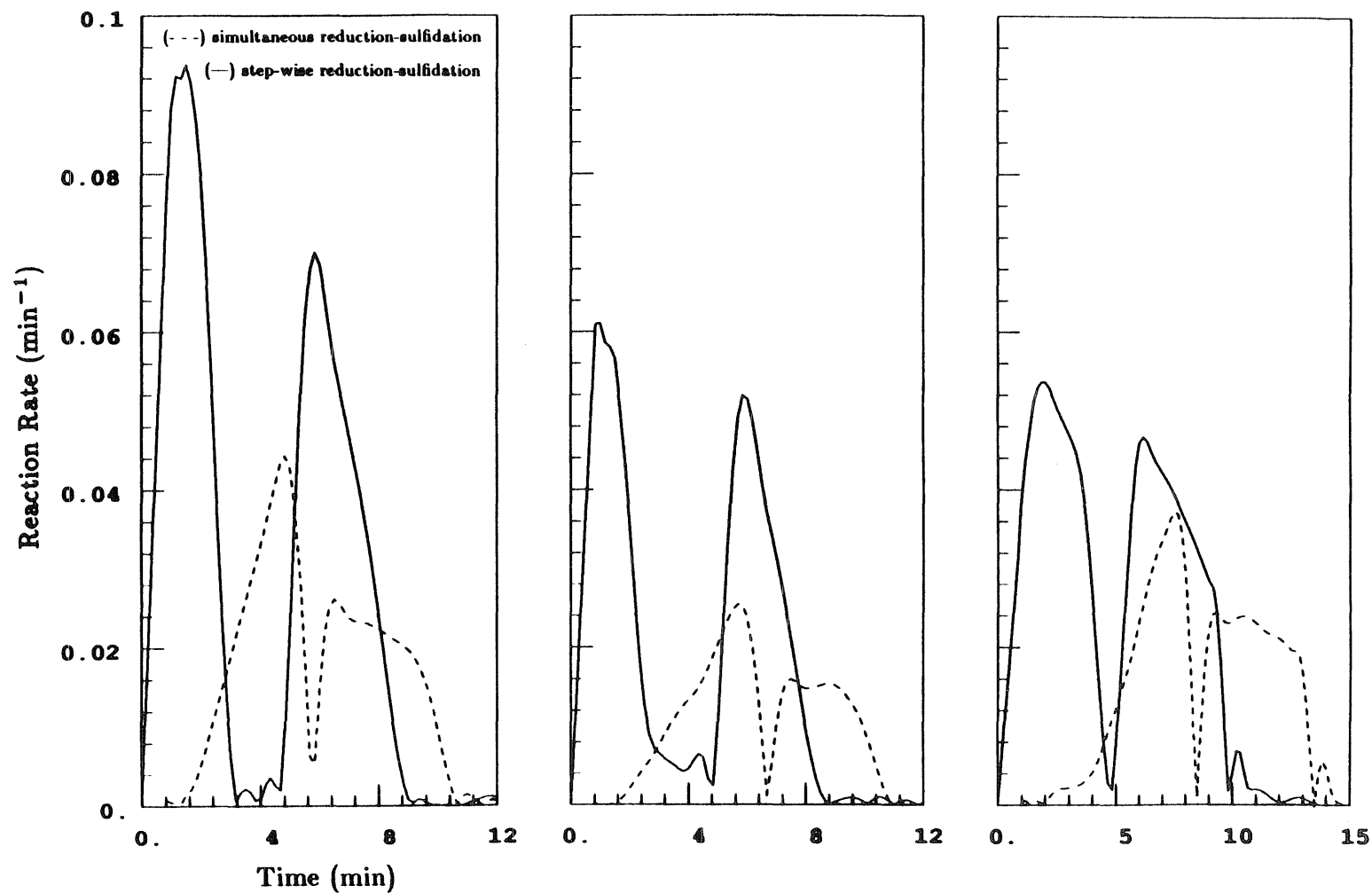


Figure 5.20: Rate of reduction (first peak) and rate of sulfidation (second peak) versus time for samples 72-1-CA (left), 33-1-CA6 (middle), and 11-1-CA3 (right) at 700°C.

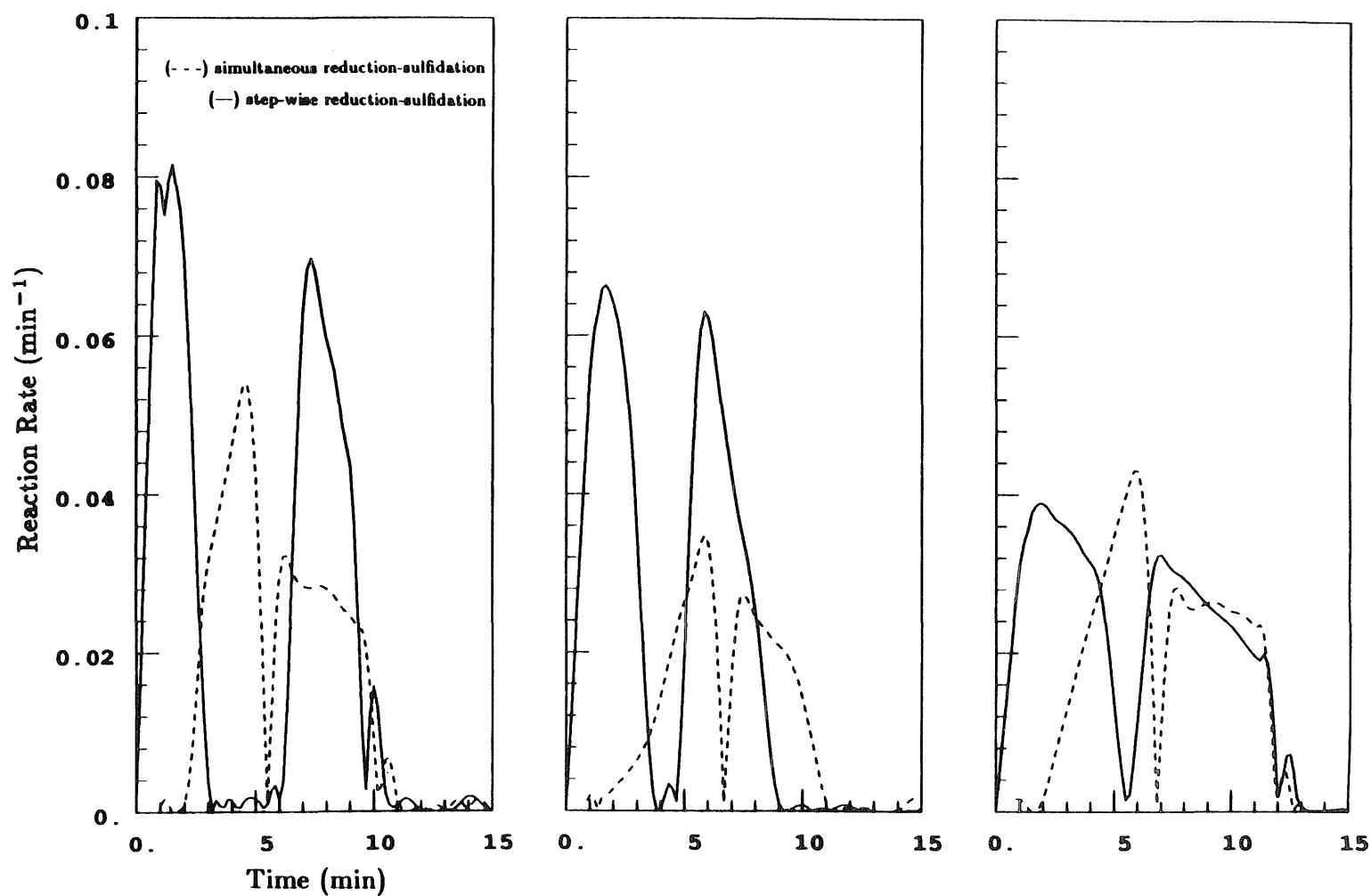


Figure 5.21: Rate of reduction (first peak) and rate of sulfidation (second peak) versus time for samples 72-1-CA (left), 33-1-CA6 (middle), and 11-1-CA3 (right) at 800°C.

CHAPTER VI

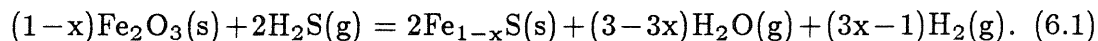
*Reduction and Sulfidation
of
Mixed Iron-Aluminum Oxidic Powders*

(The contents of this chapter, together with work by P.K. Sharma,
are under preparation for publication.)

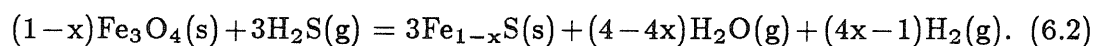
6.1 Background

Hot-gas desulfurization is an important step for optimizing the process economics of new schemes for power generation from coal [1]. These schemes involve integration of a coal gasification unit with advanced high-efficiency technology for conversion to energy such as combined-cycle mechanical conversion, and chemical conversion in fuel cells. Previous work [2] has shown that mixed oxide sorbents such as $\text{CuO} \cdot \text{Fe}_2\text{O}_3$, $\text{CuO} \cdot \text{Al}_2\text{O}_3$, and $\text{CuO} \cdot \text{Fe}_2\text{O}_3 \cdot \text{Al}_2\text{O}_3$ have desulfurization properties superior to those of the pure oxides in that the level of H_2S in the product gas is substantially lower than the level obtained with the pure copper oxide, or predicted from thermodynamic equilibrium based on the pure copper oxide. Although the sulfidation performance of copper-containing sorbents is very good, regeneration must be carried out under somewhat restrictive conditions to avoid sulfate formation. Furthermore, regeneration with elemental sulfur as the principal product is not possible for copper-containing sorbents.

Iron oxide is attractive as a high-temperature desulfurization sorbent because it has the potential for sulfur recovery during regeneration [3]. For example, previous work at Air Products and Chemicals [4] showed that regeneration of sulfided iron oxide sorbents by a mixture containing 95% H_2O and 5% air can produce as much as 75% elemental sulfur with the balance being SO_2 . However, iron oxide, like copper oxide, does not provide the required level of sulfur removal primarily because of rapid reduction in the fuel gas atmosphere prior to sulfidation. In particular, iron oxide has favorable sulfidation equilibrium in the following reaction:



Hematite (Fe_2O_3), however, rapidly transforms to magnetite (Fe_3O_4) in the reducing environment of a typical hot coal gas. Magnetite exhibits less favorable sulfidation equilibrium in the following reaction than hematite in reaction 6.1:



For example, at 650°C the outlet equilibrium concentration for H_2S , assuming $x=0$, is approximately 60 and 120 ppm for reactions 6.1 and 6.2, respectively.

In an effort to stabilize hematite against reduction during high-temperature desulfurization, iron oxide was associated with alumina by a low-temperature complexation technique [5]. A $\text{CuO} \cdot \text{Al}_2\text{O}_3$ sorbent synthesized by the same technique was found by a thermogravimetric study to contain an interaction between CuO and Al_2O_3 that was responsible for retarding reduction by hydrogen of CuO (Chapter III). The observed sulfidation performance of this material was attributed to this interaction (Chapter V). The purpose of this chapter was to obtain mechanistic and kinetic information about the reduction and sulfidation of binary iron-aluminum oxides. To this end, thermogravimetric analysis (in isothermal or temperature-programmed mode) has been used extensively in combination with XRD, SEM, and BET experiments.

6.2 Experimental Techniques

6.2.1 Sorbent Preparation

A well-known complexation method, the citrate method [5], was used to synthesize the mixed oxide sorbents in a highly dispersed state. The complexing agent (citric acid) equimolar to total metal cations was added to an aqueous solution of metal nitrates present in the desired stoichiometric proportions. An

amorphous citrate precursor was prepared by evaporation of this solution. A small volume of solution (determined experimentally), which afforded an optimum evaporation rate for synthesis of a well-dispersed product, was used. Evaporation proceeded first at atmospheric pressure and at 70°C until a marked increase in viscosity of the solution was observed and then for several hours (4-16) in a vacuum oven at 70°C until an amorphous solid foam formed. The foam was carefully broken up and calcined at the desired temperature (between 600°C and 800°C) in air under flow to produce the final mixed oxide. A total of ten samples will be referred to in this chapter with calcination temperatures, duration of calcination, and molar ratio of Fe^{+3} to Al^{+3} restricted to the ranges 600 to 800°C, 4 to 16 hours, and 0.5 to 2.0, respectively. A sample containing no aluminum component was also prepared as a reference. The notation used for sample identification is based on the molar ratio Fe:Al and the calcination temperature of the sample. For example, F650, FA600, 2FA700, and F2A800 denote samples of stoichiometry Fe_2O_3 , $\text{Fe}_2\text{O}_3 \cdot \text{Al}_2\text{O}_3$, and $2\text{Fe}_2\text{O}_3 \cdot \text{Al}_2\text{O}_3$, and $\text{Fe}_2\text{O}_3 \cdot 2\text{Al}_2\text{O}_3$, and of calcination temperatures 650°C, 600°C, 700°C, and 800°C, respectively.

6.2.2 X-Ray Diffraction

A Norelco intermittent diffractometer employing Ni-filtered $\text{Cu}(\text{K}\alpha)$ radiation (1.54056 Å) was used for qualitative chemical analysis of the polycrystalline components present in a sample. The x-ray tube was operated at 45kV and 20mA. X-ray powder diffraction patterns in a 2θ range of 25° to 70° were obtained that could detect the presence of hematite (Fe_2O_3), magnetite (Fe_3O_4), wustite (Fe_{1-x}O), hercynite (FeAl_2O_4), iron, $\gamma\text{-Al}_2\text{O}_3$, pyrrhotite (Fe_{1-x}S), and other iron sulfides. Samples were finely ground and slurried in acetone with a

small amount of Duco cement as binder. The slurry was carefully packed (i.e., to avoid preferred orientations) into the $11 \times 5 \times 1$ mm depression of a bakelite sample holder. Spectra were scanned at 0.1° intervals (in 2θ) for 60 seconds per interval.

6.2.3 Scanning Electron Microscopy

The samples were examined by an ETEC Corporation electron microscope operating at 20 kV with a resolution of 70 Å. The sample was carefully ground and sprinkled on a metal stub containing a light coat of silver paste. This metal stub was then coated with a gold-palladium film 100 Å in thickness prior to observation.

6.2.4 Thermogravimetric Analysis

A Dupont 951 thermogravimetric analyzer interfaced through an analog-to-digital converter to a microcomputer served to measure the sample weight continuously. The same configuration, gas-flow rates, and gas compositions described in Chapter V, Section 5.2.4, were used. Typically, a 45 mg sample of particles, 120-170 mesh fraction, was employed. It was verified experimentally that for the range of flow rates and sample sizes employed, the reactions were free of internal and external, mass-transfer effects.

6.3 Sorbent Characterization

6.3.1 Mechanism of Sorbent Reduction

The XRD patterns of Figure 6.1 reveal that iron oxide prepared from an equimolar mixture of Fe^{+3} and Al^{+3} cations (sample FA650) contains a significant amount of magnetite (Fe_3O_4), and a lesser amount of hercynite (FeAl_2O_4), in addition to the primary component, hematite (Fe_2O_3). On the other hand, iron oxide prepared in the absence of alumina (sample F650) contains hematite exclusively and is more crystalline than FA650 predominantly because of the absence of alumina present in an amorphous or microcrystalline ($\leq 50\text{\AA}$) state. It is interesting that both magnetite and $\gamma\text{-Al}_2\text{O}_3$ possess the same crystal structure, spinel, because an interaction between these species may explain the incomplete conversion of iron to a +3 oxidation state during calcination. The TPR (temperature-programmed reduction) profiles of Figure 6.1 demonstrate the greater reducibility of F650 as compared to FA650. Since both sorbents were subjected to identical calcination conditions (*i.e.*, firing at 650°C in air for 4 hours), the differences between the TPR profiles must be due to a chemical association between iron oxide and aluminum oxide rather than to a sintering phenomenon. In addition, FA650 has a higher overall surface area than F650 because of the presence of free alumina, and this property further confounds an interpretation of the reduction profiles based on sintering of the iron-oxide phase.

The first discontinuity in slope of the TPR profiles (Figure 6.1) is located at $W_N=0.89$ for F650 and $W_N=0.83$ for FA650, where W_N is a normalized weight factor defined as follows:

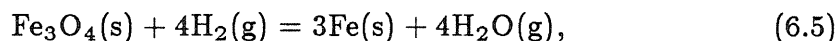
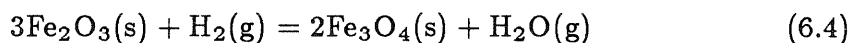
$$W_N = \frac{m - m_f}{m_o - m_f}, \quad (6.3)$$

where m = instantaneous mass

m_o = initial mass

m_f = final mass at complete reduction to Fe^0 .

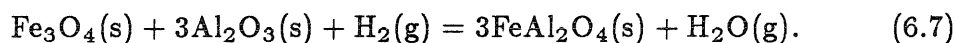
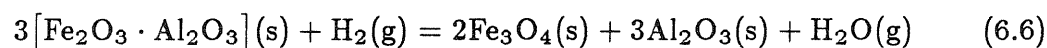
A discontinuity in slope at $W_N=0.89$ is consistent with a two-stage reduction of Fe_2O_3 , according to the following sequence of reactions:



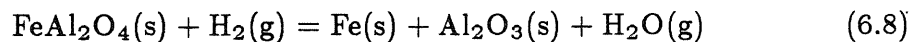
where reaction 6.4 accounts for weight loss in the range $W_N = 1$ to 0.89, and reaction 6.5 accounts for weight loss in the range $W_N=0.89$ to 0, assuming that the reactions occur consecutively. XRD analysis confirmed this trend with no detection of wustite (Fe_{1-x}O) as an intermediate to reaction 6.5. For example, samples of F650 were partially reduced by TPR and then quenched to room temperature under a flow of reactant gas for subsequent examination by XRD. The results are presented in Figure 6.2, where the good reproducibility of TPR data can be seen. This reaction scheme is consistent with a recent TEM (transmission electron microscopy) investigation of hematite reduction [6].

A discontinuity in slope at $W_N=0.83$ indicates the absence of a distinct stage for conversion of Fe^{+3} to Fe^{+2} (*i.e.*, $W_N=1$ to 0.89) during TPR of FA650. In addition, there are three stages of reduction for the FA650 sample, $W_N=1$ to 0.83, $W_N=.83$ to 0.43, and $W_N=0.43$ to 0, in which the third stage was not completely monitored because it was so slow. According to Figure 6.3, both Fe_3O_4 and FeAl_2O_4 are detected by XRD as intermediates to the reduction of FA650.

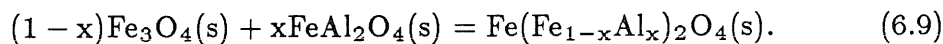
X-ray peaks for magnetite are, sharp indicating high crystallinity, while those for hercynite are broad, characteristic of microcrystallinity. It must be pointed out that XRD patterns of fresh and partially reduced FA650 gave evidence for the presence of amorphous phases. Therefore, failure to detect peaks for alumina suggests that alumina is in the form of small crystallites (*e.g.*, $\leq 50\text{\AA}$), or in the form of an amorphous phase, or both. Furthermore, a fraction of the iron-containing phases are amorphous. The available information, however, suggests that the following reactions are occurring simultaneously during the first stage of reduction:



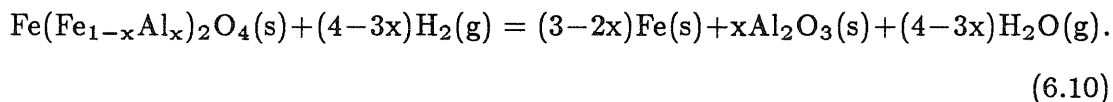
The formation of hercynite suggests that reduction of magnetite (reaction 6.5) is relatively slow, since hercynite is typically prepared by solid-state reaction at high temperatures (*e.g.*, $> 1000^\circ\text{C}$). The appearance of Fe^o during the second stage of reduction (sharp peak at $2\theta \sim 44.7^\circ$) is due to reaction 6.5, and to the reduction of hercynite as follows:



A close examination of the XRD patterns in Figure 6.3 indicates the formation of a spinel solid solution between magnetite and hercynite during the second stage of reduction as follows:



For example, in Figure 6.3, peaks for two individual spinel phases are discernable in the top pattern, corresponding to lattice parameters of $\sim 8.32\text{\AA}$ for Fe_3O_4 and $\sim 7.96\text{\AA}$ for FeAl_2O_4 , while peaks for only one spinel phase are seen in the bottom pattern, corresponding to a lattice parameter of $\sim 8.15\text{\AA}$, which lies between those of the individual phases. The lattice parameters estimated for Fe_3O_4 and FeAl_2O_4 are within 2% of reported values [7]. Formation of a spinel solid solution suggests that reduction of both hercynite and magnetite is relatively slow. While reactions 6.6 and 6.7 occur simultaneously in the first stage, reactions 6.5, 6.7, 6.8, and 6.9 comprise the second stage, and reduction of the spinel solid solution comprises the third stage:



Plots of reaction rate, $\frac{d\alpha}{dt}$ (α is the conversion of Fe^{+3} to Fe^0), versus time, t , for TPR of F650 and FA650 provide evidence for a specific interaction between iron-containing phases and alumina. The two peaks for each sample in Figure 6.4 correspond to the first two stages of reduction in Figure 6.1. The first peak represents the conversion of hematite to magnetite (reaction 6.4) for F650, and the simultaneous production of magnetite (reaction 6.6) and hercynite (reaction 6.7) for FA650, while the second peak represents the conversion of magnetite to iron (reaction 6.5) for F650, and the conversion of both magnetite and hercynite (reaction 6.8) to iron for FA650. The maximum rate of reduction during the first stage is 1.5 times greater for F650 and occurs at a lower temperature than for FA650. Therefore, the reduction of hematite in FA650 is hindered. Furthermore, the maximum rate of reduction during the second stage is 6 times greater for F650 and occurs at a lower temperature than for FA650, suggesting that the

reduction of magnetite is hindered in FA650, and that the reduction of FeAl_2O_4 is slow. The hindered reduction of Fe_2O_3 and Fe_3O_4 in FA650 is attributed to an interaction of these phases with alumina. An interaction between Fe_2O_3 and Al_2O_3 has been observed in $\text{Fe}_2\text{O}_3/\text{Al}_2\text{O}_3$ materials prepared by the method of impregnation. For example, in a Mössbauer investigation of 3 wt% Fe_2O_3 in $\gamma\text{-Al}_2\text{O}_3$, a weak interaction between the supported oxide and alumina was reported [8]. In addition, a TPR study of alumina-supported Fe_2O_3 revealed the formation of a surface Fe^{+3} species with different reduction behavior than observed for bulk Fe^{+3} [9].

6.3.2 Effect of Different Fe:Al Ratios

XRD patterns of the remaining ten mixed iron-aluminum oxides are further proof of the complexities inherent in this system. Table 6.1 summarizes the preparation conditions and the crystalline phases identified by XRD for these samples. The x-ray patterns indicate a high ratio of amorphous-to-crystalline phases (*i.e.*, > 1) by the presence of an amorphous halo in a 2θ range of $\sim 20\text{-}26^\circ$. The formation of such a high content of amorphous phases may be due to the rapid cooling, following calcination of the samples. The rapid cooling was induced by rapid transfer of the crucible containing the sample from the hot calcining furnace to a platform at room temperature. The large fraction of amorphous material comprising the samples makes characterization by XRD extremely difficult because the x-ray signals are weak and are only a partial representation of all the phases present. XRD indicates, however, that both crystallinity and Fe_2O_3 content increase with calcination temperature regardless of aluminum content. Here again the detection of Fe_3O_4 and FeAl_2O_4 in fresh samples suggests a chemical barrier to the complete oxidation of iron to

the +3 oxidation state during calcination. The chemical barrier is correlated to the presence of an aluminum component because iron oxidation states below +3 are not found for syntheses conducted in the absence of aluminum. In further support of the correlation between aluminum content and the extent of iron oxidation, for a given calcination temperature, both crystallinity and Fe_2O_3 content increase with decreasing aluminum content.

The TPR profiles of Figure 6.5 display three stages of reduction as noted for FA650 earlier with one exception, sample F2A600. Sample F2A600 is an exception to trends observed by BET measurements and SEM analysis as well. For example, in samples with Fe:Al molar ratios of 1 and 2, BET surface area decreases with increasing calcination temperature and increasing Fe:Al ratio (Table 1). Analogous to Cu-Al-O materials (Chapter III, Section 3.4), the high values of overall surface area reflect a predominant contribution from unassociated alumina, which loses surface area with increasing calcination temperature that is due to sintering. The surface area of F2A600, however, is lower than that for samples prepared with the same Fe:Al ratio at higher calcination temperatures, and prepared with higher Fe:Al ratios at the same calcination temperature. The implication is that F2A600 contains a significant amount of FeAl_2O_4 as compared to the other samples.

As in the case of BET measurements, sample F2A600 appears significantly different from other samples according to SEM analysis. For example, the scanning electron micrographs of Figure 6.6 reveal a coarsely textured surface for F650 at one extreme, and a smooth, untextured surface for F2A600 at the other extreme. The surfaces of samples FA600 and 2FA600 display a granular texture, which could be construed as a combination of the two extreme textures, smooth and coarse. In fact, the coarseness of the surface increases with increasing iron

content. In analogy to the Cu-Al-O system in which copper was visible on the solid surface by SEM when present as a separate phase (*e.g.*, CuO or Cu) but was invisible when present as a compound with Al₂O₃ (*e.g.*, CuAl₂O₄) [6], F2A600 must contain predominantly FeAl₂O₄, while FA600 and 2FA600 contain mostly a mixture of oxides (*e.g.*, Fe₂O₃, Fe₃O₄, and Al₂O₃). The presence of FeAl₂O₄ in F2A600 can not be confirmed by XRD, suggesting that this phase is either microcrystalline, or amorphous, or a combination of the two.

To gain complementary information, the TPR profiles depicted in Figure 6.5 are transformed to profiles of reaction rate, $\frac{d\alpha}{dt}$ (α is the conversion of Fe⁺³ to Fe^o) in Figure 6.7. Each stage of the TPR profile produces a peak in the corresponding profile of reaction rate. These profiles are significantly different from that obtained for reduction of pure iron oxide, F650 (Figure 6.4). In particular, alumina-containing samples exhibit 3 peaks as compared to the two peaks exhibited by pure iron oxide, and the alumina-containing samples experience a maximum rate of reduction during the first stage of reduction (with the exception of sample FA800), rather than during the second stage of reduction as is the case for pure Fe₂O₃. The second peak is most pronounced for samples containing a molar ratio Fe:Al of 2, and least pronounced for samples containing a molar ratio Fe:Al of 0.5. In fact, comparing the maximum rate of reduction of the second peak, r_2 , to that of the third peak, r_3 , reveals that r_2/r_3 is less than one for samples containing an Fe:Al ratio of 1:2 but greater than one for samples containing an Fe:Al ratio of 1:1 or 2:1 (Table 6.2).

Samples calcined at 600°C, but containing different contents of alumina, displayed the largest diversity in reducibility. The reaction rate profile of sample FA600 resembles that of sample FA650 (Figure 6.4), for which a solid solution between magnetite and hercynite was proposed to form during reduction. The

second and third peaks for these samples are observed to be broad and overlapping, perhaps characteristic of the reduction of this solid solution. On the other hand, the second and third peaks in the reaction rate profile of sample F2A600 are quite distinct. In this case, the second peak is difficult to distinguish and, in fact, may be absent so that the observed high-temperature shoulder of the first peak actually characterizes another species, such as a surface Fe^{+3} species. Since F2A600 has been postulated to contain a large fraction of FeAl_2O_4 , the third peak is assigned to the reduction of this component. Finally, the third peak in the reaction rate profile 2FA600 appears as a high-temperature shoulder to the high-intensity second peak. This second peak is believed to characterize the hindered reduction of Fe_3O_4 in the presence of alumina as compared to the reduction of Fe_3O_4 in the absence of alumina (Figure 6.4). The temperature for which the reduction rate is a maximum during the third stage (*i.e.*, third peak) is the same for samples FA600 and 2FA600, implying that a solid solution between Fe_3O_4 and FeAl_2O_4 also forms in the case of 2FA600. In contrast, the temperature for which the reduction rate is a maximum during the final stage for sample F2A600 is notably higher: 860°C for F2A600 as compared to 770°C for 2FA600 and FA600. This difference in temperature for which reduction rate is a maximum suggests the greater reducibility of a magnetite-hercynite solid solution as compared to pure hercynite. In addition, the position of the third peak characterizes the extent of interaction between Fe^{+2} and alumina.

For samples calcined at 800°C , the temperature for which the reduction rate is at a maximum during the third stage is between 770°C and 810°C for different alumina contents. Furthermore, the reaction rate profiles for samples 2FA800 and FA800 are nearly identical, suggesting similar Fe_3O_4 - FeAl_2O_4 interactions in these samples. For an Fe_3O_4 - FeAl_2O_4 solid solution, $\text{Fe}(\text{Fe}_{1-x}\text{Al}_x)_2\text{O}_4$, dif-

ferent phases are possible, depending on the value of x . For example, a value of 0.59 has been reported for x in order to establish a complete solid solution between Fe_3O_4 and FeAl_2O_4 [7], implying that other values of x lead to the existence of two immiscible phases: an alumina-rich Fe_3O_4 spinel-type phase, and an iron-rich FeAl_2O_4 spinel-type phase.

Considering the stages of reduction, the first peak characterizes primarily the reduction of Fe^{+3} to $\text{Fe}^{+\frac{8}{3}}$; the second peak characterizes primarily the reduction of $\text{Fe}^{+\frac{8}{3}}$ to Fe^{+2} , and the third peak characterizes primarily the reduction of Fe^{+2} to Fe^0 . These events are not independent as can be seen by the values of conversions observed between the stages (Table 6.2), and by the shapes of the reaction rate profiles. Furthermore, interactions between iron of different oxidation states and alumina hinders the reduction of the iron. For example, low rates of reduction resulting in peak broadening during the first stage of reduction in samples FA600, d F2A600, and F2A700 could be due to the presence of a surface Fe^{+3} species. The formation of hercynite during the second stage of reduction implies that an interaction between Fe_3O_4 and Al_2O_3 exists. Depending on the position of the peak maximum, the third stage has been attributed to reduction of the following species listed in order of decreasing reducibility: an alumina-rich Fe_3O_4 spinel-type phase, an Fe_3O_4 - FeAl_2O_4 solid solution, an iron-rich FeAl_2O_4 spinel-type phase, and pure FeAl_2O_4 . A conversion of 0.513 at the onset of the final stage of reduction for F2A600 implies that this sample contains 95 mol% FeAl_2O_4 in its fresh state, assuming that only Fe_2O_3 , FeAl_2O_4 , and Al_2O_3 are present initially, and that no FeAl_2O_4 forms from Fe_2O_3 during the course of reduction.

The presence of Fe_3O_4 and FeAl_2O_4 in fresh samples has been attributed to incomplete oxidation of iron to +3 during calcination. This is supported by the

observed disappearance of these phases upon oxidation of reduced samples in air at 912°C. For example, following TPR of FA600, FA700a, FA700b, 2FA600 and 2FA700, the reduced samples were oxidized in air at 912°C and then examined by XRD to reveal Fe_2O_3 as the only crystalline phase present. The same analysis for F2A700, however, revealed a small amount of FeAl_2O_4 , in addition to Fe_2O_3 . Therefore, FeAl_2O_4 appears to be a stable phase in the oxidizing environment described, provided enough Al_2O_3 is available, while Fe_3O_4 is not a stable phase under these conditions.

6.4 Sorbent Reduction and Sulfidation

6.4.1 Simultaneous Reduction-Sulfidation

Sulfidation of a pure iron oxide, F650, and a mixed iron-aluminum oxide, FA650, was carried out with a mixture of 13% H_2 , 3.6% H_2S , and the balance N_2 at 700°C with subsequent regeneration in air after ~ 35 minutes. Figure 6.8 shows the results in terms of the normalized weight factor, W_N , defined above. In each case there is an initial weight loss because the initial rate of reduction is faster than that of sulfidation. As the rate of reduction slows down, the rate of sulfidation dominates, resulting in weight gain. It is seen that sulfidation of the compound sorbent FA650 is faster and results in larger sulfur uptake compared to that of the pure iron oxide F650. FA650 demonstrates faster kinetics of reduction and sulfidation than F650 because of a higher dispersion of iron-containing phases induced by the presence of free alumina. The larger sulfur uptake exhibited by FA650 in comparison to that exhibited by F650 is attributed to the preservation of higher oxidation states of iron in the reducing environment. The higher the oxidation state of iron, the better the sulfidation equilibrium be-

tween iron and H_2S (Table 6.3). Furthermore, characterization studies provide evidence for the existence of interactions between iron-containing species and alumina based on a lower reducibility of these iron-containing phases.

XRD analysis of sulfided FA650, obtained from a separate run in which air regeneration was replaced by quenching to room temperature under the reactant gas, identified monoclinic 4C-type pyrrhotite as the only crystalline phase. The 4C-type pyrrhotite is a superstructure based on an NiAs-type subcell with alternating rows of ordered iron vacancies [10-15]. The 4C-type pyrrhotite is one of the many reported phases of pyrrhotite, Fe_{1-x}S , stable at low temperatures. Naturally occurring monoclinic 4C-type pyrrhotite is often described as having a composition corresponding to $x=0.125$ (*i.e.*, Fe_7S_8); however, synthetic 4C-type pyrrhotites have been reported to have compositions in the range $0.115 < x < 0.134$ [16,17]. The significance of the composition $x=0.125$ is that this composition corresponds to a concentration of vacancies that can be arranged into a simple and completely ordered structure [18]. It is well known that monoclinic 4C-type pyrrhotite arises from cooling the high-temperature, hexagonal, 1C-type pyrrhotite, which contains a disordered array of iron vacancies. This high-temperature, 1C-type phase is unquenchable and has a large composition range that increases with increasing temperature. A value $W_N=1.35$ following sulfidation of FA650 corresponds to $x < 0$ in Fe_{1-x}S , assuming sulfidation of all iron present. The negative value calculated for x , assuming complete sulfidation suggests incomplete sulfidation of the iron present.

6.4.2 Consecutive Reduction-Sulfidation

Desulfurization of coal gas by Fe_2O_3 or mixed iron-aluminum oxides involves

simultaneous reduction and sulfidation of the sorbent as in the experiment of the previous section. For the purpose of estimating the reactivity of different phases and measuring reaction rates, however, it is useful to separate reduction and sulfidation. Therefore, the remaining sorbents have been exposed to 5% H_2 in N_2 for ~ 8 minutes, then to 4.2% H_2S in N_2 for the next ~ 35 minutes, and finally to 4.2% H_2S in N_2 for the remaining time necessary to cool the sample.

An example of typical weight curves for isothermal reduction and sulfidation of mixed iron-aluminum oxides at $600^\circ C$ is shown in Figure 6.9. Extent of reduction was similar for these samples that contain an Fe:Al ratio of 2; however, both the rate of sulfidation and sulfur uptake decreased with increasing calcination temperature. Similar experiments were performed using three samples with an Fe:Al ratio of 1 and three samples with an Fe:Al ratio of 0.5. Results for all nine samples were summarized by a plot (Figure 6.10) of W_N following sulfidation (corresponding to a total elapsed time of 50 minutes) versus W_N following reduction (corresponding to a total elapsed time of between 8 and 10 minutes). There was good correlation between the extent of reduction and sulfur uptake with the exception of samples F2A800, FA800, 2FA700, and 2FA800. Samples 2FA700 and 2FA800 exhibited the lowest rates of sulfidation, while those for the remaining samples were approximately identical. The lower rates of sulfidation for samples 2FA700 and 2FA800 implied the presence of sintered iron-oxide phases in these samples which, in addition to lowering the rate of sulfidation, may also be responsible for lower sulfur uptake. Since it was observed in the $CuO \cdot Al_2O_3$ system that the presence of Al_2O_3 suppressed sintering of copper (Chapter III, Section 3.3.2), it is not surprising to find evidence for sintering of iron-oxide crystallites in the samples containing the lowest content of alumina. In the case of samples FA800 and F2A800, the presence of phases with very

slow sulfidation kinetics is proposed. A closer look at Figure 6.10 combined with XRD and SEM analyses provided further information for identification of such phases.

Further examination of Figure 6.10 reveals that for a given calcination temperature, sulfur uptake increases with increasing Fe:Al ratio. The difference in sulfur uptake for different Fe:Al ratios is most pronounced for a calcination temperature of 600°C, and the difference decreases with increasing calcination temperature. Extent of reduction is highest for a sample calcined at 600°C with an Fe:Al ratio of 0.5, and lowest for a sample calcined at 800°C with an Fe:Al ratio of 2. In fact, samples in order from most reducible to least reducible are F2A600, F2A700, F2A800, FA600, FA700a, FA700b, FA800, 2FA600, 2FA700, and 2FA800. The general trends of Figure 6.10 suggested that the reducibility of Fe-Al-O materials calcined at 600°C was due, in part, to the degree of dispersion of iron oxide in which increasing the ratio of iron to aluminum causes a marked decrease in dispersion, and increasing the calcination temperature causes a smaller but discernible decrease in dispersion. Not only is the rate of reduction affected by the dispersion of iron oxide, but the rate of sulfidation is lowered as a function of calcination temperature in samples containing a ratio Fe:Al of 2. For example, the rate of sulfidation for samples with Fe:Al ratios of 0.5 or 1 was independent of calcination temperature; on the other hand, the rate of sulfidation for samples with an Fe:Al ratio of 2 decreased with increasing calcination temperature, suggesting that to protect iron that is formed during reduction against sintering, samples containing a ratio of $\text{Fe:Al} \leq 1$ are required.

XRD analysis of quenched sulfided samples revealed monoclinic 4C-type pyrrhotite in all cases, which resulted from quenching the high-temperature, hexagonal, 1C-type pyrrhotite phase. There were also low-intensity broad peaks

discernible for an FeAl_2O_4 phase in most cases. These results suggested that FeAl_2O_4 has slow sulfidation kinetics, and thus, its presence may lead to low sulfur uptake. In support of this conclusion, sample F2A600 was reported earlier to contain a significant fraction of FeAl_2O_4 based on TPR, SEM, and BET data and demonstrated the lowest sulfur uptake of all samples studied as well as the highest crystalline FeAl_2O_4 content, according to XRD following sulfidation (Figure 6.11). Moreover, in sulfidation studies of $\text{CuO} \cdot \text{Al}_2\text{O}_3$, the compound CuAl_2O_4 was concluded to have slow sulfidation kinetics (Chapter V, Section 5.5.1), while CoAl_2O_4 was reported to be unsulfidable at 400°C [19]. Both CoAl_2O_4 and FeAl_2O_4 are normal spinels, with their divalent cations occupying exclusively tetrahedral sites and Al^{+3} occupying octahedral sites, while CuAl_2O_4 is a partially inverse spinel with 40% of Cu^{+2} occupying octahedral sites. Formation of a compound between the metal oxide and alumina apparently leads to decreased accessibility of the metal to sulfidation.

The extent of reduction exhibited by the series of samples containing an Fe:Al ratio of 1 (*i.e.*, $\alpha \sim 0.26$) falls in the second stage of reduction, where one would expect a small amount of FeAl_2O_4 to be present, depending on the relative rates of reactions 6.7 and 6.9. Sulfur uptake is similar for these samples because the compositions of the fresh samples were similar, and enough alumina is present to minimize sintering of iron-containing phases. Samples containing an Fe:Al ratio of 2 exhibit the highest sulfur uptakes because there is not a high enough ratio of alumina to iron oxide for significant FeAl_2O_4 formation. These results correlate high sulfur uptake to low FeAl_2O_4 content.

Isothermal reduction followed by sulfidation at 600°C of samples calcined at 600°C (FA600, F2A600, and 2FA600) is compared to that of a pure iron oxide sorbent calcined at 650°C (F650) in Figure 6.12. Rate of sulfidation is

slowest for the F650 sorbent, probably because of the presence of sintered Fe_2O_3 , sintered Fe_3O_4 , or both, in the reduced sorbent. Assuming sulfidation of all iron present in 2FA600 to Fe_{1-x}S , the sulfur uptake corresponds to $x=0.120$. This x -value is within the composition range $0 < x < 0.145$ reported for high-temperature, hexagonal, 1C-type pyrrhotite at 600°C [20] and the composition range $0.115 < x < 0.134$ reported for synthesized low-temperature, monoclinic, 4C-type pyrrhotite. Iron sulfide conversions following reduction and sulfidation (corresponding to a total elapsed time of only 50 minutes) at 600°C are estimated in Table 6.4, assuming that the products are Fe_2O_3 and $\text{Fe}_{0.88}\text{S}$, or FeAl_2O_4 and $\text{Fe}_{0.88}\text{S}$. Actual iron sulfide yields are probably closer to the latter for sorbents with an Fe:Al ratio of 0.5, closer to the former for an Fe:Al ratio of 2, and between the two cases for an Fe:Al ratio of 1.

Scanning electron micrographs of samples reduced at 600°C (~ 15 minutes by 5% H_2 in N_2) showed some interesting features. For example, reduced samples of 2FA600 and FA600 looked very similar (Figure 6.13), both displaying a bimodal distribution of oddly shaped surface clumps. The particles at either extreme of the bimodal size distribution were notably different; those of sample FA600 were far less dispersed and had a greater size difference than those of 2FA600. On the other hand, the reduced sample of F2A600 displayed faceted crystals of hexagonal shape, which were presumably iron (Fe^0). This same crystal morphology has been reported for the reduction of FeAl_2O_4 at 911°C with H_2 [21]. When reduced samples (~ 8 minutes at 600°C under 5% H_2 in N_2) were sulfided (~ 35 minutes by 4.2% H_2S in N_2) at 600°C , SEM revealed irregular-shaped faceted crystals for both 2FA600 and FA600 (Figure 6.14). In the case of F2A600, however, the appearance of the surface was quite different. Instead of smooth, faceted crystals, sulfided F2A600 had the appear-

ance of a smooth surface with granular textured particles scattered on top of it. The smooth surface may have been characteristic of unreacted FeAl_2O_4 , or the textured particles may have been indicative of a mixture of FeAl_2O_4 and pyrrhotite. XRD identified a significant amount of both of these components, which together comprised the entire crystalline phase (Figure 6.11). It should be noted that since these specimens were obtained by quenching to room temperature, the observed surface morphology may be different from that which exists *in situ*, at high temperature. The succession of scanning electron micrographs summarized in each of Figures 6.15 and 6.16 show the different structural changes that occur to an iron-rich sorbent (2FA600, Figure 5.16) versus an alumina-rich sorbent (F2A600, Figure 5.15), upon reduction and sulfidation.

REFERENCES

1. Marqueen, T.J., Carbonne, D.J., and Ligammari, J., "Coal Gasification Combined Cycle Systems-Technical Horizons," *Proc. Amer. Pow. Conf.*, **48**, 235, 1986.
2. Tamhankar, S.S., Bagajewicz, M., Gavalas, G.R., Sharma, P.K., and Flytzani-Stephanopoulos, M., "Mixed-Oxide Sorbents for High-Temperature Removal of Hydrogen Sulfide," *I.E.C. Process Design Dev.*, **25**, 429, 1986.
3. Tseng, S.C., Tamhankar, S.S., and Wen, C.Y., *Chem. Eng. Sci.*, **36**, 1287, 1981.
4. Joshi, D., Olson, J.H., Hayes, M.L., and Shah, V., APCI Final Report to DOE under contract FE-77-C-01-2757, 1979.
5. Marcilly, C., Courty, P., and Delmon, B., "Preparation of Highly Dispersed Mixed Oxides and Oxide Solid Solutions by Pyrolysis of Amorphous Organic Precursors," *J. Amer. Cer. Soc.*, **53**(1), 56, 1970.
6. Rau, M.-F., Rieck, D., and Evans, J.W., "Investigation of Iron Oxide Reduction by TEM," *Metall. Trans. B*, **18B**, 257, 1987.
7. Turnock, A.C., and Eugster, H.P., "Fe-Al Oxides: Phase Relationships Below 1000°C", *J. Petrol.*, **3**(3), 533, 1962. , p.533, 1962.
8. Ying-Ru, D., Qi-Jie, Y., Yuan-Fu, H., Yong-Shu, J., and Jin-Heng, Q., "A Mössbauer Investigation of α -Fe₂O₃ Microcrystals Supported on γ -Al₂O₃," in *Mössbauer Spectroscopy and its Chemical Applications* ed. by J.G. Stevens and G. K. Shenoy (American Chemical Society: Washington, D.C., 1981), p. 609.
9. Lycourghiotis, A., and Vattis, D., "Temperature Programmed Reduction Study of Alumina Supported Fe⁺³ Catalysts," *React. Kin. Catal. Lett.*,

- 18(3-4), 337, 1981.
10. Morimoto, N., Nakazawa, H., Nishiguchi, K., and Tokonami, M., "Pyrrhotites: Stoichiometric Compounds with Composition $\text{Fe}_{1-n}\text{S}_n$ ($n \geq 8$)," *Science*, **168**, 964, 1970.
 11. Morimoto, N., Gyobu, A., Mukaiyama, H., and Izawa, E., "Crystallography and Stability of Pyrrhotites," *Econ. Geol.*, **70**, 824, 1975.
 12. Desborough, G.A., and Carpenter, R.H., "Phase Relations of Pyrrhotite," *Econ. Geol.*, **60**, 1431, 1965.
 13. Mukherjee, B., "Crystallography of Pyrrhotite," *Acta Cryst.*, **B25**, 673, 1969.
 14. Nakazawa, H., Motimoto, N., and Watanabe, E., *Amer. Mineral.*, **60**, p.359, 1975.
 15. Morimoto, N., Nakazawa, H., and Watanabe, E., "Direct Observation of Metal Vacancies by High-Resolution Electron Microscopy. Part I: 4C Type Pyrrhotite (Fe_7S_8)," *Proc. Jap. Ac.*, **50**, 756, 1974.
 16. Kissin, S.A., and Scott, S.D., "Phase Relations Involving Pyrrhotite Below 350°C ," *Econ. Geol.*, **77**, 1739, 1982.
 17. Carpenter, R.H., and Desborough, G.A., "Range in Solid Solution and Structure of Naturally Occurring Troilite and Pyrrhotite," *Amer. Mineral.*, **49**, 1350, 1964.
 18. Putnis, A., "Observations on Coexisting Pyrrhotite Phases by Transmission Electron Microscopy," *Contrib. Mineral. Petrol.*, **52**, 307, 1975.
 19. Chung, K.S., and Massoth, F.E., "Studies on Molybdena-Alumina Catalysts VIII Effect of Cobalt on Catalyst Sulfiding," *J. Catal.*, **64**, 332, 1980.
 20. Toulmin, P., and Barton, P.B., *Geochim. Cosmochim. Acta*, **28**(5), 641, 1964.

21. Gaballah, I., Gleitzer, C., and Emeraux, J.P., "Kinetics of Reduction of the Iron Aluminate FeAl_2O_4 (hercynite) by Hydrogen," *Mémoires Scientifiques Revue Métallurgie*, **73**(6), 425, 1976.

Table 6.1: Chemical and physical properties of fresh Fe-Al-O samples.

Sample	Fe:Al Mole Ratio	T _{calc} ^a (°C) [L ^b (hrs.)]	BET Area (m ² /g)	Fe ₂ O ₃ ^c	Fe ₃ O ₄	FeAl ₂ O ₄
F650	1:0	650[4]	2.2(±9%)	major	none	none
FA650	1:1	650[4]		major	medium	small
FA600	1:1	600[8]	91.7(±3%)	small	major	none
FA700a	1:1	700[8]	57.2(±0.2%)	major	major	medium
FA700b	1:1	700[16]	53.8(±0.6%)	major	medium	small
FA800	1:1	800[8]	18.7(±2%)	major	medium	trace
F2A600	1:2	600[8]	43.2(±1.4%)	none	none	none
F2A700	1:2	700[16]	88.7(±0.6%)	small	medium	major
F2A800	1:2	800[8]	57.0(±1.4%)	major	trace	medium
2FA600	2:1	600[10.5]	79.7(±0.8%)	medium	major	small
2FA700	2:1	700[8]	39.0(±6%)	major	medium	trace
2FA800	2:1	800[8]	14.9(±0.7%)	major	small	none

^a Calcination temperature.

^b Duration of calcination.

^c Relative composition in crystalline phase according to XRD.

Table 6.2: Kinetic data for the reduction of Fe-Al-O samples obtained from Figures 6.5 and 6.7.

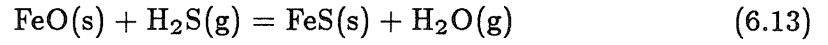
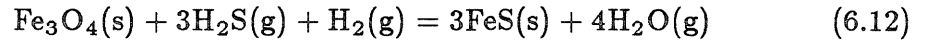
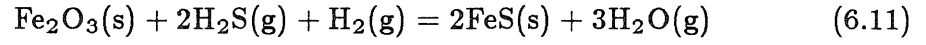
Sample	First Peak Rate (min^{-1}) [$\alpha_1^a, T_1^b(^{\circ}\text{C})$]	α_{12}^c	Second Peak Rate (min^{-1}) [$\alpha_2, T_2(^{\circ}\text{C})$]	α_{23}	Third Peak Rate (min^{-1}) [$\alpha_3, T_3(^{\circ}\text{C})$]
2FA600	0.00547[0.109,344]	0.190	0.00477[0.482,537]	0.772	0.00222[0.885, 768]
2FA700	0.00552[0.077,352]	0.155	0.00440[0.420,537]	0.727	0.00278[0.866, 797]
2FA800	0.00425[0.072,396]	0.139	0.00387[0.519,638]	0.672	0.00339[0.814, 813]
FA600	0.00346[0.114,396]	0.174	0.00382[0.519,634]	0.681	0.00311[0.846, 843]
FA700a	0.00588[0.110,345]	0.218	0.00388[0.418,530]	0.654	0.00282[0.867, 808]
FA800	0.00369[0.151,338]	0.242	0.00328[0.556,616]	0.641	0.00272[0.789, 767]
F2A600	0.00487[0.182,371]	0.357	0.00267[0.386,471]	0.513	0.00401[0.812, 859]
F2A700	0.00493[0.195,357]	0.342	0.00229[0.422,507]	0.605	0.00372[0.852, 865]
F2A800	0.00624[0.110,349]	0.286	0.00251[0.403,551]	0.540	0.00376[0.744, 794]

^a α_i Conversion at the maximum rate of reduction during stage i.

^b T_i Temperature at the maximum rate of reduction during stage i.

^c α_{ij} Conversion at the end of stage i or onset of stage j.

**Table 6.3: Sulfidation Equilibrium Constants and
Equilibrium Outlet H₂S Concentrations^a for Iron Oxide.**



T(°C)	log ₁₀ (K)			(H ₂ S) _{eq} ^b		
	6.11	6.12	6.13	6.11	6.12	6.13
600	7.20	8.50	2.55	70	395	705
650	6.99	8.19	2.40	89	502	995
700	6.81	7.90	2.28	110	627	1312
750	6.46	7.38	2.06	165	934	2177

^a For a gas with 20% H₂, 25% H₂O, 1 atm total pressure.

^b Concentration at equilibrium in ppm.

Table 6.4: Estimated conversions of Fe-Al-O samples to pyrrhotite, following consecutive reduction-sulfidation at 600°C.

Sample	Fe:Al Mole Ratio	T _{calc} (°C) [L(hrs.)]	Fe _{0.88} S [Y ^a (mole %)]	FeAl ₂ O ₄ [Y(mole %)]	Fe _{0.88} S [Y(mole %)]	Fe ₂ O ₃ [Y(mole %)]
F650	1:0	650[4]			93	7
FA600	1:1	600[8]	88	12	81	9
FA700a	1:1	700[8]	87	13	80	10
FA700b	1:1	700[16]	89	11	82	8
FA800	1:1	800[8]	85	15	76	24
F2A600	1:2	600[8]	52	48	20	80
F2A700	1:2	700[16]	75	25	58	42
F2A800	1:2	800[8]	75	25	59	41
2FA600	2:1	600[10.5]	100	0	100	0
2FA700	2:1	700[8]	92	8	87	13
2FA800	2:1	800[8]	85	15	76	24

^a Yield in mole percent.

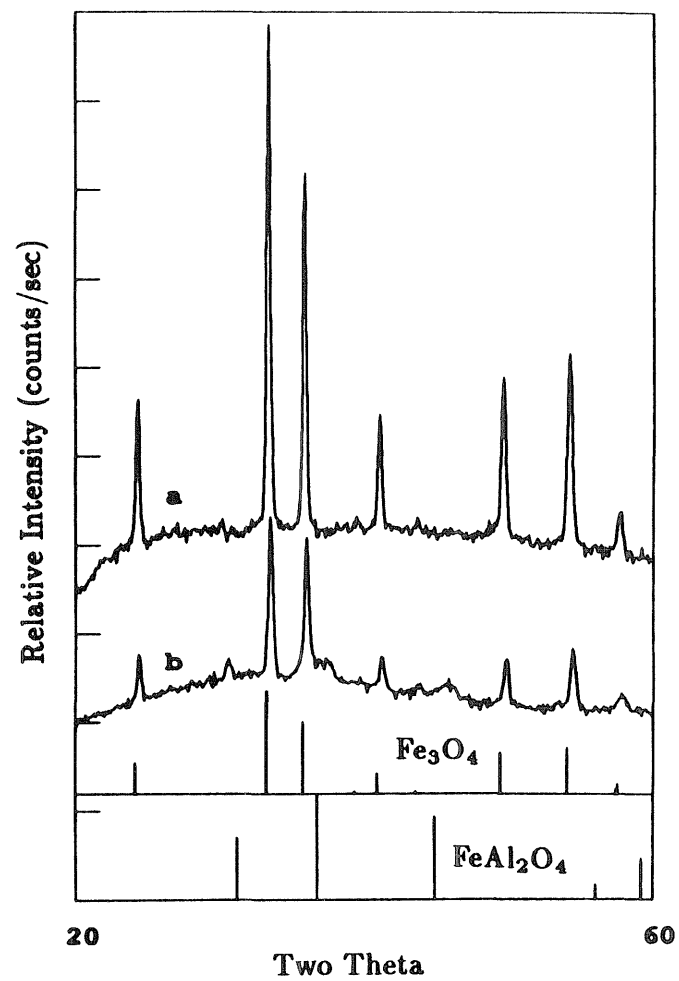
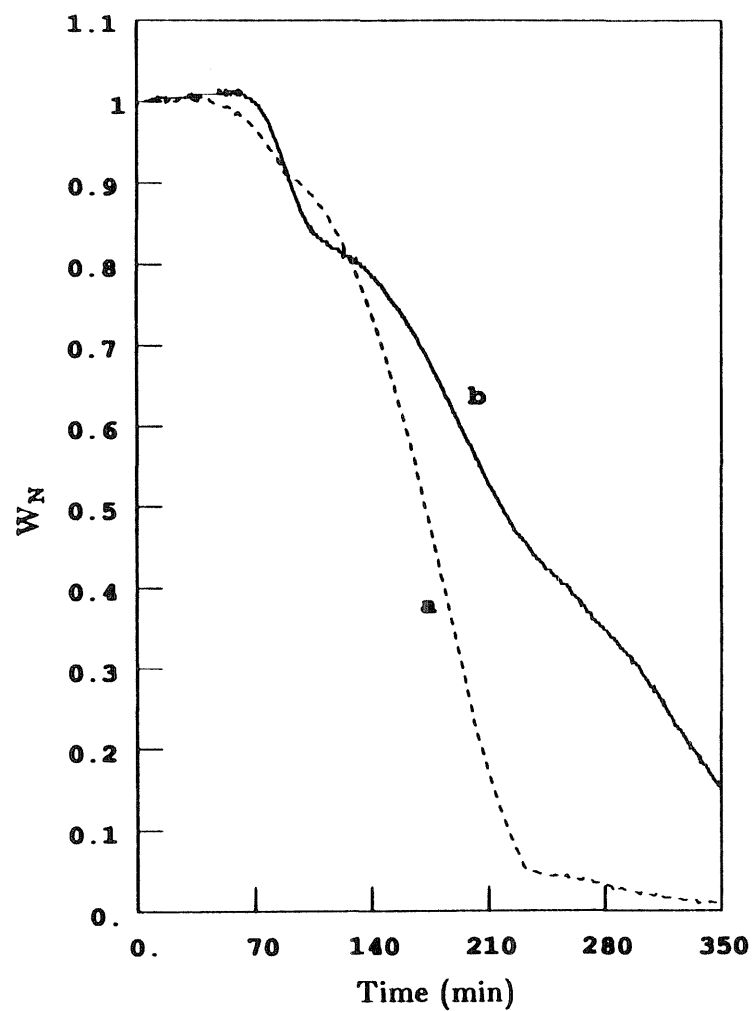


Figure 6.1: XRD patterns of fresh F650 (a) and FA650 (b), and corresponding normalized weight-loss profiles for TPR using a heating rate of $1.7^\circ\text{C}/\text{min}$ from 233°C to 912°C .

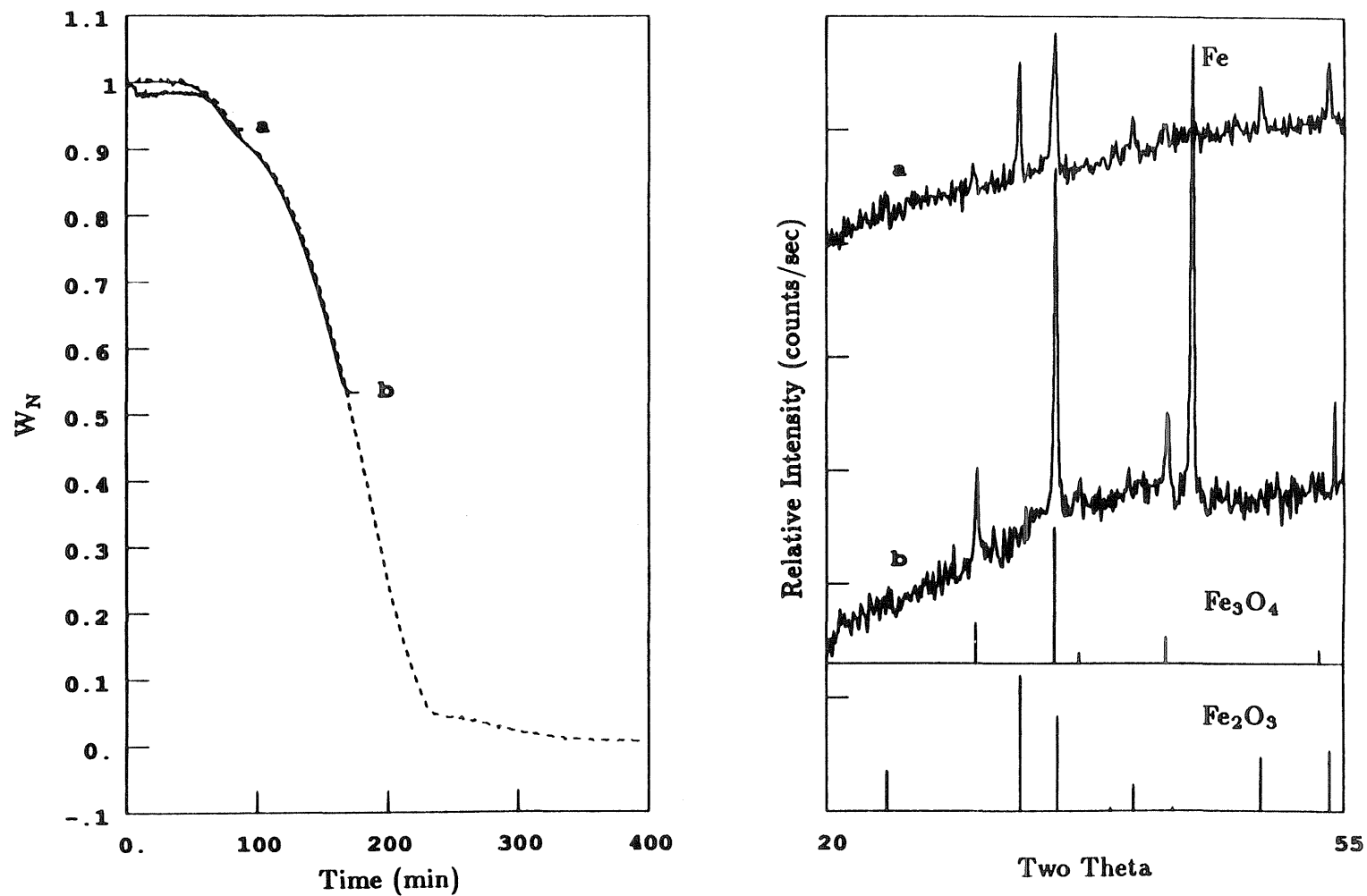


Figure 6.2: XRD patterns of partially reduced F650 after quenching during the TPR experiment as indicated (the single peak for Fe is observed only in the bottom pattern).

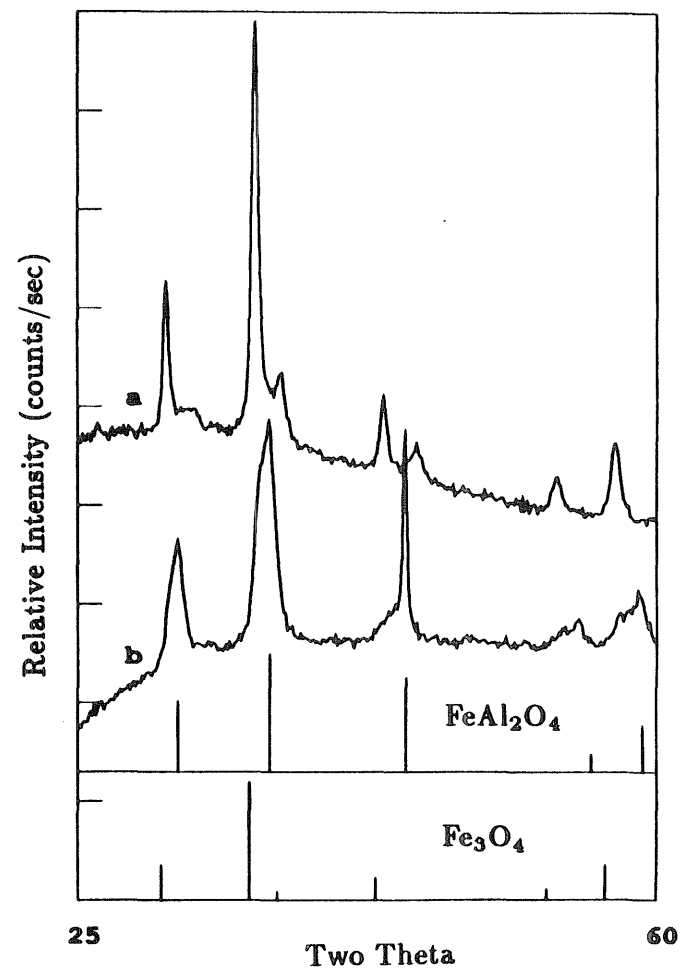
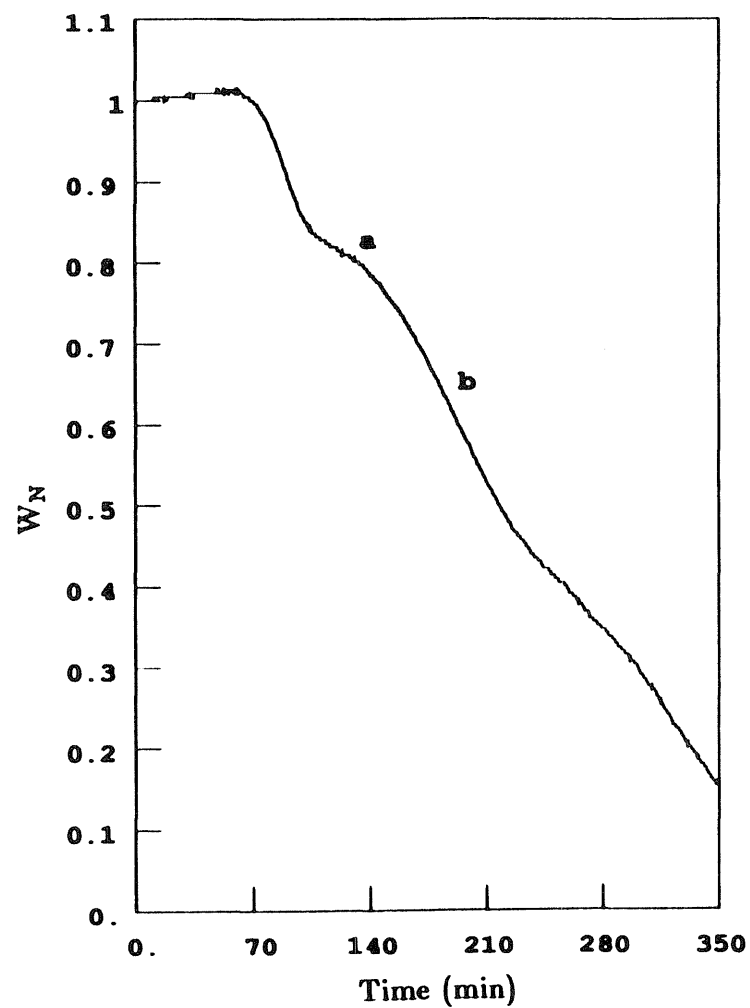


Figure 6.3: XRD patterns of partially reduced FA650 after quenching during the TPR experiment as indicated.

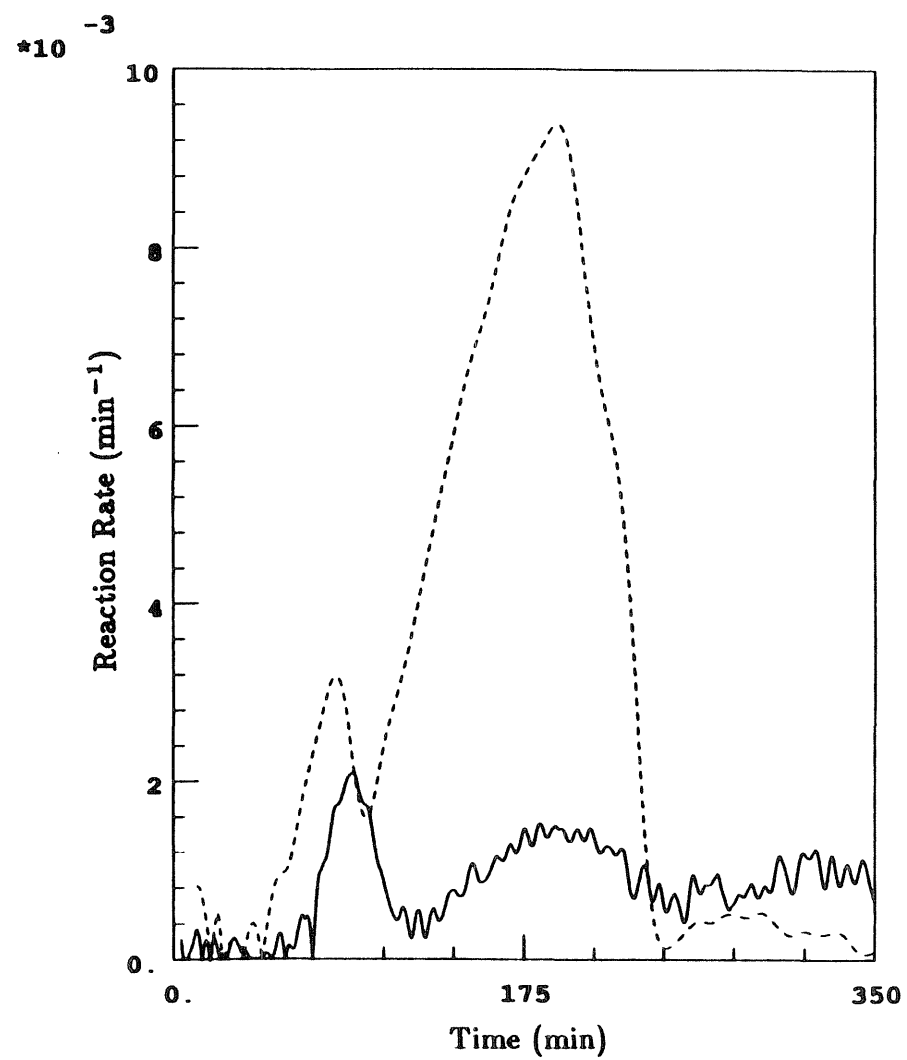


Figure 6.4: Reaction rate versus time for TPR of F650 (---) and FA650 (—).

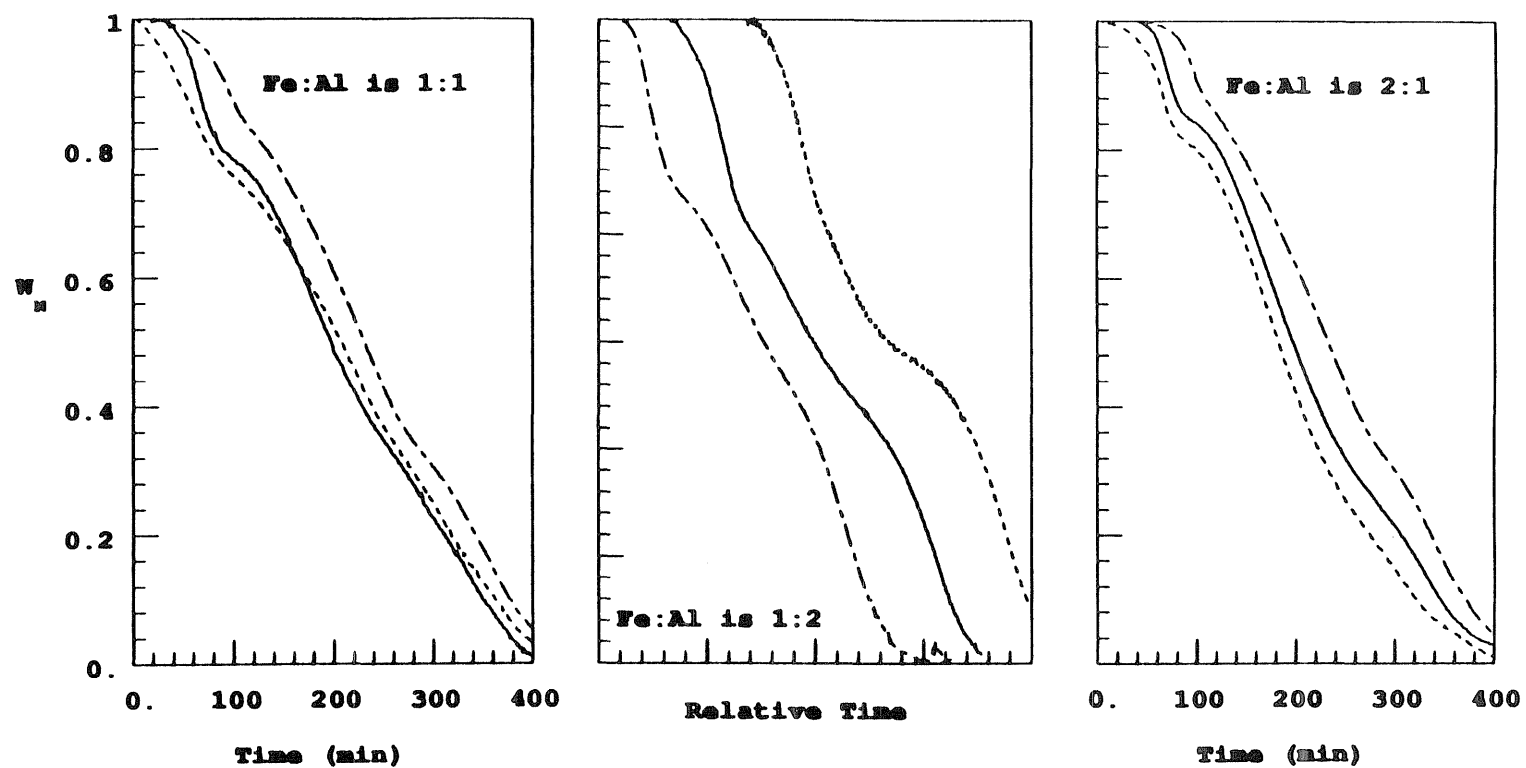
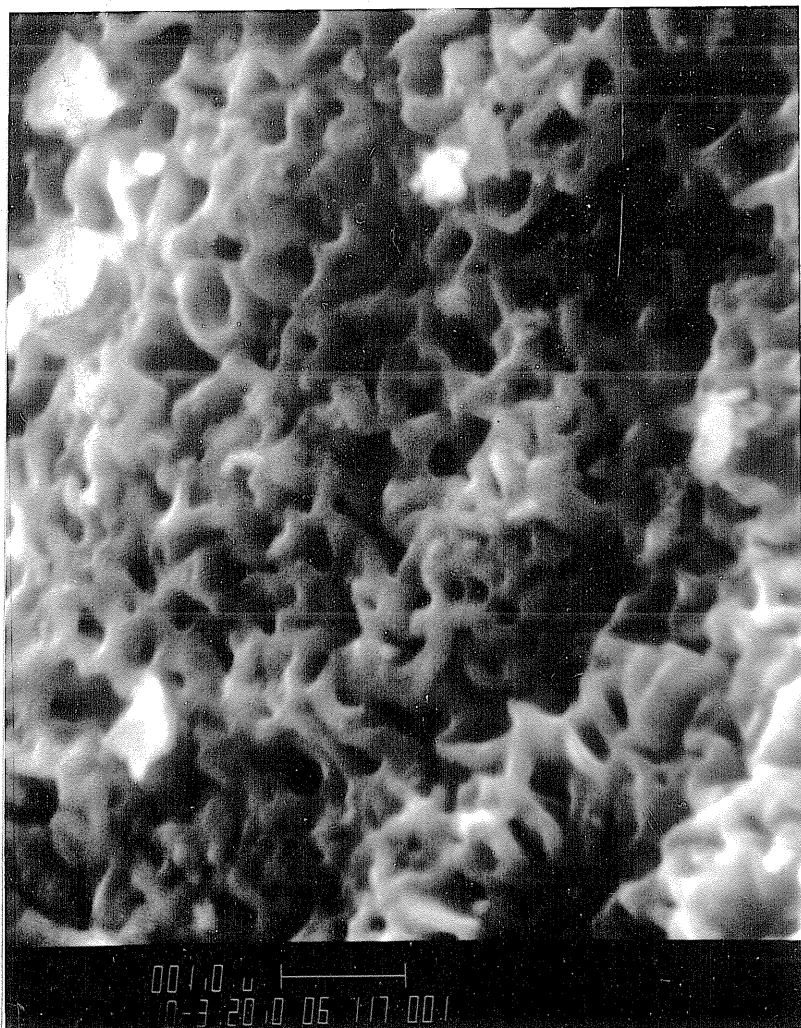
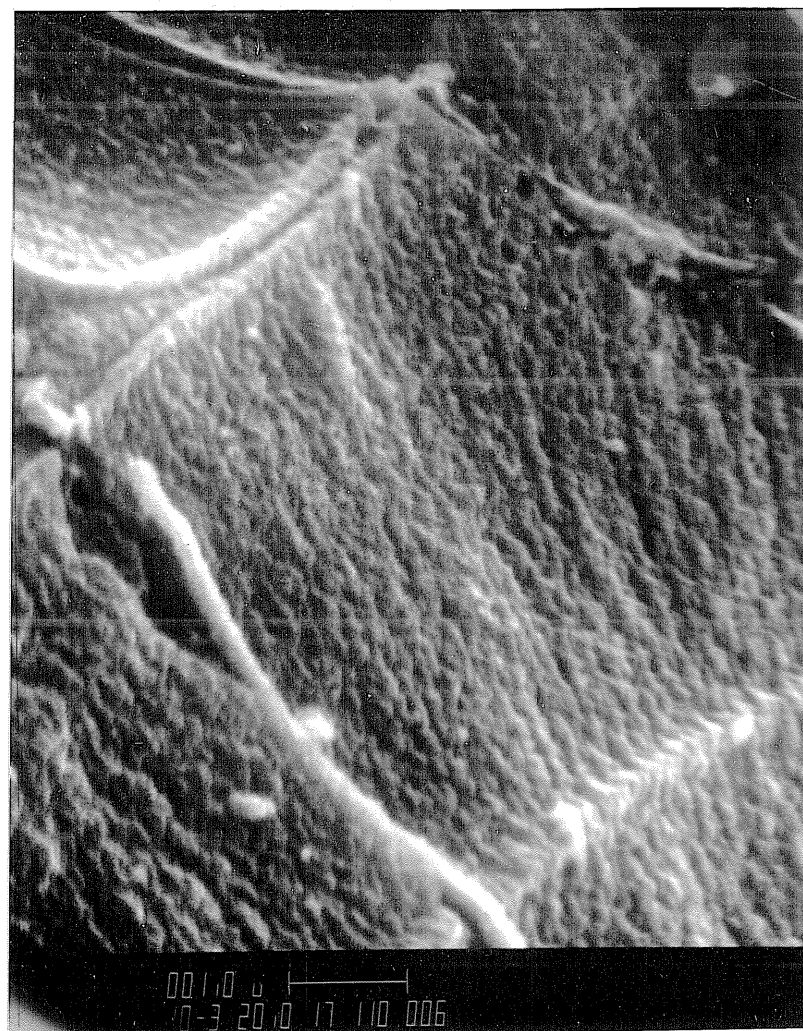


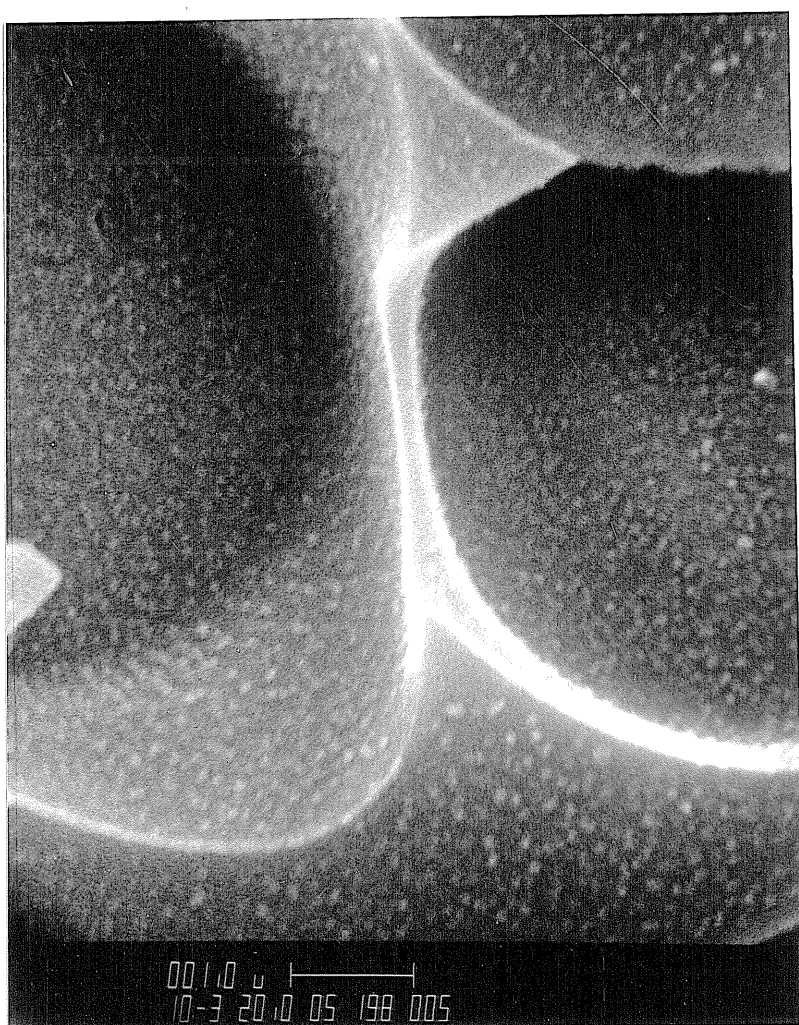
Figure 6.5: Normalized weight-loss profiles for TPR of Fe-Al-O samples calcined at 600°C (---), 700°C (—), and 800°C (— · —).



(a) F650 at 10 000×



(b) 2FA600 at 10 000×



(c) FA600 at 10 000×



(d) F2A600 at 10 000×

Figure 6.6: Scanning electron micrographs (markers are 1μ) of fresh samples comparing F650 to Fe-Al-O materials calcined at 600°C with different Fe:Al ratios.

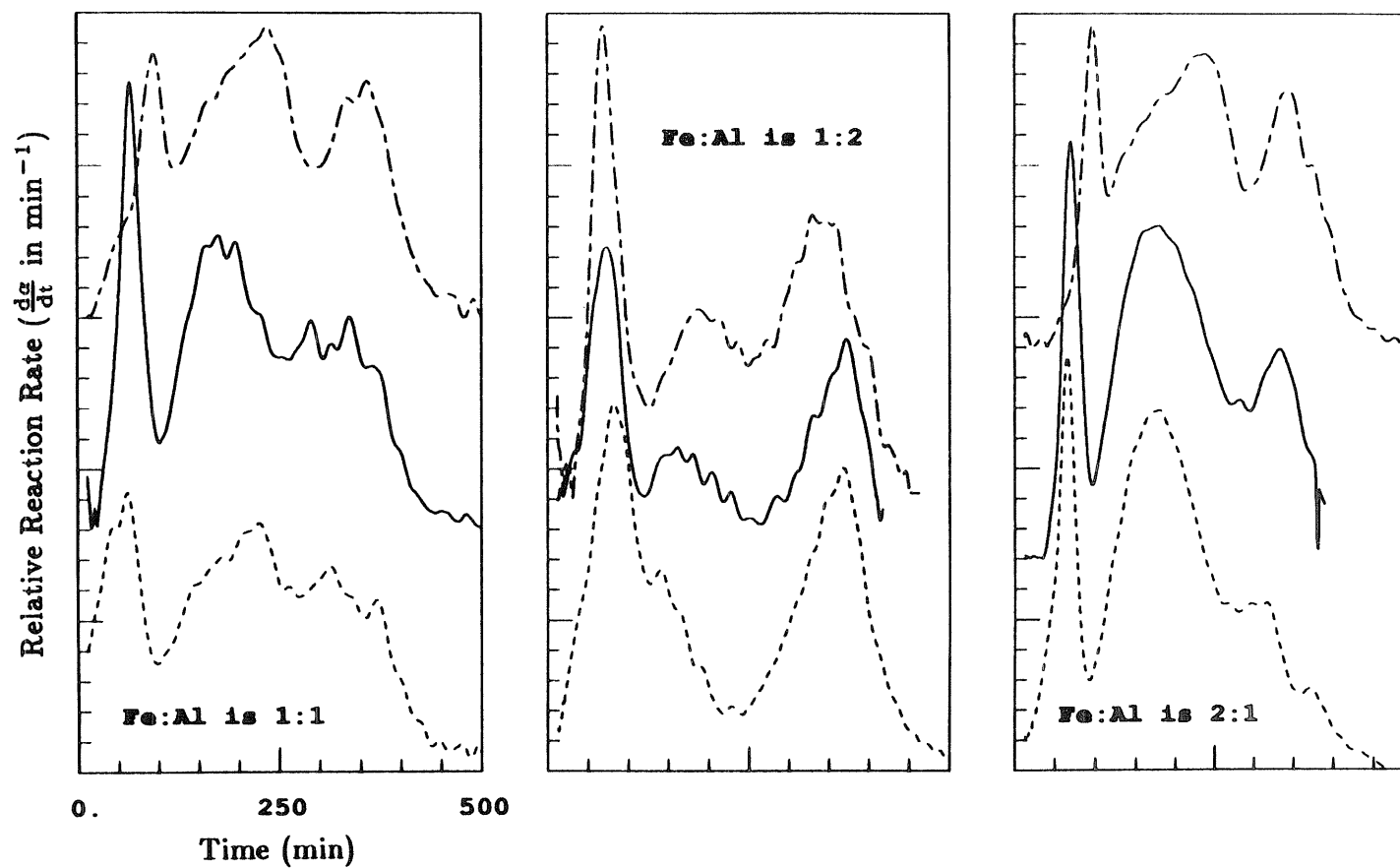


Figure 6.7: Reaction rate versus time for TPR of Fe-Al-O samples calcined at 600°C (- - -), 700°C (—), and 800°C (— -).

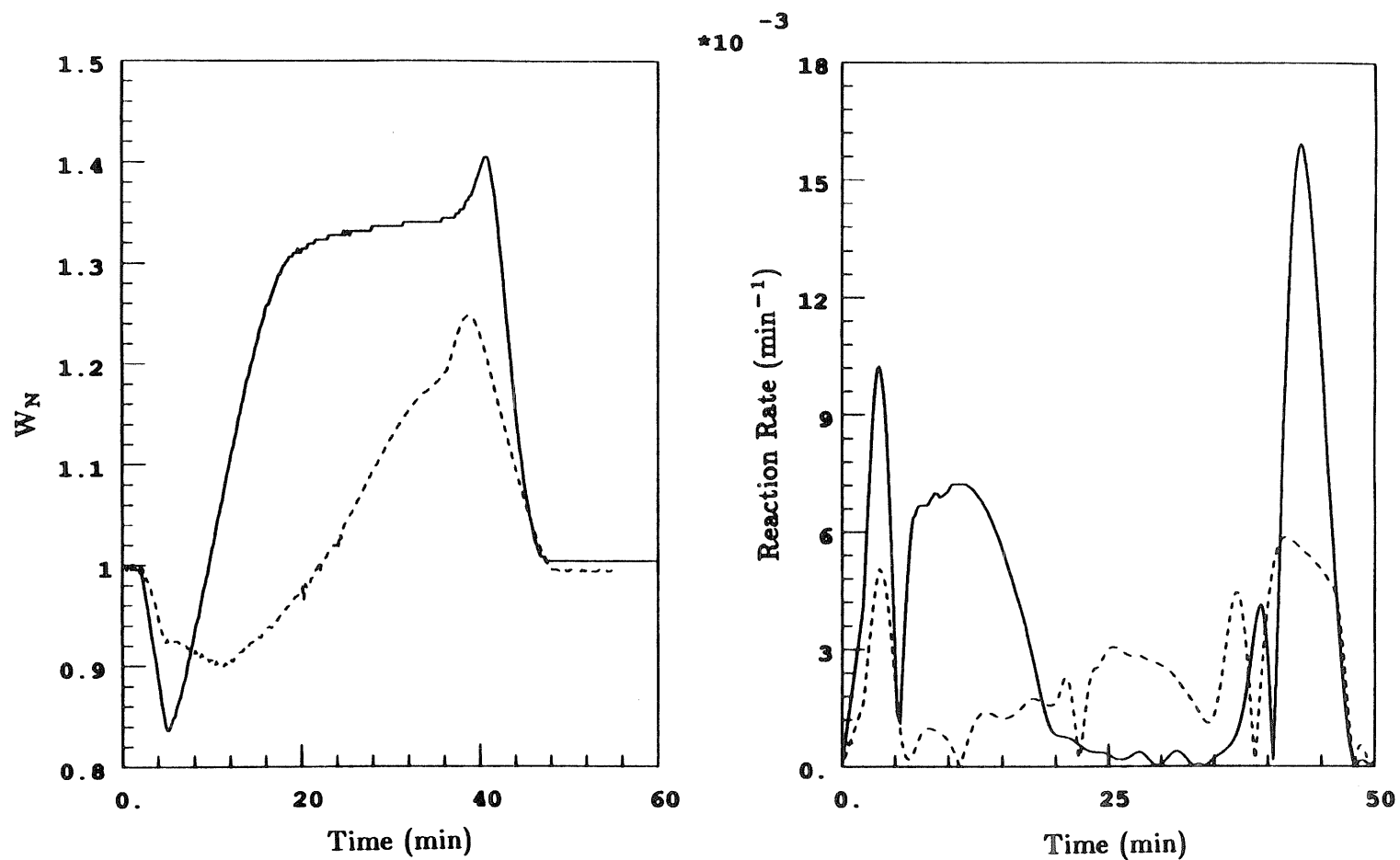


Figure 6.8: Normalized weight-loss curves for the reaction of FA650 (—) and F650 (- - -) at 700°C with a mixture containing 13% H_2 , 4% H_2S , and balance N_2 followed by regeneration in air.

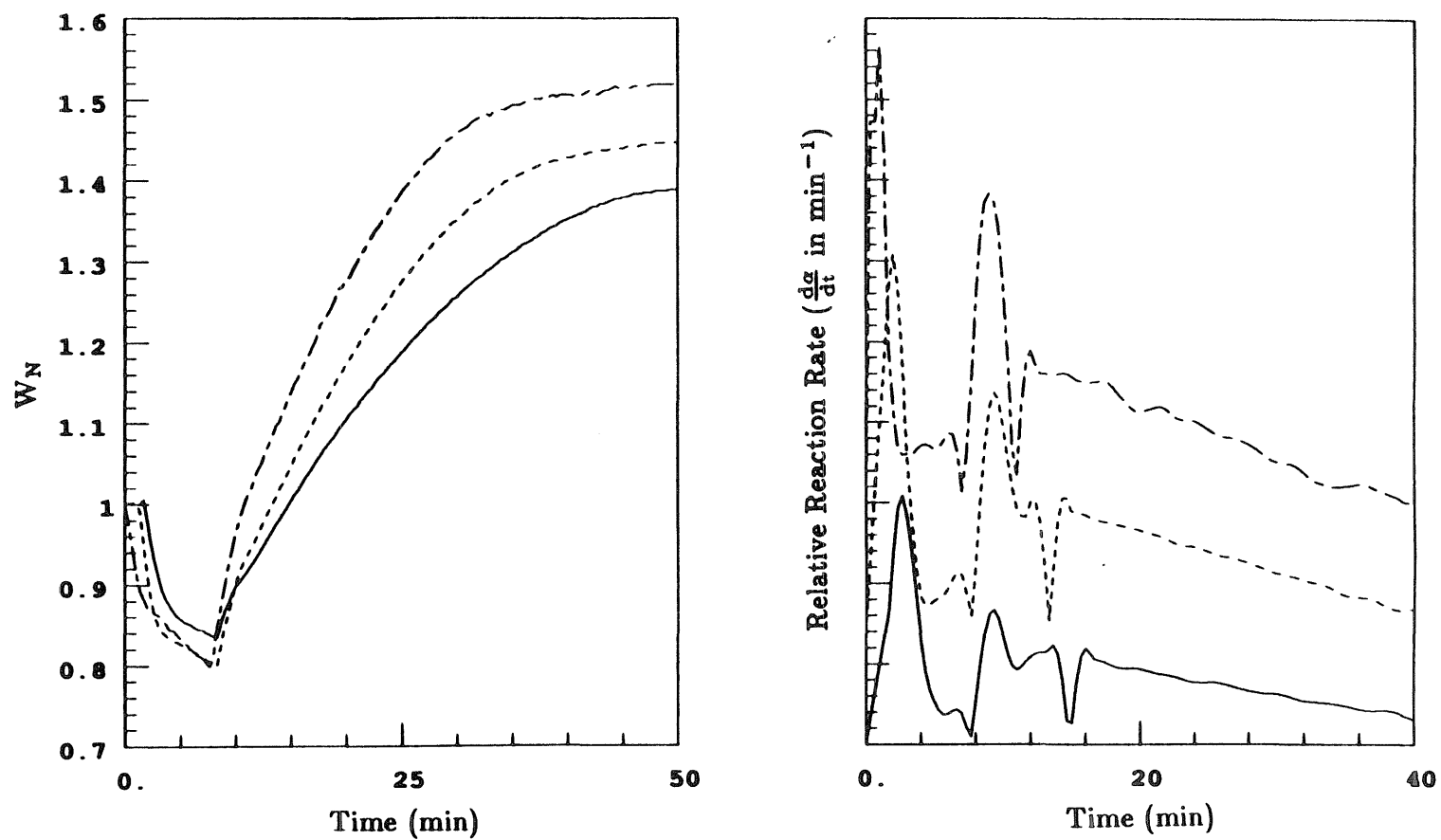


Figure 6.9: Normalized weight-loss curves for reduction followed by sulfidation at 600°C of 2FA600 (—), 2FA700 (---), and 2FA800 (— ·).

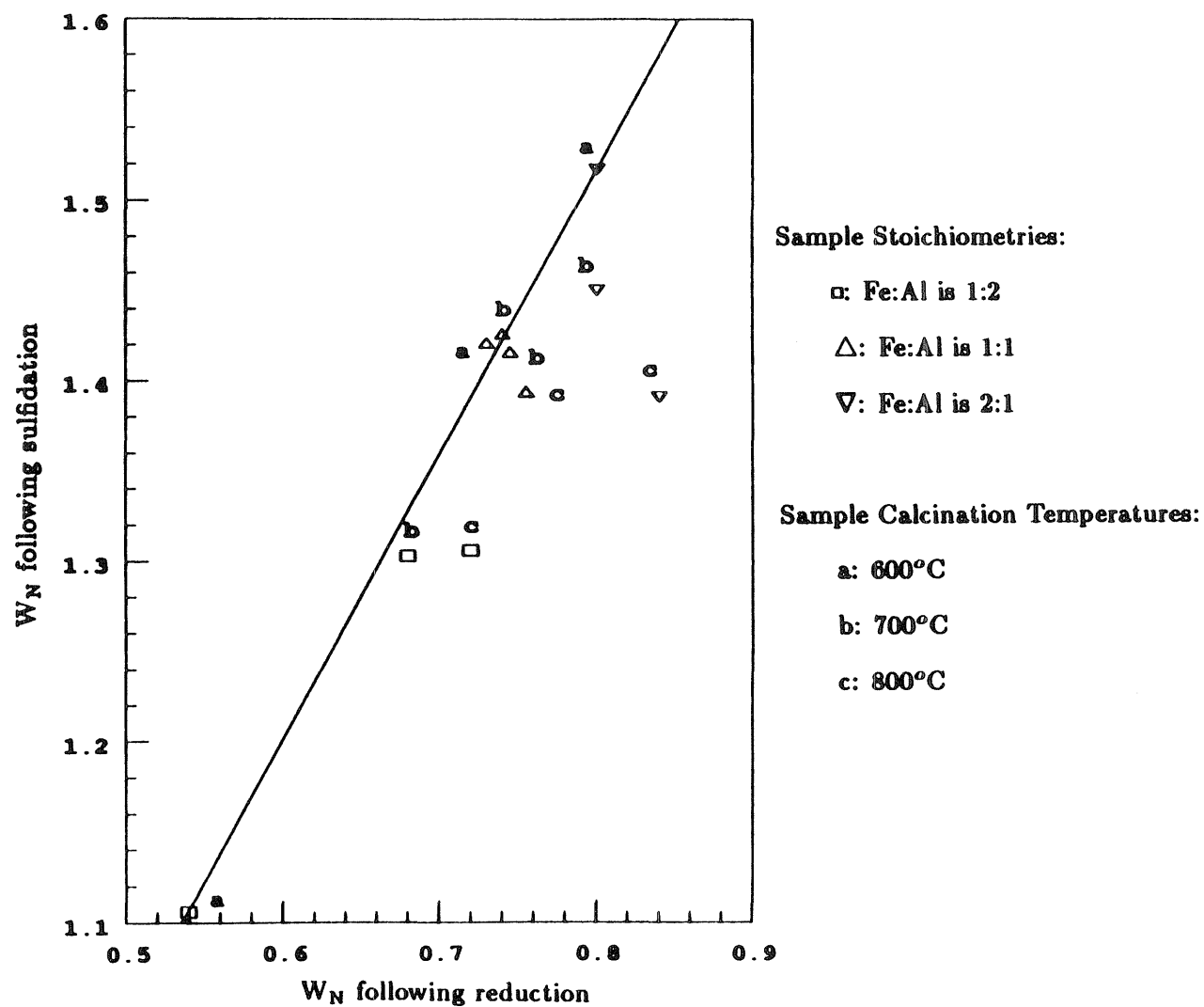


Figure 6.10: Sulfur uptake versus extent of reduction for different Fe-Al-O samples.

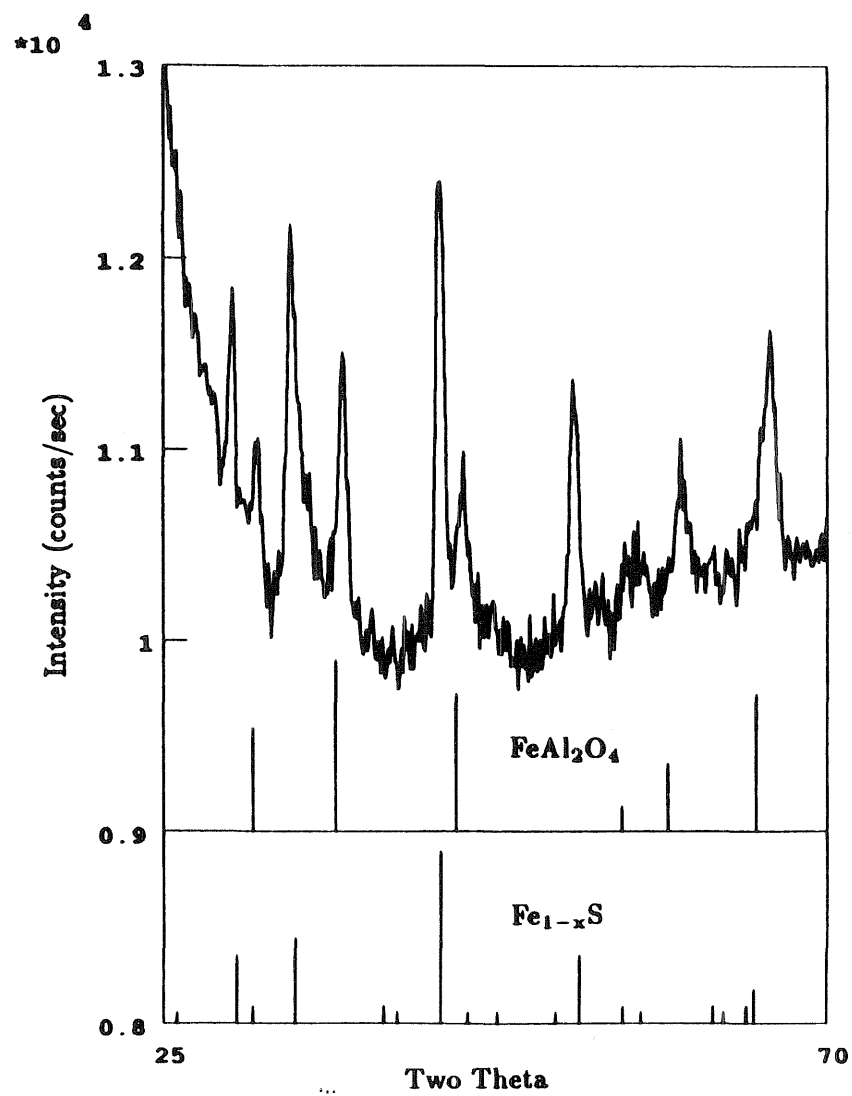


Figure 6.11: The XRD pattern of F2A600 sulfided at 600°C.

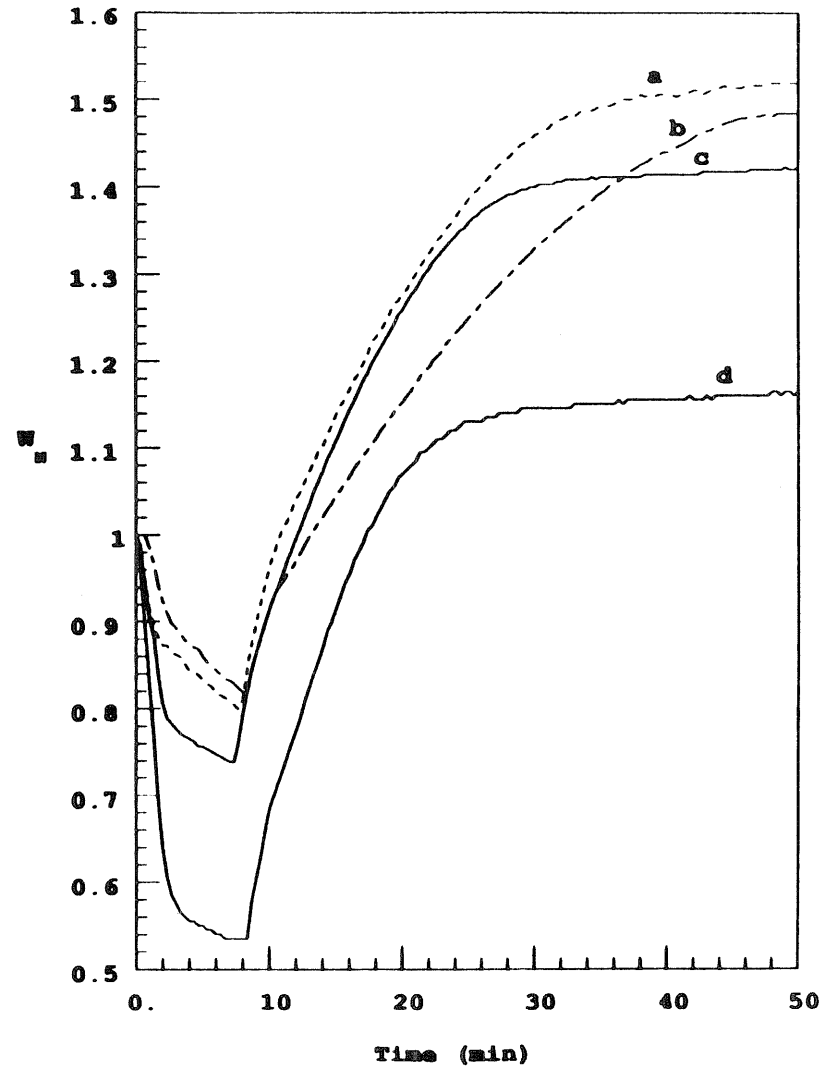
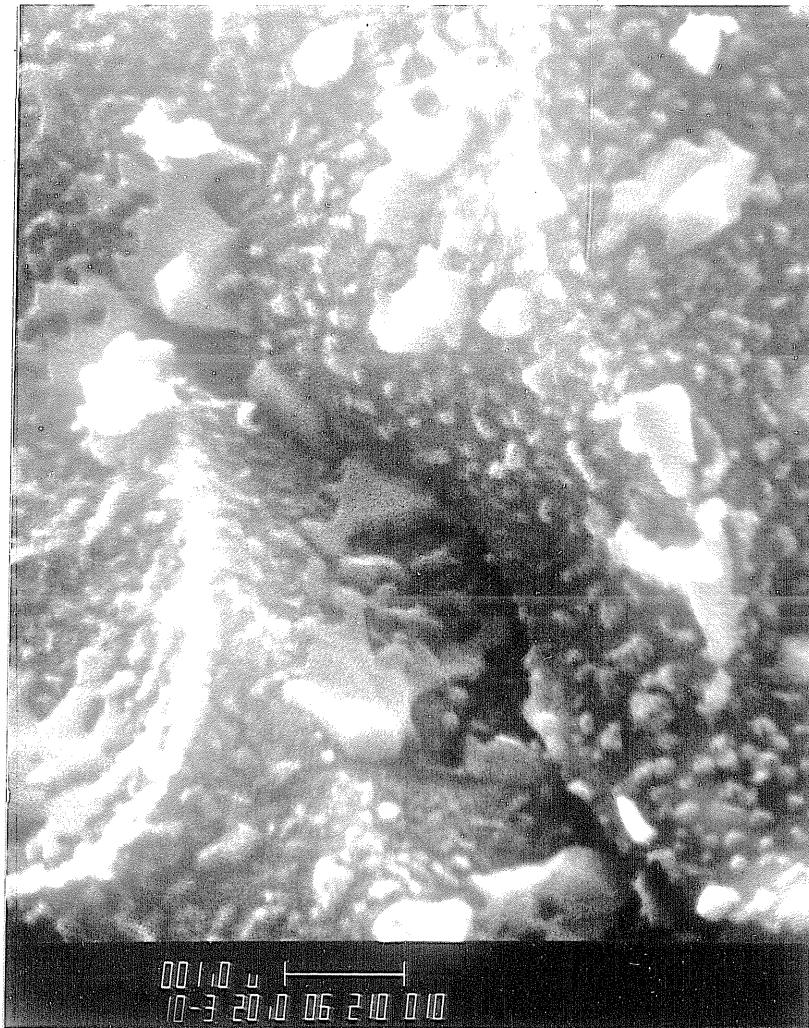


Figure 6.12: Normalized weight-loss curves for reduction followed by sulfidation at 600°C of 2FA600 (a), F650 (b), FA600 (c), and F2A600 (d).



(a) 2FA600 at 10 000×

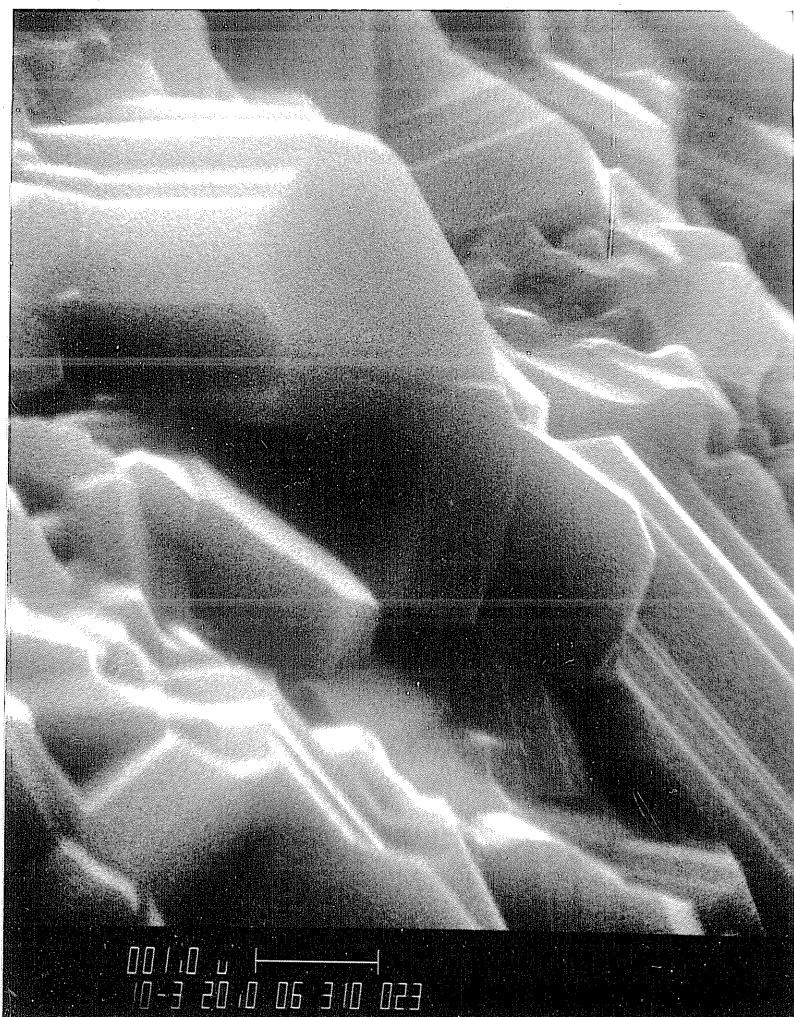


(b) FA600 at 10 000×



(c) F2A600 at 10 000×

Figure 6.13: Scanning electron micrographs (markers are 1 μ m) of Fe-Al-O samples reduced at 600°C for \sim 15 minutes.



(a) 2FA600 at 10 000×



(b) FA600 at 10 000×

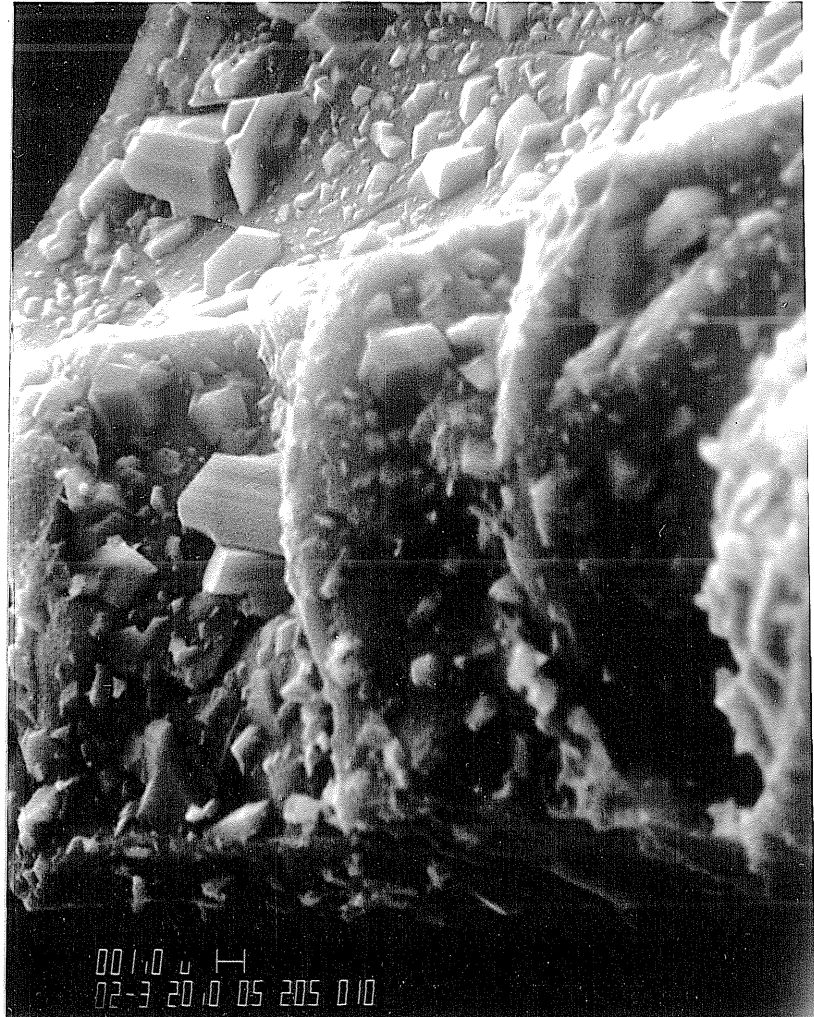


(c) F2A600 at 10 000×

Figure 6.14: Scanning electron micrographs (markers are $1\mu\text{m}$) of Fe-Al-O samples sulfided at 600°C for ~ 35 minutes.



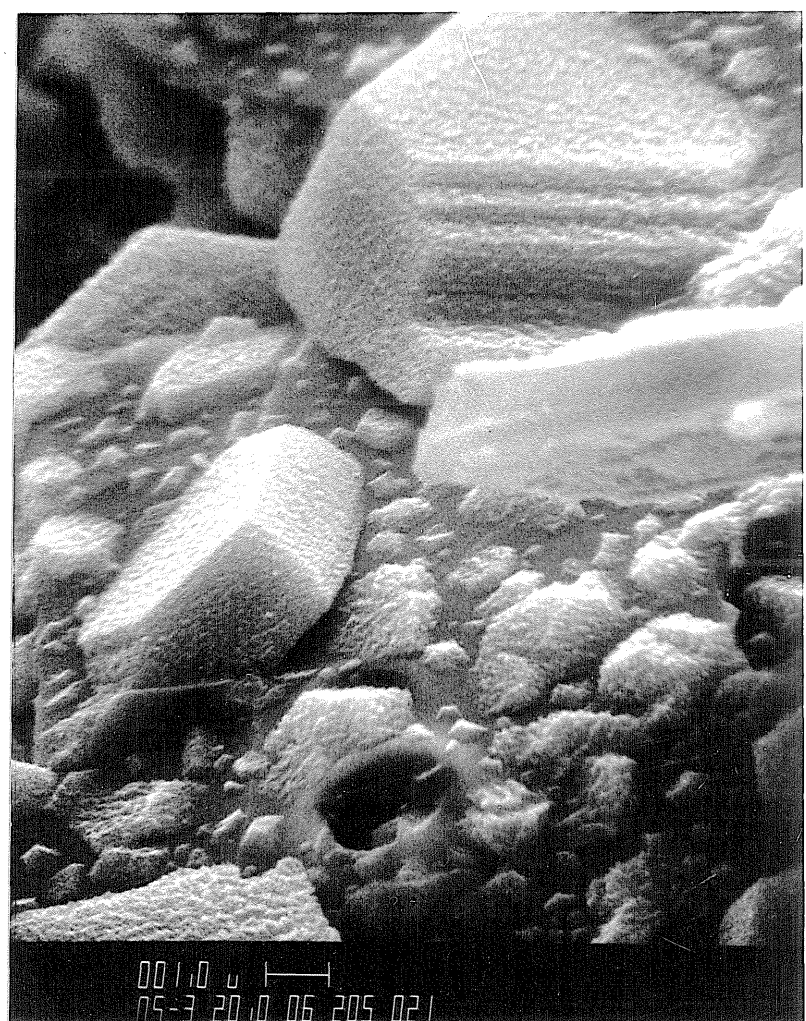
(a) Fresh at 2000×



(b) Reduced at 2000×

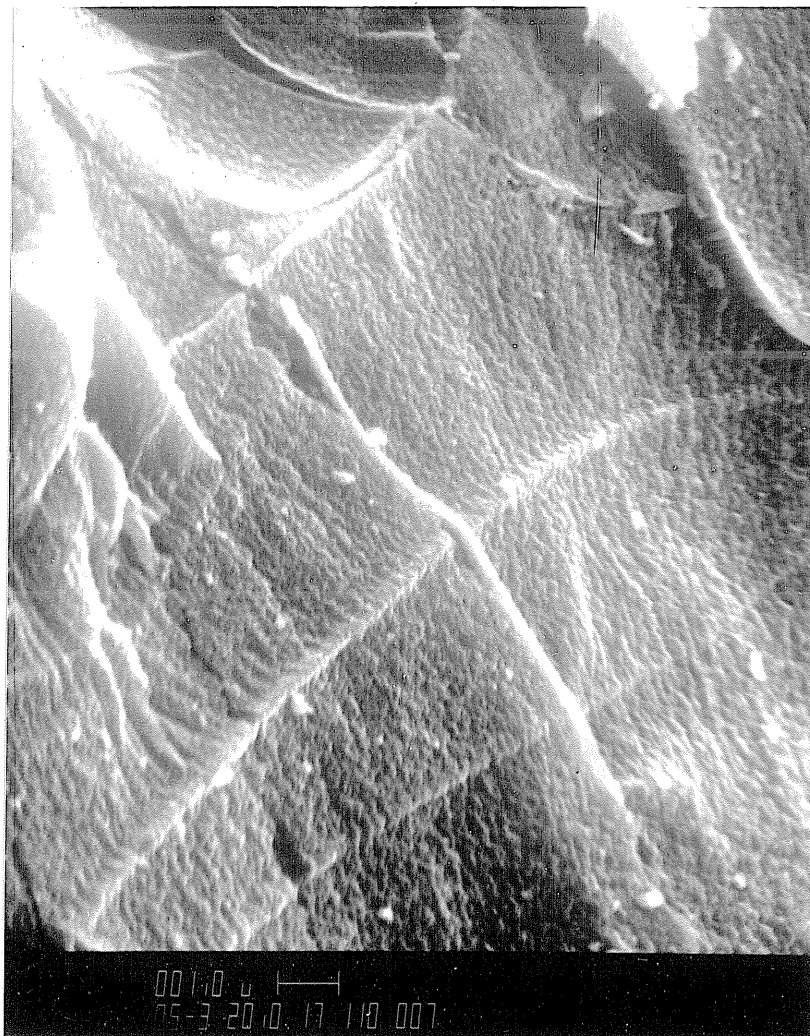


(c) Sulfided at 2000×

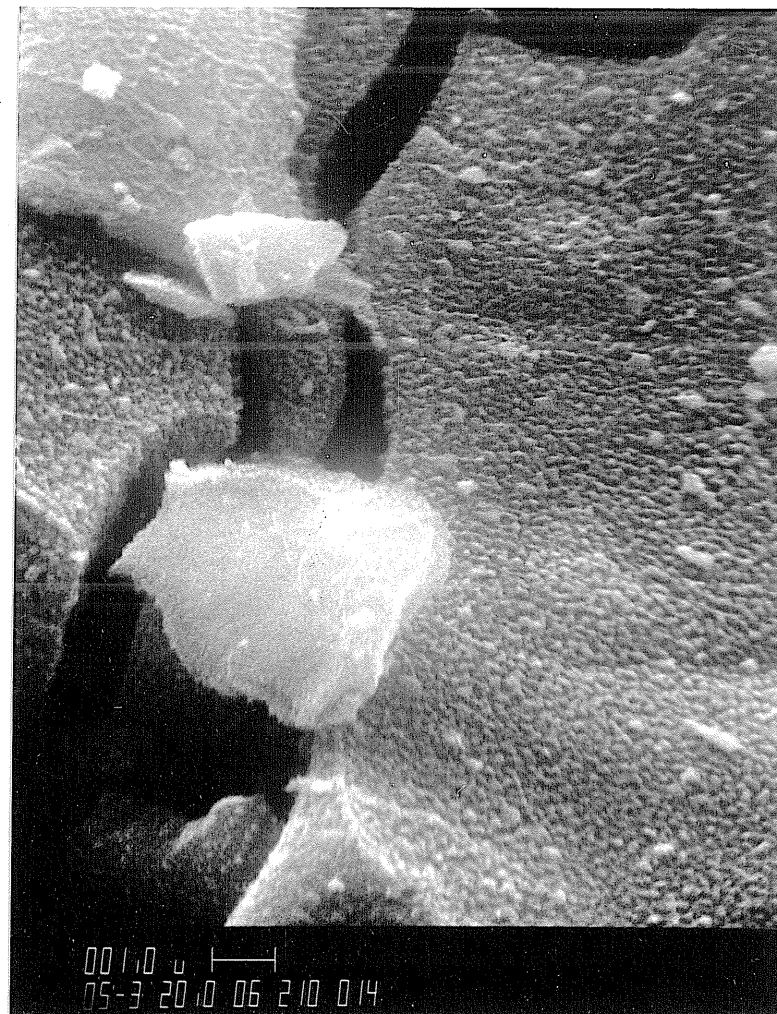


(d) Sulfided at 5000×

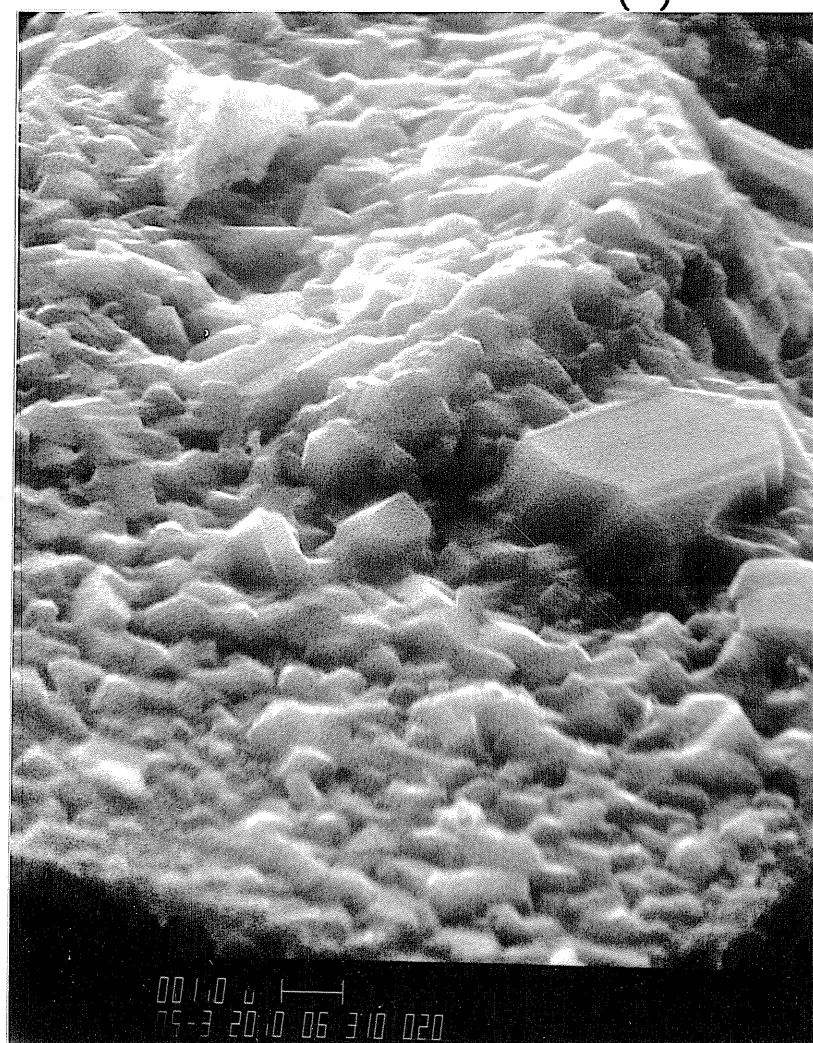
Figure 6.15: Scanning electron micrographs of F2A600 (markers are 1 μ m) in a fresh state (a), after reduction at 600°C (b), and after step-wise reduction-sulfidation at 600°C (c), with an enlargement of micrograph c (d).



(a) Fresh at 5000×



(b) Reduced at 5000×



(c) Sulfided at 5000×

Figure 6.16: Scanning electron micrographs of 2FA600 (markers are $1\mu\text{m}$) in a fresh state (a), after reduction at 600°C (b), and after step-wise reduction-sulfidation at 600°C (c).

CHAPTER VII

Conclusions and Recommendations

7.1 Conclusions

Mixed copper-aluminum oxides prepared by the citrate process over a composition range from $1:\frac{5}{2}$ to 5:1 in molar ratio of CuO to Al_2O_3 , and over a calcination temperature range from 350°C to 900°C consist of varying amounts of compound oxide, CuAl_2O_4 , and mixed oxide, CuO and Al_2O_3 , with the fraction of compound oxide increasing with calcination temperature. Extraction of these mixed copper-aluminum oxides with a solution of hot nitric acid removes bulk CuO leaving behind CuAl_2O_4 , and possibly smaller amounts of bulk CuO in close association with Al_2O_3 . X-ray diffraction (XRD) patterns of these mixed copper-aluminum oxides indicate a high content of crystalline phases, and contain no evidence of alumina, suggesting that alumina is present as microcrystallites ($\leq 50\text{\AA}$).

In contrast, XRD patterns of mixed iron-aluminum oxides prepared by the citrate process indicate a high content of amorphous phases in addition to a fraction of crystalline, iron-containing phases. Furthermore, mixed iron-aluminum oxides that contain a molar ratio of either 1:1 or 2:1, Fe_2O_3 to Al_2O_3 , and that are calcined between 600°C and 800°C consist, predominantly, of a mixture of Fe_2O_3 and Al_2O_3 , and smaller amounts of Fe_3O_4 and FeAl_2O_4 . Mixed iron-aluminum oxides that contain a molar ratio of 1:2, Fe_2O_3 to Al_2O_3 , and that are calcined between 600°C and 800°C , however, contain varying amounts of compound oxide, FeAl_2O_4 , and mixed oxide, Fe_2O_3 , Fe_3O_4 , and Al_2O_3 , with the fraction of compound oxide apparently decreasing with increasing calcination temperature.

Temperature-programmed reduction (TPR) of pure CuO to elemental copper is rapid, complete by a temperature of 270°C . Likewise, reduction of the

major fraction of the bulk CuO in mixed copper-aluminum oxides is rapid. By contrast, the CuAl_2O_4 component, the form of CuO in close association with Al_2O_3 , and a certain fraction of bulk CuO reduce very slowly. The latter two components are formed in mixed copper-aluminum samples prepared by calcination at temperatures between 350°C and 700°C. In addition, XRD patterns of these samples show an anomalous intensity for the CuO $\langle 002 \rangle$ peak, which is attributed to the close association between CuO and Al_2O_3 . Diffuse reflectance spectra of these samples indicate a small amount of octahedrally coordinated Cu^{+2} in addition to bulk CuO, suggesting that the close association between CuO and Al_2O_3 resembles the "surface spinel" species reported to exist in certain CuO/ Al_2O_3 catalysts. Finally, Raman spectra of these samples show that the interaction between CuO and Al_2O_3 affects an unassigned vibration between copper and oxygen atoms such that the characteristic peak is shifted in frequency from that for CuO or CuAl_2O_4 .

TPR of pure Fe_2O_3 consists of two stages corresponding to a step-wise conversion of, first, Fe_2O_3 to Fe_3O_4 , and, second, Fe_3O_4 to Fe, with a maximum reaction rate occurring during the second stage. On the other hand, TPR of mixed iron-aluminum oxides is more complex, with three stages of reduction and a maximum rate occurring during the first stage of reduction. In addition, the nature of the second and third stages of reduction for different mixed iron-aluminum oxides suggests the presence of slowly reducing forms of Fe^{+3} , $\text{Fe}^{+\frac{8}{3}}$, and Fe^{+2} . These species are proposed to be, for Fe^{+3} , a surface phase that results from close association between Fe_2O_3 and Al_2O_3 as is observed in certain $\text{Fe}_2\text{O}_3/\text{Al}_2\text{O}_3$ catalysts; for $\text{Fe}^{+\frac{8}{3}}$, a close association between Fe_3O_4 and Al_2O_3 and a solid solution between Fe_3O_4 and FeAl_2O_4 ; and for Fe^{+2} , the compound FeAl_2O_4 .

The mechanism for TPR of mixed iron-aluminum oxides is more complex than that for TPR of mixed copper-aluminum oxides because of the greater number of oxidation states observed for iron (i.e., +3, $+\frac{8}{3}$, +2, and 0) as compared to copper (i.e., +2, +1, and 0). For example, in mixed copper-aluminum oxides, a large fraction of bulk CuO reduces in series with CuAl_2O_4 , with slowly reducing forms of CuO reducing in parallel with CuAl_2O_4 . CuO reduces directly to Cu with no detectable intermediates, while the reduction of CuAl_2O_4 proceeds by the formation of CuAlO_2 as the primary intermediate, and some Cu_2O as a secondary intermediate. The formation of CuAlO_2 preserves copper in a +1 oxidation state for temperatures up to 630°C because of a slow conversion of CuAlO_2 to Cu, while Cu_2O reduces rapidly to Cu. On the other hand, intermediates to the reduction of mixed iron-aluminum oxides include Fe_3O_4 , $\text{Fe}(\text{Fe}_{1-x}\text{Al}_x)_2\text{O}_4$, and FeAl_2O_4 . The rates of reduction of Fe_2O_3 to Fe_3O_4 , and of Fe_3O_4 to FeAl_2O_4 are comparable during the first stage of reduction; however, subsequent stages of reduction reveal slowly reducing forms of Fe_2O_3 and Fe_3O_4 , and reveal that FeAl_2O_4 has the slowest reduction kinetics of all the identified iron-containing species.

Results from independent experiments indicate sintering of CuAl_2O_4 at temperatures in excess of 700°C. For example, in fresh Cu-Al-O materials calcined at different temperatures, a plot of the Carter equation reveals a marked reduction in activation energy for a calcination temperature between 700 and 800°C that is due to the formation of sintered CuAl_2O_4 (Chapter II, Section 2.3.2). In substantiation of this observation, the size of CuAl_2O_4 crystallites in fresh samples increases dramatically for a calcination temperature between 700°C and 800°C (Chapter III, Section 3.4). Some indirect evidence for sintering of CuAl_2O_4 at temperatures in excess of 700°C includes the observation

of a sharp transition from a rapid weight loss to a very slow weight loss at a conversion of 88% during isothermal reduction (at a temperature of 774°C) of a sample prepared by calcination at 900°C (Chapter IV, Section 4.4), and the detection of CuAlO_2 after regeneration of a sulfided sample at 900°C which is the result of incomplete oxidation because of the formation of sintered CuAl_2O_4 (Chapter V, Section 5.4.2).

The extent to which copper sinters during reduction depends on the nature of the fresh sample. For example, the reduction of a sample containing 95 mole% mixed oxide, CuO and Al_2O_3 , leads to smaller copper particles as viewed by scanning electron microscopy (SEM) than reduction of a sample containing 6 mole% mixed oxide (micrographs 3.13d versus 3.14c, and 5.6b versus 5.11b). In addition, repeated, isothermal reduction-oxidation (REDOX) experiments show extensive sintering of copper in pure CuO as compared to a Cu-Al-O sample containing 95 mole% mixed oxide (Chapter III, Section 3.3.2). Similarly, repeated isothermal REDOX experiments show a higher conversion to CuAl_2O_4 for a sample containing 95 mole% mixed oxide than for a sample containing 4 mole% mixed oxide, indicating more extensive sintering of copper during the reduction of the latter sample. Finally, a sample containing 95 mole% mixed oxide attains a higher sulfidation rate following reduction than either pure CuO or a sample containing 4 mole% mixed oxide primarily because of the amount of sintered copper present in each case following reduction (Chapter V, Section 5.5.4).

Crystalline, nonstoichiometric sulfides are formed in the thermogravimetric analyzer (TGA) for all sulfidation experiments involving Cu-Al-O sorbents and Fe-Al-O sorbents. In the case of the Cu-Al-O sorbents, the crystalline sulfide phase is low digenite, $\text{Cu}_{9+x}\text{S}_5$, which results from quenching high digenite to

room temperature, while for the Fe-Al-O sorbents, the crystalline sulfide phase is low-temperature, monoclinic, 4C-type pyrrhotite, Fe_{1-x}S , which results from quenching high-temperature, hexagonal, 1C-type pyrrhotite to room temperature. For consecutive reduction-sulfidation, the sulfur uptake of pure copper oxide prepared by calcination at 550°C was higher than that of Cu-Al-O samples prepared by calcination at 550°C and 900°C . On the other hand, for consecutive reduction-sulfidation of iron-containing samples, the sulfur uptake of pure iron oxide prepared by calcination at 650°C was slightly lower than that of a sample containing a 2:1 molar ratio of Fe_2O_3 to Al_2O_3 and prepared by calcination at 600°C , however, slightly higher than that of a sample containing a 2:1 molar ratio of Fe_2O_3 to Al_2O_3 and prepared by calcination at 700°C . Furthermore, CuAl_2O_4 is resistant to sulfidation as compared to pure CuO or mixed oxide, CuO and Al_2O_3 , and, likewise, FeAl_2O_4 is resistant to sulfidation as compared to pure Fe_2O_3 or mixed oxide, Fe_2O_3 and Al_2O_3 . This may be a consequence of the fact that both CuAl_2O_4 and FeAl_2O_4 possess spinel-type structures.

For step-wise reduction-sulfidation of Fe-Al-O samples calcined between 600°C and 800°C and containing a 2:1 molar ratio of Fe_2O_3 to Al_2O_3 , the rate of sulfidation, and consequently, the sulfur uptake, decreases with increasing calcination temperature of the sample. This trend is not observed for samples containing either a 1:1 or 1:2 molar ratio of Fe_2O_3 to Al_2O_3 . In addition, extent of reduction correlates to extent of sulfidation in these experiments for all samples except those exhibiting slower rates of sulfidation or those prepared by calcination at 800°C . Finally, sulfur uptake is most strongly correlated to FeAl_2O_4 content, decreasing significantly with increasing FeAl_2O_4 content.

Regeneration of sulfided Cu-Al-O sorbents and sulfided CuO in air reveal an increased amount of copper sulfate formation in the presence of free alumina.

A mechanical mixture of CuO and γ -Al₂O₃, in fact, produces sulfate following sulfidation and regeneration under conditions in which pure CuO did not produce sulfate. Therefore, it appears that alumina enhances sulfate formation by chemisorbing SO₂, which experiences a high mobility on the alumina surface, and migrates to CuO to form sulfate.

7.2 Recommendations for Future Work

The work contained in this thesis is a compilation of several interesting results that open new doors for further research. It is the purpose of this section to enumerate research proposals for continued work in this area.

A central theme to this project is the “chemical interaction” proposed to exist between CuO and Al₂O₃, which is distinct from the stoichiometric compound, CuAl₂O₄, and is responsible for a sulfidation performance superior to that of pure CuO [1]. In addition, “chemical interactions” are reported to exist between Fe₂O₃ and Al₂O₃, and between Fe₃O₄ and Al₂O₃. In the case of Fe-Al-O sorbents, in contrast to Cu-Al-O sorbents, however, no stoichiometric compounds exist between Fe₂O₃ and Al₂O₃ or between Fe₃O₄ and Al₂O₃, but solid solutions have been reported to exist among some of these components at high temperatures [2-5]. As in the case of Cu-Al-O materials, Fe-Al-O materials demonstrate better H₂S removal than pure iron oxide because of increased stability of iron against reduction by interaction with alumina [6]. It is important to develop techniques to better quantify the interactions between alumina and transition metal oxides. In particular, XRD analysis of Fe-Al-O materials provides limited information because these materials exhibit a high content of amorphous phases. Other methods need to be developed for characteriza-

tion of mixed iron-aluminum samples such as wet chemical techniques, diffuse reflectance spectroscopy [7], Mössbauer spectroscopy [8-11], electron-spin resonance (ESR), and Raman spectroscopy. Once the physicochemical properties of Fe-Al-O samples are better understood, it should be possible to characterize Cu-Fe-Al-O materials for application to high-temperature desulfurization.

Chemical interactions proposed to exist between Al_2O_3 and copper oxide, or between Al_2O_3 and iron oxides in samples prepared by the citrate process are comparable to similar interactions reported for catalysts containing the transition metal oxide supported on alumina. Extension of this analogy to include other catalytic systems that have reported specific types of interactions between the supported phase and the support leads to new candidates to test as high-temperature desulfurization sorbents. For example, copper in alumina-supported CuCr_2O_4 is reported to be more stable than copper present as a surface spinel species in alumina-supported CuO [12]. Therefore, Cu-Cr-Al-O samples prepared by the citrate process might be good candidates for high-temperature H_2S removal, depending on the sulfidability of the phases present. It would also be interesting to test the feasibility of synthesizing Cu-Ti-O and Cu-Si-O samples by the citrate process, using the chloride salts of the component metal cations. Since silicon-supported CuO is reported to possess enhanced reducibility as compared to pure, unsupported CuO [13], this behavior should be reproducible by Cu-Si-O samples prepared by the citrate process. An experiment should be conducted to test for this anticipated behavior.

An investigation of the sulfidability and reducibility of several pure compound oxides would help to screen potential multicomponent metal oxides for application to high-temperature desulfurization. For example, CoAl_2O_4 has been reported to be unsulfidable at 400°C [14]. It would be informative to test

the sulfidability of this phase prepared by the citrate process at temperatures between 600°C and 900°C, and compare the results to the sulfidability of other spinels such as other aluminates (i.e., CuAl_2O_4 , FeAl_2O_4 , ZnAl_2O_4 , NiAl_2O_4 , MgAl_2O_4 , etc.) and ferrites (i.e., CuFe_2O_4 , MgFe_2O_4 , ZnFe_2O_4 , NiFe_2O_4 , etc.). Correlations between sulfidability and calcination temperature, sulfidability and reducibility, and sulfidability and equilibrium cation distribution of the spinel should be sought.

To convert the bench-scale synthesis of mixed metal oxides by the citrate process to an industrial scale, the drying step needs to be performed in a spray dryer. A small-scale apparatus for spray drying should be designed, keeping in mind the following: corrosion problems associated with the production of nitric acid from the nitrate anions of the component metal cations; environmental problems associated with the decomposition of nitric acid to NO_x , if the operating pressure and temperature favor this reaction; and flexibility problems associated with operating at different temperatures and pressures to tailor products to possess some range of specific physicochemical properties. In general, a spray dryer will have to operate at a higher temperature and pressure than those used in the vacuum evaporation step of the citrate process; however, the increased product homogeneity associated with a more rapid evaporation in the case of spray drying might offset the resulting decreased product surface area associated with the higher operating temperature. Based on evidence presented in this thesis, increased product homogeneity at the expense of decreased surface area will produce a high-performance desulfurization sorbent, if interactions between the metal oxides are maximized without compound formation (i.e., CuAl_2O_4 or FeAl_2O_4). The production of sorbents using spray drying as the evaporation step should be integrated with a project to develop techniques

of pelletizing sorbents while maximizing active surface area.

REFERENCES

1. Patrick, V., and Gavalas, G.R., accepted for publication in *Ind. Engrg. Chem. Res.*
2. Muan, A., "On the Stability of the Phase $\text{Fe}_2\text{O}_3 \cdot \text{Al}_2\text{O}_3$," *Amer. J. Sci.*, **256**, 413, 1958.
3. Atlas, L.M., and Sumida, W.K., "Solidus, Subsolidus, and Subdissociation Phase Equilibria in the System Fe-Al-O," *J. Amer. Cer. Soc.*, **41**(5), 150, 1958.
4. Turnock, A.C., and Eugster, H.P., "Fe-Al Oxides: Phase Relationships Below $1,000^\circ\text{C}$," *J. Petrol.*, **3**(3), 533, 1962.
5. Meyers, C.E., Mason, T.O., Petuskey, W.T., Halloran, J.W., and Bowen, H.K., "Phase Equilibria in the System Fe-Al-O," *J. Amer. Cer. Soc.*, **63**(11-12), 659, 1980.
6. Patrick, V., Gavalas, G.R., and Sharma, P.K., in preparation.
7. Vratny, F., and Kokalas, J.J., "The Reflectance Spectra of Metallic Oxides in the 300 to 1000 Millimicron Region," *Appl. Spectrosc.*, **16**(6), 176, 1962.
8. Bhide, V.G., and Date, S.K., "Mössbauer Effect for Fe^{57} in Al_2O_3 —Effects of a Variety of Heat Treatments," *Phys. Rev.*, **172**(2), 172, 1968.
9. Yoshioka, T., Koezuko, J., and Ikoma, H., "Mössbauer Spectral Observations on the Supported Iron Catalyst," *J. Catal.*, **16**, 264, 1970.
10. Carbucicchio, M., "Mössbauer Analysis of Fe_2O_3 - MoO_3 Supported on SiO_2 and Al_2O_3 ," *J. Chem. Phys.*, **70**(2), 784, 1979.
11. Ying-Ru, D., Qi-Jie, Y., Yuan-Fu, H., Yong-Shu, J., and Jin-Heng, Q., "A Mössbauer Investigation of α - Fe_2O_3 Microcrystals Supported on γ -

- Al_2O_3 " in *Mössbauer Spectroscopy and Its Chemical Applications* ed. by J.G. Stevens and G.K. Shenoy (American Chemical Society: Washington, D.C., 1981), p.609.
12. Severino, F., Brito, J., Carías, O., and Laine, J., "Comparative Study of Alumina-Supported CuO and CuCr_2O_4 as Catalysts for CO Oxidation," *J. Catal.*, **102**, 172, 1986.
 13. Jenkins, J.W., McNicol, B.D., and Robertson, S.D., "Characterized Catalysts via Temperature-Programmed Reduction," *Chem. Technol.*, **7**, 316, 1977.
 14. Chung, K.S., and Massoth, F.E., "Studies on Molybdena-Alumina Catalysts VIII. Effect of Cobalt on Catalyst Sintering," *J. Catal.*, **64**, 332, 1980.